

A SEARCH FOR WINO PAIR PRODUCTION WITH $B - L$ R -PARITY VIOLATING CHARGINO DECAY TO A TRILEPTON RESONANCE WITH THE ATLAS EXPERIMENT

Leigh C. Schaefer

A DISSERTATION

in

Physics and Astronomy

Presented to the Faculties of The University of Pennsylvania
in Partial Fulfillment of the Requirements for the Degree of Doctor of Philosophy
2019

Evelyn Thomson, Associate Professor, Physics and Astronomy
Supervisor of Dissertation

Joshua Klein, Edmund J. and Louise W. Kahn Professor, Physics and Astronomy
Graduate Group Chairperson

Dissertation Committee

James Aguirre, Associate Professor, Physics and Astronomy

I. Joseph Kroll, Professor, Physics and Astronomy

Elliot Lipeles, Associate Professor, Physics and Astronomy

Burt Ovrut, Professor, Physics and Astronomy

Evelyn Thomson, Associate Professor, Physics and Astronomy



A SEARCH FOR WINO PAIR PRODUCTION WITH $B - L$ R -PARITY
VIOLATING CHARGINO DECAY TO A TRILEPTON RESONANCE
WITH THE ATLAS EXPERIMENT

COPYRIGHT
2019
Leigh C. Schaefer

Acknowledgements

Firstly I'd like to thank Evelyn Thomson for being such a great and supportive advisor. This PhD would not have been possible without your mentorship and insight, about the big picture as well as the details of tackling a difficult task. Your dedication to, and patience in, instructing me, and your attention to my well-being as a person as well as a physicist really made my time in graduate school not only enlightening and enriching but also enjoyable. I would not have had nearly as successful and rewarding a grad school experience if it were not for your guidance. You've been, and I'm sure will continue to be, such a wonderful rôle model. Thanks as well to all the Penn ATLAS faculty for being great surrogate advisors: Joe Kroll, Elliot Lipeles, and Brig Williams. The supportive environment in the group was also crucial to my success, and I'm sure to the success of all students in the group. The collaborative example set by the faculty really informs and cultivates the cooperation among the students, and it's one of the best things about the Penn ATLAS group.

Thanks to the formative advisors and instructors I had before joining Penn, who established my love of physics and molded my scientific thinking: James Battat, Kate Scholberg, and Mr. Bross. Thanks as well to all the Bryn Mawr physics faculty: Peter Beckmann, Mike Noel, Michael Schulz, May Cheng, Liz McCormack, and Mark Matlin; and thanks to Miss Albarelli for encouraging me to consider a women's college. I doubt I would have majored in physics in undergrad, much less gotten a PhD, if it weren't for the encouragement and guidance from each of you.

Thanks to Brett Jackson and Jeff Dandoy, the physicists I most closely witnessed design and execute searches from start to finish. You both taught me an incredible amount about how to perform an analysis, how to meet deadlines, and how to be successful in a team. It was staggering and inspiring to watch the vigor and dedication you brought to your work, and I hope to embody that passion in my own endeavors.

Thanks to others I worked with closely on analysis: Giuseppe Lerner, Ian Dyckes, and Lucas

Flores. It was remarkably rewarding to work with each of you and create such powerful searches together.

Thanks to Burt Ovrut, Austin Purves, Sogee Spinner, and Sebastian Dumitru for the fruitful interdisciplinary collaboration. My thesis work would not have been possible without your phenomenological exploration of the $B - L$ model, and in our meetings I learned so much about the theory as well as the mind and thought process of a theorist.

Thanks to all the TRT software colleagues. Anatoli Romaniouk, Fred Luehring, Philippe Calfayan, Andrew Beddall, Narei Lorenzo Martinez, and Joany Manjarres, you were excellent leaders who taught by example how to be successful TRT software managers. A special thank you to Fred for your detailed explanations, throughout my time in the software group. Your advocacy and encouragement of new students is invaluable in the TRT group and in the collaboration overall. Many thanks as well to other distinguished TRT software experts KyungEon Choi, Doug Davis, Dimitrii Krasnopevtsev, Peter Hansen, and Christian Greife, among many others. Thanks as well to the TRT operations colleagues who have a magnificent amount of software knowledge: Dominik Derendarz and Andrea Bocci. It was a pleasure to work with all of you.

Thanks to all the senior grad students who helped get me started and welcomed me into the group, and taught me more than they know about being a successful grad student: Liz Hines, Kurt Brendlinger, Alex Tuna, Rami Vanguri, Jamie Saxon, Chris Lester, Jon Stahlman, Doug Schaefer, and John Alison. Thanks especially to Kurt for suggesting the local occupancy project to me, which got me involved in the TRT group, and again to Brett for spending countless hours explaining and reexplaining the fundamentals of particle physics and good coding practices, and for picking me up from the airport and walking me to CERN on my first day. Thanks as well to all the Penn postdocs that I haven't already mentioned: Joana Machado Miguéns, Sarah Heim, Keisuke Yoshihara, Tae Min Hong, Chris Meyer, and Shion Chen. Thanks especially to Joana for debugging HistFitter with me, and to Sarah for giving me a tour of the innards of ATLAS.

Thanks to all my grad student friends and colleagues who made working in DRL not only manageable but actually enjoyable: Rob, Billy, Will, Bijan, Khilesh, Joey, Rachael, Christian, Elodie, Ian, Lucas, Ben, and James. Together we really formed an unforgettable group culture. I'll miss all our outlandish lunchtime and coffee conversations, our HEST sessions, and all the pranks and jokes. Thanks Khilesh for managing the Kool Coffee Klub and designing the unmistakable Penn ATLAS logo. Joey, thanks for your constant cheerfulness, in particular laughing so loudly I could hear you from the elevators. Bijan, thanks for teaching me about Persian folklore and bingeing mockumentaries with me. Thanks to the three of you for hosting the break room office.

Your hospitality and willingness to be distracted were greatly appreciated by everyone in the group. Elodie, thanks for all the strolls and chats, both at Penn and at CERN, always validating and encouraging me. Will, thanks for being a great office mate for all these years, even though we could never agree on the optimal office temperature. James, thanks for the unique greetings. It has really been a pleasure to watch you learn and grow over the past few years, and I know you're going to rock the full Run 2 stop search.

Thanks to my wonderful Candyland/Marigold Memory Palace roommates: Bijan, Rob, and Jake. I know that in spirit we have finally changed the WiFi password. Thanks as well to Kelvin and Sophia, for the real talk and late nights. All of you truly made Geneva feel like home and I'll always hold our time there near to my heart.

Thanks to all my friends outside of Penn ATLAS: Lisa, Erika, Jacinda, Cat, Paulinha, Ramya, and Eric. I love each of you dearly and the past 6+ years definitely would have been a less exciting, formative, and fun time of growth and learning without each of you. I'll always cherish ranking Philly's dim sum options, gossiping at the bench press (and bumping up our weight too!), exploring new music and going to concerts, marveling at the magic of the SEPTA trolley, and just spending time together. As much as I love the city of Philadelphia, I know you are the ones who make it so special to me.

Finally, thanks to my family. Mom and Anna, thanks for supporting me unconditionally from the start, even when I didn't want you to look at me, talk to me, or touch me. Dad, thanks for nurturing my scientific curiosity. I miss you. Little, thanks for always greeting me at the door and for being the sweetest lap cat. Aunt Susan and Uncle Frank, thanks for making sure I always got to school on time and for always making me do my own research instead of just telling me the answer. Mr. and Mrs. Wilkoc, thanks for your constant support and friendliness. I know I owe this PhD to all of you and I love you all so much.

ABSTRACT

A SEARCH FOR WINO PAIR PRODUCTION WITH $B - L$ R -PARITY VIOLATING CHARGINO DECAY TO A TRILEPTON RESONANCE WITH THE ATLAS EXPERIMENT

Leigh C. Schaefer

E. Thomson

This dissertation presents several searches for supersymmetric partners (superpartners) to Standard Model particles. These analyses are performed using proton-proton collision data from the Large Hadron Collider (LHC) collected by the ATLAS experiment. The $B - L$ Minimal Supersymmetric Standard Model predicts that these superpartners will have small R -parity violating couplings and the lightest superpartner will therefore decay to Standard Model particles. Two searches are presented for pair production of scalar top quarks (stops) which subsequently decay to a b -quark and a charged lepton. Limits are set as a function of the stop decay rate to each lepton flavor. The first analysis, performed with 20.3 fb^{-1} of $\sqrt{s} = 8 \text{ TeV}$ data, sets limits on the stop mass between 500 and 1000 GeV, while the second analysis, which used 36.1 fb^{-1} of $\sqrt{s} = 13 \text{ TeV}$ data, sets stop mass limits between 900 and 1500 GeV. In both analyses, the best limits are achieved for the scenario where the stop decays to a b -quark and an electron more than 95% of the time. Additionally, a search for charged and neutral winos (superpartners to the Standard Model gauge bosons) is presented. One possible decay of the charged wino is to a charged lepton and a Z boson. If the Z then also decays to two charged leptons, the four-vector of the three leptons reconstructs that of the charged wino. In this way, the wino search is performed via a trilepton mass resonance. This search utilizes several reconstruction techniques to have sensitivity to many different charged and neutral wino decays in addition to the trilepton resonance. Stringent limits are set on the wino mass for many possible lepton and boson branching ratios. This analysis uses 139 fb^{-1} of $\sqrt{s} = 13 \text{ TeV}$ data and it represents the first trilepton resonance result in the campaign of analyses performed with 13 TeV LHC data.

Contents

Acknowledgements	iii
Abstract	vi
Contents	vii
List of Tables	xi
List of Figures	xiii
List of Common Abbreviations	xviii
Preface	xx
1 Introduction	1
2 Theoretical Framework	3
2.1 The Standard Model	3
2.2 Supersymmetry	5
2.2.1 R -parity violating SUSY	7
2.3 The $B - L$ model	8
2.3.1 Theoretical motivation	8
2.3.2 Phenomenology of the $B - L$ MSSM	9
2.3.3 The stop LSP	11
2.3.4 The wino LSP	13

3	LHC and the ATLAS Detector	21
3.1	The Large Hadron Collider	21
3.2	The ATLAS Detector	25
3.2.1	The Inner Detector	27
3.2.1.1	Pixel Detector	27
3.2.1.2	Semiconductor Tracker	27
3.2.1.3	Transition Radiation Tracker	28
3.2.2	The Calorimeters	29
3.2.2.1	Liquid Argon Calorimeters	30
3.2.2.2	Tile Calorimeters	31
3.2.3	The Muon Spectrometer	31
3.2.4	Particle Identification and Reconstruction	32
3.2.5	The Trigger System	34
4	Interpreting Data from the TRT	36
4.1	Tracking in the TRT	36
4.2	Electron Identification in the TRT	40
4.3	TRT Local Occupancy	41
4.3.1	Occupancy Granularity	42
4.3.2	Comparison of Online and Offline Occupancy	51
4.3.3	Summary	56
4.4	Tracking at high luminosity in the TRT	57
5	Search for Stop LSP Decays to a b-jet and a Lepton	64
5.1	Analysis Overview	65
5.1.1	Leptonic event selection	65
5.1.2	Branching ratio reweighting	66
5.1.3	Backgrounds	67
5.2	Run 1 analysis	70
5.2.1	Dataset and Monte Carlo simulated samples	70
5.2.2	Event Reconstruction	71
5.2.3	Event Selection	73
5.2.4	Systematic Uncertainties	77

5.2.5	Results	80
5.3	Run 2 analysis	86
5.3.1	Dataset and Monte Carlo simulated samples	86
5.3.2	Event reconstruction	88
5.3.3	Event selection	90
5.3.3.1	Single-top control region	93
5.3.3.2	$t\bar{t}$ control region	94
5.3.3.3	Z/γ^* +jets control region	95
5.3.3.4	Validation regions	95
5.3.4	Systematic uncertainties	96
5.3.5	Results	99
5.4	Prospects	104
5.4.1	Similar searches	104
5.4.1.1	Third-generation leptoquark search	104
5.4.1.2	RPC stop searches	106
5.4.2	Future improvements to this search	107
6	Search for Wino LSP Decays with a Trilepton Resonance	109
6.1	Analysis Overview	111
6.2	Dataset and Monte Carlo simulated samples	114
6.3	Event Reconstruction	116
6.4	Fake Factor Method	120
6.5	Event Selection	125
6.5.1	3L regions	126
6.5.2	4L regions	133
6.6	Systematic Uncertainties	141
6.7	Results	145
6.7.1	Model-dependent exclusion fit	146
6.7.2	Model-independent fit	152
6.8	Prospects	152
7	Conclusion	154

Appendices	156
A 13 TeV Stop Search: Signal Region Optimization	157
B Wino Search: Truth Final States	164
C Wino Search: SROL4ℓ Object Matching	167
C.1 OL4 ℓ m_{Zl} optimization	167
C.2 HistFitter-based OL4 ℓ optimization	169
D Wino Search: Bin Size Optimization	171
D.1 Optimization Based On Individual Bins	171
D.2 Optimization Based On HistFitter	172
E Wino Search: Lepton ID Working Point Comparison	177
E.1 Electrons	177
E.2 Muons	178
F Wino Search: Overlap Removal	181
G Wino Search: Signal Contamination	184
H Wino search: 3ℓ Region Optimization	186
H.1 SROL3 ℓ	187
H.2 CRWZ	196
H.3 VRMet and VRmTmin	197
I Wino search: 4ℓ Region Optimization	198
I.1 4 ℓ 2Z optimization	199
I.2 SROL4 ℓ	201
I.3 SRTL	209
I.4 CRZZ	210
I.5 VRZZ	212
I.6 CRttZ	212
I.7 VRttZ	214
Bibliography	215

List of Tables

2.1	The values of the B and L quantum numbers for quarks q , anti-quarks \bar{q} , leptons ℓ and anti-leptons $\bar{\ell}$	7
5.1	Electron and muon triggers used for each year.	67
5.2	Summary of signal, control, and validation regions used for this analysis.	74
5.3	The number of expected signal events passing each of the signal region cuts.	74
5.4	The observed and expected event yields in the CRs and VRs.	77
5.5	Summary of the effect of each considered source of systematic uncertainty on the background estimate in SR400 and SR600.	80
5.6	The expected and observed event yields in SR400.	81
5.7	The expected and observed event yields in SR600.	81
5.8	The event and object kinematics for the two events passing the signal region selection. .	82
5.9	MC simulation details by physics process.	87
5.10	Summary of the selections of the signal, control, and validation regions.	93
5.11	Summary of the dominant experimental and theoretical uncertainties in SR800 and SR1100. .	98
5.12	The observed and expected background yields in SR800 and SR1100.	100
6.1	The chosen binning for the shape fit of the $m_{Z\ell}^{\text{shifted}}$ distribution.	114
6.2	Electron and muon triggers used for each year.	117
6.3	Summary of electron selection criteria.	118
6.4	Summary of muon selection criteria.	118
6.5	Summary of jet selection criteria.	119
6.6	Selection criteria used to define the Z/γ^* +jets dominated fake factor measurement region.	122
6.7	Selection criteria used to define the Z/γ^* +jets fake factor validation region.	123
6.8	The relative contributions of each process to the fake and total background in various analysis regions.	124
6.9	Kinematic selections for each region used in the wino analysis.	126
6.10	Expected pre-fit yields in all SRs for all SM backgrounds and two C1C1 mass points. . .	127
6.11	Expected pre-fit yields in all CRs and VRs for all SM backgrounds and two C1C1 mass points.	127
6.12	Breakdown of uncertainty on background estimates in SROL3 ℓ	142
6.13	Breakdown of uncertainty on background estimates in SROL4 ℓ	143
6.14	Breakdown of uncertainty on background estimates in SRTL	144

6.15	Normalization factors obtained from the background-only fit.	146
6.16	Expected and fitted results for all 3ℓ CRs and VRs.	147
6.17	Expected and fitted results for ZZ and ttZ CRs and VRs.	147
6.18	Expected and fitted results for SROL 3ℓ signal regions.	148
6.19	Expected and fitted results for SROL 4ℓ signal regions.	148
6.20	Expected and fitted results for SRTL signal regions.	151
A.1	Raw number of Monte Carlo events in SR800 and SR1100.	158
A.2	S/\sqrt{B} for various b -tagging working points, in SR800 and SR1100.	162
A.3	Raw number of signal Monte Carlo events for various b -tagging working points, in SR800 and SR1100.	163
A.4	Raw number of background Monte Carlo events for various b -tagging working points, in SR800 and SR1100.	163
A.5	Expected number of signal Monte Carlo events for various b -tagging working points, in SR800 and SR1100.	163
A.6	Expected number of background Monte Carlo events for various b -tagging working points, in SR800 and SR1100.	163
D.1	Bin widths tested, and the maximum $m_{Z\ell}$ value to which each width was tested.	173
D.2	The chosen binning for the shape fit of the $m_{Z\ell}$ distribution.	174
G.1	Effect of signal contamination on estimated sensitivity in CRWZ.	185
G.2	Effect of signal contamination on estimated sensitivity in CRZZ.	185
H.1	Raw MC yields for each background process in each 3ℓ region.	187
H.2	Signal contamination as a percentage of total background yield in each 3ℓ CR and VR.	187
I.1	Raw MC yields for each background process in each 4ℓ region.	199
I.2	Signal contamination as a percentage of total background yield in each 4ℓ CR and VR.	199

List of Figures

2.1	The fundamental particles which comprise the SM.	4
2.2	SM predictions and measured values for production cross-sections of various processes. .	6
2.3	Proton decay due to B - and L -violating couplings.	8
2.4	Parameter scan of couplings for R -parity violating and conserving points.	10
2.5	LSP likelihood in the $B - L$ MSSM.	11
2.6	Pair production cross-sections for SUSY particles.	12
2.7	Stop decay length as a function of θ_t	13
2.8	Ratio of $\text{BR}(\tilde{t} \rightarrow t\nu)$ to $\text{BR}(\tilde{t} \rightarrow b\ell)$ as a function of θ_t	13
2.9	Possible values of $\tilde{t} \rightarrow b\tau$ versus $\tilde{t} \rightarrow be$ branching ratio.	14
2.10	Mass splitting between LSP and nLSP for both charged and neutral wino LSP.	15
2.11	Mass spectrum of the LSP for both charged and neutral wino LSP.	15
2.12	Branching ratios for the possible boson decay channels of the charged wino LSP, split into various $\tan\beta$ ranges and shown for several mass values.	16
2.13	Branching ratios for the possible boson decay channels of the neutral wino LSP, split into various $\tan\beta$ ranges and shown for several mass values.	17
2.14	Branching ratios for the possible lepton decay channels of the charged wino LSP, split into the boson decay types and shown for the normal and inverted neutrino hierarchies as well as two possible values of θ_{23}	18
2.15	Branching ratios for the possible lepton decay channels of the neutral wino LSP, split into the boson decay types and shown for the normal and inverted neutrino hierarchies as well as two possible values of θ_{23}	19
2.16	Decay length of charged wino LSP as a function of its mass, shown for both normal and inverted neutrino hierarchies.	20
2.17	Decay length of neutral wino LSP as a function of its mass, shown for both normal and inverted neutrino hierarchies.	20
3.1	The LHC and the CERN accelerator complex.	22
3.2	Total luminosity delivered to ATLAS as a function of data-taking year.	23
3.3	Mean number of interactions per crossing for all Run 2 data-taking years.	24
3.4	Peak instantaneous luminosity delivered to ATLAS in 2015 and 2018.	24
3.5	Event display of a high-pileup event.	25
3.6	General cut-away view of the ATLAS detector.	26

3.7	The ATLAS Inner Detector.	28
3.8	The ATLAS Calorimeter system.	30
3.9	The ATLAS Muon System.	31
3.10	Schematic illustrating the detector signatures of various Standard Model particles.	33
4.1	Drift radius as a function of drift time in the TRT.	37
4.2	TRT hit type classification.	39
4.3	High threshold probability as a function of Lorentz factor.	40
4.4	Global TRT occupancy as a function of $\langle\mu\rangle$	42
4.5	Global TRT occupancy distribution.	43
4.6	Distributions of partition occupancies as a function of global TRT occupancy.	44
4.7	Distributions of local occupancies as a function of global TRT occupancy.	45
4.8	Partition average occupancy as a function of Global TRT occupancy.	45
4.9	Endcap wheel occupancy as a function of Global TRT occupancy.	46
4.10	Barrel layer occupancy as a function of Global TRT occupancy.	46
4.11	Local track occupancy as a function of global TRT occupancy.	47
4.12	Local track occupancy as a function of track pseudorapidity.	47
4.13	Local track occupancy distributions based on different granularities.	48
4.14	Difference in local track occupancies based on different granularity calculations.	49
4.15	Relative difference in local track occupancies based on different granularity calculations.	49
4.16	Ratio of local track occupancies based on different granularity calculations.	50
4.17	CPU consumption per event as a function of granularity of local occupancy calculation.	51
4.18	Amount of CPU required to calculate local track occupancies for each track.	52
4.19	Example of a trigger RoI in the TRT barrel.	52
4.20	Difference in online and offline reconstructed track hits and local track occupancy.	54
4.21	Difference in online and offline local track occupancy, as a function of global occupancy.	55
4.22	Difference in online and offline reconstructed track hits and local track occupancy, removing all zero-occupancy tracks.	55
4.23	Difference in online and offline local track occupancy, removing all zero-occupancy tracks.	56
4.24	Relative difference in online and offline local track occupancy, removing all zero-occupancy tracks.	56
4.25	Relative difference in online and offline local track occupancy as a function of offline global TRT occupancy, removing all zero-occupancy tracks.	57
4.26	Online local track occupancy as a function of offline local track occupancy, removing all zero-occupancy tracks.	57
4.27	Reason for failed TRT extension.	58
4.28	Average number of Loose and Tight tracks per event as a function of pileup.	59
4.29	TRT extension fraction as a function of $\langle\mu\rangle$, global TRT occupancy, and local track occupancy for various PHF cuts.	60
4.30	TRT extension fraction as a function of track occupancy for various PHF cuts, for “true” and “fake+pileup” tracks.	61
4.31	Number of TRT outliers on track for both successful and failed TRT extensions, for various PHF cuts.	61
4.32	Number of TRT tube hits on track, for various PHF cuts.	62
4.33	Momentum resolution for tracks with successful and failed TRT extensions, for various PHF cuts.	63
4.34	Momentum resolution for tracks with successful and failed TRT extensions and with PHF<0.5, for various PHF cuts.	63

5.1	Feynman diagram for stop pair production in the $B - L$ MSSM.	65
5.2	Efficiency of passing each 2012 trigger broken down by flavor channel.	68
5.3	Efficiency of passing either the EF_e24vhi_medium1, the EF_e60_medium1, or the EF_mu36_tight trigger for each flavor channel.	69
5.4	Efficiency of passing the single-electron 2012 triggers for several ranges of electron p_T	69
5.5	Position of the regions in the E_T^{miss} significance versus H_T space.	75
5.6	Distributions of the variables which are used to define the SRs.	76
5.7	The number of observed and expected events in the validation regions, inclusively and broken down by flavor channel.	78
5.8	The $m_{b\ell}^0$ distribution in Top VR 3 (left) and Z VR (right).	79
5.9	The H_T distribution in Top VR 3 (left) and Z VR (right).	79
5.10	$m_{b\ell}^0$ (left) and H_T (right) distributions in SR400.	80
5.11	Expected and observed limit on the branching ratios for the stop decaying to different lepton flavors shown for different stop mass hypotheses between 400 GeV and 1 TeV.	84
5.12	The observed mass limit on the stop at 95% CL.	85
5.13	Distributions of $m_{b\ell}^0$, $m_{b\ell}^{\text{asym}}$, H_T , $m_{\ell\ell}$, and $m_{b\ell}^1(\text{rej})$ in SR800.	92
5.14	Distributions of m_{CT} in CRst and $m_{b\ell}^1(\text{rej})$ in CRtt.	95
5.15	Comparison of the observed data and expected numbers of events in the CRs, VRs, and SRs.	96
5.16	Distributions of $m_{b\ell}^0$ in VR $m_{b\ell}^0$, $m_{b\ell}^1(\text{rej})$ in VR $m_{b\ell}^1(\text{rej})$, H_T in VR H_T , and $m_{\ell\ell}$ in VRZ.	97
5.17	Expected and observed limit curves as a function of \tilde{t} branching ratios for various mass values between 600 and 1500 GeV.	102
5.18	The observed lower limits on the \tilde{t} mass at 95% CL as a function of \tilde{t} branching ratios.	103
5.19	Pair production and decay of LQ $_3^u$	105
5.20	Expected and observed 95% CL upper limits on up-type third-generation leptoquark, for $\mathcal{B}(\text{LQ} \rightarrow b\tau) = 100\%$	105
5.21	Expected and observed 95% CL upper limits on up-type third-generation leptoquark, as a function of $\mathcal{B}(\text{LQ} \rightarrow b\tau)$ versus LQ mass.	106
5.22	Summary of the dedicated ATLAS searches for top squark (stop) pair production based on pp collision data taken at $\sqrt{s} = 13$ TeV.	107
5.23	Expected number of events with “visible” stops as a function of stop mass with 150 fb $^{-1}$ at $\sqrt{s} = 13$ TeV.	108
6.1	Feynman diagram for mass-degenerate chargino pair production and chargino-neutralino production, with at least one $\tilde{\chi}_1^\pm \rightarrow Z\ell \rightarrow \ell\ell\ell$ decay.	110
6.2	Schematic flow chart describing the object criteria for each SR.	113
6.3	$Z/\gamma^* + \text{jets}$ fake factors for electrons (left) and muons (right), binned in p_T^{cone}	123
6.4	Distributions of $m_{Z\ell}$, electron and muon multiplicity, and E_T^{miss} in VRZj.	124
6.5	N-1 distributions in SROL3 ℓ	129
6.6	$m_{Z\ell}$ distribution in SROL3 ℓ	129
6.7	N-1 distributions in CRWZ.	130
6.8	$m_{Z\ell}$ distribution in CRWZ.	130
6.9	N-1 distributions in VRMet.	131
6.10	$m_{Z\ell}$ distribution in VRMet.	131
6.11	N-1 distributions in VRmTmin.	132
6.12	$m_{Z\ell}$ distribution in VRmTmin.	132
6.13	N-1 distributions in SROL4 ℓ	135
6.14	$m_{Z\ell}$ distribution in SROL4 ℓ	135
6.15	N-1 distributions in SRTL.	136

6.16	$m_{Z\ell}$ distribution in SRTL.	136
6.17	N-1 distributions in CRZZ.	137
6.18	$m_{Z\ell}$ distribution in CRZZ.	137
6.19	N-1 distributions in VRZZ.	138
6.20	$m_{Z\ell}$ distribution in VRZZ.	138
6.21	N-1 distributions in CRttZ.	139
6.22	$m_{Z\ell}$ distribution in CRttZ.	139
6.23	N-1 distributions in VRttZ.	140
6.24	$m_{Z\ell}$ distribution in VRttZ.	140
6.25	Data/SM agreement in all CRs and VRs.	149
6.26	Data/SM agreement in all SRs.	150
6.27	Expected and observed limits for two wino masses, for $\mathcal{B}(\tilde{\chi}_1 \rightarrow \tau)=100\%$	151
6.28	Model-independent p-value and significance for any BSM processes in each $m_{Z\ell}^{\text{shifted}}$ bin.	152
A.1	Efficiency and raw MC yield as a function of cut on $m_{b\ell}^1(\text{rej})$	158
A.2	S/\sqrt{B} for $m_{\tilde{t}} = 1000$ GeV in the 2D planes of various discriminating variables, in SR800.	159
A.3	S/\sqrt{B} for $m_{\tilde{t}} = 1300$ GeV mass point in the 2D planes of various discriminating variables, in SR1100.	160
A.4	The b -tagging efficiencies as a function of jet p_T for the Fixed 77% working point.	162
B.1	Acceptance of each truth final state in SROL3 ℓ , SROL4 ℓ , and SRTL, for several wino mass points.	166
B.2	Acceptance of targeted truth final states in SROL3 ℓ , SROL4 ℓ , and SRTL, for several wino mass points.	166
C.1	The unit-normalized L_T distributions for various wino masses in OL4 ℓ event types.	168
C.2	The correct lepton selection efficiency as a function of L_T cut and wino mass in C1C1 OL4 ℓ event types, before any cuts are applied.	168
C.3	95% CL upper limit on the signal strength $\sigma/\sigma_{\text{SUSY}}$ for each C1C1 mass point in SROL4 ℓ , for various lepton matching schemes.	169
C.4	Relative difference between each lepton matching scheme and the best-performing scheme (“minimum”) for each C1C1 mass point.	170
D.1	$m_{Z\ell}$ distributions with corresponding fixed bin size Z_N ratio plots in each of the signal regions.	172
D.2	$m_{Z\ell}$ distributions with corresponding variable bin size Z_N ratio plots in each of the signal regions.	173
D.3	Upper limit on C1C1 $\sigma/\sigma_{\text{SUSY}}$ as a function of bin width, for each mass point in each SR.	175
D.4	Upper limit on C1C1 $\sigma/\sigma_{\text{SUSY}}$ as a function of bin width, for mass points 350 GeV and above in each SR.	176
E.1	True and fake electron multiplicity for each working point choice.	178
E.2	Signal efficiency as a function of signal mass (in GeV) for each WP choice in the preselection region.	179
E.3	True and fake muon multiplicity for each working point choice.	180
E.4	Signal efficiency as a function of signal mass (in GeV) for each WP choice in the preselection region.	180
F.1	b -jet multiplicity for each overlap removal scheme.	182

F.2	Leading electron p_T for each overlap removal scheme.	182
F.3	Signal efficiency as a function of chargino mass for each overlap removal scheme.	182
F.4	True electron multiplicity for each overlap removal scheme.	183
F.5	Fake electron multiplicity for each overlap removal scheme.	183
H.1	Expected yields of each background in SROL3 ℓ , before any cuts.	186
H.2	E_T^{miss} and m_T^{min} distributions for signal and background.	188
H.3	E_T^{miss} distribution as a function of truth final state for each event that was reconstructed as OL3 ℓ , for several C1C1 mass points.	189
H.4	E_T^{miss} as a function of $m_{Z\ell}$ for several mass points.	191
H.5	m_T^{min} versus m_T for various chargino mass points, as well as for WZ and all backgrounds.	192
H.6	Standard and alternate m_T^{min} for signal and background.	193
H.7	S/\sqrt{B} as a function of m_T^{min} and E_T^{miss} for several mass points.	194
H.8	$m_{Z\ell}$ before and after E_T^{miss} and m_T^{min} cuts in SROL3 ℓ	195
H.9	Expected yields of each background in SROL3 ℓ , assuming 140 fb $^{-1}$	195
H.10	Expected yields of each background in CRWZ, assuming 140 fb $^{-1}$	196
H.11	$\Delta R(Z, \ell)$ for signal and background in CRWZ.	197
H.12	Expected yields of each background in VRMet and VRmTmin, assuming 140 fb $^{-1}$	197
I.1	Expected yields of each background in SROL4 ℓ before any cuts are applied.	198
I.2	$m_{Z\ell}$ distributions for each tested $m_{\ell\ell}$ window in SROL4 ℓ	200
I.3	Expected background yields for each tested $m_{\ell\ell}$ window in SROL4 ℓ	201
I.4	$m_{Z\ell}$ distributions for each tested $m_{\ell\ell}$ window in SRTL.	202
I.5	Expected background yields for each tested $m_{\ell\ell}$ window in SRTL.	203
I.6	Expected background yields for each tested $m_{\ell\ell}$ window in CRZZ.	204
I.7	Expected background yields for each tested $m_{\ell\ell}$ window in VRZZ.	204
I.8	Boolean describing if event satisfies 4 ℓ 2Z criterion in SROL4 ℓ , before any cuts.	205
I.9	E_T^{miss} distribution for SROL4 ℓ events after 4 ℓ 2Z veto.	205
I.10	E_T^{miss} distribution as a function of truth C1C1 final state for each event that was reconstructed as OL4 ℓ	206
I.11	E_T^{miss} distribution for C1C1 final states which are targeted for, and reconstructed in, SROL4 ℓ	207
I.12	Flavor and sign breakdown for all SROL4 ℓ events after 4 ℓ 2Z veto, for the two leptons that are not assigned to the Z	207
I.13	A comparison of $m_{Z\ell}$ distributions before and after $E_T^{\text{miss, SF}}$ cut and 4 ℓ 2Z veto in SROL4 ℓ	208
I.14	Expected yields of each background in SROL4 ℓ , assuming 140 fb $^{-1}$	208
I.15	Boolean describing if event satisfies 4 ℓ 2Z criterion in SRTL, before any cuts.	209
I.16	E_T^{miss} distribution for SRTL events after 4 ℓ 2Z veto.	210
I.17	$m_{Z\ell}$ asymmetry distribution for SRTL events after 4 ℓ 2Z veto.	210
I.18	A comparison of $m_{Z\ell}$ distributions before and after $m_{Z\ell}$ asymmetry cut and 4 ℓ 2Z veto in SRTL.	211
I.19	Expected yields of each background in SRTL, assuming 140 fb $^{-1}$	211
I.20	Expected yields of each background in CRZZ, assuming 140 fb $^{-1}$	211
I.21	Expected yields of each background in VRZZ, assuming 140 fb $^{-1}$	212
I.22	Expected $t\bar{t} + V$ yields split into $t\bar{t}Z$, $t\bar{t}W$, and $t\bar{t}\gamma$, at preselection.	213
I.23	Expected background yields in the CRttZ region, assuming 140 fb $^{-1}$	213
I.24	$m_{Z\ell}$ distribution in the CRttZ region assuming 140 fb $^{-1}$	213
I.25	Expected background yields in the VRttZ region, assuming 140 fb $^{-1}$	214
I.26	$m_{Z\ell}$ distribution in the VRttZ region assuming 140 fb $^{-1}$	214

List of Common Abbreviations

BR branching ratio. [12](#), [14](#), [65–67](#), [105](#), [110](#), [113](#), [127](#), [150](#), [153](#), [155](#), [187](#), [197](#), [199](#)

BSM Beyond the Standard Model. [1](#), [5](#), [22](#), [34](#), [83](#), [100](#), [105](#), [153](#)

CERN the European Organization for Nuclear Research. [1](#), [22](#)

electron identification the process of discriminating between electrons and other particles, which leave similar signatures in the detector. [37](#), [42](#)

EWK electroweak. [4](#), [110](#), [111](#), [121](#)

HLT High Level Trigger. [52](#), [155](#)

ID Inner Detector. [28](#), [33](#), [36](#), [37](#), [90](#)

LHC Large Hadron Collider. [1](#), [7–9](#), [22](#), [155](#)

local track occupancy TRT occupancy along a track. Mathematically defined as a weighted average of the local occupancies L_i in each of the 192 TRT regions i , weighted by the number of track hits in that region n_i . [43](#), [45](#), [61](#), [155](#)

LSP lightest supersymmetric particle. [xiii](#), [7](#), [10](#), [15](#), [65](#), [105](#), [110](#)

MC Monte Carlo. [43–54](#), [71](#), [87](#), [115](#), [121](#), [158](#)

missing transverse energy the negative vector sum of the momentum of reconstructed and calibrated physics objects as well as the calorimeter energy clusters not associated with reconstructed objects. [34](#), [74](#)

MS Muon Spectrometer. [32](#), [33](#), [36](#), [90](#)

MSSM Minimal Supersymmetric Standard Model. [6](#)

nLSP next-to-lightest supersymmetric particle. [xiii](#), [14](#), [15](#)

npv number of primary vertices. [42](#)

- PDF** parton distribution function. [71](#), [88](#), [100](#), [106](#), [108](#), [116](#), [142](#)
- PHF** precision hit fraction. [40](#), [58](#), [155](#)
- PID** particle identification. [37](#), [42](#), [155](#)
- QCD** quantum chromodynamics. [3](#), [36](#)
- QED** quantum electrodynamics. [4](#)
- RoI** region of interest. [36](#), [52](#)
- RPC** *R*-parity conserving. [7](#), [10](#), [65](#), [105](#), [107](#)
- RPV** *R*-parity violating. [8](#), [10](#), [14](#), [65](#), [88](#), [105](#), [108](#), [110](#)
- Run 1** The LHC data-taking campaign from 2010 to 2012, operating at 7 TeV (2010-2011) and 8 TeV (2012) and with 50 ns bunch crossings. [22](#), [42](#), [65–67](#), [87](#), [96](#), [105](#), [109](#), [111](#), [154](#), [155](#)
- Run 2** The LHC data-taking campaign from 2015 to 2018, operating at 13 TeV and with 25 ns bunch crossings. [13](#), [22](#), [28](#), [38](#), [42](#), [66](#), [67](#), [87](#), [108–110](#), [155](#)
- SFOS** same-flavor, opposite-sign. [69](#), [74](#), [113](#), [123](#), [126](#), [129](#), [134](#), [154](#), [168](#), [189](#)
- SM** Standard Model of particle physics. [1](#), [3](#), [5](#), [7](#), [8](#), [22](#), [26](#), [33](#), [68](#), [74](#), [81](#), [87](#), [100](#), [105](#), [110](#), [111](#), [129](#), [142](#), [154](#), [155](#)
- SUSY** Supersymmetry. [1](#), [5](#), [7–9](#), [22](#), [105](#), [107](#), [110](#), [155](#)
- TR** transition radiation. [37](#), [41](#)
- TRT** Transition Radiation Tracker. [2](#), [28](#), [35](#), [37](#), [155](#)
- TTWD** track-to-wire distance. [38](#)
- vev** vacuum expectation value. [9](#), [14](#)

Preface

I started graduate school at Penn in September 2013 and officially joined the Penn ATLAS group in January 2014. For my first semester I was unsure which research group to join, but the decision was easy after Brig Williams invited me to a group lunch at Han Dynasty (the official Penn ATLAS lunch venue) in November 2013 “celebrating our first year students on (or interested in) ATLAS”.

An excerpt from Brig’s email:

Justin Khoury stopped by my office yesterday to express with great enthusiasm how well our first year HEP students did on his first quantum mechanics mid-term, both individually and collectively (making up more than 50% of the top third of the class).

Congratulations Will, Bill, Bijan, Joey, Khilesh, and Leigh.

It seems they have already gotten into the Penn graduate student culture of inspiring one another to great accomplishments.

I taught lab at that time so I initially declined the invitation, but Brig convinced me to join the lunch and in so doing (and as far as I can tell unknowingly) convinced me to join the group. This interaction is a perfect example of how strongly the faculty advocate for the students, even those who are not yet involved in the group. The same is true for the older graduate students who immediately made me feel very welcome and suggested that I work on projects in which they were personally invested, so that they helped me get ramped up on these projects. This camaraderie was a constant throughout my time in graduate school.

My first project with the group was getting involved on a search for a supersymmetric partner to the top quark (“stop”), using LHC data collected in 2012 with a center-of-mass energy of 8 TeV [1]. With advice from Evelyn Thomson and Joe Kroll, the analysis team primarily consisted of Brett Jackson, who really took me under his wing and taught me an incredible amount about

LHC physics. This analysis was of particular interest to the group because it is motivated by a model developed in part by Penn and former-Penn theorists Burt Ovrut, Sogee Spinner, and Austin Purves. I think my first project was checking the efficiency of various kinematic selections on our signal objects. My most notable contribution during this time was checking the signal efficiency of the triggers we planned to use. This led to the revelation that we needed to use an additional high-momentum lepton trigger to avoid a rapid drop in efficiency for the high mass signal points, which generally have decay products with higher momentum. I also performed truth-level studies to compare the exclusion potential of analyses performed with 8 TeV and 13 TeV data, which I presented as a poster at the US ATLAS meeting in Seattle in August 2014 [2].

In summer 2014, I made my first trip out to CERN to learn about the Transition Radiation Tracker (TRT), one of the ATLAS subdetectors. I was nominally on the TRT Data Acquisition (DAQ) team for those few weeks in the summer, although my most notable accomplishment in this group was getting the permissions necessary to crawl around the detector. Sarah Heim, at the time a Penn postdoc who led the DAQ team, took time out of her incredibly busy day to give me a tour around the cavern and to take the obligatory picture of me in front of the detector.

During the same CERN visit, I became involved in the TRT software group. Kurt Brendlinger proposed a TRT software project to me while we were sitting in Cobra (the Penn office at CERN). As a very active member of the electron identification efforts, Kurt recognized that it would be useful to have a local description of the occupancy surrounding a track in the TRT, so he suggested that I jump in and spearhead this effort. Ultimately TRT software ended up being the group I was most involved in throughout my graduate career, so I'm grateful to Kurt for suggesting this project to me that day in Cobra. I spent about a year working on the local occupancy studies while also taking classes and helping out where I could on the stop search. This project became my qualification task, which on completion deemed me worthy of being an author on the ATLAS collaboration. At this point I started to get involved in other aspects of the TRT software group, the grand majority of which will not be described in more detail in this dissertation, but which are outlined below.

I took many shifts to monitor the quality of the TRT data being collected. This consists of the prompt daily assessment of new data to ensure that its quality meets certain standards. This monitoring occurs in two stages for each data run: the rapid "Tier0" processing of new data is used to check for major issues in the detector during the run, such as noisy or dead parts of the detector, and to see if new calibrations are necessary. In the TRT, this is a calibration of the relation between drift radius and drift time, to ensure that the TRT tracks are as accurate as possible. If needed, a new calibration is then performed and uploaded to the database. In the second stage of

the monitoring, all the data is re-processed with any new calibrations or other database updates from all subdetectors, after which a second sign-off is performed for each run. This monitoring is crucial to the health of the ATLAS data, to ensure that all data is processed with good-quality calibrations, as well as to ensure that physics analyses only use data that is of good quality.

A few years after taking my first shift, I put some effort into improving the calibration procedure, in particular to keep an updated database of live and dead TRT straws. This database had not been regularly updated during data taking, but it is important to maintain a current list in order to accurately know which straws can have hits or not. This is very important for tracking as well as for occupancy calculations. I also put a large amount of effort into improving the documentation which the “shifters” use as guidelines.

Some time in the summer or autumn of 2015, I took over DAOD production for the TRT group. A DAOD, or Derived Analysis Object Data, is a type of data format which keeps all the useful information about each event and gets rid of as much of the useless information as possible. Of course each team has a different opinion on what is useful and what is useless, so there are many DAOD formats in the collaboration. I took on the role of producing and maintaining the TRT DAODs for the use of everyone doing studies in the TRT software group. This required a surprising amount of samples, as most of the active work in the TRT software group is developing algorithms and tools which affect the output in the DAODs. This included, for example, different gas geometries (distributions of xenon and argon in the straws), different calibration procedures, different methods of simulating the pulse shape of a charged particle traversing a straw, or some combination thereof. Many iterations of samples were necessary as studies progressed. Sometimes it was necessary to do this from an early stage of simulated processing, called digitization, and this took a good amount of effort to stabilize as well, since this is a very CPU-intensive procedure. All the examples above are possible variations for simulated samples, but of course it was important to have data samples available for the group as well. In this context I developed a set of criteria to select and store specific events in the data samples, and reject all other events from the output. This was greatly beneficial to the size of the TRT DAODs, since only interesting events were being stored. In addition to creating the samples that were needed for everyone’s studies, a large part of my task was defining and adding all the variables that were needed in the TRT DAODs, as well as maintaining the storage and bookkeeping of all the samples, and documenting the procedure used.

In September 2016, I became coordinator of the TRT software group, in which role I served until the following September. I moved out to CERN for the 2017 calendar year to more effectively perform the associated duties. This is a managerial role usually reserved for postdocs, so it was

a very unique opportunity for me to take this leadership position in the collaboration. This role consisted of many responsibilities, which can generally be summarized by the jobs of coordinating the work within the group and communicating with other groups such as software management and tracking performance. Both of these roles required attending, and running, many hours of meetings every week. Coordinating the work within the group required me to understand all the projects being actively worked on in the group, motivate the analyzers to keep up good progress, and identify areas that could use more attention as well as the best person to provide that attention. This also consisted of making sure younger students had the support they needed and assigning appropriate projects to newcomers to the group. It also required a certain amount of crisis management, putting out any fires that may come up. One example of this sort of crisis was a drop in TRT track extension efficiency that was observed with high-pileup data, which we needed to understand and mitigate. The other managers and I worked incredibly quickly to provide a reasonable solution to this issue in order to reach a deadline for an upcoming software release. Beyond the work within the TRT software group, it was also my responsibility to present our progress to external groups. To this end I gave several collaboration-wide presentations, including an ATLAS week talk. I'm very grateful I had the opportunity to give a talk in the Main Auditorium at CERN during my time in graduate school, although each of these meetings made me keenly aware of how difficult my first name is for Europeans to pronounce. I saw a moment of confusion on the face of a member of the ATLAS management before he called me Schaefer and later Catherine.

Around late summer 2016, efforts were underway to revamp the stop search with LHC data collected at the higher center-of-mass energy of 13 TeV [3]. The analysis team consisted of Evelyn Thomson and Jeff Dandoy, a Penn postdoc that joined the group in summer 2016, as well as three analyzers from the University of Sussex: Guiseppe Lerner, Kerim Suruliz, and Iacopo Vivarelli. TRT software coordinating took the grand majority of my time, but I helped with the stop search in a few ways. I optimized some selections like the b -tagging working point, and some kinematic cuts to define signal regions. I was able to present these results both at the American Physical Society's meeting of the Division of Particles and Fields at Fermilab in August 2017 [4], and as a poster in Particles In Collision in September 2017 in Prague [5]. I was awarded best poster at that conference, and my prize was a uranium-doped tumbler glass, which was super cool.

By the time my TRT responsibilities were over, the stop search was more or less finalized. With no observed deviations from the Standard Model, Evelyn, Jeff, and I started renewing conversations amongst ourselves and then with Burt, Austin, and Burt's then-new graduate student Sebastian Dumitru, to choose the next reasonable place to look for supersymmetry. We experimentalists were

intrigued by a final state involving a trilepton resonance, and we asked the theorists to investigate if this was a feasible and likely signature within their model. They really ran with this idea and delved into this new possibility, providing so much useful information for us to design a realistic search, and ultimately getting two papers out of the studies as well. This experience was very awe-inspiring and rewarding for both teams. It is certainly unique for experimentalists and theorists to meet weekly and compare notes, in order to design a search that's realistic within the framework of a certain model, and again speaks to the distinctive environment that is fostered in the Penn physics department.

The analysis that came from these conversations represents the bulk of my physics work in my graduate career. I led the effort of this analysis from start to finish, which was incredibly rewarding and enlightening. My efforts included generating signal samples for charged wino pair production, optimizing event reconstruction and selection in order to keep signal and reject background events, developing background estimation and limit-setting strategies, developing the framework, managing the lists, production, and storage of our samples, as well as documenting the entire procedure start to finish. Two other of Evelyn's graduate students were also quite involved in this analysis. Ian Dyckes drove the effort to estimate the background from fake leptons, as well as optimizing some object-matching strategies to reconstruct the correct trilepton mass. Lucas Flores spearheaded the generation of charged-neutral wino production, optimized the regions used to constrain the $t\bar{t}Z$ background and validate this constraint, and contributed to the choice of bin width used in the trilepton mass distribution. Last but not least, in addition to many great insights and ideas for the analysis as a whole, Jeff derived the theory uncertainties. The results from this analysis are still being finalized, so some results presented in this dissertation are still preliminary. The analysis team is working very actively so we expect to have final results soon.

All the projects I've worked on have been incredibly rewarding, especially as TRT software coordinator and leader of the wino analysis. I'm so grateful that I had the opportunity to work with such a large collaboration of extremely smart and dedicated physicists from all over the world, and I feel especially lucky to have been part of the very welcoming, encouraging, and collaborative environment in the Penn physics department. It was such a fulfilling experience and I know I will carry it with me wherever I go after this.

Leigh Catherine Schaefer

Philadelphia, September 2019

CHAPTER 1

Introduction

Particle physics has been a lively and exhilarating field for over a century. From the discovery of the electron to the Higgs boson, and everything in between, each discovery has led to a more complete understanding of the most fundamental building blocks of nature, with the goal of understanding the conditions immediately after the Big Bang and how these conditions evolved into the universe in which we live today.

Alongside the observation of each of these particles, and the development of more and more sophisticated experiments with which to search for them, were the development of theories to explain them all. These theories sometimes worked retroactively, trying to explain some phenomenon that had already been observed, and they sometimes worked proactively, predicting particles that had not yet been observed based on the knowledge at the time. These theories were accepted, rejected, and modified over time to adapt to the most recent observations, and ultimately coalesced into the so-called [Standard Model of particle physics \(SM\)](#). This is a quantum field theory which mathematically, and very elegantly, explains all of the known particles and their interactions. With the 2012 discovery of the Higgs boson by the ATLAS and CMS experiments, the SM is considered complete, meaning that all of the particles it predicts have been confirmed experimentally to exist.

However there are many experimental observations which are left with no feasible explanation in the SM. For this reason there are still many new “[Beyond the Standard Model \(BSM\)](#)” theories being developed, working proactively to try to explain these observations. One of the most popular of these theories is [Supersymmetry \(SUSY\)](#), which is actually comprised of a large suite of theories that fall under this umbrella term. SUSY (as well as most, if not all, BSM theories) predicts many new particles which are then enthusiastically searched for in experiments. Many of these searches are performed at the [Large Hadron Collider \(LHC\)](#) at the [European Organization for Nuclear Research](#)

(CERN), the world’s largest and highest-energy particle collider, and the experiments that collect its data, such as ATLAS.

This dissertation presents some of the research conducted with the ATLAS experiment to search for novel signatures of Supersymmetry, using LHC data from 2012 to 2018, and is organized as follows. Chapter 2 provides a brief explanation of the Standard Model, including some of its shortcomings. It then introduces Supersymmetry as providing solutions to these shortcomings, and explains the specific supersymmetric model that is used to motivate the searches presented in this thesis. One remarkable feature in this model is that the predicted supersymmetric particles can decay to SM particles, leading to unique experimental signatures. The experimental setup of the LHC as well as the ATLAS detector is described in Chapter 3, which also explains how the data collected is translated into information about the physics interactions created in the proton-proton (pp) collisions. Chapter 4 provides specific details about the [Transition Radiation Tracker \(TRT\)](#), one of the ATLAS subdetectors that contributes to the momentum measurement of charged particles and provides electron discrimination. This chapter presents efforts to maintain and improve the software analysis of the TRT data, to ensure that momentum measurements and electron identification are as accurate as possible in the difficult environments at the LHC. Chapter 5 details two searches for the supersymmetric partner of the top quark (called a “stop”) which were conducted with two independent LHC datasets. In both searches, the stop decays to a b -quark and a lepton, leading to final states with 2 leptons and 2 b -jets, which when paired correctly reconstruct the stop mass. Chapter 6 presents a search for the supersymmetric partner of the gauge bosons (called a “wino”). One interesting possibility is for the charged wino to decay to a Z boson and a charged lepton. If the Z boson then subsequently decays to a pair of charged leptons, the final state consists of three charged leptons which reconstruct the wino mass. The analysis presented in this chapter describes the trilepton resonance search for a wino signature. Finally, the dissertation will conclude in Chapter 7.

CHAPTER 2

Theoretical Framework

This chapter describes the theoretical background which motivates the research presented in the rest of this thesis.

2.1 The Standard Model

The [SM](#) of particle physics is a very well-established quantum field theory which mathematically explains much of the known phenomena in this field [6–8], in particular all the known particles, which are summarized in Figure 2.1, and their interactions. These particles can be grouped into fermions, gauge bosons, and the Higgs boson. Fermions are spin-1/2 particles which comprise what is commonly considered matter, such as quarks and leptons. There are three generations (flavors) of each fermion type; the only difference between generations is their mass. Gauge bosons are spin-1 particles which mediate the interactions between other particles. The Higgs boson is a spin-0 particle which is responsible for the mass of all fundamental particles as well as the breaking of the electroweak symmetry into its electromagnetic and weak components via the Higgs mechanism, as described below. The SM encompasses the current understanding of the electromagnetic, weak, and strong interactions with a local (gauge) $SU(3)_C \times SU(2)_L \times U(1)_Y$ symmetry.

The $SU(3)_C$ symmetry describes the strong force, or [quantum chromodynamics \(QCD\)](#). The strong force dictates interactions between quarks and gluons, and is mediated by massless gluons. Quarks and gluons are charged under a quantum number called “color” which can be red, green, or blue. Particles with color charge have never been observed to exist alone in nature. Rather, it is energetically favorable to pull new colored particles out of the vacuum and create a colorless state. This process is known as “hadronization”, as hadrons are colorless bound states of quarks.

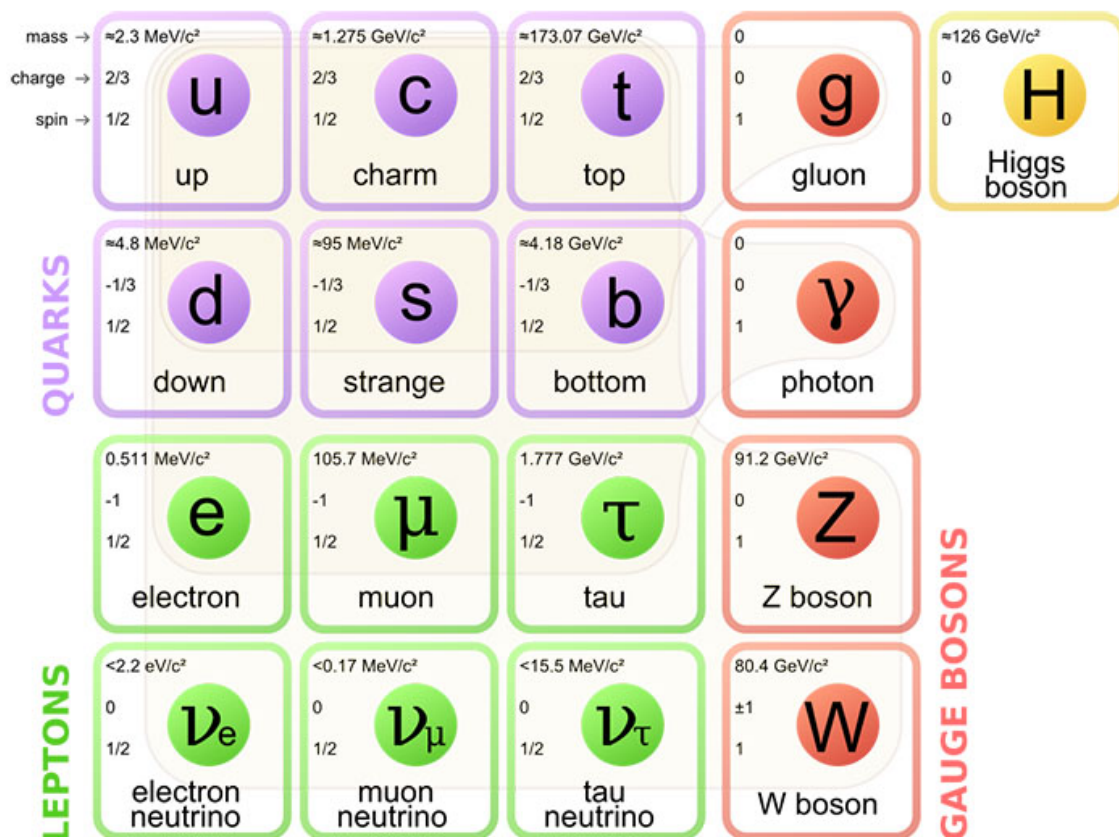


Figure 2.1: The fundamental particles which comprise the SM, grouped by type. The fermions are the quarks (purple) and the leptons (green). The bosons are the force-carriers (red) and the Higgs (yellow). The numbers in the top left of each box show, in descending order, the mass, electric charge, and spin of each particle [9].

The $SU(2)_L \times U(1)_Y$ symmetries describe the weak force and the electromagnetic force, or [quantum electrodynamics \(QED\)](#). At high energies these forces unite and so it is common to refer to them as the [electroweak \(EWK\)](#) interaction, and their separation at low energies is referred to as electroweak symmetry breaking. The fields which describe these interactions are the W and B fields, and the boson mass eigenstates are admixtures of these fields. QED is mediated by massless photons and describes QED interactions between charged particles. The weak force is mediated by massive W^\pm and Z bosons and describes weak interactions such as nuclear decay.

The SM has been extremely successful at predicting measured phenomena, as can be seen from Figure 2.2 which compares SM predictions for the production cross-sections of various processes to the measured values. However it also has many shortcomings; in particular it cannot provide

explanations for many observed phenomena in the universe. For example, gravity, the fourth fundamental force, is not included in the SM. It is reasonable to expect that a force carrier called a graviton would mediate gravitational force in the same way that other gauge bosons mediate the three forces in the SM, but this has not been successfully incorporated into the SM framework. It is necessary to have a quantum description of gravity at very high energies, namely at the Planck scale, which is roughly 10^{18} GeV. There is also no reason why the mass of the Higgs boson should be so light compared to the Planck scale. The physical mass of the Higgs is obtained through quantum corrections from every particle that couples to the Higgs. These corrections are proportional to a scale where new physics must become relevant. Indeed this has been explored in the context of grand unified theories (GUTs), which introduce new heavy gauge bosons that couple to the Higgs. These couplings correct the Higgs mass with terms that are proportional to the square of the GUT scale, which has current bounds above roughly 10^{16} GeV [6]. Since the Higgs mass corrections are proportional to such a large number, it is puzzling how the Higgs mass itself can be so small in comparison (roughly 125 GeV). This issue is called the “hierarchy problem”, and it raises the concern that this exact cancellation of the corrections, to obtain physical masses at the EWK scale, does not seem very natural. It is reasonable to wonder if this mass hierarchy can be explained by a more fundamental reason than this apparent “fine-tuning”. Additionally, the SM apparently has no particle which could be a candidate for the dark matter observed in the universe.

2.2 Supersymmetry

There are many theories, collectively referred to as **BSM** theories, which attempt to provide answers where the **SM** falls short. One of the most popular is **SUSY**, which elegantly resolves many of the SM’s issues [11]. SUSY introduces a new symmetry which relates fermions and bosons, such that the SM fermions each get a “superpartner” spin-0 particle called a scalar fermion or sfermion, and the SM bosons get superpartner spin-1/2 particles called winos, binos, and higgsinos. The winos and binos are components of supermultiplets corresponding to the W and B fields, and the higgsinos correspondingly belong to a supermultiplet with the SM Higgs. Two Higgs doublets are required to cancel anomalies, and the SM Higgs is an admixture of the neutral components of both of these doublets. The mass eigenstates of the SUSY spin-1/2 particles are called charginos and neutralinos, according to their electric charge, and are generally admixtures of the wino, bino, and higgsino fields, analogous to the Z and photon in the SM which are admixtures of the neutral W and B fields.

SUSY is able to resolve many of the mysteries left unanswered by the SM. Firstly, when SUSY

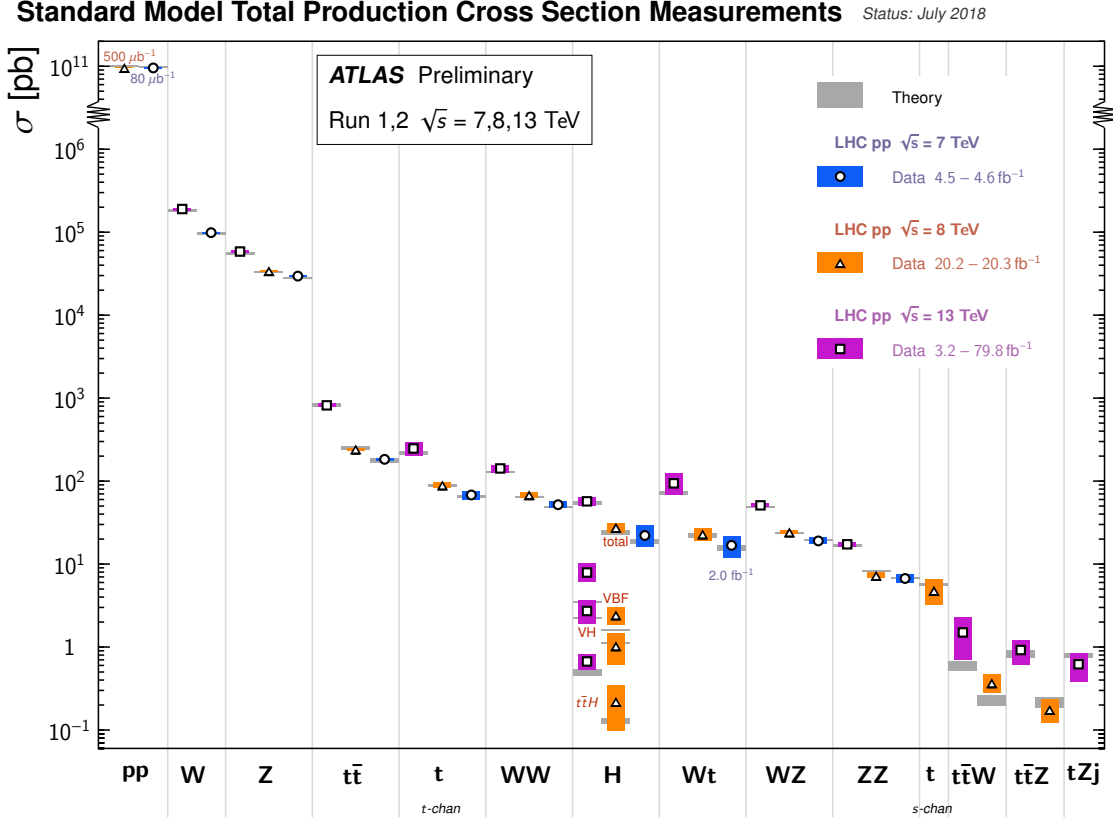


Figure 2.2: Comparison of SM predictions for the production cross-sections of various processes to the values measured by the ATLAS experiment using $\sqrt{s} = 7, 8$, and 13 TeV pp collisions [10].

is gauged, it automatically incorporates quantum gravity since the gravitino (the superpartner to the graviton) acts as mediator of local SUSY transformations. Additionally, each SUSY particle is directly related to a SM particle such that all their properties except their spin are in principle identical, including their masses. And because fermions and bosons contribute to the Higgs mass corrections with opposite sign, these corrections now cancel in a straightforward way and it is natural to obtain a Higgs mass at the EWK scale. Of course SUSY must be broken since we have not yet observed these extra particles at the corresponding SM masses. Finally, the suite of new particles introduced in SUSY provide several dark matter candidates.

There are many possible models which fall within the SUSY framework. One of the most common is the [Minimal Supersymmetric Standard Model \(MSSM\)](#) which is the simplest anomaly-free extension to the SM.

2.2.1 R -parity violating SUSY

The simplest SUSY superpotential that can be written following the description above includes terms which violate baryon number (B) and lepton number (L):

$$\begin{aligned} W_{\Delta L=1} &= \frac{1}{2} \lambda^{ijk} L_i L_j \bar{e}_k + \lambda'^{ijk} L_i Q_j \bar{d}_k + \mu^i L_i H_u \\ W_{\Delta B=1} &= \frac{1}{2} \lambda''^{ijk} \bar{u}_i \bar{d}_j \bar{d}_k. \end{aligned} \quad (2.1)$$

The supermultiplet Q_i has $B = +1/3$ and $L = 0$, and \bar{u}_i and \bar{d}_i have $B = -1/3$ and $L = 0$. Similarly L_i has $B = 0$ and $L = +1$ and \bar{e}_i has $B = 0$ and $L = -1$. H_u has $B = 0$ and $L = 0$. The B and L quantum numbers for SM matter and anti-matter particles are shown in Table 2.1. These terms lead to rapid proton decay as illustrated in Figure 2.3. This is obviously in conflict with observation, which sets the limit on proton lifetime above 10^{32} years [11]. To mitigate this obvious discrepancy, many SUSY models impose conservation of a quantum number called matter parity [12]:

$$P_M = (-1)^{3(B-L)} \quad (2.2)$$

or equivalently, R -parity which includes the spin s :

$$R = (-1)^{3(B-L)+2s}. \quad (2.3)$$

The inclusion of s is purely for convenience, since with this definition SM particles have $R = +1$ and SUSY particles have $R = -1$. The conservation of this quantum number forbids the terms listed in Equation 2.1 and so the proton's stability is ensured. This also requires an even number of SUSY particles at each vertex, so the lightest supersymmetric particle (LSP) cannot decay. Experimental limits from astronomical observations prohibit a stable LSP from having color or electric charge. Thus it provides a convenient dark matter candidate, and is invisible in experimental signatures at the LHC, typically leading to a large amount of missing energy. The SUSY models which require R -parity are called R -parity conserving (RPC) models.

Alternatively, it can be argued that imposing exact conservation of both B and L is somewhat excessive, since only one must be conserved to avoid processes such as the one shown in Figure 2.3

	B	L
q	$1/3$	0
\bar{q}	$-1/3$	0
ℓ	0	1
$\bar{\ell}$	0	-1

Table 2.1: The values of the B and L quantum numbers for quarks q , anti-quarks \bar{q} , leptons ℓ and anti-leptons $\bar{\ell}$.

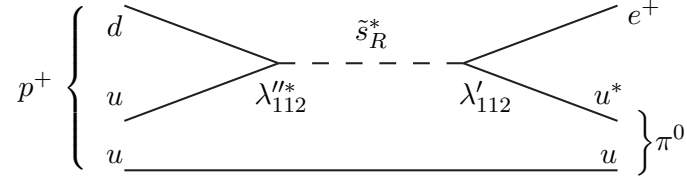


Figure 2.3: Proton decay via a strange squark due to B - and L -violating couplings. The B -violating vertex is on the left of the diagram and the L -violating vertex is on the right [11].

which threaten the stability of the proton. There are many SUSY models which do not impose R -parity, and hence are labeled *R -parity violating (RPV)* models. Experimentally, the most important difference between searches for RPC and RPV models is the fact that in RPV models, the LSP can decay to *SM* particles. This means that it can have color and electric charge without coming into conflict with experimental constraints. This opens a large suite of possibilities for experimental signatures at the *LHC*. These signatures also tend to have less missing energy than the RPC counterparts. In these models, the gravitino (the superpartner to the graviton) is typically considered a possible dark matter candidate.

2.3 The $B - L$ model

This section describes the specific *SUSY* model used to motivate the searches which will be presented in Chapters 5 and 6.

2.3.1 Theoretical motivation

The reason why R -parity conservation is imposed in many models, rather than directly imposing B and L conservation, is because these are not exactly conserved in nature. This is due to non-perturbative electroweak effects [13]. For example the process $p + n \rightarrow \bar{e} + \bar{\mu}$ is very rare but possible, and it violates both B and L by 2. It should be noted that these types of processes violate $B + L$ but never $B - L$.

Since $B - L$ is an exact, albeit accidental, symmetry in nature, it is reasonable to localize (gauge) it. From a philosophical point of view, all symmetries should be gauged, to preserve causality for example. However the simplest way to include this symmetry leads to a new chiral anomaly which leads to divergences in the *SM*. To avoid this, the sum of $B - L$ needs to equal 0 for all fermions in a generation. The sum of the left-handed states already equals 0: the up quark and down quark

states add to 2 and the electron and neutrino add to -2 . However for the right-handed states, the sum of $B - L$ equals -1 , since there is no right-handed neutrino in the SM. Hence to make a theory that includes a gauged $U(1)_{B-L}$ symmetry anomaly-free, right-handed neutrinos, along with their superpartners, need to be added to the collection of particles [14–17].

It should be noted that adding a $U(1)_{B-L}$ gauged symmetry to a theory does not automatically imply that R -parity is violated [18]. Indeed if we add to the theory two extra Higgs singlets, one with $B - L = 2$ and the other with $B - L = -2$, then either the Higgs singlets (with even $B - L$) or the right-handed sneutrinos (with odd $B - L$) can break the $B - L$ symmetry. If the symmetry is broken with one of these new Higgs singlets, then R -parity is conserved. On the other hand if the symmetry is broken with a right-handed sneutrino, then R -parity is broken. By scanning the relevant parameters, it was found that R -parity is more often broken than not, meaning that the $B - L$ symmetry is more often broken by the right-handed sneutrinos than by the Higgs singlets. This can be seen in Figure 2.4 which shows the correlation between the three couplings between singlets and sneutrinos. Thus it is reasonable to assume that the right-handed sneutrinos obtain a vacuum expectation value (vev) which then spontaneously breaks the $B - L$ symmetry as well as SUSY [14–17, 19–21]. This minimal $B - L$ model violates lepton number but not baryon number. The couplings for RPV are highly suppressed as they are related to the neutrino masses, and the model is consistent with the experimental bounds on proton decay and lepton number violation.

The remainder of this thesis will focus on scenarios where $U(1)_{B-L}$ is broken by right-handed sneutrinos, leading to R -parity violation. There is also a small vev of the left-handed sneutrinos which is small enough to be negligible. This model of SUSY is called the $B - L$ MSSM. Something unique to this model is that it is also interesting from a “top-down” perspective, where studies of $E_8 \times E_8$ heterotic M-theory led to the exact symmetry group of the $B - L$ MSSM [19, 23–26]. For this reason it is uniquely interesting to study as a very realistic SUSY model which also works at unification energies.

2.3.2 Phenomenology of the $B - L$ MSSM

There have been several studies of how the $B - L$ MSSM would manifest at energy scales accessible at the LHC. This is achieved by scanning possible values for the soft SUSY breaking parameters, and then RG evolving them from the UV scale to the TeV scale. Any points in the scan which do not break $B - L$ symmetry as well as satisfying known low-energy phenomena, such as breaking EWK symmetry, having a 125 GeV Higgs boson, and satisfying lower bounds on all SUSY particles,

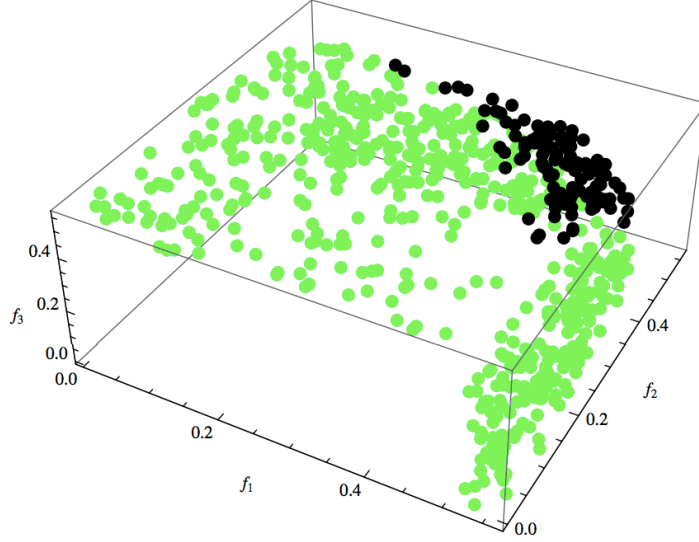


Figure 2.4: Correlation of the three couplings between Higgs singlets and right-handed sneutrinos f_i in a gauged $B - L$ theory. Green points represents points in this parameter space where R -parity is violated, and black points represent points where R -parity is conserved. Only fairly degenerate values of the three couplings lead to the black points. [22].

are rejected as invalid points.

The remaining valid points reveal the possible mass spectra of the $B - L$ MSSM in this scan. Because the [RPV](#) couplings in the $B - L$ model are related to the neutrino masses, they are very small and generally are only relevant for the decay of the [LSP](#), since this is disallowed in [RPC](#) models. Hence, of particular interest in this mass spectrum is the LSP. Figure 2.5 shows the likelihood that each SUSY particle is the LSP as a result of this parameter scan [27]. As discussed in Section 2.2, generally speaking, neutralinos ($\tilde{\chi}^0$) are an admixture of neutral winos ($\tilde{\chi}_W$), binos ($\tilde{\chi}_B$), and neutral higgsinos ($\tilde{\chi}_H$), and charginos ($\tilde{\chi}^\pm$) are an admixture of charged winos and charged higgsinos. In Figure 2.5, the charginos and neutralinos are classified according to sparticle type with the largest contribution. The SUSY particles that are never the LSP are omitted from this distribution.

Here it can be seen that there is not a constant likelihood of each sparticle to be the LSP. Rather some particles are much more likely than others; in particular the bino $\tilde{\chi}_B^0$ is the most likely LSP in this scan. However the experimental sensitivity of observing a certain signature is also not constant for all sparticle types; in particular binos cannot be directly pair produced from pp collisions, and the production cross-section for color-charged particles is much higher than all others, as shown in Figure 2.6. For this reason several LSP possibilities have been studied in detail, in order to target

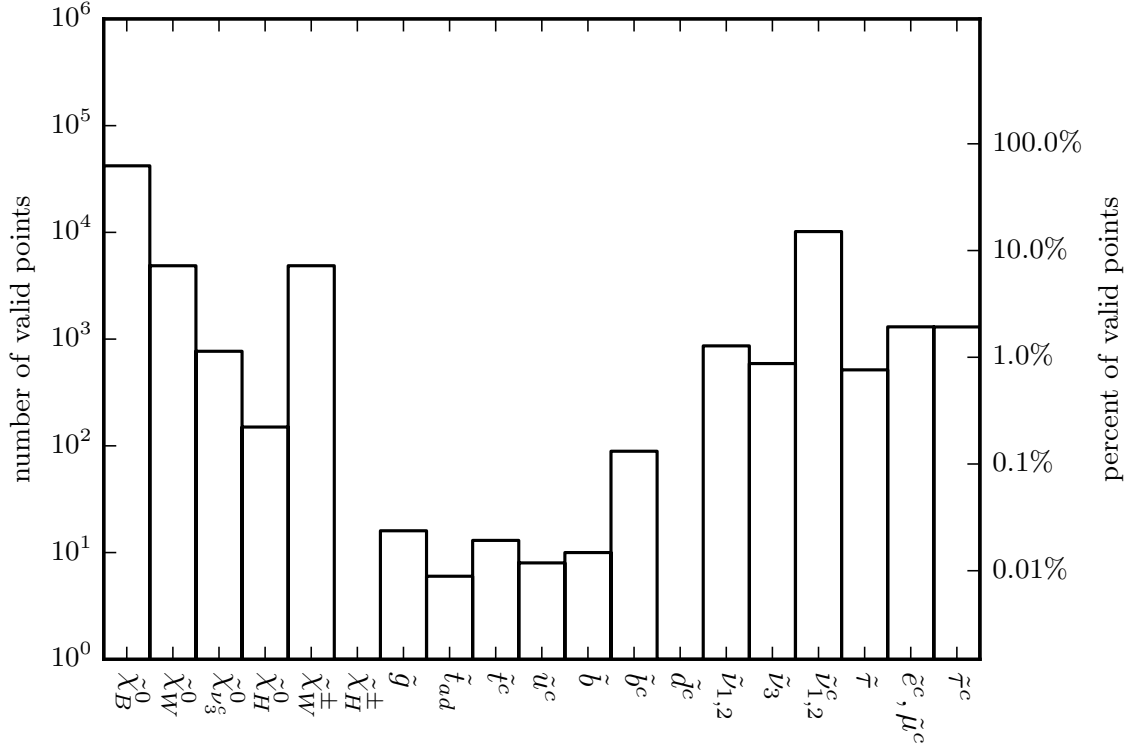


Figure 2.5: Number and percent of valid points with a given LSP obtained from scanning the soft SUSY breaking parameters and RG evolving them to the TeV scale [27].

not necessarily the most likely LSPs but rather those that would be visible at the LHC with the least data. In particular, the stop \tilde{t} [28, 29] and the wino $\tilde{\chi}_W$ [27, 30] LSPs have been studied in detail to understand the signatures they could leave at the LHC.

2.3.3 The stop LSP

The percent of points which have a stop LSP are shown in Figure 2.5 as \tilde{t}^c and \tilde{t}_{ad} , where the former represents a mostly right-handed¹ stop (over 99%) and the latter represents a left- and right-handed stop admixture. While the likelihood that either stop is the LSP is not large, the large production cross-section (see Figure 2.6) makes it an interesting LSP candidate to study as the LHC would be able to discover it with early data. The stop has two possible decays depending on its “right-handedness” θ_t [29]. It was found that a purely right-handed stop decays predominantly to a top quark and a neutrino, and it can have a decay length of 1 mm or more. Alternatively, if the stop is

¹As a scalar, a stop of course has no helicity of its own. The “helicity” of a sfermion corresponds to the helicity of its SM partner.

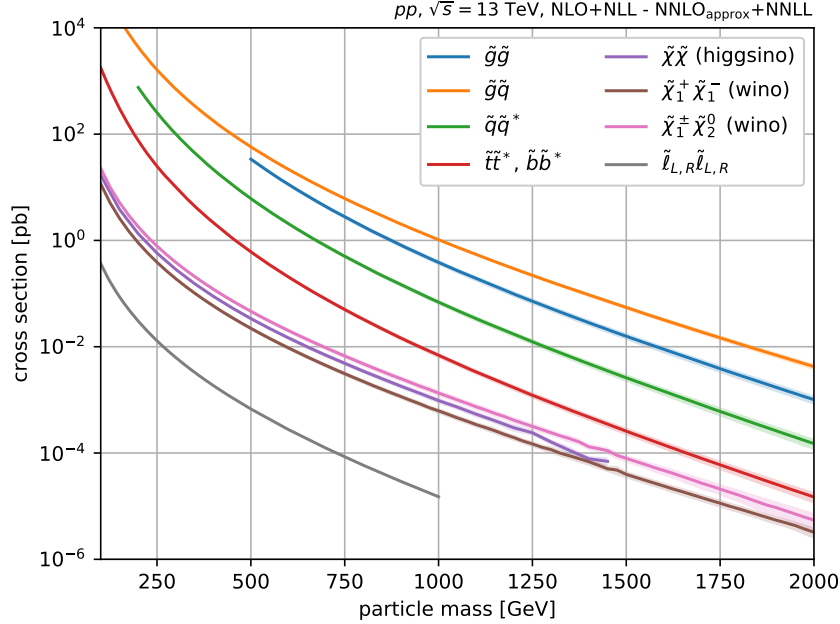
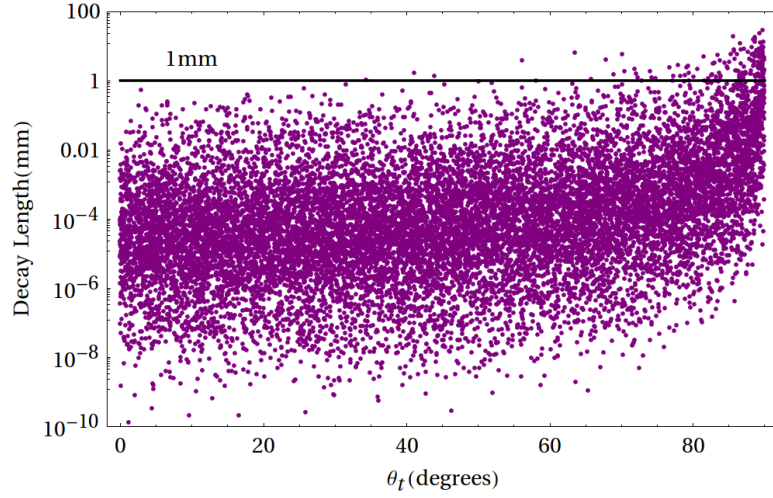
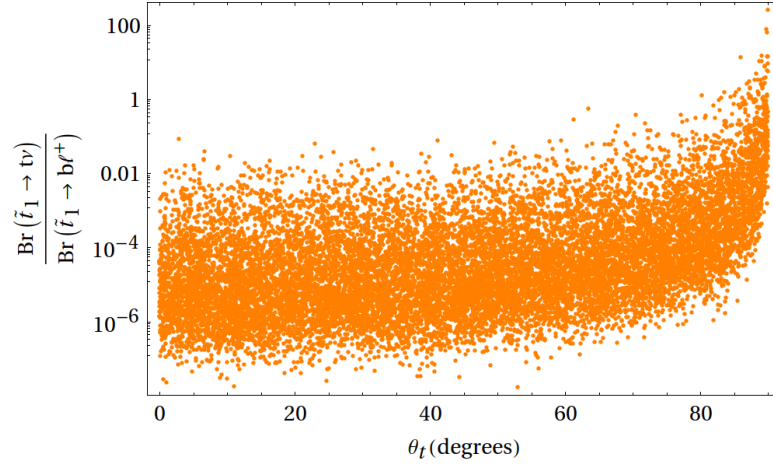


Figure 2.6: Theoretically-predicted cross-sections for pair production of various particles at $\sqrt{s} = 13 \text{ TeV}$ [31].

not purely right-handed, it decays overwhelmingly to a b -quark and a lepton, with a much shorter decay length. These effects can be seen in Figure 2.7 which shows the stop decay length as a function of θ_t (larger values of θ_t correspond to a more right-handed stop), and in Figure 2.8 which shows the ratio of the branching ratio (BR) of the two possible decays as a function of θ_t . Since much more of the parameter space favors a stop which is not purely right-handed (denoted \tilde{t}_{ad} for “admixture” in Figure 2.5), it is interesting when searching for a stop LSP to target final states with hadronized b -quarks (referred to as “jets”, to be defined in Section 3.2.4) and leptons. Henceforth in this thesis, the stop is assumed to be an admixture of left- and right-handed: $\tilde{t} \equiv \tilde{t}_{ad}$. Additionally, the BR of the stop to each lepton flavor depends on the neutrino hierarchy as can be seen in Figure 2.9, so it is interesting to consider individual lepton flavors when interpreting results. Two searches were performed for such a signature and will be described in detail in Chapter 5: one search was performed with 20.3 fb^{-1} of 8 TeV pp collision data, and the second with 36.1 fb^{-1} of 13 TeV data.

Figure 2.7: Stop decay length as a function of θ_t [29].Figure 2.8: Ratio of $\text{BR}(\tilde{t} \rightarrow t\nu)$ to $\text{BR}(\tilde{t} \rightarrow b\ell)$ as a function of θ_t , where ν can be any neutrino and ℓ can be any lepton [29].

2.3.4 The wino LSP

With the full Run 2 LHC data-taking campaign, which amassed 140 fb^{-1} of pp collision data (as will be described in Section 3.1), it is more feasible to access possible LSPs that have a smaller production cross-section. In particular, according to Figure 2.5, the charged ($\tilde{\chi}_W^\pm$) and neutral ($\tilde{\chi}_W^0$) winos are the most likely LSP candidates with reasonable production cross-sections at the LHC².

²As mentioned before, binos ($\tilde{\chi}_B^0$) cannot be pair produced at the LHC. The same is true for the second most likely LSP candidates in Figure 2.5: the 1st- and 2nd-generation right-handed sneutrinos.

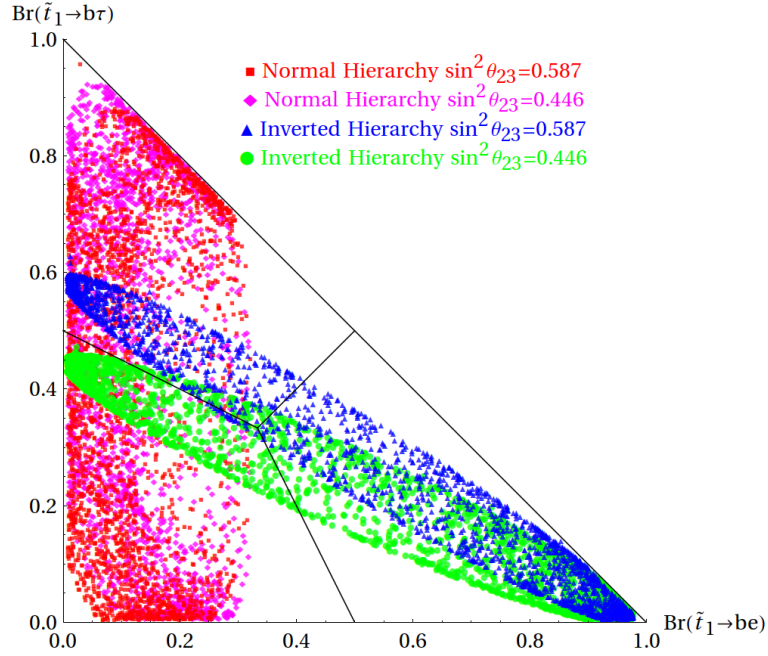


Figure 2.9: Possible values of $\tilde{t} \rightarrow b\tau$ versus $\tilde{t} \rightarrow be$ branching ratio, for both the normal and inverted neutrino hierarchies as well as two possible values of the neutrino mixing angle θ_{23} . Since $\sum_{i=1}^3 \text{BR}(\tilde{t} \rightarrow b\ell_i) = 1$, $\tilde{t} \rightarrow b\mu$ is included in this plot as well; i.e. $\text{BR}(\tilde{t} \rightarrow b\mu) = 100\%$ corresponds to the origin [28, 29].

It was mentioned above that the charginos and neutralinos in this histogram can be admixtures of winos, binos, and higgsinos; however it was found that the LSPs marked wino are indeed overwhelmingly wino [27, 30]. It was also found that for a charged (neutral) wino LSP, the [next-to-lightest supersymmetric particle \(nLSP\)](#) is consistently a neutral (charged) wino with a mass only a few MeV larger than the LSP, since both are overwhelmingly wino and therefore obtain mass from the same term in the Lagrangian. This can be seen in Figure 2.10. Since their masses are so similar, the decays $\tilde{\chi}_W^\pm \rightarrow W^\pm \tilde{\chi}_W^0$ and $\tilde{\chi}_W^0 \rightarrow W^\pm \tilde{\chi}_W^\mp$, for example, are highly suppressed. Thus if either the charged or neutral wino is the LSP, both the charged and neutral wino will decay via [RPV](#) couplings. Moreover, Figure 2.11, which shows the mass spectrum of the charged and neutral wino LSPs, demonstrates that it is quite possible for these LSPs to be within reach at the LHC.

Similarly to the stop LSP, the wino LSP has several possible decays whose relative [BRs](#) depend on the value of $\tan \beta$, which is the ratio of the Higgs [vevs](#), as well as the neutrino hierarchy. The possible decay products of the charged wino LSP are a Z boson and a charged lepton, a Higgs boson and a charged lepton, or a W boson and a neutrino. The possible decay products of the neutral

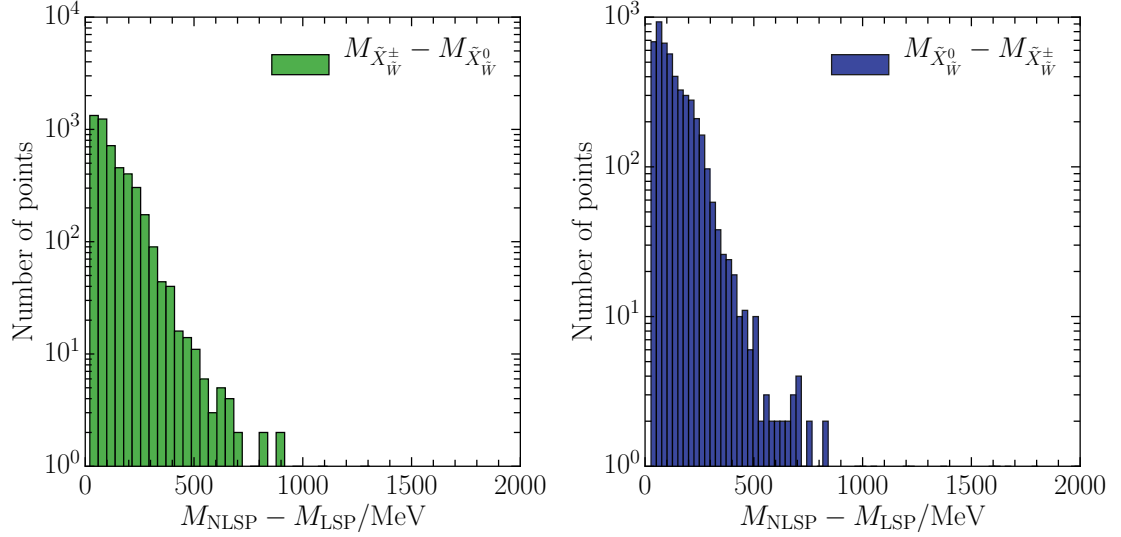


Figure 2.10: Mass splitting between **LSP** and **nLSP** for both neutral (left) and charged (right) wino LSP. The masses are almost degenerate for all valid points [30].

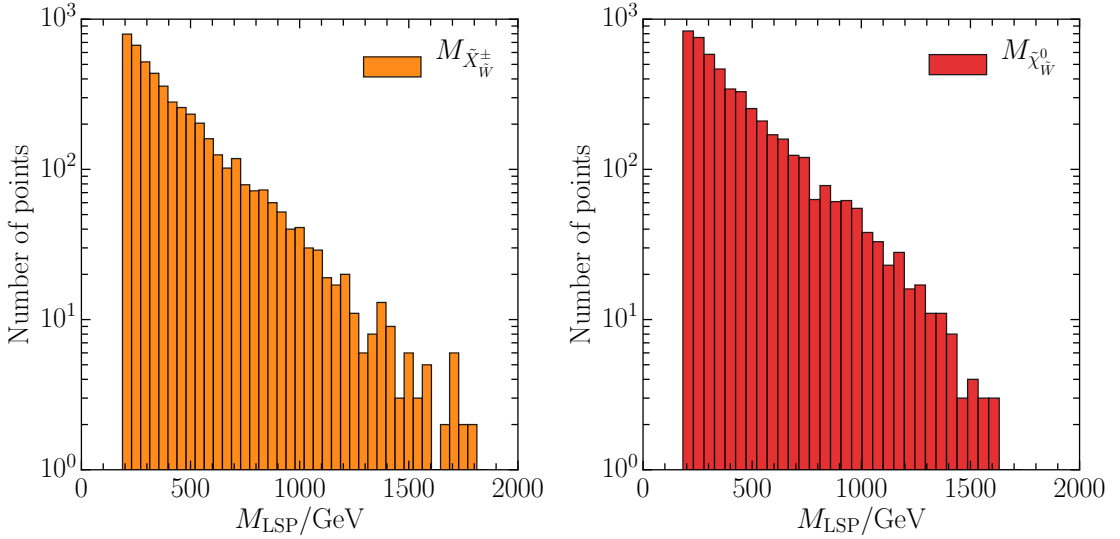


Figure 2.11: Mass spectrum of the **LSP** for both charged (left) and neutral (right) wino LSP [30].

wino LSP are a Z boson and a neutrino, a Higgs boson and a neutrino, or a W boson and a charged lepton. The possible branching ratios to different boson types are shown in Figure 2.12 for the charged wino LSP and in Figure 2.13 for the neutral wino LSP. The possible branching ratios to different lepton flavors, for each boson type, are shown in Figure 2.14 for the charged wino LSP and

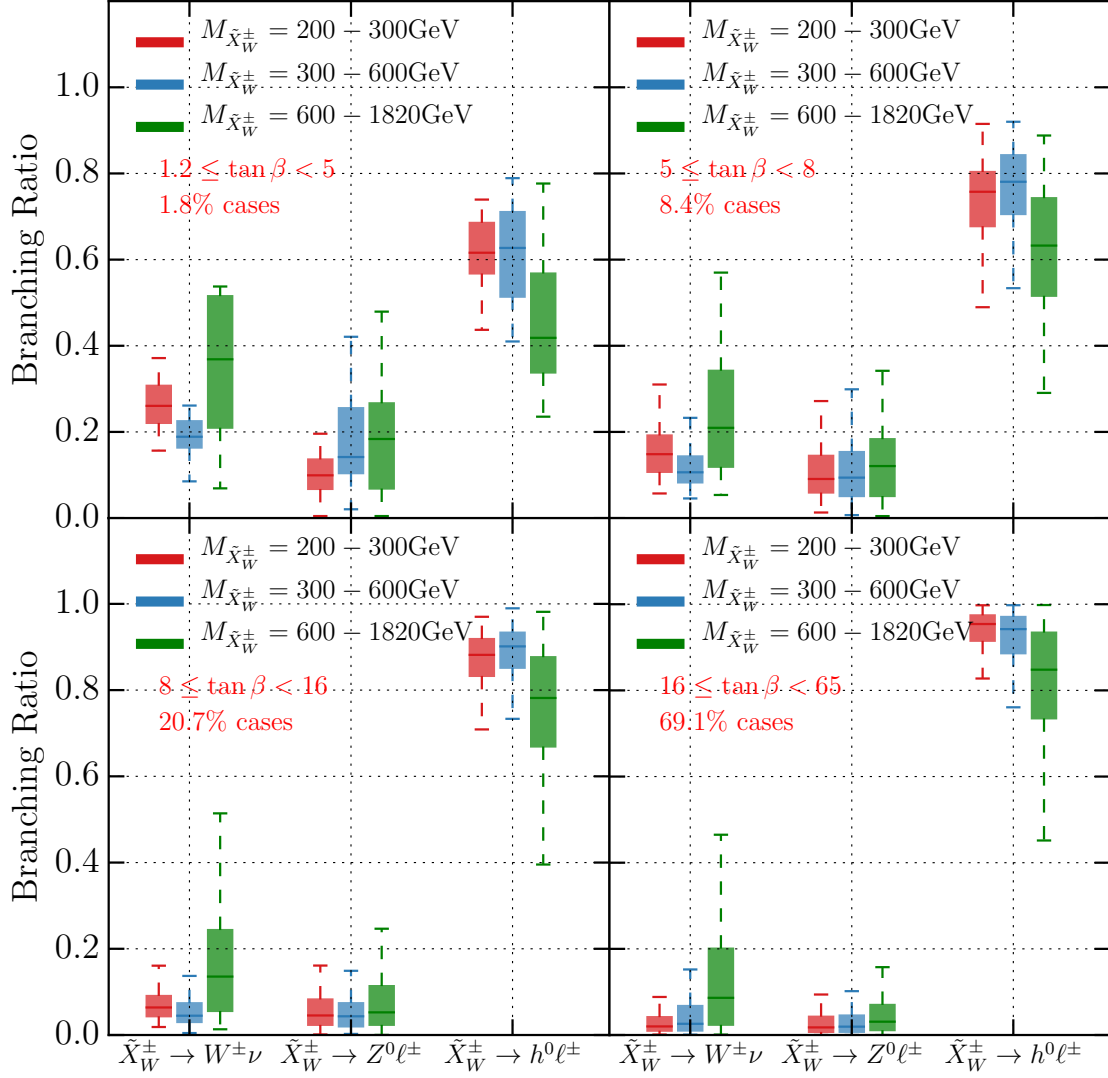


Figure 2.12: Branching ratios for the possible boson decay channels of the charged wino LSP, split into various $\tan \beta$ ranges and shown for several mass values. The colored box indicates the interquartile range, the horizontal line indicates the median, and the dashed error bars indicate the maximum and minimum values of the scan [30].

in Figure 2.15 for the neutral wino LSP. Finally, the lifetimes of the charged and neutral wino LSPs are found to be relatively short, as shown in Figure 2.16 for the chargino and in Figure 2.17 for the neutralino.

It is clear that a large amount of phase space is possible and accessible at the LHC for a charged

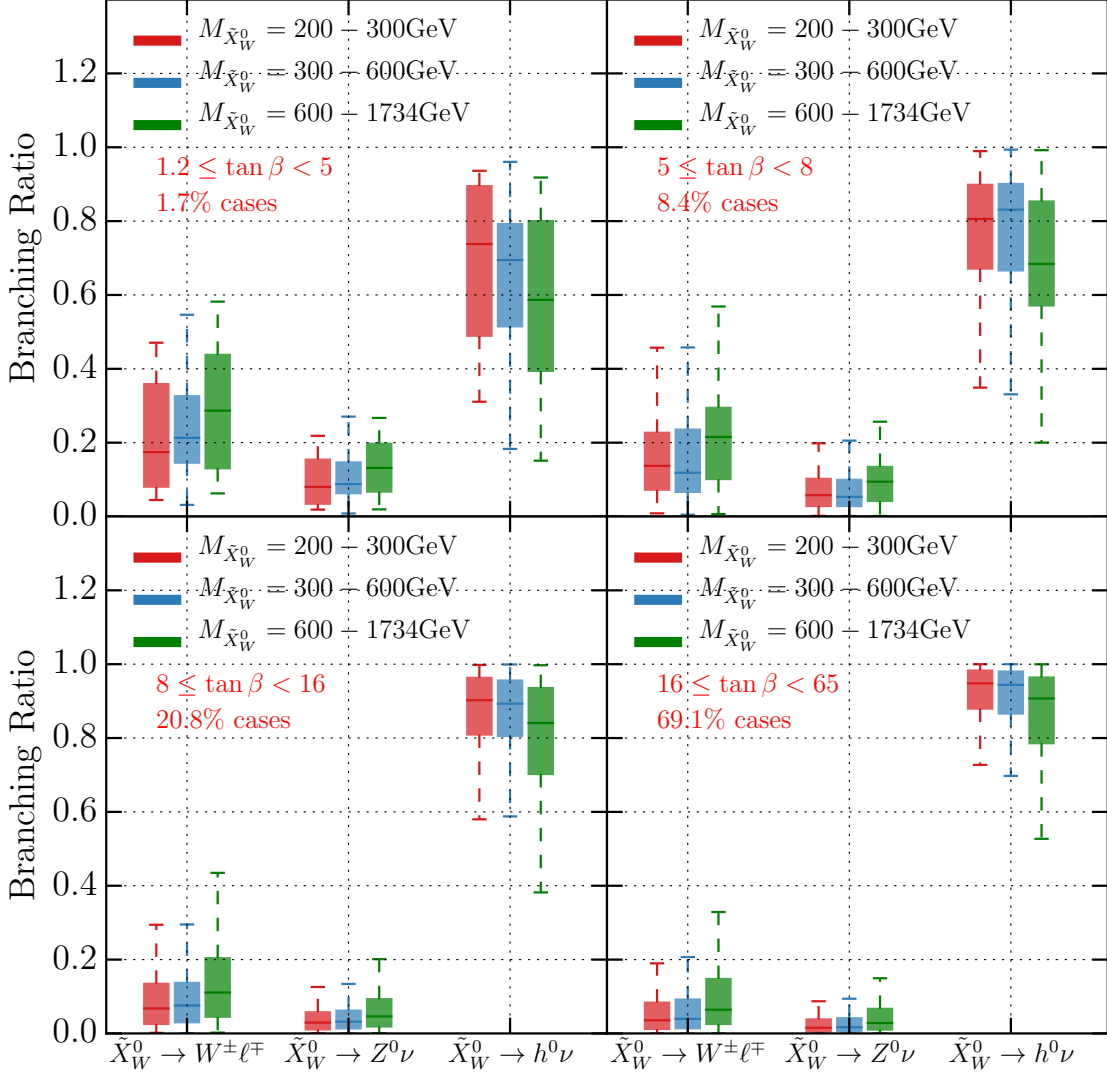


Figure 2.13: Branching ratios for the possible boson decay channels of the neutral wino LSP, split into various $\tan \beta$ ranges and shown for several mass values. The colored box indicates the interquartile range, the horizontal line indicates the median, and the dashed error bars indicate the maximum and minimum values of the scan [30].

or neutral wino LSP. It is particularly attractive to search for the chargino decay to a Z boson and a lepton, since if the Z also decays leptonically, there is a trilepton resonance which reconstructs the chargino mass with excellent resolution, allowing for a mass-dependent search. An analysis which searched for just such a signature with 140 fb^{-1} of pp collision data at the LHC will be described

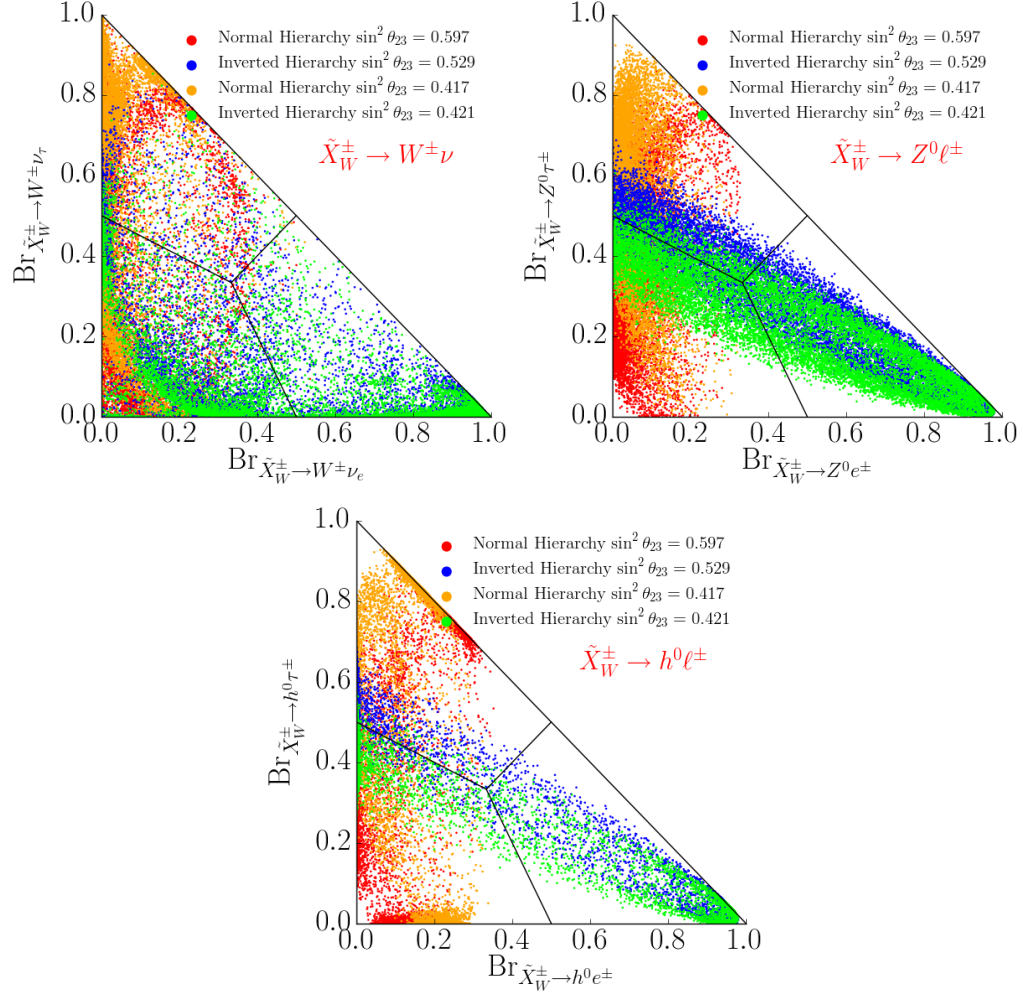


Figure 2.14: Branching ratios for the possible lepton decay channels of the charged wino LSP, split into the boson decay types and shown for the normal and inverted neutrino hierarchies as well as two possible values of θ_{23} , the neutrino mixing angle [30].

in Chapter 6. Additionally, because of the mass degeneracy of the chargino and neutralino, there is discovery potential for both with the same search.

Henceforth in this thesis, the charged wino will be referred to as a chargino ($\tilde{\chi}^\pm \equiv \tilde{\chi}_W^\pm$), and the neutral wino will be referred to as a neutralino ($\tilde{\chi}^0 \equiv \tilde{\chi}_W^0$). This is accurate nomenclature because of the finding that the LSPs are overwhelmingly wino in the $B - L$ MSSM.

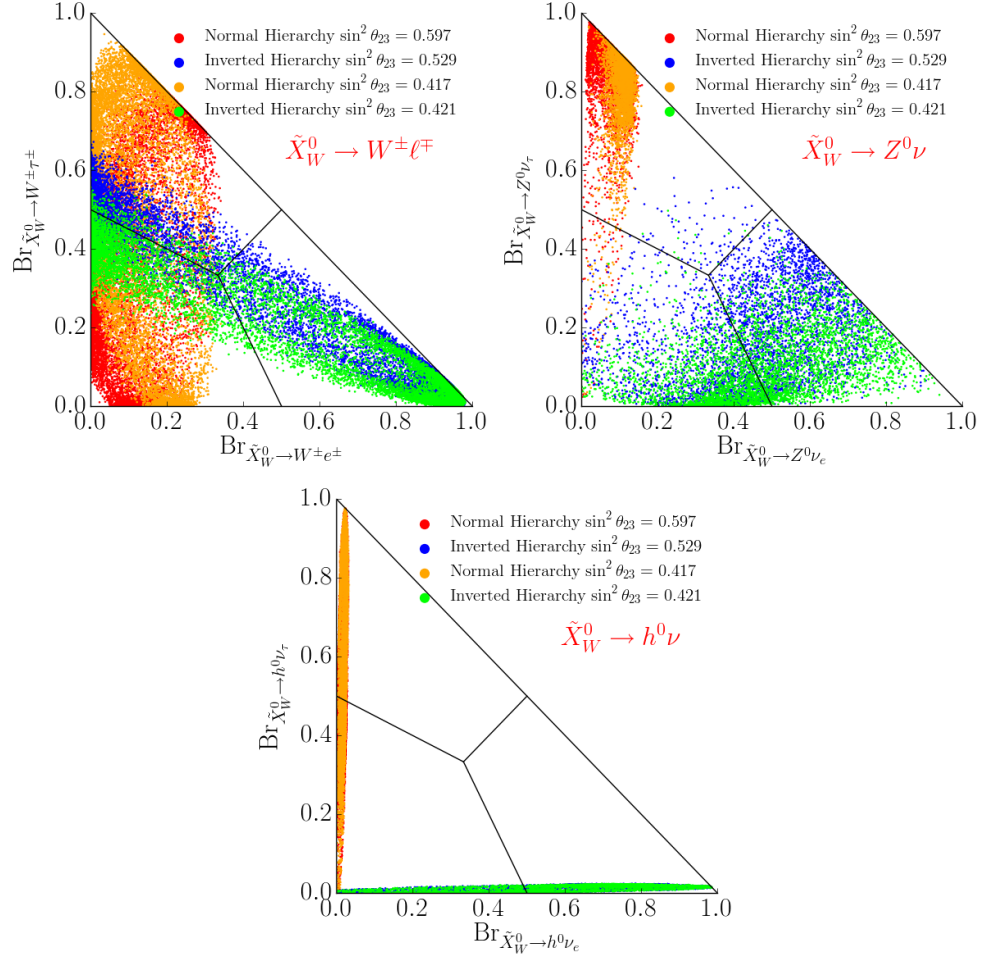


Figure 2.15: Branching ratios for the possible lepton decay channels of the neutral wino LSP, split into the boson decay types and shown for the normal and inverted neutrino hierarchies as well as two possible values of θ_{23} , the neutrino mixing angle [30].

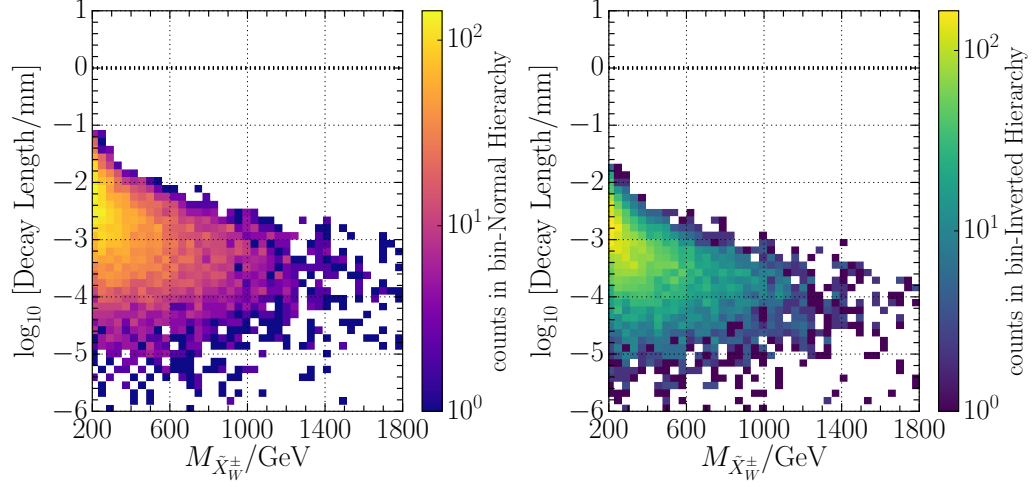


Figure 2.16: Decay length of charged wino LSP as a function of its mass, shown for both normal (left) and inverted (right) neutrino hierarchies, for all decay possibilities [30].

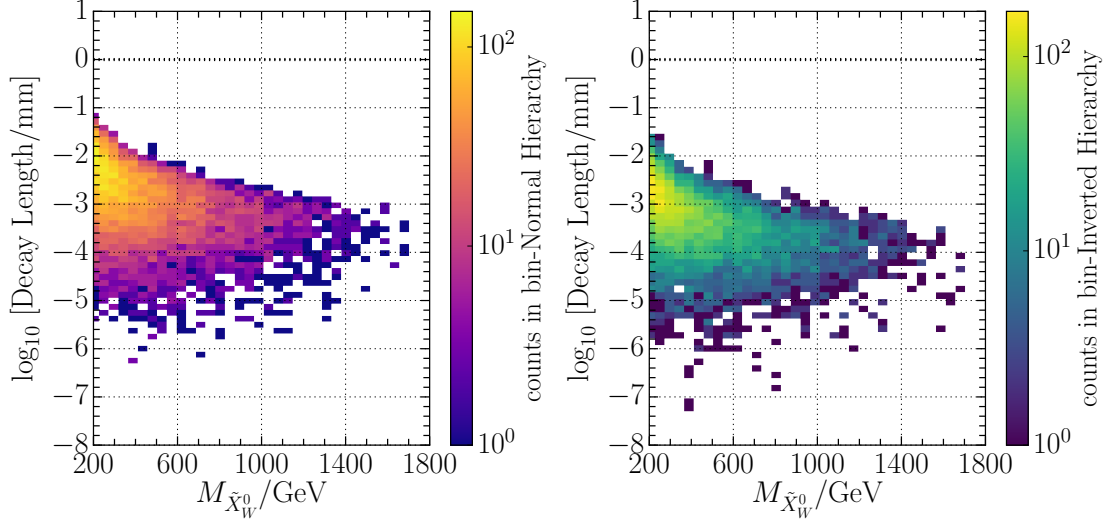


Figure 2.17: Decay length of neutral wino LSP as a function of its mass, shown for both normal (left) and inverted (right) neutrino hierarchies, for all decay possibilities [30].

CHAPTER 3

LHC and the ATLAS Detector

The [LHC](#) collides particles at very high energies with the goal of studying the [SM](#) and [BSM](#) models. Four experiments, including ATLAS, are located along the LHC ring and collect the data produced by its collisions. ATLAS performs precision measurements of the known particles to study the SM, and searches for new particles, such as the [SUSY](#) particles described in Chapter 2, to study BSM models. This chapter describes the LHC complex and the ATLAS detector, which are both necessary to perform the research presented in this thesis.

3.1 The Large Hadron Collider

[CERN](#) operates the [LHC](#) [32], a 27-km circumference ring located 100 m underground at the French-Swiss border. It accelerates protons and the nuclei of heavier elements to almost the speed of light, and then collides these accelerated hadrons at four points along the ring where experiments wait to collect the data. There have been two large data-taking campaigns at the time of writing this thesis. The first is referred to as [Run 1](#) and ran from 2010 to 2012, although only data recorded during 2012 is used in the Run 1 physics analysis which will be presented in this thesis. The second ran from 2015 to 2018 and is referred to as [Run 2](#).

The four experiments located on the LHC ring are ATLAS [33], CMS [34], ALICE [35], and LHCb [36]. ATLAS and CMS are “general purpose” detectors which perform a suite of experiments on the [SM](#) and searches for models beyond it. They complement each other by performing similar experiments with statistically independent datasets, allowing for cross-checks of results. The target of ALICE research is to understand quark-gluon plasma by studying the data produced from heavy ion collisions, and LHCb focuses on b -hadron physics to study CP violation.

Beams of particles are accelerated in a series of steps in the CERN accelerator complex before finally being injected into the LHC where they achieve their final speed. The accelerators which are included in this sequence, as well as the detectors on the LHC, are shown in Figure 3.1. Protons are injected in Linac2 where they reach 50 MeV. Next they are injected into the Booster, the Proton Synchrotron, and then the Super Proton Synchrotron, which accelerate the proton energy to 1.4 GeV, 25 GeV, and 450 GeV respectively. Finally they enter the LHC where they reach their target energy. The design energy of the LHC is 7 TeV per proton beam, resulting in collisions with a center-of-mass energy of $\sqrt{s} = 14$ TeV. The actual operation energies were 7 TeV (2010-2011) and 8 TeV (2012) during Run 1, and 13 TeV during Run 2.

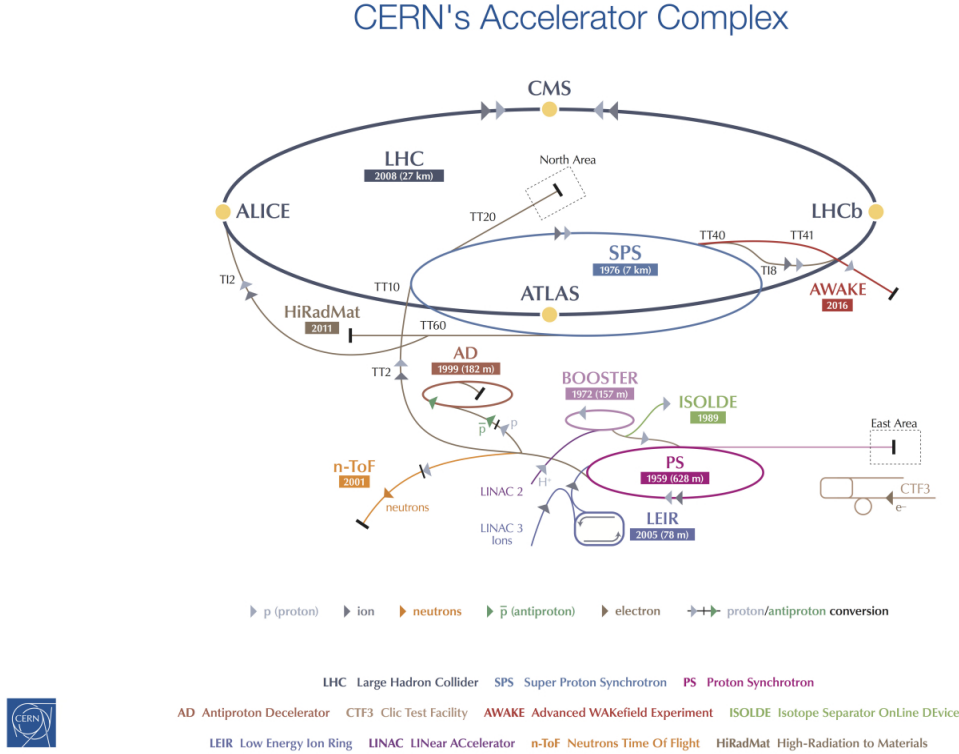


Figure 3.1: The LHC and the CERN accelerator complex [37].

The protons then collide at these well-defined center of mass energies. However since protons are not fundamental particles, the actual particles colliding are the constituents of the proton, called partons: quarks and gluons. The amount of energy that these partons have is some fraction of the total proton energy, so the initial longitudinal momentum may vary significantly from colli-

sion to collision. Conversely, since the proton collisions are head-on, the initial momentum in the transverse direction must be zero. For this reason it is very common for measurements from the LHC experiments to be in the transverse plane as this is invariant to boosts along the longitudinal direction.

The protons in the LHC are grouped together in “bunches”. Over 10^{11} protons are in a single bunch. These bunches collide at fixed time intervals. In Run 1 they collided every 50 ns and in Run 2 they collided every 25 ns. The readout time of many subsystems in the experiments’ detectors is longer than this bunch spacing, so these out-of-time collisions can have a large impact on the physics event observed in the data. This phenomenon is referred to as out-of-time pileup. There is additionally in-time pileup which is due to other pp interactions in the same bunch crossing as the high-energy pp interaction of interest. The amount of in-time pileup is dictated by the instantaneous luminosity of the proton beams. The luminosity depends on several things, most notably the number of protons in a bunch and the width of the beam, which is usually about $20\text{ }\mu\text{m} \times 20\text{ }\mu\text{m}$ at the collision point, where strong quadrupole magnets produce this intense focus, but increases as the protons circulate and collide with each other, reducing the instantaneous luminosity. The design instantaneous luminosity of the LHC is $2 \times 10^{34}\text{cm}^2\text{s}^{-1}$. When the instantaneous luminosity falls below some minimum, the beams are dumped and the LHC is refilled within a few hours.

The total (integrated) luminosity delivered to ATLAS over the course of Run 1 and Run 2 data-taking can be seen in Figure 3.2. Figure 3.3 shows the amount of data collected as a function of the average number of interactions per crossing ($\langle\mu\rangle$), for each data-taking year in Run 2, and

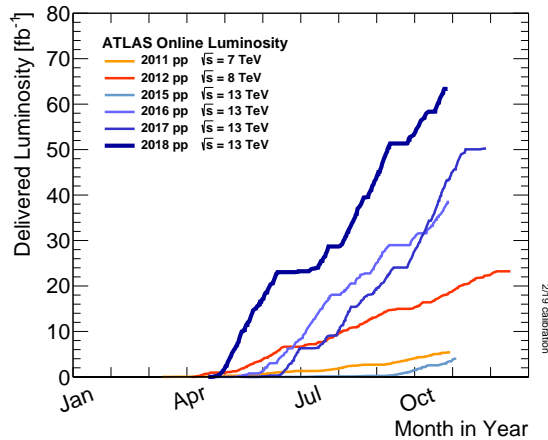


Figure 3.2: Total luminosity delivered to ATLAS at $\sqrt{s}=13\text{ TeV}$ as a function of data-taking year [38].

Figure 3.4 shows the peak instantaneous luminosity per fill for both 2015 and 2018 data. The average number of interactions per crossing is directly proportional to the instantaneous luminosity. This is well-illustrated by comparing Figures 3.3 and 3.4: in 2015 the maximum peak luminosity is $0.5 \times 10^{34} \text{ cm}^2\text{s}^{-1}$ and the average number of interactions per crossing is 13.4, whereas in 2018 the maximum peak luminosity is $2.1 \times 10^{34} \text{ cm}^2\text{s}^{-1}$ and the average number of interactions per crossing is 36.1. Both in-time and out-of-time pileup lead to difficult event reconstruction, as illustrated in Figure 3.5 which shows a candidate $Z \rightarrow \mu\mu$ event from 2017 with 65 reconstructed vertices. The impact of this effect on track reconstruction will be explored in Section 4.4, and event reconstruction will be described briefly in Section 3.2.4.

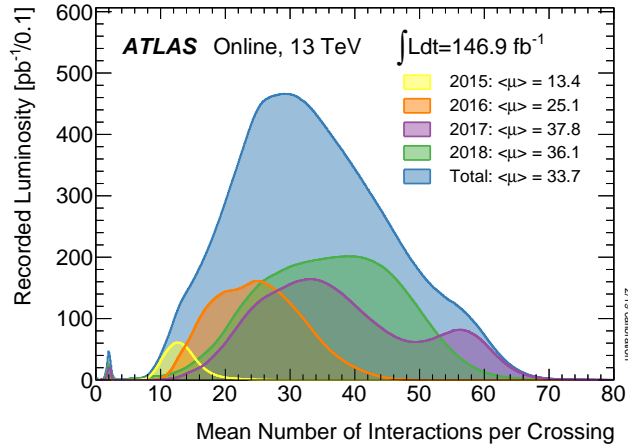


Figure 3.3: Mean number of interactions per crossing for all Run 2 data-taking years [38].

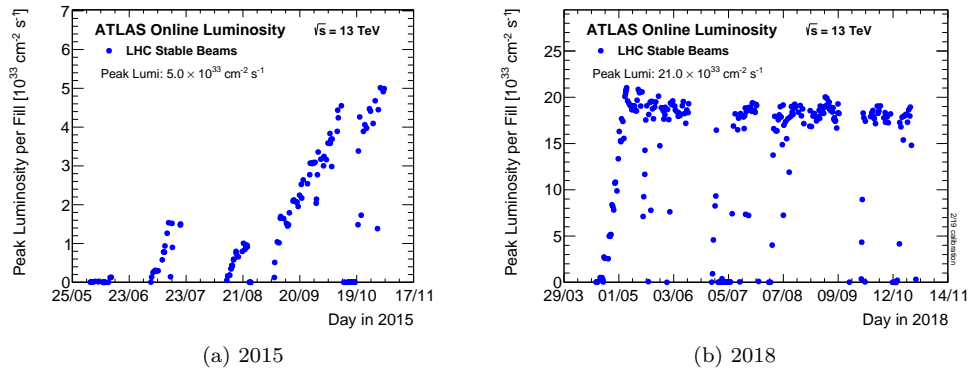


Figure 3.4: Peak instantaneous luminosity delivered to ATLAS during stable beams for pp collisions at $\sqrt{s} = 13 \text{ TeV}$ is shown for each LHC fill as a function of time in 2015 (left) and 2018 (right) [38].

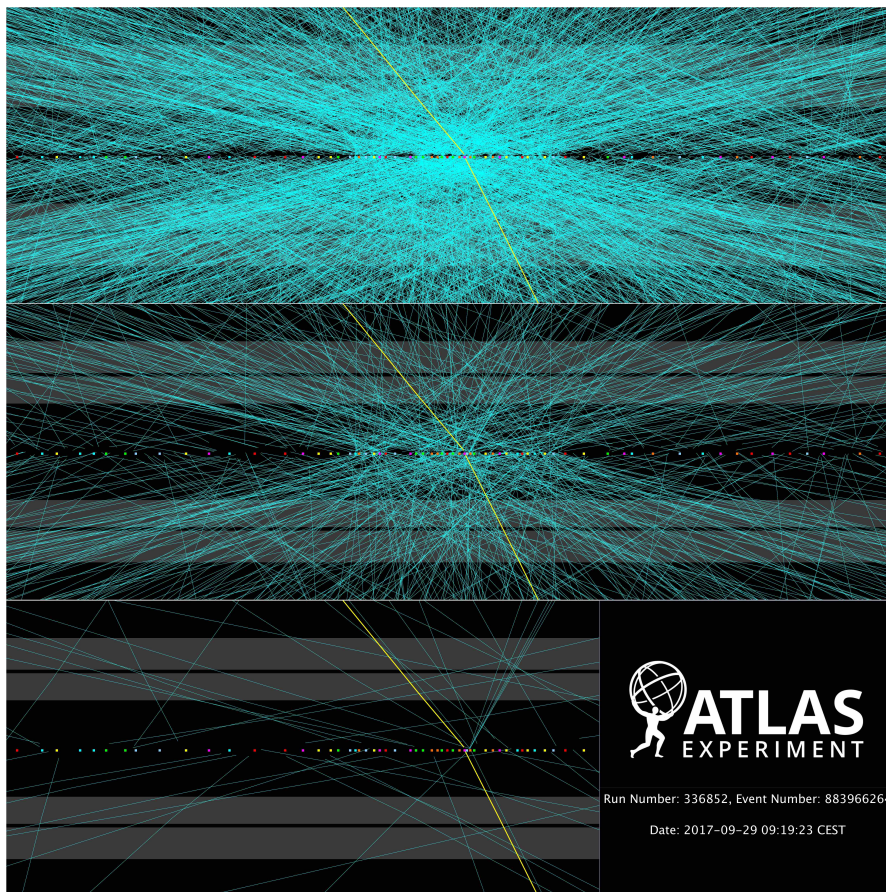


Figure 3.5: A display of a $Z \rightarrow \mu\mu$ candidate event with 65 additional reconstructed vertices from pp collisions recorded by ATLAS at $\sqrt{s} = 13$ TeV in 2017 (Run 336852, Event 883966264). The yellow lines represent the reconstructed muons, the cyan lines show the other reconstructed tracks and the multicolored dots represent the reconstructed vertices. The three panels, from top to bottom, show tracks with a p_T cut of 100 MeV, 1 GeV and 5 GeV respectively [39].

3.2 The ATLAS Detector

The ATLAS detector [33] is a general purpose detector which collects and analyzes data from LHC collisions, with the goals of observing and making precision measurements of the Higgs boson (discovered in 2012) and of observing physics beyond the SM. It has a cylindrical design, and its center is located at one of the LHC interaction points. It consists of several subdetectors, each designed to measure a different property of the particles created in the pp collisions. From inside out, these subdetectors can be categorized as the Inner Detector, which tracks the trajectory of charged particles and measures their momentum, and will be described in Section 3.2.1, the sampling

Calorimeters, which measure the energy of particles and which will be presented in Section 3.2.2, and a muon spectrometer which identifies and measures the momentum of muons, and which will be described in Section 3.2.3. Figure 3.6 shows a cut-out view of the ATLAS detector and labels each of the subdetectors.

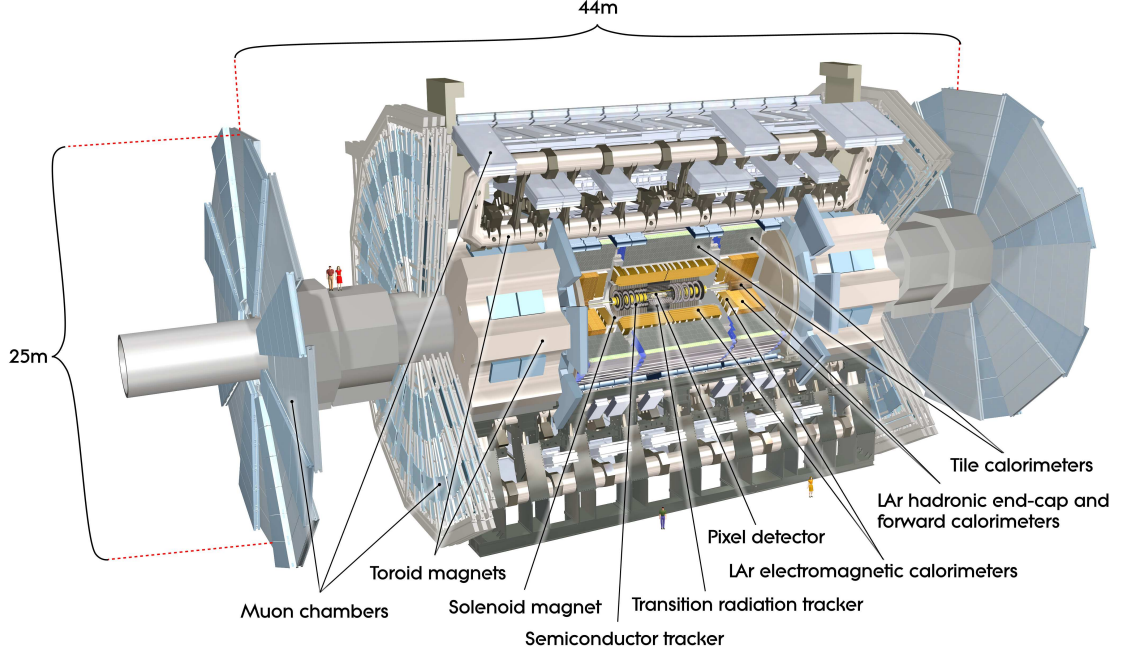


Figure 3.6: General cut-away view of the ATLAS detector [33].

ATLAS uses a right-handed coordinate system with its origin at the nominal interaction point (IP) in the center of the detector and the z -axis along the beam pipe. The x -axis points from the IP to the center of the LHC ring, and the y -axis points upward. Cylindrical coordinates (r, ϕ) are used in the transverse plane, ϕ being the azimuthal angle around the z -axis. As motivated in Section 3.1, typically the momentum and energy of particles are measured in the transverse plane, and denoted with a subscript T (as in p_T or E_T). The pseudorapidity is defined in terms of the polar angle θ as $\eta = -\ln \tan(\theta/2)$. Pseudorapidity is preferred over the polar angle because it is Lorentz invariant, as differences in pseudorapidity are invariant under longitudinal boosts, and particle production is roughly constant in η at a hadron collider. Rapidity is defined as $y = 0.5 \ln[(E + p_z)/(E - p_z)]$ where E denotes the energy and p_z is the component of the momentum along the beam direction. The angular separation between two objects is defined as $\Delta R = \sqrt{(\Delta\eta)^2 + (\Delta\phi)^2}$.

3.2.1 The Inner Detector

The [Inner Detector \(ID\)](#) is used to determine the trajectories of charged particles and to measure their momentum. These charged particle trajectories are commonly referred to as “tracks”. The ID spans the pseudorapidity range $|\eta| < 2.5$, and consists of three subdetectors: the Pixel detector, the Semiconductor Tracker (SCT), and the [TRT](#). Figure [3.7](#) shows a schematic illustration of the ID. The Pixel detector is the closest to the beampipe and so has the finest granularity channels, for precise measurements of the positions of tracks. Conversely the TRT is the farthest tracker from the beampipe and so covers the largest volume with the largest granularity. The Pixel and SCT detectors are silicon detectors. A high-energy charged particle passing through a channel in these detectors ionizes the silicon, creating electron-hole pairs, whose signal can then be recorded as a “hit”. The TRT is a straw tube detector. A charged particle passing through a TRT straw ionizes the gas in the straw, and the electrical signal from this ionization results in a TRT hit. The ID is surrounded by a thin superconducting solenoid providing an axial magnetic field of 2 T, allowing the measurement of charged-particle momenta. In preparation for [Run 2](#), a new innermost layer of the Pixel detector, the insertable B-layer (IBL) [\[40\]](#), was introduced at a radial distance of 3.3 cm from the beamline to improve vertex reconstruction and the identification of jets initiated by b -quarks.

3.2.1.1 Pixel Detector

The Pixel detector consists of four cylindrical barrel layers and three disk-shaped endcap layers. There are a total of 92 million channels in the Pixel detector. The channels in the IBL have a nominal size of $50\ \mu\text{m} \times 250\ \mu\text{m}$, while the channels in the outer three layers have a nominal size of $50\ \mu\text{m} \times 400\ \mu\text{m}$, in the $\phi - z$ plane. The resolution of the Pixel detector is $14 \times 115\ \mu\text{m}^2$.

3.2.1.2 Semiconductor Tracker

The SCT uses the same technology as the Pixel detector. The most important difference is that the SCT channels are larger than the Pixel channels, since it is not as necessary to have such fine granularity farther from the beampipe. These larger channels are referred to as “strips”. There are 6.3 million readout channels in the SCT. The SCT has nine disk-shaped endcap layers and four double barrel layers, allowing for two measurements in each layer. Each strip in the SCT barrel has a nominal size of $126\ \text{mm} \times 80\ \mu\text{m}$ and a nominal resolution of $17\ \mu\text{m}$.

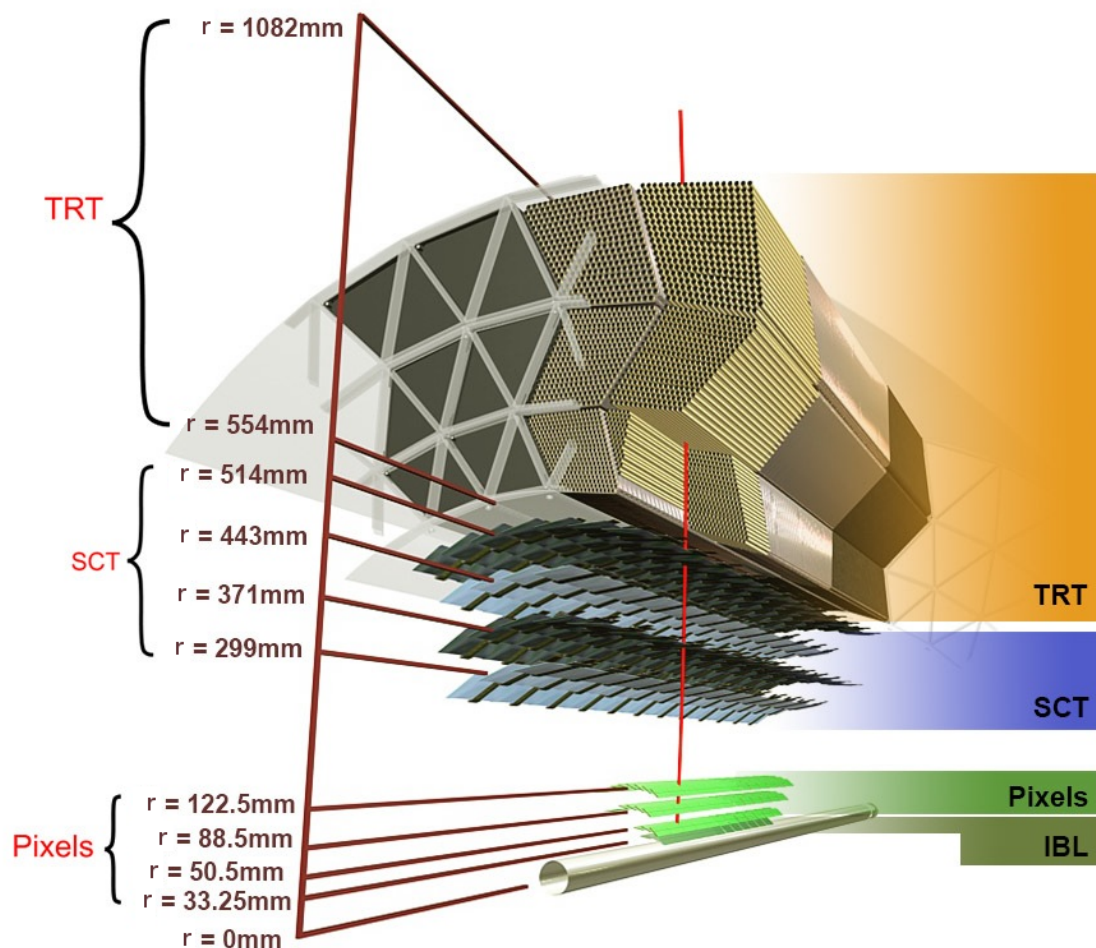


Figure 3.7: Schematic of the Inner Detector. Only the barrel is shown [41].

3.2.1.3 Transition Radiation Tracker

The Transition Radiation Tracker is the outermost component of the ID. It is comprised of almost 350,000 straws of 4 mm diameter, filled with either a xenon-based or argon-based gas mixture ³.

The straws in the TRT barrel lie along the z axis and span the length of the barrel, which is 144 cm long. The barrel straws are electrically separated at $z = 0$, but otherwise there is no spatial resolution in the z direction from the TRT barrel measurements. Similarly, the straws in the endcaps lie radially along the r direction and are 39 cm long, so there is no resolution in the r direction from

³ Over 10 years after installation, the TRT has developed several gas leaks and since xenon is quite an expensive element, the regions with the worst leaks use argon instead.

TRT endcap measurements. Hence, the TRT barrel only provides measurements in the $r - \phi$ plane, and the TRT endcap only provides measurements in the $z - \phi$ plane. Each straw has at its center an anode wire set to ground potential, and the straw wall is set to negative potential, leading to an electric field in the straw itself. When a charged particle ionizes the gas in a straw, the ionized electrons drift towards the anode and cause an avalanche of ionization in the strong electric field close to the anode, thus amplifying the signal collected at the anode. The TRT extends to an $|\eta|$ of 2.0 and has a nominal resolution of roughly $120 - 180 \mu\text{m}$, for both xenon- and argon- based gas mixtures. The TRT is also able to identify particles with high Lorentz factors, in particular electrons, by plastic inserted between straw layers. The difference in dielectric constant between the plastic and the gas in the straws causes particles to emit transition radiation in an amount proportional to their Lorentz factor. The transition radiation, which is typically $6 - 15 \text{ keV}$ for electrons, is then absorbed by the xenon or argon in the TRT straws, and the many ionized electrons are read out analogously to the original ionization from the charged particle. It is possible to have sensitivity to both the charged particle passing through the straw, with an ionization energy of usually $< 300 \text{ eV}$, and the transition radiation, with an ionization energy of a few keV, by using an electrical signal readout with a tertiary threshold. The efficiency to absorb the transition radiation photons is much higher for xenon than for argon, so this method of TRT particle identification is much more effective in straws with xenon. Chapter 4 will describe in detail this subdetector and the methods used to improve its track and particle reconstruction.

3.2.2 The Calorimeters

Outside the solenoid, the next layers in the ATLAS detector system are the calorimeters. Calorimeters are designed to measure the energy of particles traversing the detector. This is achieved by interleaving “absorbing” and “sampling” layers of materials. The absorbing layers are made of high-density materials such as lead and are designed to stop the traversing particles by inducing particle showers, such that all the energy is deposited within the calorimeter. The sampling layers then measure the energy of these showers. ATLAS has two types of calorimeter systems, an electromagnetic and a hadronic, which together cover the region $|\eta| < 4.9$. Figure 3.8 shows an illustration of these calorimeters. The electromagnetic calorimeter uses liquid argon (LAr) as the active material with lead absorber sheets in the region $|\eta| < 3.2$. The central hadronic calorimeter incorporates plastic scintillator tiles and steel absorbers in the region $|\eta| < 1.7$. The hadronic endcap calorimeter ($1.5 < |\eta| < 3.2$) and the forward calorimeters ($3.1 < |\eta| < 4.9$) use LAr with copper or tungsten

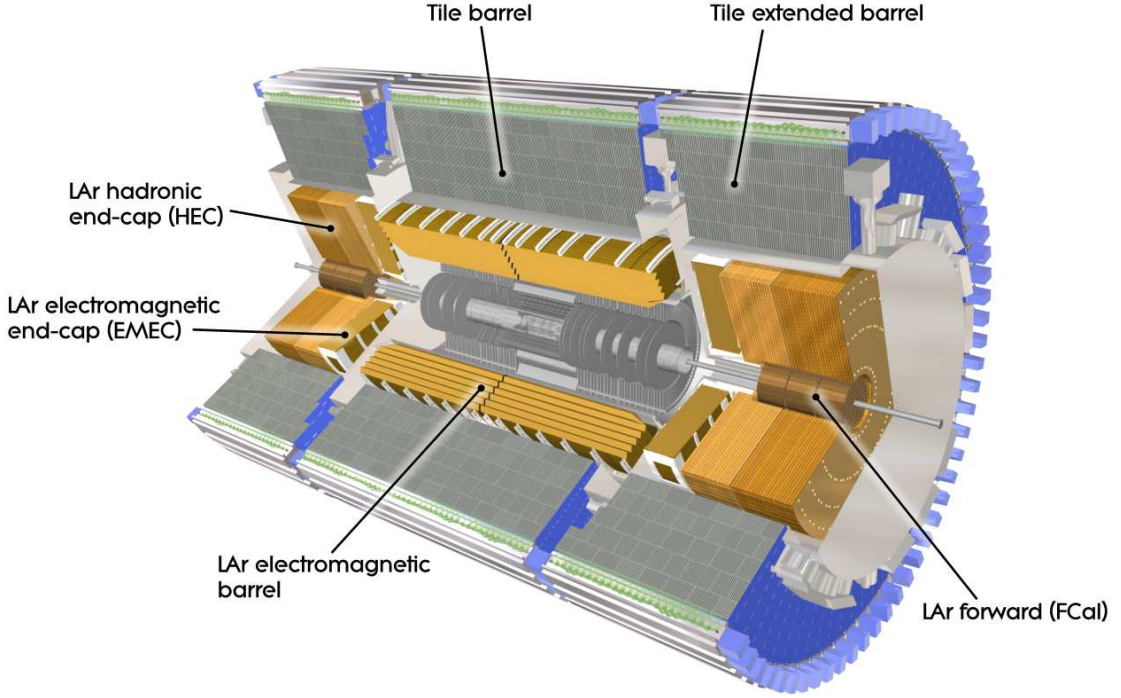


Figure 3.8: The ATLAS Calorimeter system [33].

absorbers.

3.2.2.1 Liquid Argon Calorimeters

The geometric size of the calorimeters is determined by the space required to fully stop most particles of interest. In the LAr, this is measured by the “radiation length”, which is the length that a particle moves through a material before it has $1/e$, or roughly 37%, of its energy. Lead has a radiation length of roughly 5.6 mm and the LAr calorimeters are 50 cm long, corresponding to 22 (24) radiation lengths long in the barrel (endcaps). This ensures that the majority of electrons and photons are fully stopped. The LAr has 110,000 channels total and has an accordion shape oriented radially, to ensure that measurements can be taken in the full ϕ range with no gaps. The LAr is divided into several layers with differing cell sizes. The first is a pre-sampling layer, to sample energy from showers that are initiated before the first absorber plate. Next comes a fine-granularity layer with cells of size 0.003125×0.1 in $(\eta \times \phi)$, which is especially useful for distinguishing photons and neutral pions. Next is the largest layer, at 16 radiation lengths and with size 0.025×0.0245 , and finally

another small layer of 0.05×0.0245 to estimate any remaining energy that was not sampled by the previous layer.

3.2.2.2 Tile Calorimeters

The 500,000 channels in the Tile calorimeter record scintillation from the active material which travels through fiber optics to Photo Multiplier Tubes. The full tile calorimeter is almost 2 m in radius, which covers roughly 10 hadronic interaction lengths, depending on the η direction of the particle. The calorimeter is split into three layers which have cells of size 0.1×0.1 in (η, ϕ) in the first two layers and 0.2×0.2 in the third.

3.2.3 The Muon Spectrometer

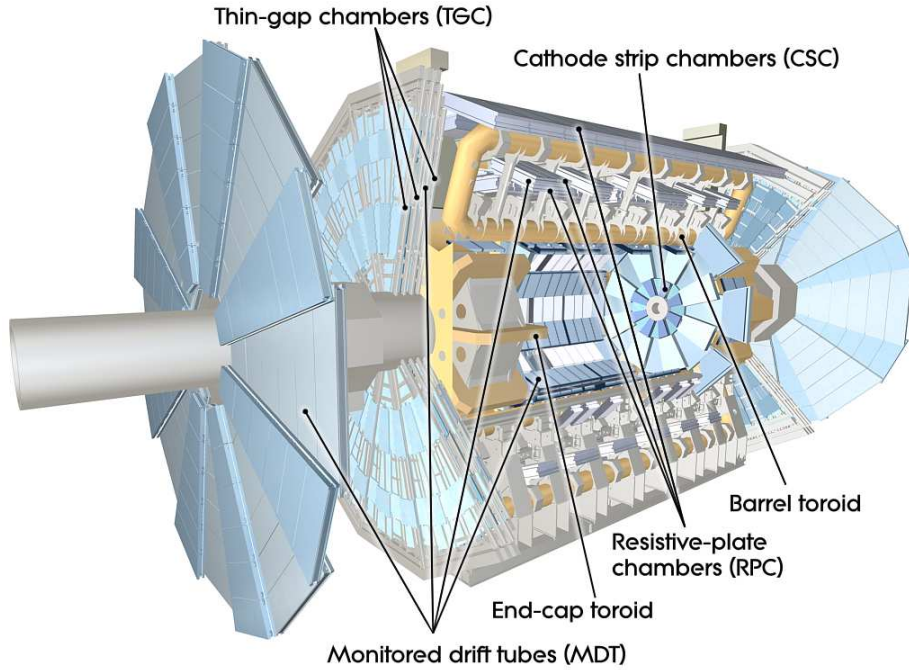


Figure 3.9: The ATLAS Muon System [33].

As muons are too massive to lose significant energy by radiation passing through the calorimeters, there is a detector system fully dedicated to muon detection. The [Muon Spectrometer \(MS\)](#) surrounds the calorimeters and measures muon tracks within $|\eta| < 2.7$ using three layers of precision tracking chambers and dedicated trigger chambers. A system of three superconducting air-core

toroidal magnets provides a magnetic field for measuring muon momenta. Figure 3.9 shows a schematic of the muon system. There are several technologies used to measure the muons. Monitored Drift Tube Chambers (MDTs) are 30 mm drift tubes which measure the momentum of the muons with a resolution of roughly 80 μm . There are 370,000 drift tubes which extend to an $|\eta|$ of 2.7, except in the innermost layer where they extend to an $|\eta|$ of 2.0. There are also Cathode Strip Chambers (CSCs) which are multiwire proportional chambers with cathode strips and which measure the position of the muons with a 60 μm resolution. The CSCs also extend from an $|\eta|$ of 2.0 to 2.7. There are also two types of detectors dedicated to triggering in the muon system: Resistive Plate Chambers (RPCs) and Thin Gap Chambers (TGCs). RPCs have a coverage of $|\eta| < 1.05$ and TGCs have a coverage of $1.05 < |\eta| < 2.4$, and are additionally used for a secondary position measurement out to an $|\eta|$ of 2.7.

3.2.4 Particle Identification and Reconstruction

Now that the ATLAS detector and the particle signatures that are recorded by the various elements have been presented, it is important to describe how these signatures are translated into identified physics objects, in particular SM particles. This is possible by combining the signatures from different detector elements, as illustrated in Figure 3.10, which shows the signatures that several particles leave in various detector elements. For example, it was discussed in Section 3.2.2 that most electrons and photons deposit all their energy in the electromagnetic calorimeter. Moreover, electrons are charged particles so they leave a track in the ID, while photons are neutral so they leave no track. Similarly, muons can be identified by complementary tracks in the ID and MS. Strongly interacting particles radiate gluons, which split to pairs of quarks and anti-quarks. A shower of particles develops that hadronizes into a collection of charged and neutral hadrons. This cascade of particles is referred to as a jet. Jets are identified by large energy deposits in the hadronic calorimeter. It is generally impossible to distinguish jets from most quark types, but b -quark-initiated jets in particular are identifiable. This is because b -quarks hadronize into B -hadrons, which have a relatively long lifetime (several picoseconds). Thus a B hadron can travel for some distance (a few mm) before decaying into several particles. The tracking detectors have excellent spatial resolution and so the reconstruction algorithms can identify that the charged particles from the B hadron decay appear to meet at a location displaced from the primary collision vertex. This is called a “displaced vertex”, and thus b -jets are identifiable. There are also efforts to be able to distinguish quark-initiated and gluon-initiated jets using deep machine learning techniques. Finally,

it was mentioned in Section 3.1 that the total momentum in the transverse plane must be zero, since the LHC partons collide head-on in the z direction. Thus any particles which do not interact with any of the detector elements, such as neutrinos or some stable neutral BSM particle, will also be indirectly detectable in the form of [missing transverse energy](#).

The process of combining the data from all detector elements to identify particles is referred to as reconstruction and occurs in several stages. Tracking is the procedure used to identify charged particle tracks and determine their momentum. This is actually done by measuring the sagitta s which gives the radius of curvature of the track. Charged particles bend in magnetic fields by an amount inversely proportional to their momentum. When converted to the units used in ATLAS, this relationship gives

$$p_T[\text{GeV}/c^2] = 0.3B[\text{T}]l^2/8s \quad (3.1)$$

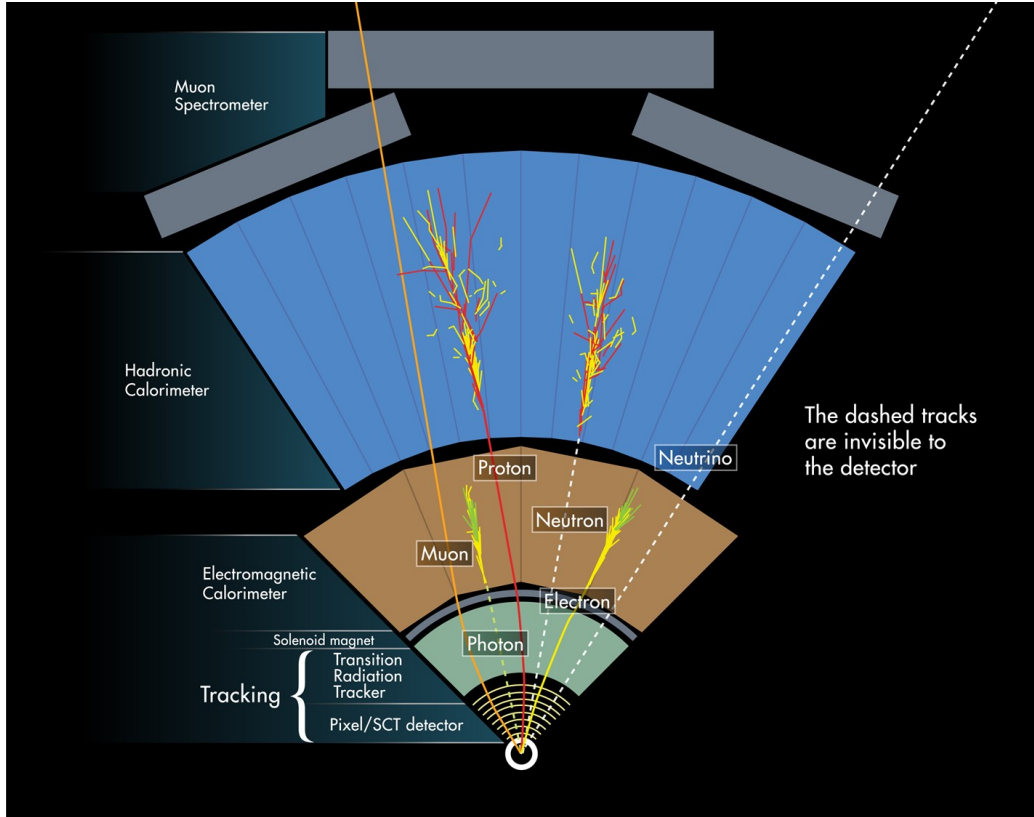


Figure 3.10: Schematic illustrating the detector signatures of various Standard Model particles [42].

where B is the magnetic field (2 T in the ID) and l is the lever arm of the measurement (the radius of the ID, roughly 1 m in ATLAS). Hence the relative p_T uncertainty goes as

$$\frac{\delta p_T}{p_T} = \frac{\delta s}{0.3Bl^2} 8p_T. \quad (3.2)$$

It can be seen that higher- p_T tracks have larger uncertainties, and that a longer lever arm greatly improves the momentum resolution. For this reason, the TRT is invaluable for momentum resolution due to its large volume, as it roughly doubles the lever arm of the ID.

Individual hits in the tracking detectors are combined using pattern recognition and track fitting algorithms such as Kalman and Global χ^2 Filter [41, 43, 44]. Vertices are then reconstructed at locations where many tracks appear to originate [45, 46]. Deposits of energy cells are combined into “clusters” [47] using either a sliding window algorithm, which builds clusters using a fixed-size grouping of cells, or a topological cluster algorithm, which builds clusters of varying size based on the energy deposits in neighboring cells.

Using these tracks and clusters, there are dedicated algorithms to identify all the particles described schematically above. Electron identification requires an electromagnetic cluster with a corresponding ID track [48]. Photon identification requires an electromagnetic cluster with no ID track [49]. There are several algorithms for muon identification but the most commonly used, including the one used in the analyses which will be described in Chapters 5 and 6, requires an MS track aligned with an ID track. Similarly, there are several jet reconstruction techniques but the one within the scope of this thesis is the anti- k_T algorithm [50, 51] with an angular size of $R = 0.4$. As mentioned above, b -jets are especially identified as originating from a displaced secondary vertex [52]. Finally, the missing transverse energy is calculated as the negative vector sum of the momenta of all visible calibrated objects in the event, including a track-based “soft” term for any objects with a momentum too low to be reconstructed as physics objects [53].

All the object reconstruction described above has several options for quality criteria, from which individual analysis teams can choose the one that gives best performance for their performance. These are designed to have varying levels of trade-off between signal efficiency and background rejection.

3.2.5 The Trigger System

Given the extremely high rate of pp collisions at the LHC, which is 40 MHz when protons are colliding every 25 ns, it is impossible to record all the events, in terms of the storage that would be necessary to record all the events to disk, as well as the bandwidth necessary for the detector

elements to read out the data from every event. Rather, it is necessary to carefully select a small subset of these events “online”, before they are read out. This procedure is called the trigger and it filters events from a rate of 40 MHz to 1 kHz. The challenge is designing these triggers to record the majority of the interesting events while still keeping within the limitations of the detector readout. Since many collisions result in relatively well-understood, low-energy QCD interactions, it is possible to achieve a rate of 1 kHz.

The ATLAS trigger system begins with a hardware-based level-1 (L1) trigger followed by a software-based high-level trigger (HLT) [54,55]. The L1 trigger uses data from the calorimeters and MS and is designed to accept events at an average rate of 100 kHz, with a maximum latency of $2.5 \mu s$. The HLT additionally makes use of the ID, reading data only from regions of interest (RoIs) which are defined by the L1, and is designed to accept events to write out to disk at an average rate of 1 kHz.

Electrons are triggered in the pseudorapidity range $|\eta| < 2.5$, where the electromagnetic calorimeter is finely segmented and track reconstruction is available. Compact electromagnetic energy deposits triggered at L1 are used as the seeds for HLT algorithms that are designed to identify electrons based on calorimeter and fast track reconstruction. The muon trigger at L1 is based on a coincidence of trigger chamber layers. The parameters of muon candidate tracks are then derived in the HLT by fast reconstruction algorithms in both the ID and MS. There are additionally hadronic and missing energy triggers which primarily use calorimeter information, but which are beyond the scope of this thesis.

CHAPTER 4

Interpreting Data from the TRT

As mentioned in Section 3.2.1, the TRT contributes to the momentum measurement of charged particles via the tracks they leave in the ID. The TRT is particularly useful to constrain this measurement because of its large radius. The details of tracking in the TRT are described in Section 4.1. The TRT is also able to contribute to electron identification due to the transition radiation (TR) between straw layers. The process of interpreting the unique signature that electrons leave in the TRT to improve their identification, referred to as particle identification (PID), will be described in Section 4.2. One input to the PID is the TRT local occupancy, which quantifies the local activity around a TRT track. This quantity is useful for both studies and calibrations, for tracking and PID alike. Studies of the TRT local occupancy will be described in Section 4.3. Finally, some of the difficulties encountered when performing tracking in a high-luminosity environment, and the actions taken to maintain performance, will be explored in Section 4.4.

4.1 Tracking in the TRT

When a charged particle traverses a TRT straw and ionizes the gas within, the freed electrons drift toward the central anode wire and the ions drift toward the straw edge. This signal is then recorded by the readout electronics. The ion drift time is much longer than the electron drift time, and can be ignored as the signal is restored to baseline by the readout electronics before the majority of the ion charge is deposited [56]. The ionized electrons are collected on the wire within about 60 ns. The TRT reports a tertiary output for each channel in a 75 ns window around each bunch crossing, with 24 low threshold (LT) bits for tracking (each LT bit corresponds to 3.125 ns) and three high threshold (HT) bits for transition radiation (each HT bit corresponds to 25 ns). The bit in which a

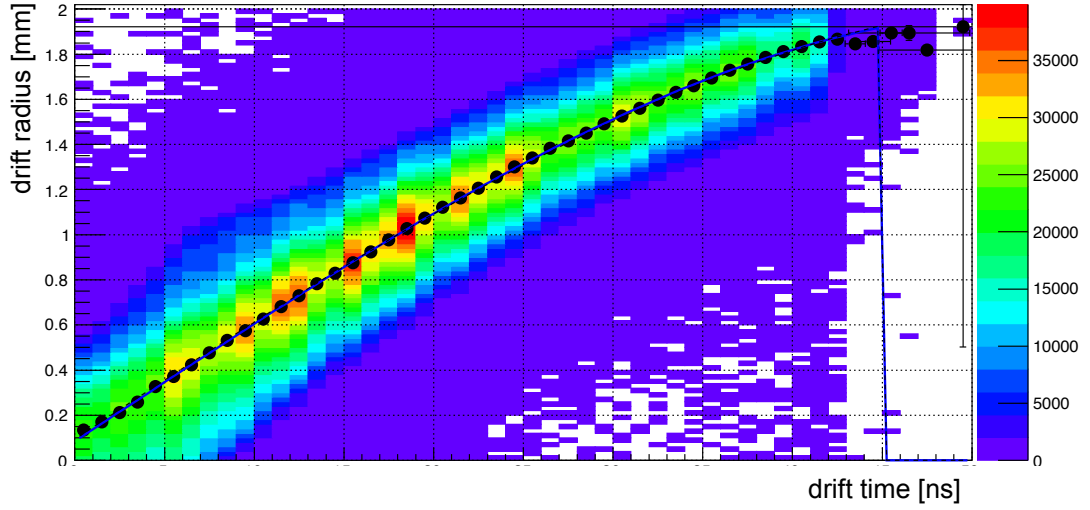


Figure 4.1: Example distribution of drift radius as a function of drift time in barrel side A for 2018 data run 350310. The z-axis represents number of hits. The black points represent the profile for each bin along the x-axis.

signal first rises above the LT is called the leading edge and corresponds to the arrival of the ionized electrons from the closest approach of the charged particle to the wire. In [Run 2](#), a validity gate is defined based on the leading edge time in order to minimize the number of hits from the adjacent bunch crossings 25 ns earlier and 25 ns later. If any of the LT bits within the validity gate are above threshold, the 27-bit word is collectively referred to as a hit or a drift circle.

The fine granularity of the LT bit pattern allows for a measurement of the track's position in the straw which is much more precise than its 2 mm radius. The leading edge has a one-to-one correspondence with the drift time of these closest electrons, which can then be converted to a drift radius, as illustrated in [Figure 4.1](#).

A quantity called the pull is used to make sure the uncertainty, or error, of the drift radius is sensible. The pull makes use of the drift radius r_{hit} and the so-called [track-to-wire distance \(TTWD\)](#) r_{track} , as well as the uncertainties on both of these measurements δr_{hit} and δr_{track} . The pull is defined as

$$\text{pull} = \frac{r_{\text{hit}} - r_{\text{track}}}{\sqrt{\delta r_{\text{hit}}^2 + \delta r_{\text{track}}^2}}, \quad (4.1)$$

The pull should be a Gaussian distribution centered at 0 and with a width of 1. If the width is greater than 1, then the hit error is underestimated and the fit will be underconstrained. On the other hand, if the width is less than 1, then the hit error is overestimated and the fit will be overconstrained. To

ensure that the width of the pull remains at 1, a drift radius “error scaling” method was introduced. This method fits iteratively and then applies a pileup-dependent scale factor to the errors [57].

The drift radius and its uncertainty are then input to tracking, to constrain the trajectory of a track. A first pass at tracking gives the expected trajectory of a track [41, 44] (this first pass may already exist from the Pixel and SCT subdetectors if this is a “Silicon-seeded” track). This trajectory establishes the straws that the track is expected to have traversed, as well as the TTWD in each straw. The residual is the numerator of the pull calculation (Equation 4.1); namely the difference between the drift radius (from the TRT measurement) and the TTWD (from the fitted track trajectory). It is used to determine how well the TRT measurement agrees with the track fit, which correspondingly classifies the TRT hit as either “precision”, “tube”, or “outlier”. These classifications are illustrated schematically in Figure 4.2 and are defined as follows. If the residual is within ± 2.5 of the drift radius error, the hit is a “precision hit”. These hits are used to constrain the track fit. If the residual is larger than this, or if the drift radius cannot be accurately measured because there is no leading edge, the hit is a “tube hit”. These hits are also used to constrain the track fit but they have large errors so they don’t constrain it as much as precision hits. “Outliers” are hits that pass $100\ \mu\text{m}$ or more outside the straw wall. These hits are used in pattern recognition but not in the track fit. Precision or tube hits can additionally be classified as outliers if the track is not successfully extended into the TRT, as described below. Finally, “holes” are identified as TRT straws which the track is expected to have traversed but which have no recorded hit.

Tracks typically have roughly 30 TRT hits, depending on their pseudorapidity and hence the region of the detector through which they pass. As mentioned before, ideally each of these hits help to constrain the momentum measurement of the track. There are several types of tracks. The type most commonly used is silicon-seeded tracks. These are tracks which originate from the Pixel or SCT detectors, which may then have “extensions” into the TRT. Tracks are not required to have TRT extensions but their momentum measurement has a much smaller uncertainty if the TRT is included, since the momentum uncertainty goes as $1/(\text{lever arm})^2$ and the TRT doubles the lever arm as described in Section 3.2.4. There are also TRT-seeded tracks which are useful for identifying photons which convert to electron-positron pairs and for long-lived particle searches, but which will not be discussed in this thesis.

Silicon-seeded tracks are extended if the extension candidate meets several quality criteria. There are requirements on the quality of the Si-only track, as well as the following requirements on the extension itself:

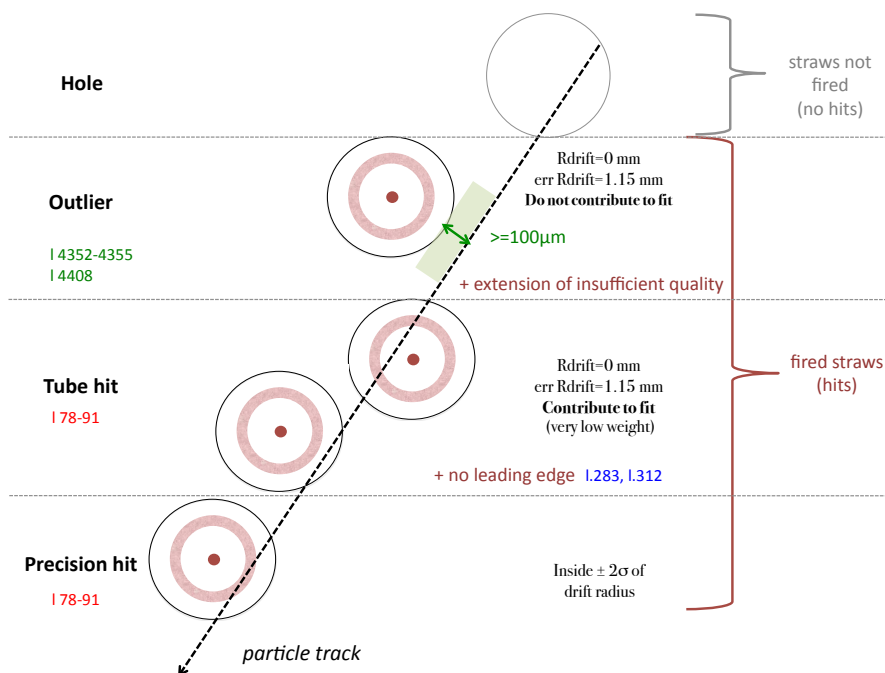


Figure 4.2: Illustrative classifications of different TRT hit types. The drift radius and its uncertainty are shown by the red annulus. The trajectory of the track is shown by the dashed line. The center of each straw is shown as a red dot, and the straw wall is shown as the black circle. Courtesy of Narei Lorenzo Martinez.

- There must be at least 9 TRT hits on the extension.
- If there are at least 15 TRT hits on the extension, at least 30% of them must be precision hits. This value is called the **precision hit fraction (PHF)** and is designed to prevent low-quality TRT extensions from degrading the overall quality of an otherwise good track. (This criterion was 50% until recently. See Section 4.4 for a discussion of this.)
- The combined Si+TRT fit must yield $\chi^2_{\text{Si+TRT}} \leq 2$ and $\chi^2_{\text{Si+TRT}} \leq 2 * \chi^2_{\text{Si-only}}$

If a TRT extension fails the criteria outlined above, then all the TRT precision and tube hits are re-classified as outliers. Tracking at high occupancy led to a reduction in the number of successful TRT extensions. This was investigated and improved, a discussion of which can be found in Section 4.4.

4.2 Electron Identification in the TRT

In addition to the tracking capabilities of the TRT, it can also be used to help identify electrons [58]. This is achieved by inserting plastic, which has a different dielectric constant than the gas in the straws, between layers of the TRT. As charged particles traverse boundaries between media with different dielectric constants, they emit an amount of TR proportional to their Lorentz factor γ . Therefore at a given momentum, electrons emit much more TR than charged pions due to the smaller value of the electron mass. The TR are X-rays that may be absorbed by the inner shell electrons of the gas in the TRT straws and cause significant ionization, which contributes a large amount to the energy read out by the straw wire. This is the reason for the tertiary readout system in the TRT. The high threshold (HT) is designed to only be exceeded by these high-TR tracks. This effect can be seen in Figure 4.3 which shows the probability that a track will exceed the HT as a function of its Lorentz factor.

Along with information about the local geometry of a track and the event environment, its HT bit pattern is input to a tool which calculates the likelihood that a track is from an electron. Xenon

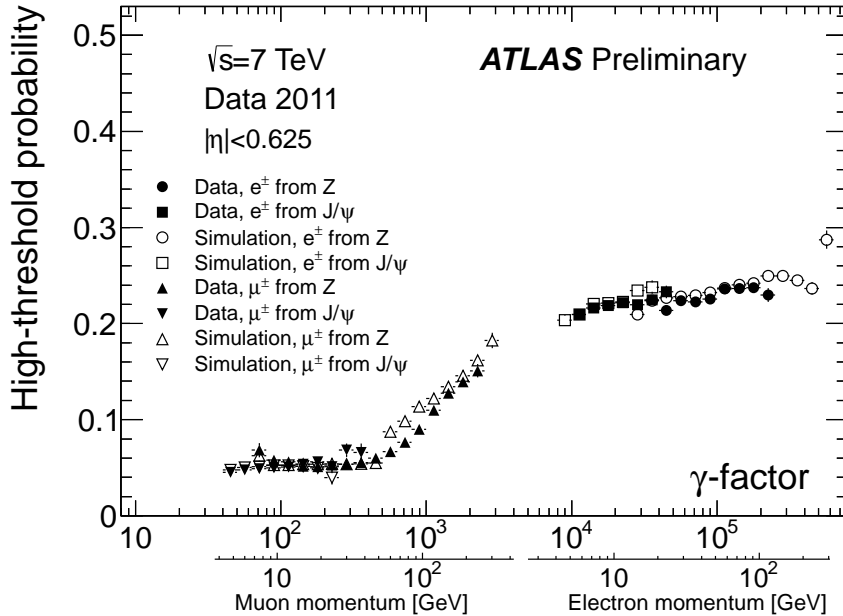


Figure 4.3: High threshold probability as a function of Lorentz factor and electron or muon momentum, in data and simulation, for tracks with $|\eta| < 0.625$ corresponding to the barrel region of the TRT [59].

is more efficient at absorbing the TR than argon, hence the xenon hits provide better discrimination power. The output of this tool is used by the [electron identification](#) described in Section 3.2.4 to improve discrimination.

The PID likelihood has many dependences. One of these is the amount of detector activity around a track. Regardless of whether the track was truly an electron or not, increased activity around the track increases the probability that the HT will be exceeded. For this reason it is useful to input the occupancy around a track as input to the PID calculation.

4.3 TRT Local Occupancy

Many processes in the ATLAS detector have a dependence on pileup, which is the amount of overall activity in an event. Detector responses as well as calibrations and working points may change based on the pileup around an object of interest. For this reason it is important to understand how pileup affects tracking and PID in the TRT, with the goal of accounting for and correcting this dependence.

In [Run 1](#) of data taking, two quantities were considered as handles to correct the PID dependence on pileup, which both have drawbacks in a high-pileup environment. One quantity is the number of [number of primary vertices \(npv\)](#) in a bunch crossing, counted using track reconstruction. At high pileup, when there are many proton-proton collisions which are close together, it gets difficult to resolve individual vertices. Since the calculation of npv itself depends on pileup [60], npv is not ideal in high-pileup conditions. The other quantity considered is the mean number of inelastic proton-proton collisions per bunch crossing ($\langle\mu\rangle$), which is linear with pileup and can describe the changes in the instantaneous luminosity over the course of minutes and hours of each run, but cannot provide an event-by-event quantity. It is averaged over all bunch crossings in a luminosity block (which is about one minute long) so it does not reflect the pileup of a given event. It is therefore not optimal for determining the effect of pileup on an event-by-event basis.

In [Run 2](#), a new option was introduced to characterize the pileup on an event-by-event basis. The occupancy of the TRT is defined as:

$$\frac{\text{number of TRT straws which have a low-level hit within a validity gate}}{\text{total number of live TRT straws}} \quad (4.2)$$

TRT occupancy has several advantages over npv and $\langle\mu\rangle$. Firstly, it is much more linear with pileup than npv is, so it provides a more realistic description of the detector activity in a high-pileup environment. Figure 4.4 shows that the global TRT occupancy is relatively linear with $\langle\mu\rangle$. Secondly, it can be calculated for every event, and to any desired granularity, so it can provide a

more accurate and local description of the detector activity than $\langle\mu\rangle$. Global TRT occupancies are calculated once per event, to have an estimate of the general activity in the event. In addition, [local track occupancies](#) are calculated for every track that enters the TRT PID tool, so that a local description of the detector activity can be used to correct PID variables which are ultimately used as input to the electron likelihood.

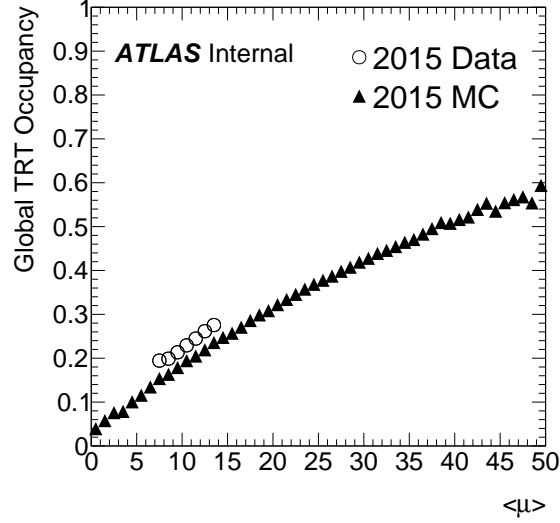


Figure 4.4: Global TRT occupancy as a function of $\langle\mu\rangle$, for 2015 data and [Monte Carlo \(MC\)](#).

Several studies were performed to measure and validate the use of TRT occupancy in this context. In [Section 4.3.1](#), typical occupancy distributions and the choice of granularity are described. [Section 4.3.2](#) presents a comparison of the occupancy calculated in reconstruction to that calculated in the online trigger environment.

4.3.1 Occupancy Granularity

The occupancy of the TRT, as well as the occupancy of regions of the TRT, can vary greatly depending on the activity of an event. [Figure 4.5](#) shows the distribution of global TRT occupancy for events with $\langle\mu\rangle$ between 10 and 16. The spread is not exceptionally large, but if we look in smaller regions of the TRT the spread increases. The occupancy is calculated in several regions, at two different granularities. Six coarse “partition occupancies” are calculated per event, for Barrel, Endcap type-A wheels, and Endcap type-B wheels, for either side A or side C of the detector. The finer granularity “local occupancy” splits the detector into 192 regions, for each of 32 phi sectors in

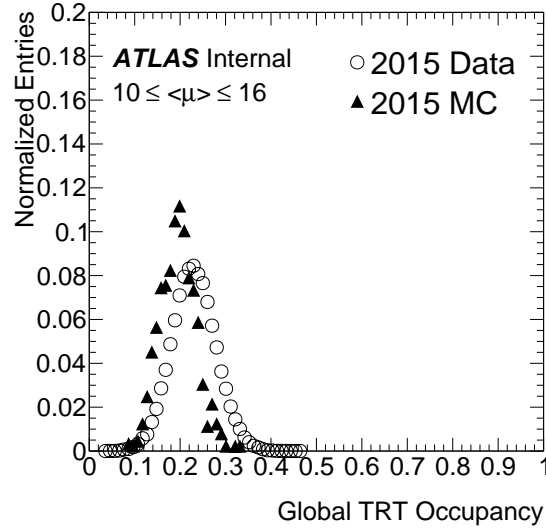


Figure 4.5: Global TRT occupancy distribution, for 2015 data and [MC](#).

all 6 partitions.

Figure 4.6 shows the distribution of partition occupancies, and Figure 4.7 shows the distribution of local occupancies, each as a function of global TRT occupancy. It is clear that the smaller regions have a larger spread, simply because smaller regions are more susceptible to variations in activity in a given event. It can also be noted that the slopes of the distribution in each partition are not the same. This is demonstrated more clearly in Figure 4.8, which plots the average occupancy for each partition as a function of global occupancy on one axis. It is clear that Endcap B typically has the highest occupancy, and Endcap A has the lowest. This is because most activity in an event is in the forward region of the detector. In general, the differential cross-sections for jet production in proton-proton collisions are approximately constant in pseudorapidity, implying roughly equal numbers of jets are observed in each interval of pseudorapidity. This means most of the activity will be in the forward endcaps of the detector, and so Endcap B will have higher occupancy than Endcap A. This is shown in Figure 4.9, which shows the occupancy of every other wheel in the endcap. The wheels are numbered from 0 to 13, and the lower-numbered wheels are at lower $|z|$. It is clear that these wheels have lower occupancy than the wheels at higher $|z|$. Similarly, the inner barrel layer has higher average occupancy than the outer barrel layer because most of the charged particle tracks passing through the inner layer of the barrel will exit into the endcap. In addition, the larger surface area of the outer barrel layer compared to the inner barrel layer means there are more channels per charged particle and so there is lower occupancy in the outer barrel layer than

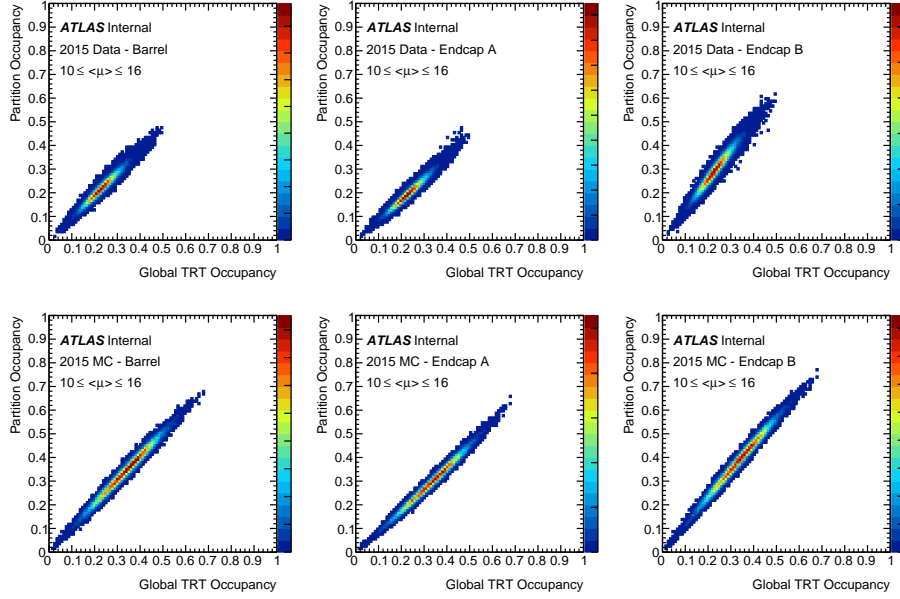


Figure 4.6: Distributions of partition occupancies as a function of global TRT occupancy, in 2015 data (top) and MC (bottom).

the inner barrel layer, as demonstrated in Figure 4.10. Figure 4.10a shows the average barrel layer occupancy, and Figure 4.10b shows the distributions.

Because of this spread in local occupancy which is dependent on detector geometry, it is beneficial to consider smaller TRT regions when using occupancy to correct for pileup effects, as the local activity around a track provides a more accurate description of the conditions which might affect this track. Similarly, since a single track can pass through several partitions, it is useful to define a **local track occupancy** which describes the local detector activity along a track. This is a weighted average of the local occupancies L_i in each of the 192 regions i , weighted by the number of track hits in that region n_i . This is described by the expression

$$\text{Track Local Occupancy} = \frac{\sum_{i=\text{region}} L_i * n_i}{\sum_{i=\text{region}} n_i}. \quad (4.3)$$

Figure 4.11 shows the local track occupancy as a function of global occupancy, and Figure 4.12 shows the local track occupancy as a function of track pseudorapidity. The shape of the latter is an effect of the difference in occupancy distributions in different TRT partitions, as demonstrated in Figure 4.8. A track with $|\eta| \leq 0.9$ goes primarily through the barrel, while a track with $0.9 < |\eta| \leq 1.55$ goes

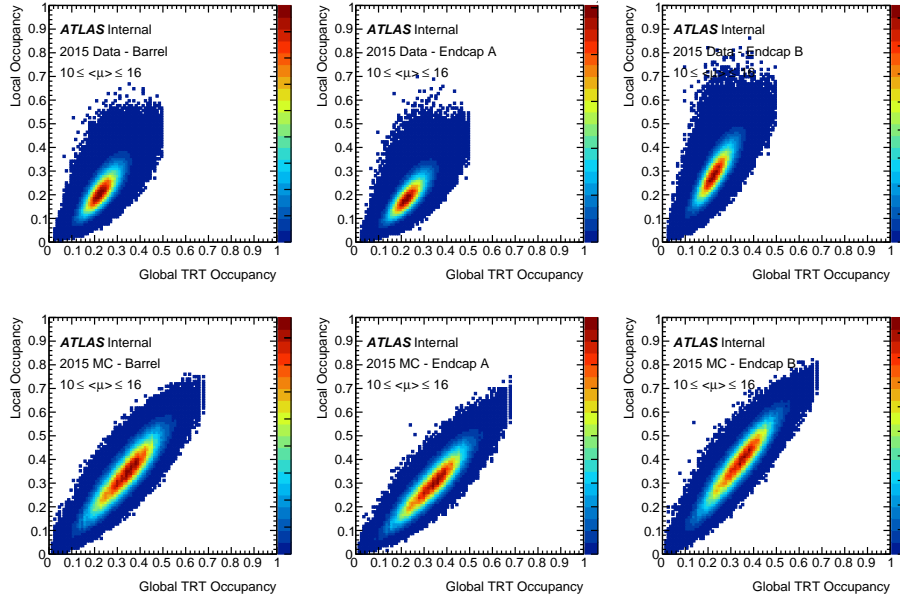


Figure 4.7: Distributions of local occupancies as a function of global TRT occupancy, in 2015 data (top) and MC (bottom).

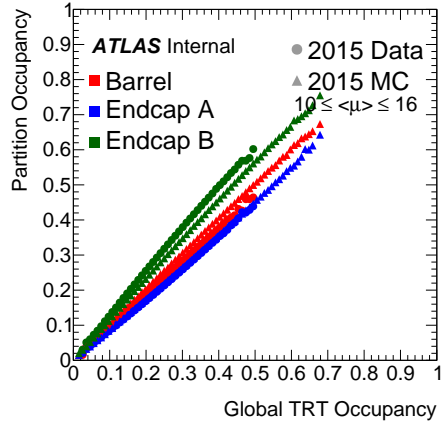


Figure 4.8: Partition average occupancy as a function of Global TRT occupancy, in 2015 data and MC.

mostly through the Endcap A, and a track with $|\eta| > 1.55$ only goes through the Endcap B wheels. The higher occupancy in the Endcap B wheels is clearly seen for tracks at the highest $|\eta|$ values.

Several studies were performed to determine the optimal granularity to use, to have a realistic description of the occupancy around the track while minimizing CPU consumption. Three granularities were studied in detail: The coarsest granularity (Gran1) is the granularity of partition

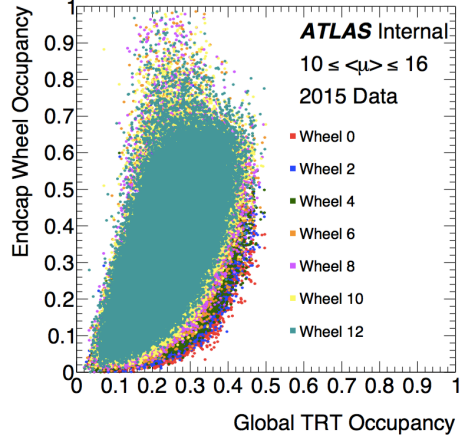


Figure 4.9: Endcap wheel occupancy as a function of Global TRT occupancy, in 2015 data. One data point corresponds to one event. Only every other wheel is included; there are 14 total. “Wheel 0” corresponds to the wheel at smallest $|z|$, closest to the interaction point, and “Wheel 12” is the second outermost wheel, in the most forward region of the TRT.

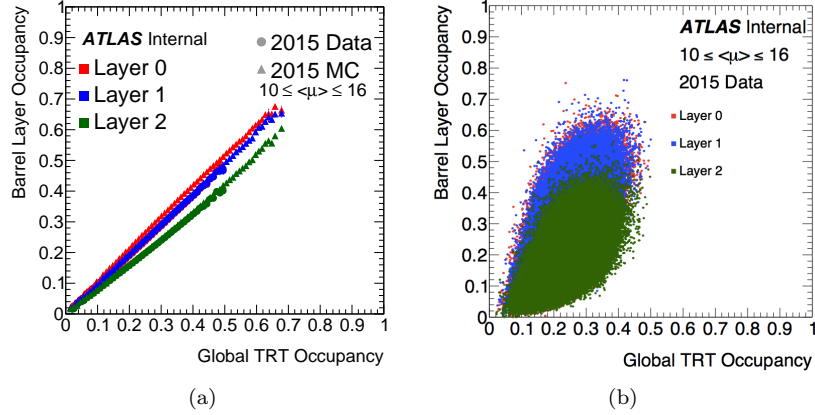


Figure 4.10: Average (a) and event-by-event (b) barrel layer occupancy as a function of Global TRT occupancy, in 2015 data and MC. “Layer 0” corresponds to the innermost layer, closest to the beampipe, and “Layer 2” is the outermost layer, at farthest radius from the beampipe.

occupancies. The middle-sized granularity (Gran2) is the granularity of the 192 local occupancies, which divide each partition into 32 sections in ϕ . The finest granularity (Gran3) calculates a number for each of the 192 regions in Gran2, further divided into the three layers for the barrel, and the 14 wheels in the endcaps, for a total of 1088 regions. Any of these granularities can be chosen to define the region i used to calculate the track occupancy defined in Equation 4.3. Figures 4.13–4.16

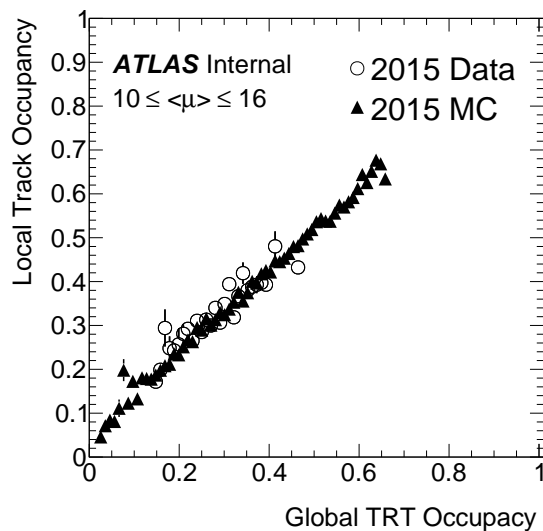


Figure 4.11: Local track occupancy as a function of global TRT occupancy, in 2015 data and [MC](#).

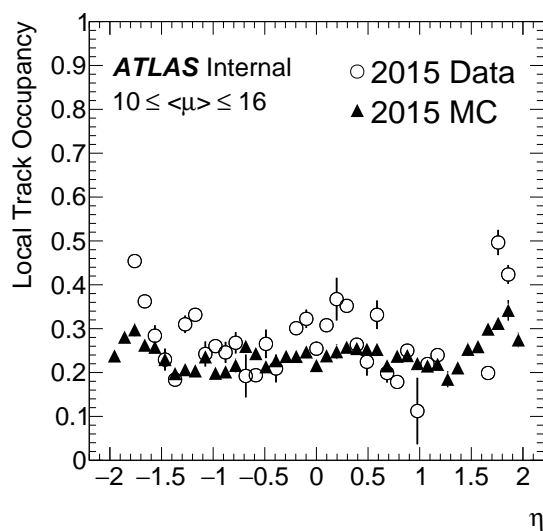


Figure 4.12: Local track occupancy as a function of track pseudorapidity, in 2015 data and [MC](#).

compare the local track occupancy for each track, calculated using each of the three granularities. Figure 4.13 demonstrates that on average, Gran3 leads to a slightly higher local track occupancy, but this will have no physical consequences for the electron likelihood, since once we pick a granularity, the PID tool is optimized based on these occupancy values. Figure 4.14 shows the difference in the value of the local track occupancy from each possible pair of granularity options, for example

Gran1 - Gran2. Figure 4.15 shows the relative difference, after dividing by the smallest local track occupancy, for example $(\text{Gran1} - \text{Gran2})/\min(\text{Gran1}, \text{Gran2})$. Figure 4.16 shows the ratio of the values of the local track occupancy, for example $\text{Gran1}/\text{Gran2}$. These distributions show that there is only a small difference between Gran2 and Gran3. This is expected because each track is going across several barrel layers or endcap wheels, so any occupancy differences between individual layers or wheels is smeared away due to the averaging in Equation 4.3. The differences between Gran1 and Gran3 are only slightly more pronounced than those between Gran1 and Gran2.

One interesting feature about this set of plots is that in Figure 4.14b, only a small dependence on global TRT occupancy is visible. However, if we look at Figures 4.15b and 4.16b, a slight dependence can be seen. As the global occupancy increases, the relative difference between granularities decreases and the ratio between them approaches unity. This is an artifact of the linear relationship between local track occupancy and global occupancy. Figure 4.14 shows that the difference between two granularities is quite flat with global occupancy, so as global occupancy increases, the numerator of the relative difference stays the same while the denominator increases. This leads to a relative difference that approaches zero, as seen in Figure 4.15. The same effect can be seen in a slightly different way in Figure 4.16. As the global occupancy increases, each granularity also increases but the difference remains constant, such that the ratio approaches one.

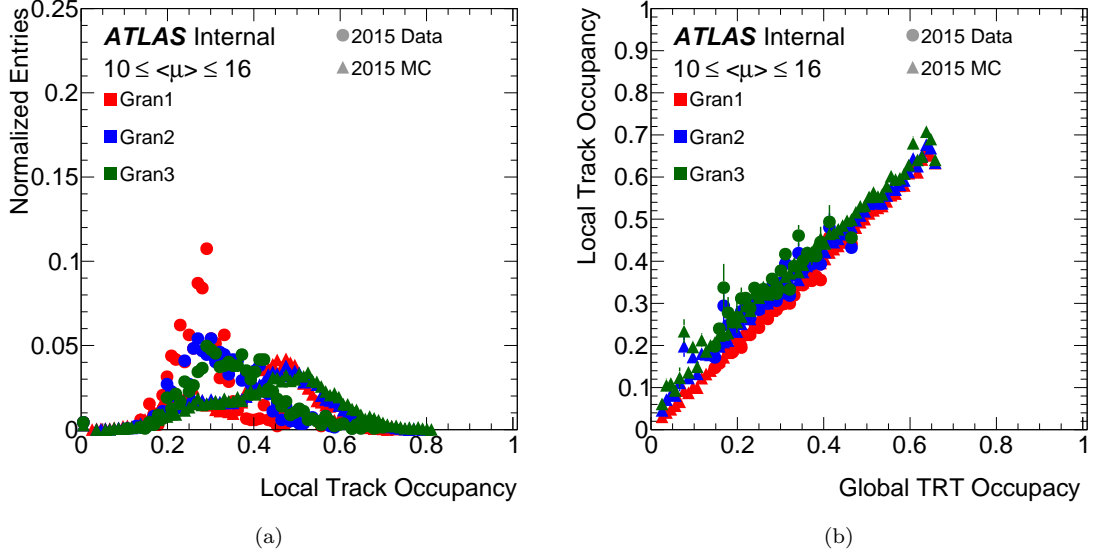


Figure 4.13: Local track occupancy distributions based on different granularities, in 2015 data and MC. The obvious difference between data and MC in (a) is due to the difference in global occupancy distributions, as can be seen by considering (b) where the distributions match perfectly.

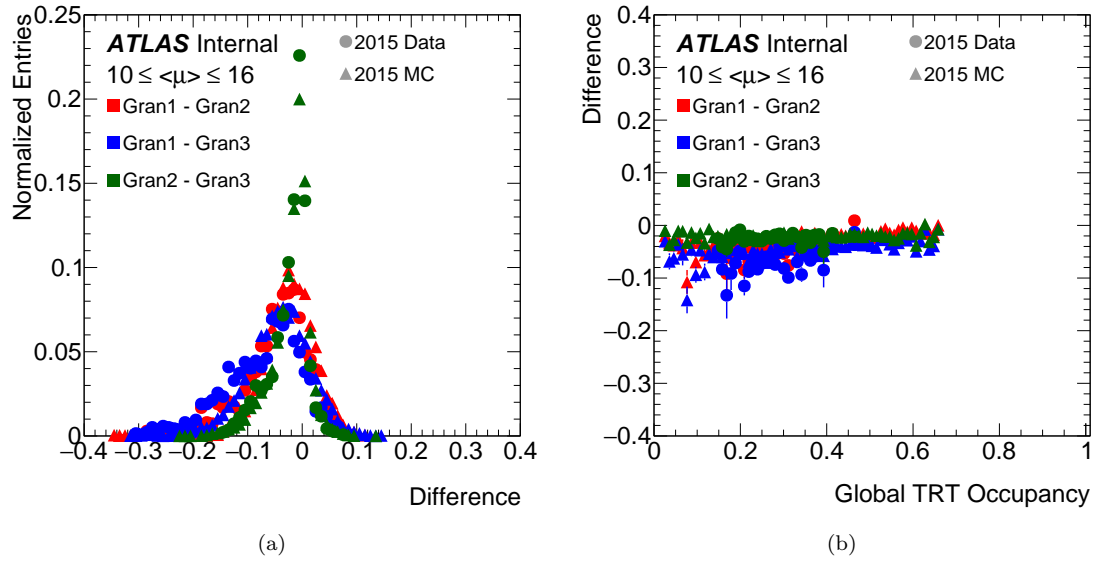


Figure 4.14: Difference in local track occupancies based on different granularity calculations, in 2015 data and MC.

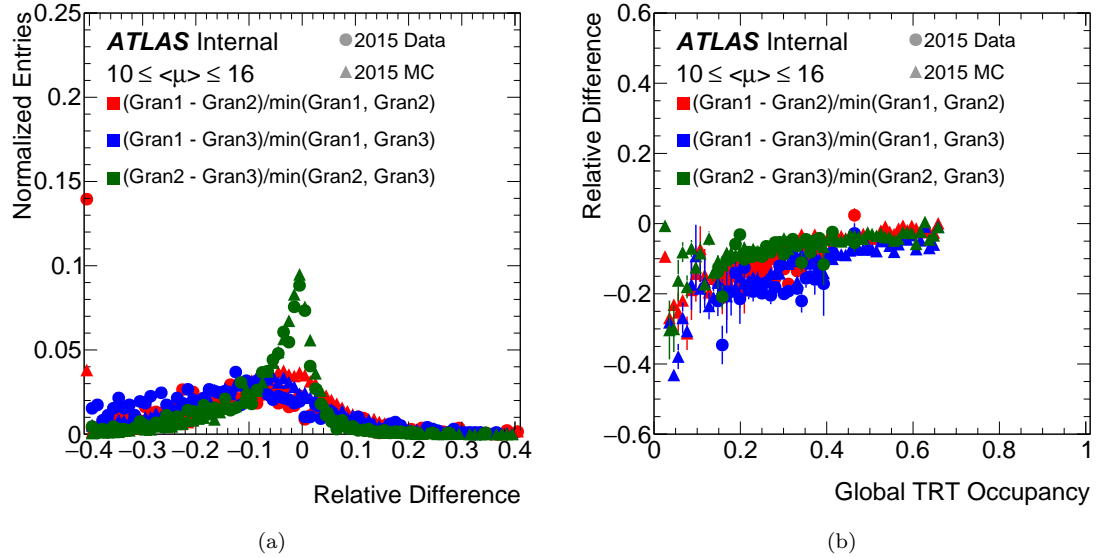


Figure 4.15: Relative difference in local track occupancies based on different granularity calculations, in 2015 data and MC.

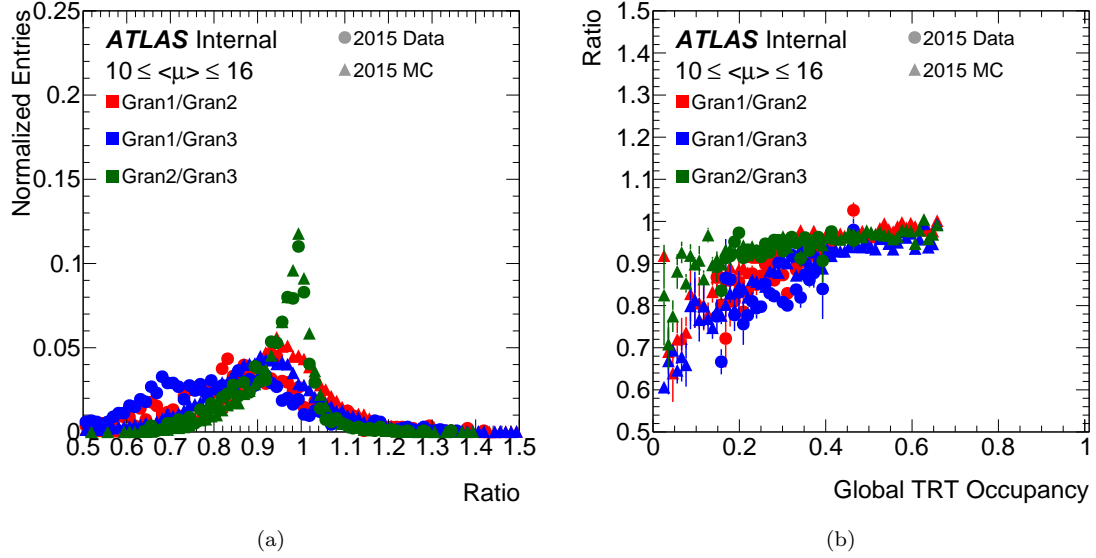


Figure 4.16: Ratio of local track occupancies based on different granularity calculations, in 2015 data and MC.

Figure 4.17 compares the CPU consumption of each granularity, for three 2014 MC $Z \rightarrow ee$ samples. The x -axis markers labeled “GranX” show the CPU required for each of the three granularities described. The other markers show the CPU consumption of reconstruction before the local occupancy calculation is added, to give a sense of scale. The data point on the far left, labeled “No TRT”, corresponds to the CPU per event of Inner Detector reconstruction without any TRT tracking. Next to the left, “No Local Occ”, is the CPU consumption including TRT reconstruction but before the Local Occupancy Tool is added. Then, on the far right is the CPU consumption for the “Whole Detector”, which includes the calorimeters and the muon system. It is clear that the addition of the TRT local occupancy tool does not contribute significantly to the CPU required for an event. The difference between the three MC samples is due to their different average global occupancy, shown as “ $\langle \text{occ} \rangle$ ” in the legend, which is directly proportional to the number of charged particles that have to be reconstructed in each event. If the CPU per event is scaled by the average number of tracks per event, there is much better agreement for the different global occupancy ranges. This is shown in Figure 4.18. Figure 4.18a shows the average CPU per event and Figure 4.18b shows the average CPU per number of tracks. The scale on the left spans 14 s, whereas the scale on the right spans 20 ms. Note that the x -axis of this figure is different from that of Figure 4.17. In this figure, the furthest left point shows the CPU consumption including TRT reconstruction but before any

local occupancy calculation is added. This is identical to the second-left point in Figure 4.17. The middle point shows the CPU consumption if we calculate the local occupancy in each of 192 regions, corresponding to Gran2, but without calculating individual local track occupancies. Finally on the right we see the additional CPU required when the individual local track occupancies are calculated, according to Equation 4.3. For the highest occupancy sample (green data points), calculating the local track occupancy increases the average CPU per average number of tracks by 0.10 ms.

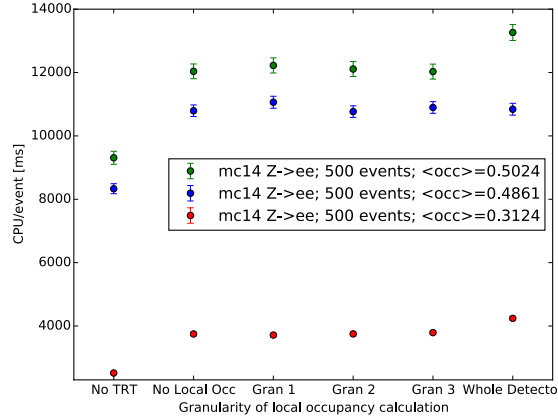


Figure 4.17: CPU consumption per event as a function of granularity of local occupancy calculation, calculated with 2014 MC $Z \rightarrow ee$ samples. The furthest left point, marked “No TRT”, corresponds to the CPU consumption when no TRT tracking is performed in the reconstruction. The furthest right point, marked “Whole Detector”, corresponds to the CPU required to reconstruct the entire event. The other points only reconstruct the Inner Detector. It is clear that the choice of granularity for the occupancy calculation does not change the CPU consumption. The huge difference in scale, depending on the sample used, depends highly on the number of tracks and therefore the occupancy in that sample. In the legend, “ $\langle \text{occ} \rangle$ ” refers to the global TRT occupancy.

Gran2 is chosen as the nominal granularity for the track local occupancy calculation, since it provides a better local description than the coarser Gran1, and is not very different from the finer Gran3, with very little difference in CPU requirement.

4.3.2 Comparison of Online and Offline Occupancy

There are differences in data access between offline reconstruction and the online [High Level Trigger \(HLT\)](#). In reconstruction, there is unlimited time to access all information in the detector, and so all TRT data is available at once. In the HLT, constraints are set in order to minimize processing time to reach a trigger decision for each event. Only portions of the data are read out at a time. [RoIs](#) are defined by towers in the electromagnetic calorimeter, and only portions of the TRT data that

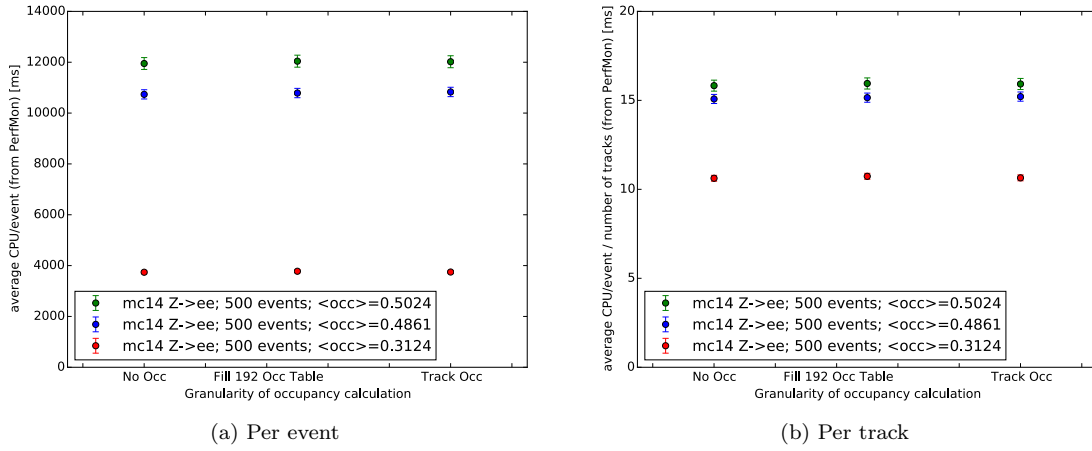


Figure 4.18: Amount of CPU required to calculate local track occupancies for each track, calculated with 2014 MC $Z \rightarrow ee$ samples. It is clear that the addition of the Local Occupancy Tool adds negligible CPU. Note the difference in scale on the plots in each panel. The CPU required to reconstruct each track is relatively constant (hence the scale of 20 ms on the plot on the right), but an event with higher occupancy has more tracks to reconstruct. This leads the overall CPU of the event to increase, hence the scale of 14 s on the plot on the left. In the legend, “ $\langle \text{occ} \rangle$ ” refers to the global TRT occupancy.

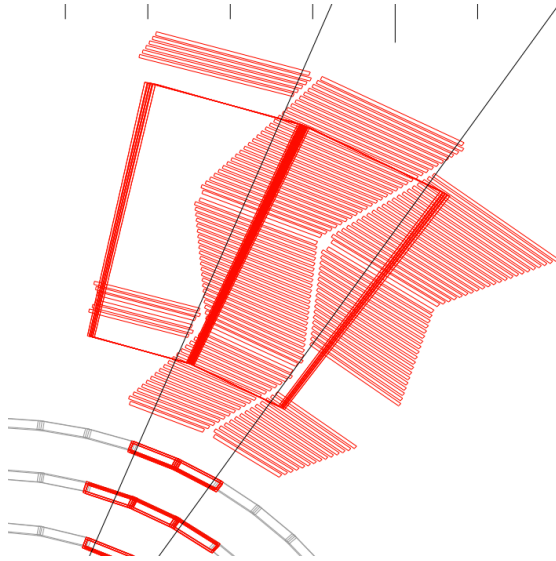


Figure 4.19: Example of a trigger RoI in the TRT barrel, courtesy of Mark Sutton. The black lines mark the limits of the RoI, and the red strips include all straw layers whose data are included for this RoI.

align with the RoI are processed and stored. An example is shown in Figure 4.19. The black lines mark the boundaries of the RoI, and the red strips include all straw layers whose data are within these boundaries. RoI are not all found at once, but rather several are found at a time as the event is processed, so the amount of TRT information available is not constant throughout the processing of an event. For this reason it is impossible to find the global or partition TRT occupancies in the HLT. Additionally, these RoI are 0.2 wide in pseudorapidity η and 0.2 wide in azimuthal ϕ , so only rarely do they conveniently align with the boundaries of TRT phi sectors, which in the barrel have the same trapezoidal shapes as the mapping of the TRT barrel straws to the front-end electronics boards, as can be seen in Figure 4.19. It is not immediately straightforward to calculate the local occupancies as defined in Section 4.3.1, since the RoI do not find all drift circles within one of the 192 regions. They do however have access to all straw words (or Raw Data Objects, RDOs) within one of these regions, since the structure of the data readout requires that all data on a ReadOut Driver (ROD) must be read out at once. Again, the RODs follow the geometry of the front-end electronics boards and so correspond to complete phi sectors. We can thus conveniently select all RDOs in the appropriate phi sector, and apply the same validity gate that is applied to the drift circles. Then, the number of RDOs inside the validity gate will match exactly the number of drift circles, and the local occupancy matches exactly with that which will be found offline. There is one slight complication in Endcap A, where the wheel at highest $|z|$ is included in the Endcap B ROD. Therefore when an Endcap A ROD is retrieved by an RoI, and the Endcap B ROD at the corresponding phi sector was not retrieved, the Endcap A occupancy needs to be rescaled to count only 5 of the 6 wheels in the denominator. If, in the same event, the Endcap B ROD is later retrieved, then the Endcap A occupancy is again corrected to count all 6 wheels.

The largest alteration to the Local Occupancy Tool for the online implementation is the fact that unlike the offline implementation, which calculates all local occupancies in all 192 regions at once, the online tool calculates occupancies only within regions through which a track has passed. Once the occupancy for a region is calculated, the number is stored to avoid recalculating its occupancy. The limited data access also means that it is impossible to calculate partition occupancies in the HLT, so only local occupancies are calculated.

To test the efficacy of the Local Occupancy Tool online and offline, 1936 events of 2014 MC samples were processed in Athena release 20.7.3.8. All plots shown in this section were made with these samples. The same events were processed in the regular offline reconstruction as well as in a trigger testing environment, which uses the Athena command `trigtest.pl --test ElectronSliceAthenaTrigRDO_MC`. When running these tests, it is preferential to compare the online and offline occupancies for indi-

vidual tracks. To make sure that the same tracks are compared directly, the tracks are matched using their kinematic variables η , ϕ and p_T . Only tracks that pass the following criteria are included in the figures shown: $|\eta^{\text{off}} - \eta^{\text{on}}| < 0.02$, $|\phi^{\text{off}} - \phi^{\text{on}}| < 0.02$, and $|p_T^{\text{off}} - p_T^{\text{on}}| < 0.1$ GeV. Out of the 1936 processed events, 25383 tracks were matched between the online and offline samples. The figures that are split into three partitions are filled depending on the pseudorapidity η of the track, such that tracks with $|\eta| \leq 0.9$ fill the “Barrel” plot, tracks with $0.9 < |\eta| \leq 1.55$ belong in the “EndcapA” plot, and tracks with $1.55 < |\eta| < 2$ go in the plot labeled “EndcapB”.

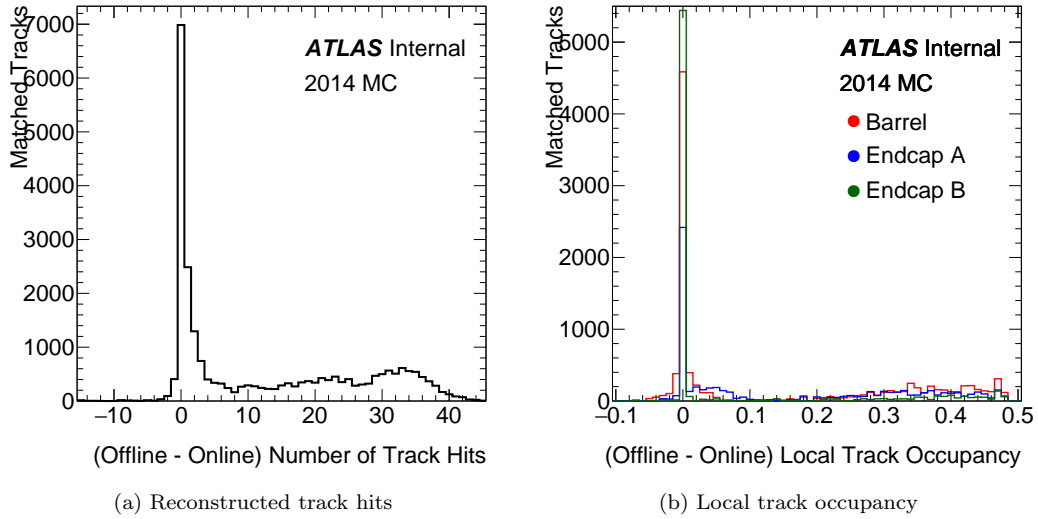


Figure 4.20: Difference in online and offline reconstructed track hits (a) and local track occupancy (b).

There is one more complication, which is that the track hits which are found online do not match exactly with those found offline, as shown in Figure 4.20a which plots the difference in number of track hits found offline and online. Typically, the offline reconstruction associates more hits to a track, since there is more time to comb thoroughly through the event. Online, many tracks do not have any associated TRT hits. This difference is inevitable, and for this reason, the local track occupancy found online does not always match exactly with that found offline. Figures 4.20b and 4.21 show that most tracks have zero difference, but there is a branch that spreads off and increases with global occupancy. This wing can be explained by the fact that many of the online tracks do not find any TRT hits. We see that the effect disappears if we remove all tracks with no track hits (and therefore zero track occupancy) from these plots, as in Figures 4.22a and 4.23, which are replicas of Figures 4.20a and 4.21 respectively, just with no zero-occupancy tracks. Now the online

and offline distributions match quite nicely. It is also clear that there is no dependence on global occupancy. Figures 4.24 and 4.25 show the relative difference in local track occupancy, that is, $(\text{offline} - \text{online})/\text{online}$ local track occupancy. The relative difference is consistently less than 15%, and only a few outliers exceed a relative difference of 10%. Finally, Figure 4.26 plots online local track occupancy as a function of offline local track occupancy, with a dashed line drawn along $y = x$. It is clear that while the two occupancies do not match up perfectly for each track, they follow the $y = x$ trend quite well.

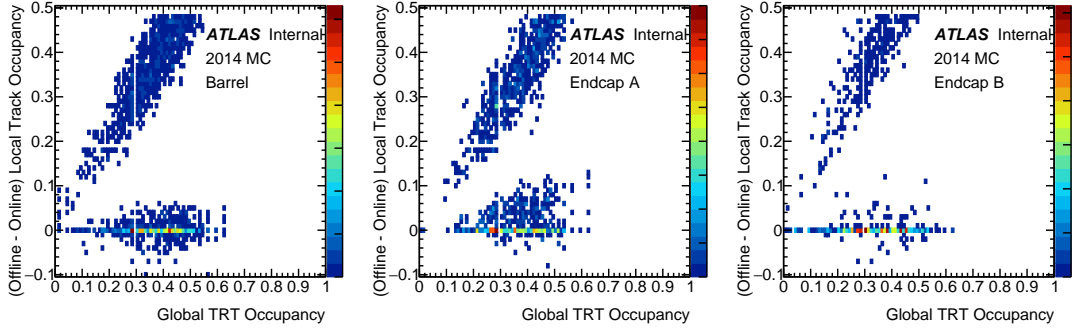


Figure 4.21: Difference in online and offline local track occupancy, as a function of global occupancy.

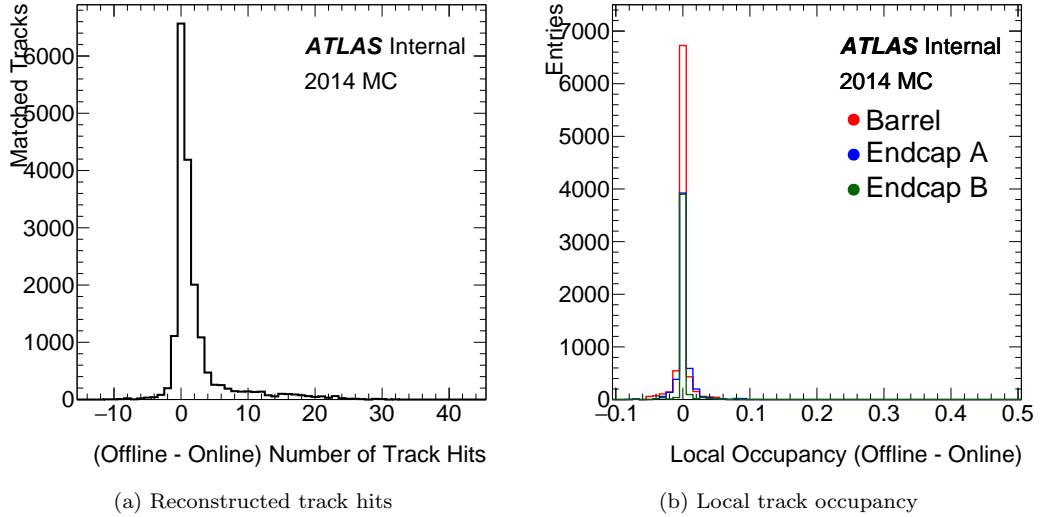


Figure 4.22: Difference in online and offline reconstructed track hits (a) and local track occupancy (b), removing all zero-occupancy tracks.

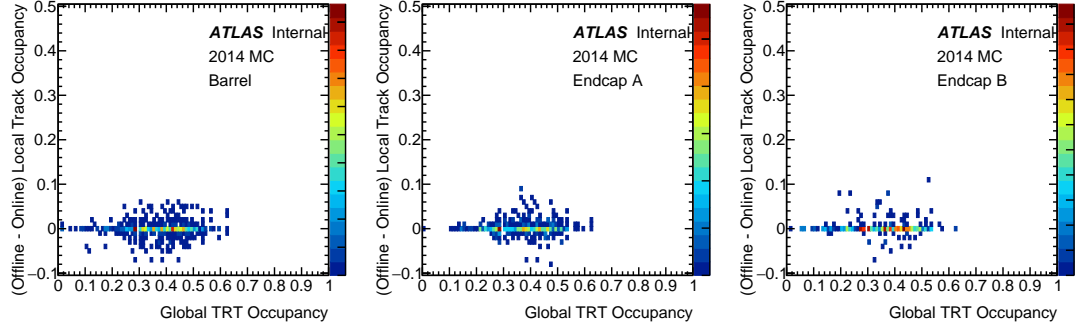


Figure 4.23: Difference in online and offline local track occupancy, removing all zero-occupancy tracks.

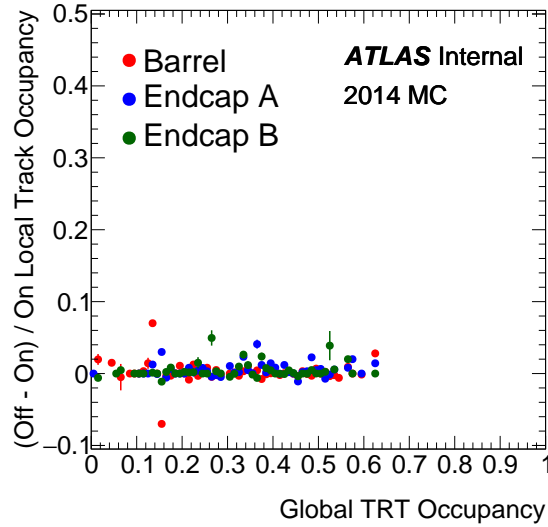


Figure 4.24: Relative difference in online and offline local track occupancy, removing all zero-occupancy tracks.

4.3.3 Summary

The Local Occupancy Tool calculates the TRT occupancy at two different granularities, as a means to handle pileup globally in an event, as well as locally. This is useful in order to understand the detector activity in the vicinity of a track. This tool has been developed, validated and optimized to work in offline reconstruction as well as online in the trigger. The granularities were chosen in order to minimize CPU consumption as well as the amount of numbers stored per event, while still being effective at gleaning local activity. Output from the tool has been used to tune the TRT PID, which in turn improves electron identification.

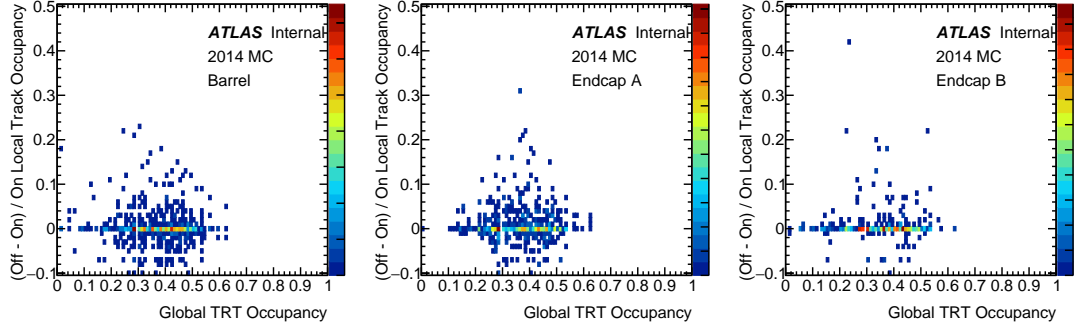


Figure 4.25: Relative difference in online and offline local track occupancy as a function of offline global TRT occupancy, removing all zero-occupancy tracks.

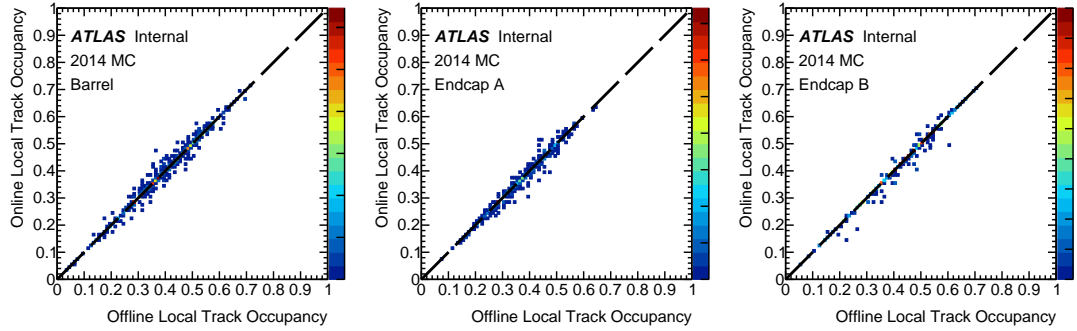


Figure 4.26: Online local track occupancy as a function of offline local track occupancy, removing all zero-occupancy tracks.

4.4 Tracking at high luminosity in the TRT

In 2016 data it was noticed that the error scaling described in Section 4.1 does not properly ensure the width of the pull (defined in Equation 4.1) is 1 at high occupancies. Instead, the pull width increases with larger occupancy. This issue is more prevalent in data than in Monte Carlo, although the effect is seen in both. If the pull width is larger than 1, then hit errors are underestimated and therefore fewer hits will be classified as precision since fewer hits will satisfy the requirement that the residual be within ± 2.5 of the hit error. This leads to a smaller PHF and ultimately fewer TRT extensions. This has a significant impact on the efficiency of reconstructed objects, most notably muons where a 0.5% drop in efficiency was seen in data, and also on TRT standalone tracks which are used to reconstruct converted photons.

In fact, there are several possible reasons why TRT extensions can be rejected from a track. These reasons, and the frequency at which each of them are the cause for a failed extension as

a function of $\langle\mu\rangle$, can be seen in Figure 4.27. This plot shows that the largest reason for failed TRT extensions at high $\langle\mu\rangle$ is external to TRT, usually due to a large number of Silicon holes. It is perhaps expected that the overall quality of Silicon tracks degrades at high $\langle\mu\rangle$, since high occupancy leads to more possible combinations of hits, which in turn leads to more “fake” or low-quality tracks. This can be seen from Figure 4.28 which shows that the average number of “Loose” (lower quality) tracks increases more rapidly as a function of pileup than “Tight” (higher quality) tracks do. There is clearly nothing that can be done in the TRT algorithms to improve these tracks, so they will be ignored for the remainder of this discussion. The second largest reason for failed TRT extensions at high pileup is the PHF requirement. For this reason, it is worth investigating if this requirement can be reoptimized for high pileup without degrading the resultant track quality.

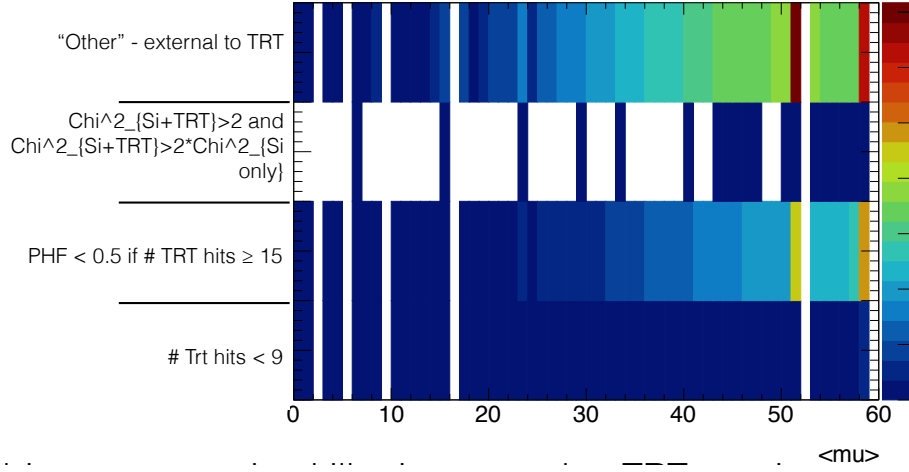


Figure 4.27: Reason for failed TRT extension.

To study the PHF requirement on TRT extension efficiency, good quality muon tracks were selected from a Monte Carlo $Z \rightarrow \mu\mu$ sample, using the following criteria defined by the tracking subgroup in Ref. [61]:

- at least 1 Pixel hit
- at least 5 SCT hits
- no more than 2 Silicon holes

True and Fake tracks were also selected using the following definitions provided by the tracking subgroup (see Ref. [62]):

True tracks:

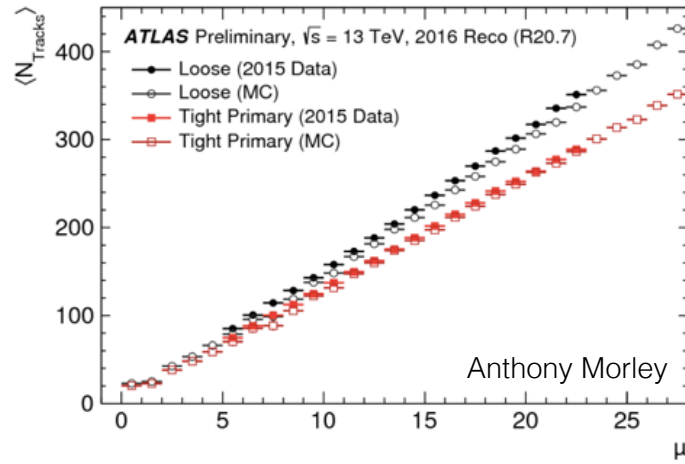


Figure 4.28: Average number of Loose and Tight tracks per event as a function of pileup, in 2015 data and Monte Carlo. Courtesy of Anthony Morley.

- at least 7 Silicon hits
- no more than 2 shared silicon hits
- no more than 2 silicon holes
- no more than 1 Pixel hole
- Truth match probability ≥ 0.5
- Status=1, charge!=0
- $p_T > 400$ MeV and $|\eta| \leq 2.5$
- Associated truth particle is a primary particle

Fake tracks:

- at least 7 Silicon hits
- no more than 2 shared silicon hits
- no more than 2 silicon holes
- no more than 1 Pixel hole
- either truth match probability < 0.5 or no associated truth particle or barcode of associated truth particle = 0.

It should be noted that this definition of fake tracks includes all pileup tracks, since no truth pileup information is accessible. Only tracks with $p_T > 3$ GeV and $|\eta| < 2$ are used in the following studies. PHF cuts from 10% to 50% were studied, with a goal of increasing the number of tracks with high-quality TRT extensions without significantly increasing the number of tracks with low-quality TRT extensions.

The plots in the remainder of this section show the TRT extension fraction, which is the ratio of all successful TRT extensions to all extension candidates. Figure 4.29 shows the TRT extension fraction as a function of $\langle\mu\rangle$ (a), global TRT occupancy (b), and local track occupancy (c). There is a much larger dependence on track occupancy than $\langle\mu\rangle$ and global occupancy, which again demonstrates the usefulness of this variable. The various colors shown in these distributions represent different PHF cuts on the TRT extension. As expected, loosening the PHF cut increases the TRT extension fraction. A great increase is seen by lowering the cut from 50% to 30%, where tracks with occupancy 80% experience a 35% increase in efficiency. This PHF cut also results in a TRT extension fraction which is nearly flat with occupancy. Loosening the cut beyond 30% does not increase the TRT extension fraction significantly.

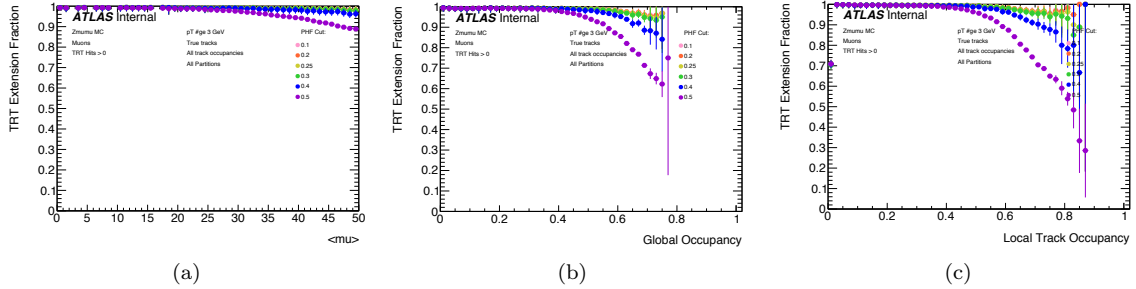


Figure 4.29: TRT extension fraction as a function of $\langle\mu\rangle$ (a), global TRT occupancy (b), and local track occupancy (c), for various PHF cuts, in $Z \rightarrow \mu\mu$ Monte Carlo.

Figure 4.30 compares the TRT extension fraction as a function of track occupancy for various PHF cuts, split by the tracks' classification as true (a) or fake+pileup (b) following the criteria listed above. Here it is seen that the collection of fake+pileup tracks also experiences an increase in TRT extension efficiency at high occupancy. However it should be remembered that these fake tracks already existed; they just did not have an extension. The loosening of the PHF cut does not increase the number of fake tracks but rather the fraction of those tracks which have a TRT extension.

Another way to visualize this increase in TRT extensions is shown in Figure 4.31, which plots

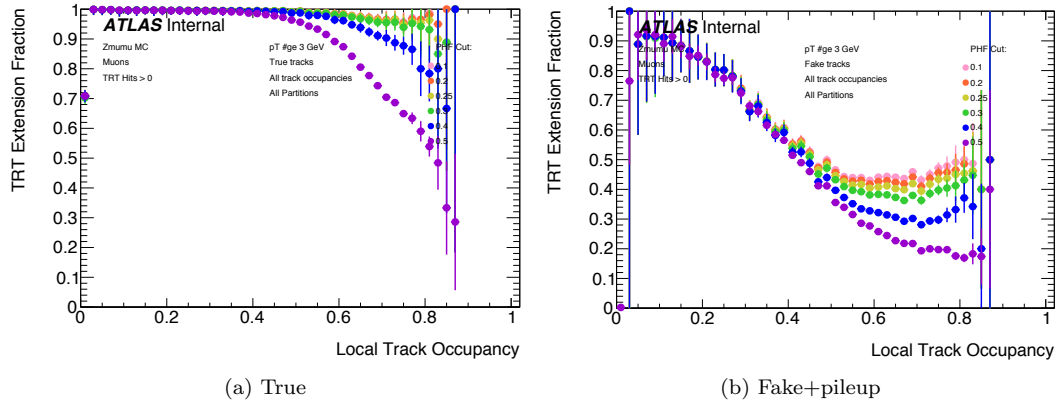


Figure 4.30: TRT extension fraction as a function of track occupancy for various PHF cuts, split by the track's true (a) or fake+pileup (b) classification, in $Z \rightarrow \mu\mu$ Monte Carlo.

the number of TRT outliers on track for both successful and failed TRT extensions, separately for the barrel and the endcaps. As mentioned in Section 4.1, all TRT hits on track with a failed TRT extension are reclassified as outliers. This can be seen in Figure 4.31, where the tracks with 9 or more outliers all have failed TRT extensions, as marked with an open circle. Correspondingly it is very rare for a track with a successful TRT extension (marked with a closed circle in these figures) to have more than 1 outlier. The drop in number of tracks with a large number of outliers corresponds to the drop in tracks with a failed TRT extension, due to the loosened PHF cut.

Similarly, Figure 4.32 shows the number of tube hits on track for various PHF cuts. As expected, the number of tube hits increases slightly with the decreased PHF cut. This motivates an exami-

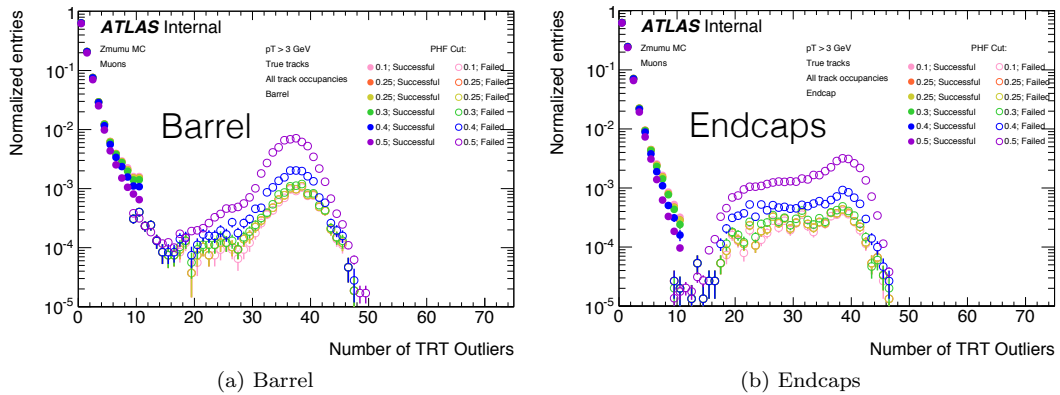


Figure 4.31: Number of TRT outliers on track for both successful and failed TRT extensions, for various PHF cuts, in $Z \rightarrow \mu\mu$ Monte Carlo.

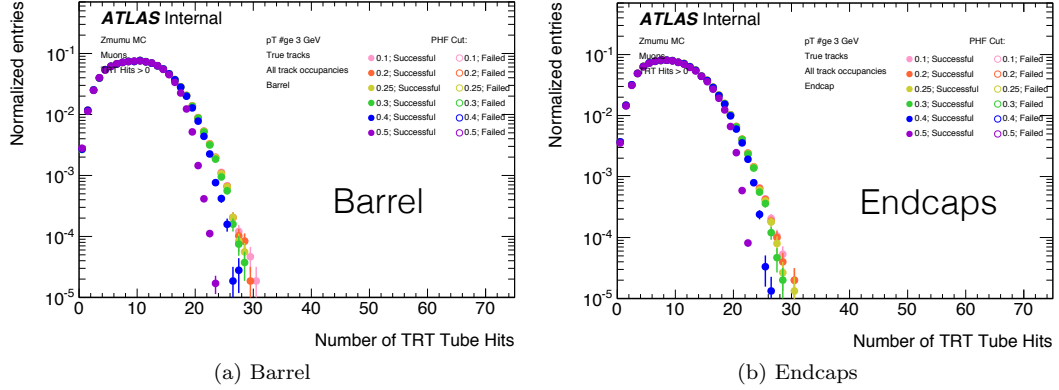


Figure 4.32: Number of TRT tube hits on track, for various PHF cuts, in $Z \rightarrow \mu\mu$ Monte Carlo.

nation of the momentum resolution of the tracks with TRT extensions, to ensure that the loosened PHF cut does not worsen the track momentum measurement.

The (transverse) momentum resolution is defined as

$$\frac{1/p_T^{\text{measured}} - 1/p_T^{\text{truth}}}{1/p_T^{\text{truth}}}, \quad (4.4)$$

where the inverse momentum is used to ensure a Gaussian distribution because the actual measurement is the sagitta, as described in Section 3.2.4. Figure 4.33 shows the momentum resolution for successful (a) and failed (b) TRT extensions for several PHF cuts, with the width of the Gaussian fit for each PHF cut also shown in the legend. By comparing the widths reported for each PHF cut in (a) and (b), it can be seen that on average, tracks with a successful TRT extension have better resolution than tracks with a failed TRT extension. This illustrates the motivation to recover as many TRT extensions as possible. It can also be seen by focusing on (a) that the resolution of tracks with successful TRT extensions using the PHF>30% cut is only very slightly (less than 1%) larger than that using the PHF>50% cut.

To hone in on the effect of loosening the PHF cut, it is useful to compare the resolution of tracks that are newly included in the TRT extension population with the loosened PHF cut. Figure 4.34 provides this direct comparison. The plot on the right (b) is the same as Figure 4.33b, but the plot on the left (a) shows the tracks with successful TRT extensions but with PHF<0.5 so that this plot is only filled with tracks that pass the new PHF cut, and not all the tracks that always had a successful extension even with the old tight cut. This distribution shows that if the PHF cut is loosened to 30%, the resolution of the tracks with newly successful TRT extensions is 2.70%,

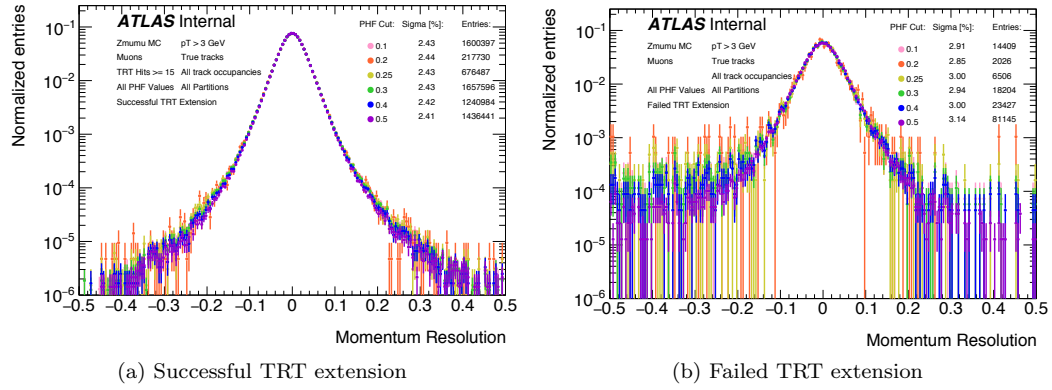


Figure 4.33: Momentum resolution for tracks with successful and failed TRT extensions, for various PHF cuts, in $Z \rightarrow \mu\mu$ Monte Carlo.

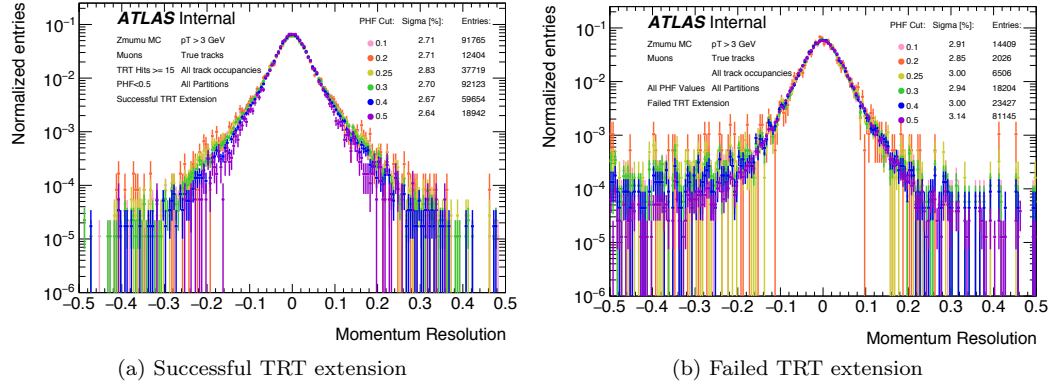


Figure 4.34: Momentum resolution for tracks with successful and failed TRT extensions and with $\text{PHF} < 0.5$, for various PHF cuts, in $Z \rightarrow \mu\mu$ Monte Carlo.

compared to 3.14% with the old 50% PHF cut. This is a sizable improvement in the resolution of these tracks.

The PHF cut at 50% was found to be the main reason for an observed drop in TRT extension efficiency at high pileup for otherwise good-quality tracks. Studies show that loosening this cut to 30% results in a significant recovery of the TRT extension efficiency. This is especially beneficial because of the improved momentum resolution for tracks with TRT extensions. Additionally, the increase in the rate of low-quality tracks with newly accepted TRT extensions due to the loosened PHF cut was deemed acceptable, since these tracks were already being reconstructed. For the reasons outlined here, it was decided to reduce the PHF cut from 50% to 30% for the ATLAS software Release 21 and the reprocessing of all data with this release.

CHAPTER 5

Search for Stop LSP Decays to a b -jet and a Lepton

As motivated in Section 2.3.3, it is interesting to search for supersymmetry via direct stop pair production due to the large cross-section of this process. Of particular interest is the scenario where the stop (\tilde{t}) is the LSP in the $B - L$ MSSM, in which case each \tilde{t} decays via an RPV coupling to a b -quark and a charged lepton ($\tilde{t} \rightarrow b\ell$), as shown in Figure 5.1. In contrast to RPC searches for the stop, there is no significant missing transverse momentum in these RPV decays. The \tilde{t} decay BRs to each lepton flavor are related to the neutrino mass hierarchy [28,29], and a large phase space in the BR plane is available, as was shown in Figure 2.9. With an inverted mass hierarchy the BR to the $b\mu$ final state may be as large as 100%, and with a normal mass hierarchy the BR to the $b\mu$ final state may be as high as 90%. The experimental signature is therefore two oppositely charged leptons of any flavor and two b -jets, with two lepton-jet resonances at the same mass.

Previous searches with similar final states have targeted the pair production of first-, second-, and third-generation leptoquarks at ATLAS [63,64] and at CMS [65,66]. However, they consider final states within the same generation ($eejj$, $\mu\mu jj$, $\tau\tau bb$, where j indicates a light-flavor jet) and do not focus on final states with both b -jets and electrons or muons ($eebb$, $\mu\mu bb$), nor consider final states with leptons of different flavors (for example $e\mu bb$). The results of the Run 1 leptoquark searches were reinterpreted for the \tilde{t} mass and its decay BRs in the $B - L$ model [28,29], setting lower mass limits between 424 and 900 GeV at a 95% confidence level. These limits are weakest for BRs that are equal to all lepton flavors, since final states with different lepton flavors are not considered.

In this chapter, two analyses for this stop signature will be presented. The dominant backgrounds

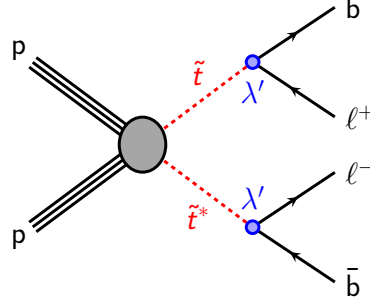


Figure 5.1: Feynman diagram for stop pair production, with \tilde{t} and anti- \tilde{t} (\tilde{t}^*) decay to a charged lepton of any flavor and a b -quark through an R -parity-violating coupling λ' .

and many search strategies are identical between the two analyses, so an overview of both analyses will be presented in Section 5.1. The first analysis was performed with 20.3 fb^{-1} of 8 TeV proton-proton data from the Run 1 LHC campaign, and will be described in detail in Section 5.2. This analysis was the dissertation topic of Brett Jackson [67] and was published as a conference note [1] before the focus shifted to Run 2 data. Because of the large increase in center-of-mass energy between Run 1 and Run 2, the reach of the Run 2 search is expanded by hundreds of GeV beyond that of the Run 1 search. The second analysis, which was performed with data collected during the early Run 2 (2015-2016) LHC campaign, corresponding to 36.1 fb^{-1} of 13 TeV proton-proton data, will be described in Section 5.3 [3]. This was the dissertation topic of Giuseppe Lerner [68]. Throughout this chapter, “Run 2” refers to the 36.1 fb^{-1} of data collected during 2015 and 2016, and excludes the additional luminosity collected during 2017 and 2018 unless otherwise noted. Finally, future prospects and similar searches which also have sensitivity to this model, as well as an updated third-generation leptoquark search with 36.1 fb^{-1} of 13 TeV data, will be discussed in Section 5.4.

5.1 Analysis Overview

5.1.1 Leptonic event selection

It was mentioned above that the stop can have non-negligible BR to all lepton flavors when considering both the normal and inverted neutrino hierarchies, and so it is interesting to look at final states of all combinations of lepton flavors. However because of the short lifetime of the tau, and given that it decays hadronically roughly 65% of the time, it provides for a much cleaner analysis to only

directly consider final states with light leptons (electrons and muons). Events where the stop decays to a tau can be included when the tau decays leptonically. In both rounds of this analysis, only events with electron or muon signatures are selected, and final states are split by flavor into ee , $e\mu$, and $\mu\mu$ selections. Moreover in the [Run 1](#) search, the signal samples do not simulate $\tilde{t} \rightarrow b\tau$ events. These decays are included in the [Run 2](#) search. Events are selected using unprescaled single-electron and single-muon triggers which vary by year and are all listed in [Table 5.1](#).

The efficiency of each trigger used with 2012 data, split by lepton flavor channel, can be seen in [Figure 5.2](#) as a function of stop mass, and the efficiency of passing at least one these triggers can be seen in [Figure 5.3](#). The lowest efficiency of passing at least one of the selected triggers is $92.7 \pm 0.9\%$, for flavor_mm events, and it is more than $98.3 \pm 0.3\%$ for all flavor_ee and flavor_em events.

It is necessary to use both a low- p_T and a high- p_T trigger to ensure high trigger efficiency for all events. While `EF_e24vhi_medium1` has high efficiency for electrons with $p_T < 100$ GeV, the efficiency drops off for electrons with higher p_T . This is because high- p_T electrons leave a more jet-like signature in the detector⁴ and so are accepted less often by the triggers which are optimized for low- p_T electrons. In contrast, the efficiency of `EF_e60_medium1` increases with p_T . This effect can be seen in [Figure 5.4](#), which show the trigger efficiencies of flavor_e μ events, for several ranges of electron p_T . Particularly noticeable is the decrease in efficiency of the `EF_e24vhi_medium1` trigger with increasing p_T in [Figure 5.4a](#), as well as the much lower efficiency for electrons with $p_T < 100$ GeV in [Figure 5.4b](#). It is therefore beneficial to have two electron triggers, one for low transverse momentum and one for high. This momentum-dependent efficiency is not seen in the flavor channels including muons. While the distributions shown here only include the triggers used in 2012 data, the same reasoning applies to the triggers used in all years.

5.1.2 Branching ratio reweighting

Signal samples are generated with a fixed [BR](#) of stop to lepton flavor. Signal events can then be reweighted by truth \tilde{t} decay to each lepton flavor, to emulate any BR hypothesis, using the formula

$$\text{weight} = N_{\text{decays}}^2 \prod_{i=e,\mu,\tau}^{N_{\text{decays}}} \mathcal{B}_{\text{target}}(\tilde{t} \rightarrow b\ell_i)^{N_{\text{truth}} \tilde{t} \rightarrow b\ell_i}, \quad (5.1)$$

⁴High- p_T electrons are less likely to deposit all of their energy in the electromagnetic calorimeter and so some of this energy will be deposited in the hadronic calorimeter. This causes a larger-than-typical value for the variable R_{had} , which is the ratio of transverse energy deposited in the hadronic to the electromagnetic calorimeter. R_{had} is used as a discriminant in electron triggers, so high- p_T electrons can be less likely to pass a cut on R_{had} in the low- p_T triggers.

Muon Triggers	Electron Triggers
2012	
EF_mu24i_tight EF_mu36_tight	EF_e24vhi_medium1 EF_e60_medium1
2015	
HLT_mu20_iloose_L1MU15 HLT_mu50	HLT_e24_lhmedium_L1EM20VH HLT_e60_lhmedium HLT_e120_lhloose
2016	
HLT_mu26_ivarmedium HLT_mu50	HLT_e26_lhtight_nod0_ivarloose HLT_e60_lhmedium_nod0 HLT_e140_lhloose_nod0

Table 5.1: Electron and muon triggers used for each year. “EF” is used for the Run 1 triggers and “HLT” is used for the Run 2 triggers; they both correspond to the last level of the trigger. Next the name of the trigger includes either “mu” or “e” which signifies whether a muon or electron candidate is required. Then the p_T cut of the trigger is specified in GeV. “L1” with some string following refers to the L1 seed; this seed is required for all triggers but it is not explicitly included in all trigger names. Text with “i” refers to the trigger-level isolation criteria, where “ivar” indicates a variable sized cone isolation requirement. “vh” indicates a pseudorapidity-dependent transverse energy threshold and a hadronic isolation requirements applied in the L1 seed. Text such as “tight”, “medium”, and “loose” refers to the trigger-level identification criteria, where “lh” signifies that a likelihood-based identification is used. “nod0” means there is no requirement on d_0 or $d_0/\sigma(d_0)$ [69–71].

where N_{decays} represents the number of possible \tilde{t} decays allowed in the simulation (3 in the Run 2 search, for the 3 lepton flavors, and 2 in the Run 1 search, as $\tilde{t} \rightarrow b\tau$ is not simulated in this search), $\mathcal{B}_{\text{target}}$ is the BR hypothesis of interest, and $N_{\text{truth } \tilde{t} \rightarrow b\ell_i}$ represents the number of truth decays of the target type in each simulated event. Indeed, in the absence of an observed excess, limits are set across the plane of $\mathcal{B}(\tilde{t} \rightarrow b\tau)$ versus $\mathcal{B}(\tilde{t} \rightarrow be)$ by making use of this exact reweighting scheme.

5.1.3 Backgrounds

The major SM backgrounds in this search are other processes which lead to two b -jets and two leptons. Most notable are top quark pair production ($t\bar{t}$), single top production (single-top), and $Z/\gamma^* + \text{jets}$ production. Other SM processes which contribute less significantly are $W + \text{jets}$, diboson, and $t\bar{t} + W/Z$.

The lepton–jet pair from each \tilde{t} decay generally reconstructs the invariant mass $m_{b\ell}$ of the original \tilde{t} . In an event with two leptons and two jets, two pairings are possible; one that reconstructs the

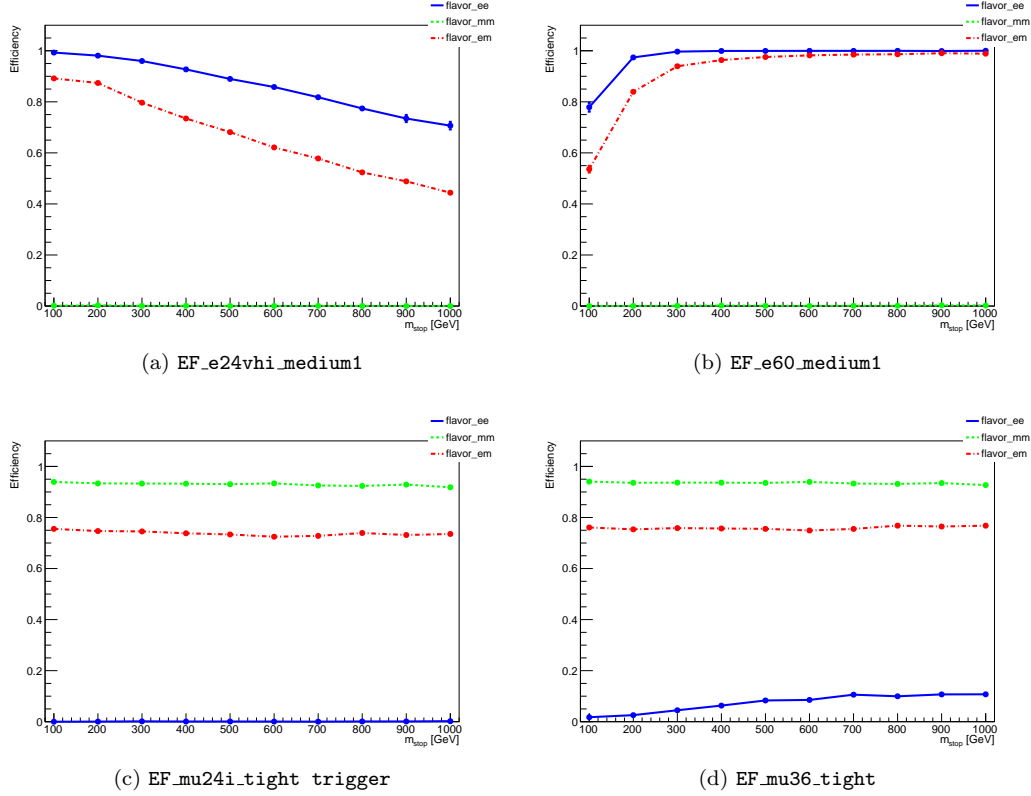


Figure 5.2: Efficiency of passing each 2012 trigger broken down by flavor channel.

correct \tilde{t} masses, and one which inverts the pairing and incorrectly reconstructs the masses. As the two masses should be roughly equal, the pairing that minimizes the mass asymmetry between $m_{b\ell}^0$ and $m_{b\ell}^1$ is chosen, defined as

$$m_{b\ell}^{\text{asym}} = \frac{m_{b\ell}^0 - m_{b\ell}^1}{m_{b\ell}^0 + m_{b\ell}^1}. \quad (5.2)$$

Here $m_{b\ell}^0$ is chosen to be the larger of the two masses. Events are further selected to have small mass asymmetry in order to reduce the contamination from background processes, whose random pairings lead to a more uniform $m_{b\ell}^{\text{asym}}$ distribution.

To reject backgrounds coming from $Z/\gamma^* + \text{jets}$ processes, we veto any event with leptons that are consistent with a Z boson. In the Run 1 version of this search, leptons are considered consistent with a Z if they are **same-flavor, opposite-sign (SFOS)** and have an invariant mass within 10 GeV of the true Z mass. In the Run 2 version of this search, all SFOS leptons with an invariant mass below 300 GeV are considered consistent with a Z boson. This is an efficient selection for the very high-mass signal points targeted, where the signal leptons are very high energy.

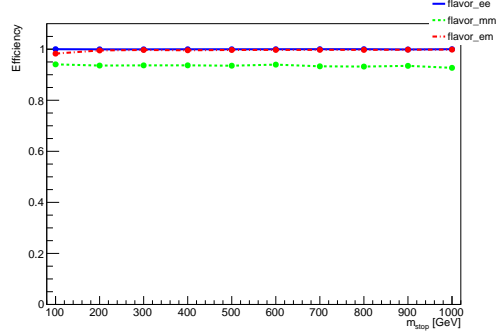


Figure 5.3: Efficiency of passing either the EF_e24vhi_medium1, the EF_e60_medium1, or the EF_mu36_tight trigger for each flavor channel.

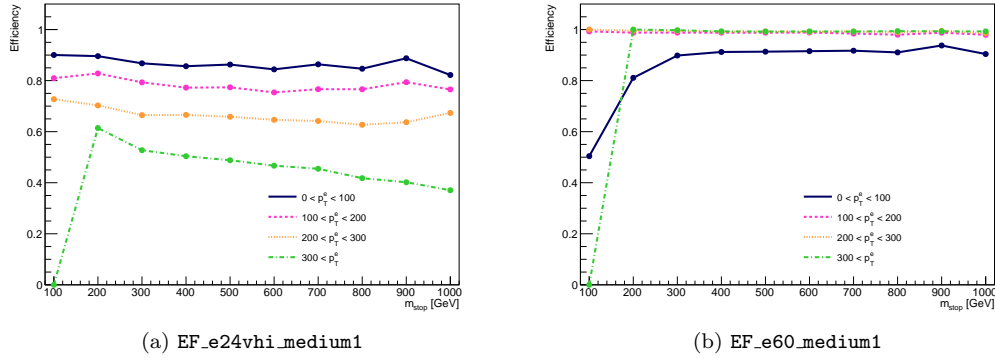


Figure 5.4: Efficiency of passing the single-electron 2012 triggers for several ranges of electron p_T . Only flavor_em events are shown.

Finally, because of the high-mass signal points targeted in both searches, events are required to have an overall large amount of energy. This is quantified using H_T which is the scalar sum of the p_T of the two leptons and two jets:

$$H_T = \sum_{i=1}^2 p_T^{\ell_i} + \sum_{j=1}^2 p_T^{\text{jet}_j}. \quad (5.3)$$

The variables defined above are used in both the Run 1 and Run 2 versions of this search. There are several more variables which are used in one or the other, based on individual optimizations of those searches. Those variables, as well as the overall region definitions, will be defined in the following sections.

5.2 Run 1 analysis

A description of the dataset and simulated samples used in this analysis are given in Section 5.2.1. The requirements on events and physics objects which are included in this analysis are given in Section 5.2.2. The kinematic requirements used to define the signal, control, and validation regions are presented in Section 5.2.3. The systematic uncertainties are detailed in Section 5.2.4, and finally the results are presented in Section 5.2.5.

5.2.1 Dataset and Monte Carlo simulated samples

The data sample used for this search was collected from proton–proton collisions at a center-of-mass energy of $\sqrt{s} = 8$ TeV in 2012. After the application of beam, detector, and data-quality requirements, the total integrated luminosity considered in this analysis corresponds to 20.3 fb^{-1} . The uncertainty on the integrated luminosity is 2.8%. It is derived following the same methodology as that detailed in Ref. [72].

MC simulation is used to estimate the detector response and efficiency to reconstruct the signal process, estimate systematic uncertainties, and to predict the backgrounds from Standard Model processes. The response of the detector is simulated using a detailed model implemented in GEANT 4 [73, 74]. Multiple overlapping pp interactions (pileup) are included in the simulation by overlaying simulated minimum bias events, generated using PYTHIA version 8.160 [75], onto the simulated hard scatter event. The simulated events are weighted such that the distribution of the average number of pp interactions per bunch crossing agrees with data. The simulated events are reconstructed with the same algorithms that are applied to collision data. The underlying event is described with the AUET2 tune [76] for all samples apart from $t\bar{t}$, which uses the Perugia 2011C tune [77], and the $Z/\gamma^* + \text{jets}$ samples which use a SHERPA-specific tune [78].

Stop pair production is modeled using MadGraph version 1.5.12 [79] to generate stop-anti-stop pairs using the CTEQ 6L1 parton distribution functions (PDFs) [80], and PYTHIA version 6.427 [81] to perform the R -parity-violating stop decay as well as the parton shower calculation. Stop pairs are generated for stop masses between 400 GeV and 1000 GeV in increments of 100 GeV. Signal cross-sections are calculated at next-to-leading order (NLO) in α_s , including the resummation of soft gluon emission at next-to-leading-logarithm accuracy (NLO+NLL) [82–84]. The nominal cross-section and the uncertainty are taken from an envelope of cross-section predictions using different PDF sets and factorization and renormalization scales, as described in Ref. [85]. The signal samples have cross sections ranging from $356 \pm 51 \text{ fb}$ for a stop mass of 400 GeV to $0.44 \pm 0.12 \text{ fb}$ for a stop

mass of 1000 GeV. In the simplified models, the stop branching ratios were set to $\mathcal{B}(\tilde{t} \rightarrow be) = \mathcal{B}(\tilde{t} \rightarrow b\mu) = 0.5$, but the events can be appropriately weighted to give any branching fraction hypothesis using Equation 5.1. Signal contributions from $\tilde{t} \rightarrow b\tau$ decays are not considered.

As previously mentioned, the largest sources of Standard Model backgrounds are $t\bar{t}$, single top production (Wt channel), and $Z/\gamma^* + \text{jets}$ production. The $t\bar{t}$ process is modeled using the next-to-leading order generator POWHEG revision 2129 [86–89] with NLO PDF set CTEQ 6L1 [80], and showered with PYTHIA version 6.426. When using the baseline POWHEG +PYTHIA $t\bar{t}$ production sample, events are reweighted in bins of the transverse mass (p_T) of the $t\bar{t}$ system to match the top quark pair differential cross-section observed in ATLAS data [90,91]. The Wt -channel and s -channel of the single top background are modeled using POWHEG revision 1556 [92] with PYTHIA version 6.426, while the t -channel is modeled using AcerMC version 3.8 [93] with PYTHIA version 6.426, both with PDF set CTEQ 6L1 [80]. The $Z/\gamma^* + \text{jets}$ production process is modeled using SHERPA version 1.4.1 [78] with NLO PDF set CT10. Charm and bottom quarks are treated as massive.

Other backgrounds considered include diboson processes, $t\bar{t}$ in association with a vector boson, W boson+jets, and Higgs boson production. These additional background sources are small compared to the three main sources.

5.2.2 Event Reconstruction

Events and physics objects are required to satisfy several quality criteria to be included in the analysis. Events recorded during stable data-taking conditions are analyzed if the reconstructed primary vertex has five or more tracks with $p_T > 400$ MeV associated with it. The primary vertex of an event is identified as the vertex with the highest Σp_T^2 of associated tracks.

Electron candidates are reconstructed from energy deposits in the electromagnetic calorimeter matched to a charged particle track in the ID. Electron candidates must satisfy the **Medium++** identification requirement of Ref. [94], have $p_T > 40$ GeV and $|\eta| < 2.47$, and be consistent with the primary vertex with impact parameter significance in the transverse plane $|d_0/\sigma_{d_0}| < 3$ and a longitudinal impact parameter $|z_0 \sin \theta| < 0.4$ mm. Muon candidates are reconstructed by combining tracks in the ID and tracks in the MS [95]. Muon candidates must have $p_T > 40$ GeV and $|\eta| < 2.4$, and be consistent with the primary vertex with $|d_0/\sigma_{d_0}| < 3$ and $|z_0 \sin \theta| < 1.0$ mm. Events containing a poorly measured muon, as determined by having incompatible momentum measurements in the ID and the MS, are rejected. In simulated samples, the efficiencies identifying electrons and muons are corrected to match those found in data.

Jets are reconstructed using the anti- k_t algorithm [50,96] with a radius parameter $R = 0.4$ from calibrated clusters of energy deposits in the calorimeters. The differences in calorimeter response between electrons, photons and hadrons are taken into account by classifying each cluster, prior to the jet reconstruction, as coming from an electromagnetic or hadronic shower on the basis of its shape [97]. The jet energy thus accounts for electromagnetic and hadronic energy deposits at the cluster level with correction factors derived from MC simulation. A further correction, used to calibrate the jet energy to the scale of its constituent particles, (JES) [97,98], is then applied. The impact of pileup is accounted for using a technique, based on jet areas, that provides an event-by-event and jet-by-jet correction [99]. Jets are required to have transverse momentum $p_T > 40$ GeV and $|\eta| < 4.9$. In order to reduce contamination from jets produced by pileup, the scalar sum of the p_T of the tracks matched to the jet and originating from the primary vertex must be at least 50% of the scalar sum of the p_T of all tracks matched to the jet. This criterion is only applied to jets with $p_T < 50$ GeV and $|\eta| < 2.4$.

Overlaps in the reconstruction of electrons, muons, and jets are removed by the following requirements. If two electrons have $\Delta R < 0.05$, then the lower- p_T electron is removed as it is assumed to be from bremsstrahlung followed by pair production. If an electron and a jet have $\Delta R < 0.20$, then the jet is removed as it is assumed to be dominated by the electron. If an electron (muon) and a remaining jet have $\Delta R < 0.40$, then the electron (muon) is removed as it is assumed to be a component of the jet. Of the remaining leptons, if an electron and a muon have $\Delta R < 0.01$, then both are removed. If two muons have $\Delta R < 0.05$, then both are removed. Finally, if two remaining electrons (muons) have an invariant mass less than 12 GeV, then both electrons (muons) are removed to reject leptons from low mass resonances.

After overlap removal, surviving electron (muon) candidates are required to be isolated to suppress heavy flavor decays. The ratio of the sum of the p_T of the charged particle tracks within $\Delta R < 0.30$ of the electron (muon) to the minimum of 60 GeV and the p_T of the electron (muon) ($\sum_{\Delta R \leq 0.3} p_T^{\text{track}} / \min(p_T, 60 \text{ GeV})$) must be less than 0.1.

The identification of b -jets uses the MV1 flavor tagging algorithm [100,101], which is based on an artificial neural network algorithm that exploits the impact parameters of charged particle tracks, the parameters of reconstructed secondary vertices, and the topology of b - and c -hadron decays inside a jet. The operating point corresponds to an overall 80% b -tagging efficiency, as measured in simulated $t\bar{t}$ events, to a rejection factor of 25 for jets originating from light quarks or gluons, and to a rejection factor of 3 for jets originating from charm quarks. In simulated samples the efficiency of identifying b -jets and the probability of misidentifying jets originating from the fragmentation of

light-flavor quarks, gluons, and charm quarks are corrected to match those found in data.

The vector momentum imbalance in the transverse plane is obtained from the negative vector sum of the reconstructed and calibrated physics objects and the calorimeter energy clusters not associated with reconstructed objects. This is denoted as [missing transverse energy](#), and the symbol E_T^{miss} is used for its magnitude. The E_T^{miss} calculation is described elsewhere [102].

5.2.3 Event Selection

Two overlapping signal regions (SRs) are defined to search for an excess of signal-like events, which are inconsistent with the prediction from the [SM](#) alone. In order to achieve a large expected signal to background ratio in the SRs, MC simulation is used to optimize the selection requirements.

The scalar sum of the p_T of the two b -tagged jets and two leptons (H_T) effectively separates the signal processes from the major sources of Standard Model background. Events in the SRs are required to have H_T above 1100 GeV. Events with two [SFOS](#) leptons with invariant mass within 10 GeV of the Z -boson mass are vetoed to reduce the backgrounds from Z -boson production.

The SRs additionally require a mass asymmetry (defined in Equation 5.2) of less than or equal to 0.2. Finally, $m_{b\ell}^0$ is used to define the two SRs. SR400 has a requirement of $m_{b\ell}^0 \geq 400$ GeV, and is optimal for lower stop masses, while SR600 has a requirement of $m_{b\ell}^0 \geq 600$ GeV, and is optimal for higher stop masses.

The background estimates of the $t\bar{t}$ and the $Z/\gamma^* + \text{jets}$ backgrounds use MC simulation normalized in dedicated control regions (CRs), the top control region (Top CR) and Z control region (Z CR) respectively. The remaining backgrounds are estimated using simulation. Several validation regions (VRs) are defined to validate the extrapolation from the CRs to regions with different kinematics.

Both the Top CR and Z CR require H_T to be less than or equal to 500 GeV to reduce the amount of signal contamination in the regions. A cut of $m_{b\ell}^{\text{asym}} \leq 0.2$ is applied to match the signal regions, and $m_{b\ell}^0$ is required to be above 200 GeV. No requirement is made on the invariant mass of the second pair.

The E_T^{miss} significance variable is used to define CRs that are relatively pure in $t\bar{t}$ or $Z/\gamma^* + \text{jets}$, where

$$E_T^{\text{miss}} \text{ significance} = \frac{E_T^{\text{miss}}}{\sqrt{H_T}}. \quad (5.4)$$

Processes like $t\bar{t}$, with real E_T^{miss} , tend to have large E_T^{miss} significance, while $Z/\gamma^* + \text{jets}$, where the E_T^{miss} is from mismeasurement, tend to have low E_T^{miss} significance. For this reason, the Top CR

Region	$m_{b\ell}^0$ [GeV]	H_T [GeV]	E_T^{miss} significance [GeV $^{1/2}$]	$m_{b\ell}^{\text{asym}}$	Z window
SR400	≥ 400	≥ 1100	–	≤ 0.2	Veto
SR600	≥ 600	≥ 1100	–	≤ 0.2	Veto
Top CR	≥ 200	≤ 500	≥ 4	≤ 0.2	Veto
Z CR	≥ 200	≤ 500	≤ 4	≤ 0.2	Select
Top VR 1	≥ 200	≤ 500	< 4	≤ 0.2	Veto
Top VR 2	≥ 200	≤ 500	–	> 0.2	Veto
Top VR 3	≥ 200	> 500	> 4	> 0.2	Veto
Z VR	≥ 200	> 500	–	≤ 0.2	Select

Table 5.2: Summary of signal, control, and validation regions used for this analysis. All regions require two b -tagged jets and two oppositely charged leptons. An event is in the Z window if it contains two same-flavored leptons with an invariant mass within 10 GeV of the mass of the Z boson.

requires E_T^{miss} significance ≥ 4 GeV $^{1/2}$ and the Z CR requires E_T^{miss} significance ≤ 4 GeV $^{1/2}$.

The full selection criteria for the analysis regions is outlined in Table 5.2 and Figure 5.5.

The H_T , $m_{b\ell}^{\text{asym}}$, and $m_{b\ell}^0$ distributions are shown in Figure 5.6 for the simulated background processes and three signal models. In this figure, all the SR selections apart from that on the variable being shown are applied. The number of expected signal events (for the same three signal models) passing each selection requirement is shown in Table 5.3. The estimates shown in Figure 5.6 and Table 5.3 are taken from MC simulation, and the event yields are normalized to 20.3 fb $^{-1}$.

The normalization of the $t\bar{t}$ and the $Z/\gamma^* + \text{jets}$ backgrounds are determined using a simultaneous fit, which takes into account cross-contamination of the different background processes between the CRs as well as the statistical and systematic uncertainties (described in Section 5.2.4) [103]. The

Selection	$m_{\tilde{t}} = 500$ GeV	$m_{\tilde{t}} = 800$ GeV	$m_{\tilde{t}} = 1000$ GeV
$\sigma \cdot L$	1750 ± 260	59 ± 12	8.9 ± 2.5
$b\bar{b}\ell\ell$	624 ± 4	19.65 ± 0.18	2.68 ± 0.05
Z veto	619 ± 4	19.62 ± 0.18	2.68 ± 0.05
$H_T \geq 1100$ GeV	122.9 ± 1.8	16.01 ± 0.17	2.50 ± 0.04
$m_{b\ell}$ asymmetry ≤ 0.2	112.8 ± 1.7	14.00 ± 0.15	2.11 ± 0.04
$m_{b\ell} \geq 400$ GeV	110.3 ± 1.7	13.74 ± 0.15	2.09 ± 0.04
$m_{b\ell} \geq 600$ GeV	7.7 ± 0.4	12.86 ± 0.15	1.99 ± 0.04

Table 5.3: The number of expected signal events parsing each of the signal region cuts. This is shown for stop masses of 500 GeV, 800 GeV, and 1000 GeV. The estimated yields are taken from MC simulation, and are normalized to 20.3 fb $^{-1}$, and the uncertainty given is the MC statistical uncertainty. The signal models have an assumed branching fraction of $\mathcal{B}(\tilde{t} \rightarrow be) = \mathcal{B}(\tilde{t} \rightarrow b\mu) = 0.5$.

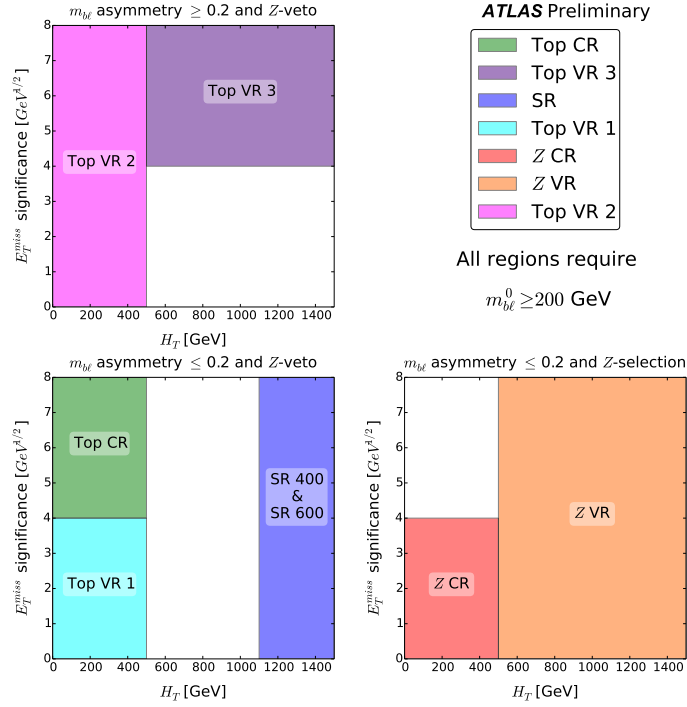


Figure 5.5: Position of the regions in the E_T^{miss} significance versus H_T space. The two SRs apply a different requirement on the invariant mass of the higher-mass $b\ell$ pair. SR400 requires $m_{b\ell}^0 \geq 400$ GeV, and SR600 requires $m_{b\ell}^0 \geq 600$ GeV.

remaining background estimates, due to single top and other SM processes, are taken from the MC simulation. The number of observed events as well as the expected number of events in each of the CRs and VRs are shown in Table 5.4. The agreement between the observed number of events and the fitted event yields in the VRs is summarized in Figure 5.7. Using the fitted backgrounds, the dominant process in the same-flavor channels of the SRs is $Z/\gamma^* + \text{jets}$ followed by single top and $t\bar{t}$. In the $e\mu$ channel, the $Z/\gamma^* + \text{jets}$ background does not contribute, thus, the largest backgrounds are single top and $t\bar{t}$. As a result of the fit, the $Z/\gamma^* + \text{jets}$ background is scaled up by approximately 40%. Due to this large normalization factor, the background is over-predicted in the Z VR. This over-prediction is taken as an additional systematic uncertainty, described in Section 5.2.4.

The extrapolation from low H_T CRs to the high H_T region where the SRs are located is validated using the Top VR 3 and Z VR. These validation regions show fair agreement between the observed and predicted event yields as well as for the shape of the $m_{b\ell}^0$ and H_T distributions as shown in Figures 5.8 and 5.9.

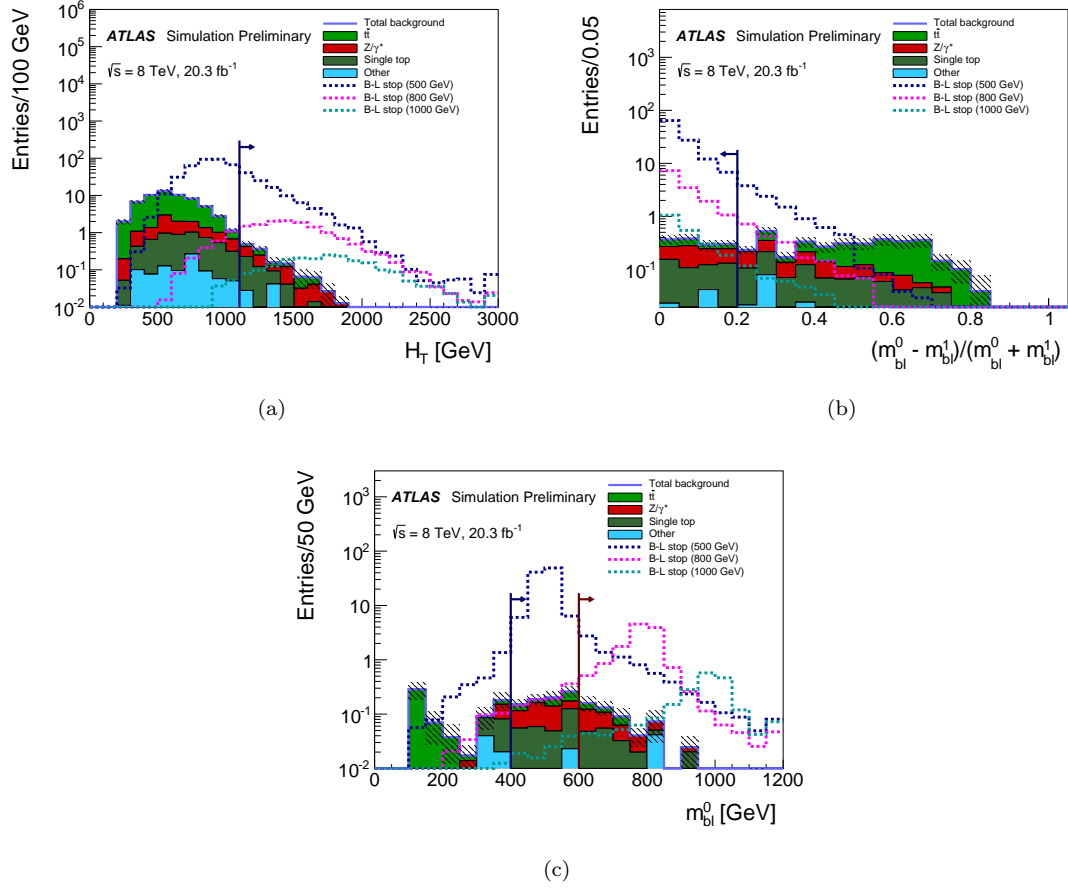


Figure 5.6: Distributions of the variables which are used to define the SRs. These plots show the MC simulated background samples and three signal models, and are made after applying all the SR selection criteria except for that on the variable shown. The top two plots show the H_T and $m_{b\ell}^{\text{asym}}$ variables, and the bottom plot shows the $m_{b\ell}^0$ distribution. The arrows show the SR requirement on the variable being shown. In each plot, the last bin includes the overflow for values beyond the maximum shown. The hashed error bands show only the statistical uncertainty on the background MC simulation samples. The signal models have an assumed $\mathcal{B}(\tilde{t} \rightarrow b e) = \mathcal{B}(\tilde{t} \rightarrow b \mu) = 0.5$.

	Top CR	Z CR	Top VR 1	Top VR 2	Top VR 3	Z VR
Observed	369	327	645	606	67	101
Fitted background	369 ± 19	327 ± 18	690 ± 50	630 ± 40	72 ± 5	130 ± 60
Fitted $t\bar{t}$	346 ± 19	9.1 ± 0.7	600 ± 40	497 ± 35	54 ± 5	2.99 ± 0.24
Fitted $Z/\gamma^* + \text{jets}$	3.2 ± 0.5	309 ± 18	63 ± 5	64 ± 5	1.5 ± 0.8	120 ± 60
Single top	16.7 ± 2.0	0.83 ± 0.09	23.0 ± 2.6	56 ± 6	14.1 ± 1.9	0.32 ± 0.04
Other	2.83 ± 0.27	8.64 ± 1.0	4.7 ± 0.4	8.2 ± 0.8	2.03 ± 0.27	6.4 ± 0.7
Input SM	330	230	614	557	66	93
Input $t\bar{t}$	310	8.2	543	447	49	2.7
Input $Z/\gamma^* + \text{jets}$	2.2	220	44	45	1.1	83
Input single top	17	0.8	23	57	14	0.30
Input other	2.8	8.6	4.7	8.2	2.0	6.40

Table 5.4: The observed and expected event yields in the CRs and VRs. The expected event yields are shown before and after a fit to the data in the CRs. The fitted background yields in the CRs match the observed number of events in data by construction.

5.2.4 Systematic Uncertainties

Several sources of systematic uncertainty are considered when determining the estimated signal and background contributions. The largest sources of systematic uncertainty are those related to the MC statistical uncertainty in the SRs, the JES, the b -tagging efficiency and the extrapolation of the $Z/\gamma^* + \text{jets}$ background to high H_T . The uncertainty on the lepton energy scale and resolution was considered, but shown to be negligible.

- **Jet energy scale:** The uncertainty on the JES takes into account the dependence on p_T , η , jet flavor, and the number of primary vertices. The components of the JES uncertainty are varied by $\pm 1\sigma$ in the MC simulation and propagated to the expected event yield.
- **b -tagging:** The uncertainty on the b -tagging efficiency is evaluated by varying the correction factors applied to each jet in the simulation within a range that reflects the systematic uncertainty on the measured tagging and rejection efficiencies. These uncertainties take into account the dependence on p_T and jet flavor.
- **Jet energy resolution:** The uncertainty on the jet energy resolution (JER) is evaluated by applying an additional smearing to the p_T of each of the jets in the simulation. This smearing is then propagated to the expected event yield.
- **H_T extrapolation:** An H_T extrapolation uncertainty of 50% is applied to $Z/\gamma^* + \text{jets}$ events

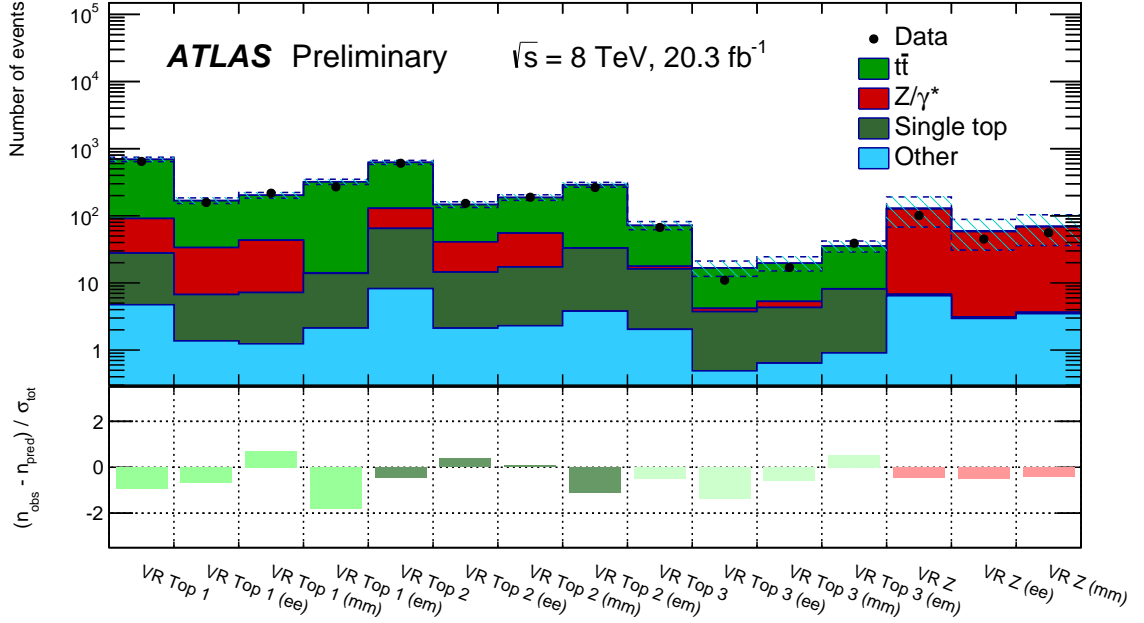


Figure 5.7: The top of this plot shows the number of observed and expected events in the validation regions, inclusively and broken down by flavor channel. The uncertainty band includes the statistical uncertainty as well as the systematic uncertainty (described in Section 5.2.4). The bottom of the plot shows the deviation of that channel's prediction from the observed number of events divided by the uncertainty on the prediction. The normalization of the background yields are determined by fitting the $t\bar{t}$ and Z/γ^* +jets backgrounds to the observed data in the two CRs.

with $H_T \geq 500 \text{ GeV}$. This is assigned to account for uncertainty on the Z/γ^* +jets H_T spectrum. This uncertainty is derived from the disagreement observed in Figures 5.7 and 5.9.

Several theoretical uncertainties are considered in the modeling of the major background processes in MC simulation. These include the uncertainty on the single top (Wt) cross-section, the uncertainty related to the renormalization and factorization scales, parton shower, and the limited number of partons included in the matrix element calculation. These theoretical uncertainties are on the order of a few percent of the total background prediction. The uncertainty on the luminosity is assessed for the signal processes, and all background processes apart from $t\bar{t}$ and Z/γ^* +jets, whose normalizations are determined using data. The relative systematic uncertainty on the total background estimate in the SRs is shown in Table 5.5.

For each of the signal models, the effects of uncertainty on the JES, b -tagging efficiency, JER, and luminosity are considered as well as the uncertainty on the signal model cross-section which ranges between 14% and 28%.

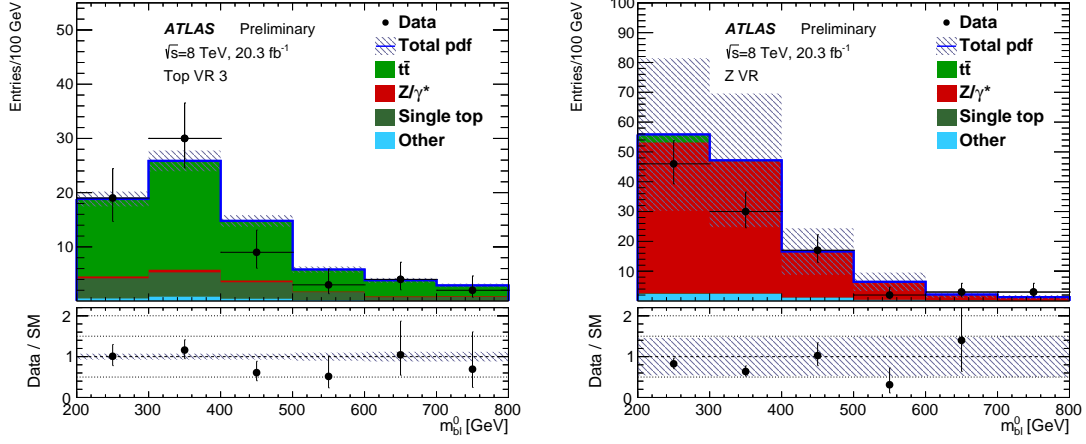


Figure 5.8: The $m_{b\ell}^0$ distribution in Top VR 3 (left) and Z VR (right). The Standard Model background prediction is shown after setting the normalization of the $t\bar{t}$ and Z/γ^* +jets backgrounds based on the observed data in the CRs. The hashed bands show the uncertainty on the fitted background prediction including all statistical and systematics uncertainties. The bottom of each plot shows the ratio of the observed data to the Standard Model background prediction.

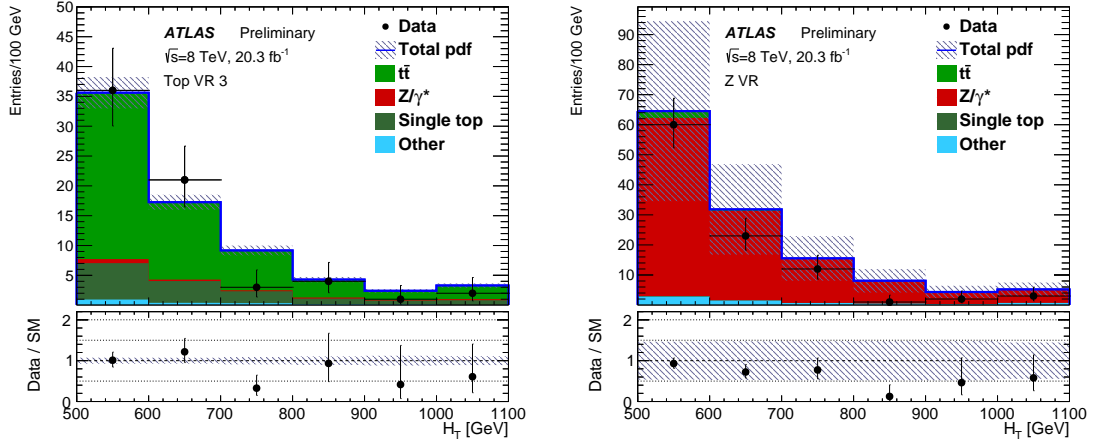


Figure 5.9: The H_T distribution in Top VR 3 (left) and Z VR (right). The Standard Model background prediction is shown after setting the normalization of the $t\bar{t}$ and Z/γ^* +jets backgrounds based on the observed data in the CRs. The hashed bands show the uncertainty on the fitted background prediction including all statistical and systematics uncertainties. The bottom of each plot shows the ratio of the observed data to the Standard Model background prediction.

Systematic Uncertainty (%)	SR400	SR600
JES	15	3
b -tagging	13	12
JER	5	1
Luminosity	1	1
H_T extrapolation	19	20
MC statistical	13	23
CR statistical	3	3
Wt cross-section	2	2
Other theory	1	2

Table 5.5: Summary of the effect of each considered source of systematic uncertainty on the background estimate in SR400 and SR600. Several sources of theoretical systematic uncertainty which have a small effect on the total background estimate are grouped into the “Other theory” category.

5.2.5 Results

The background yields in these signal regions are determined by a maximum likelihood fit [103] for the $t\bar{t}$ and Z/γ^* +jets normalizations, which are constrained by the observed data in the top and Z control regions. The systematic uncertainties described previously are included as Gaussian-distributed nuisance parameters. The fitted background yields and the observed number of events in each signal region are shown in Tables 5.6 and 5.7. Two events are observed, in agreement with the SM prediction. The kinematics of the two selected events are shown in Table 5.8 and the $m_{b\ell}^0$ and H_T distributions in SR400 are shown in Figure 5.10.

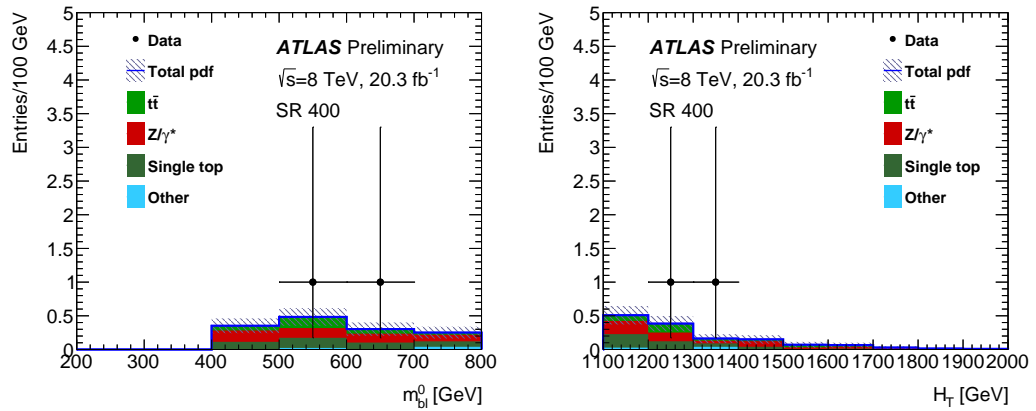


Figure 5.10: $m_{b\ell}^0$ (left) and H_T (right) distributions in SR400. The Standard Model background prediction is taken from the fitted background prediction. The hashed bands show the uncertainty on the fitted background prediction including the MC statistical and sources of systematic uncertainty.

	SR400	SR400 ee	SR400 $\mu\mu$	SR400 $e\mu$
Observed	2	0	2	0
Fitted background	1.39 ± 0.35	0.36 ± 0.15	0.57 ± 0.20	0.45 ± 0.11
Fitted $t\bar{t}$	0.33 ± 0.09	0.07 ± 0.08	0.07 ± 0.02	0.19 ± 0.05
Fitted $Z/\gamma^* + \text{jets}$	0.54 ± 0.28	0.20 ± 0.10	0.35 ± 0.18	≤ 0.01
Single Top	0.44 ± 0.08	0.10 ± 0.03	0.11 ± 0.03	0.23 ± 0.05
Other	0.07 ± 0.04	≤ 0.01	0.04 ± 0.02	0.03 ± 0.03
Input SM	1.2	0.30	0.46	0.43
Input $t\bar{t}$	0.30	0.06	0.06	0.17
Input $Z/\gamma^* + \text{jets}$	0.38	0.14	0.24	0.00
Input single Top	0.44	0.10	0.11	0.23
Input other	0.07	0.00	0.04	0.03
σ_{vis} [fb]	0.23	0.11	0.26	0.11
Observed $N_{\text{non-SM}}$	4.8	2.2	5.4	2.3
Expected $N_{\text{non-SM}}$	$4.0^{+2.2}_{-1.1}$	$3.2^{+1.7}_{-1.1}$	$3.6^{+1.9}_{-1.5}$	$3.3^{+1.8}_{-1.3}$

Table 5.6: The expected and observed event yields in SR400. The expected event yields are shown before and after performing the fit to the data in the control regions. The last three rows show the model-independent 95% CL on the visible cross-section and the number of events (expected and observed) in SR400 from a generic non-Standard Model process.

	SR600	SR600 ee	SR600 $\mu\mu$	SR600 $e\mu$
Observed	1	0	1	0
Fitted background	0.55 ± 0.15	0.15 ± 0.06	0.24 ± 0.10	0.16 ± 0.06
Fitted $t\bar{t}$	0.10 ± 0.02	0.03 ± 0.01	≤ 0.01	0.07 ± 0.03
Fitted $Z/\gamma^* + \text{jets}$	0.23 ± 0.12	0.08 ± 0.05	0.15 ± 0.08	≤ 0.01
Single Top	0.18 ± 0.04	0.03 ± 0.01	0.05 ± 0.02	0.09 ± 0.03
Other	0.04 ± 0.01	≤ 0.01	0.04 ± 0.02	≤ 0.01
Input SM	0.47	0.12	0.20	0.16
Input $t\bar{t}$	0.09	0.03	0.00	0.06
Input $Z/\gamma^* + \text{jets}$	0.16	0.06	0.10	0.00
Input single Top	0.18	0.03	0.05	0.09
Input other	0.04	0.00	0.04	0.00
σ_{vis} [fb]	0.19	0.10	0.20	0.10
Observed $N_{\text{non-SM}}$	3.9	2.1	4.0	2.1
Expected $N_{\text{non-SM}}$	$3.5^{+1.9}_{-1.4}$	$2.6^{+1.6}_{-0.6}$	$3.0^{+1.7}_{-1.0}$	$2.7^{+1.6}_{-0.7}$

Table 5.7: The expected and observed event yields in SR600. The expected event yields are shown before and after performing the fit to the data in the control regions. The last three rows show the model-independent 95% CL on the visible cross-section and the number of events (expected and observed) in SR600 from a generic non-Standard Model process.

Run number	214216	210302
Event number	121272046	2292645861
$m_{b\ell}^0$ [GeV]	558	686
ℓ_0 flavor	μ	μ
ℓ_0 charge	—	—
ℓ_0 p_T [GeV]	375	272
b_0 p_T [GeV]	330	460
ℓ_0 η	−0.11	1.22
b_0 η	0.56	0.95
ℓ_0 ϕ	2.0	−1.3
b_0 ϕ	−2.7	2.5
$m_{b\ell}^1$ [GeV]	526	528
ℓ_1 flavor	μ	μ
ℓ_1 charge	+	+
ℓ_1 p_T [GeV]	88	96
b_1 p_T [GeV]	542	374
ℓ_1 η	0.45	1.43
b_1 η	−1.1	−0.26
ℓ_1 ϕ	−2.3	−0.91
b_1 ϕ	−0.21	2.3
$m_{b\ell}^{\text{asym}}$	0.03	0.13
H_T [GeV]	1335	1203
E_T^{miss} significance [GeV $^{1/2}$]	2.9	6.4
E_T^{miss} [GeV]	107	223
$m_{\ell\ell}$ [GeV]	324	71

Table 5.8: The event and object kinematics for the two events passing the signal region selection. The first event passes the SR400 selection while the second event passes both SR400 and SR600 selections.

As the observed number of events is consistent with the Standard Model prediction, upper limits at 95% confidence level (CL) on the number of [BSM](#) events for each signal region are derived using the CL_S prescription [104] and neglecting any possible contamination in the control regions. Normalizing these by the integrated luminosity of the data sample they can be interpreted as upper limits on the visible BSM cross-section, σ_{vis} , where σ_{vis} is defined as the product of acceptance, reconstruction efficiency and production cross-section. The results are given in Tables 5.6 and 5.7.

Exclusion limits on the signal model are determined using the CL_S prescription based on a simultaneous fit of the SRs and CRs [103]. The predicted signal contamination is taken into account in the CRs. For each stop mass, exclusion fits are performed with various assumptions on the branching ratios of the stop. For each point on the branching ratio plane, the SR which provided

the best expected sensitivity, as measured by the lowest expected CL_S value, is chosen. The expected and observed limits are shown in Figure 5.11. This figure shows, for each simulated stop mass, the observed (expected) 95% exclusion limit on the branching fraction under the red (blue) line. A yellow band shows the $\pm 1\sigma$ uncertainty on the expected limit, determined from the systematic uncertainty on the signal and background prediction excluding the effect of the signal cross-section uncertainty. The effect of varying the signal cross-section on the observed limit is indicated by the dashed red lines. The final limit on the stop mass is shown in Figure 5.12. This plot shows the 95% confidence limit (CL) on the mass obtained by choosing the maximum excluded mass for each branching ratio on the plane using the nominal cross-section value. As the branching ratio of $\tilde{t} \rightarrow b\tau$ increases, the number of expected events with electrons or muons in the final state decreases for the same simulated stop mass. Therefore, the limit on the mass is strongest at the bottom of the plane. In the top corner of the plot, the SRs described in this analysis note have no sensitivity, however traditional leptoquark searches for final states with b -tagged jets and τ leptons are able to place experimental limits in this region [105].

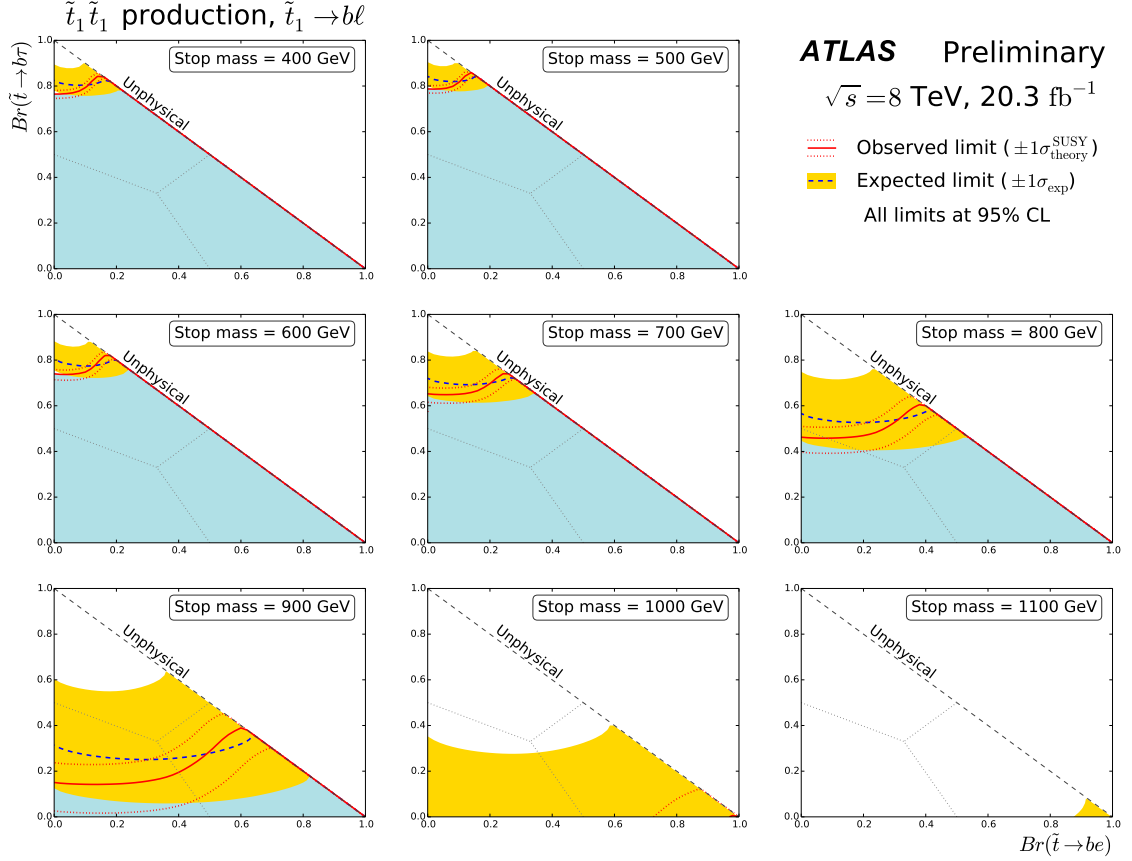


Figure 5.11: Expected and observed limit on the branching ratios for the stop decaying to different lepton flavors shown for different stop mass hypotheses between 400 GeV and 1 TeV. The shaded area under the solid line represents the branching ratios which are excluded at 95% CL for each stop mass. The dotted lines represent the uncertainty on the observed mass limit obtained by varying the signal model cross-section up and down one standard deviation from the nominal value. The dashed line shows the expected 95% CL exclusion for each stop mass, and the shaded band shows the uncertainty on this expected exclusion limit from statistical uncertainty and the sources of systematic uncertainty discussed in Section 5.2.4.

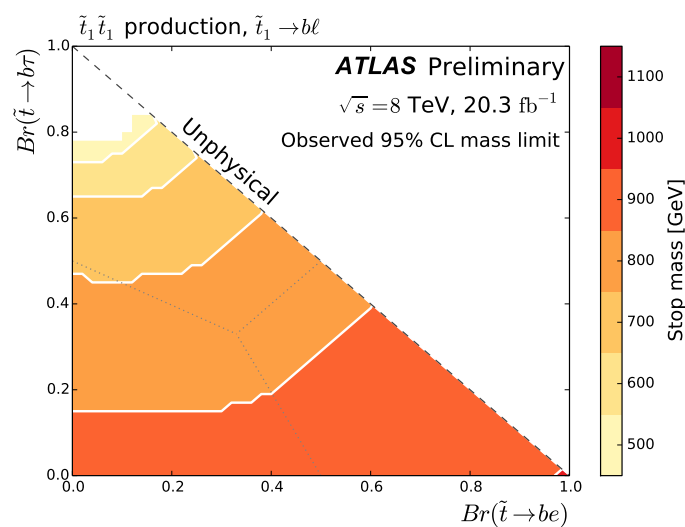


Figure 5.12: The observed mass limit on the stop at 95% CL. This limit is obtained using the nominal stop cross-section. Stop masses between 400 GeV and 1100 GeV, in steps of 100 GeV, were tested. The mass limit shown corresponds to the highest-mass stop sample which was excluded. As the branching ratio of $\tilde{t} \rightarrow b\tau$ increases, the number of expected events with electrons or muons in the final state decreases. Therefore, the limit on the mass decreases.

5.3 Run 2 analysis

Many characteristics of the early [Run 2](#) analysis are very similar to the [Run 1](#) version presented in [Section 5.2](#). One noticeable difference is that rather than requiring that each event have two b -jets, in this version of the search only one b -jet is required per event. This improves the selection efficiency of signal events over a requirement of two b -jets.

A description of the dataset and simulated samples used in this analysis are given in [Section 5.3.1](#). The requirements on events and physics objects which are included in this analysis are given in [Section 5.3.2](#). The kinematic requirements used to define the signal, control, and validation regions are presented in [Section 5.3.3](#). The systematic uncertainties are detailed in [Section 5.3.4](#), and finally the results are presented in [Section 5.3.5](#).

5.3.1 Dataset and Monte Carlo simulated samples

The data sample used for this search was collected from proton–proton collisions at a center-of-mass energy of $\sqrt{s} = 13$ TeV in 2015 and 2016. An integrated luminosity of 36.1 fb^{-1} was collected while all tracking detectors, calorimeters, muon chambers, and magnets were fully operational. The uncertainty in the combined 2015 and 2016 integrated luminosity is 3.2%. It is derived from a preliminary calibration of the luminosity scale using x – y beam-separation scans performed in August 2015 and May 2016, following a methodology similar to that detailed in Ref. [\[106\]](#). The LHC collided protons with bunch-crossing intervals of 25 ns, and the average number of interactions per bunch crossing was estimated to be $\langle\mu\rangle = 23.7$.

[MC](#) simulation is used to predict the backgrounds from [SM](#) processes, estimate the detector response and efficiency to reconstruct the signal process, and estimate systematic uncertainties. The largest sources of SM background are top quark pair production ($t\bar{t}$), single-top-quark production (single-top), and Z/γ^* +jets production, and their yields are estimated through data-driven methods described in [Section 5.3.3](#). The smaller backgrounds are W +jets, diboson, and $t\bar{t} + W/Z$ production and are estimated directly from MC simulation. The contribution from events with jets misreconstructed as leptons or with non-prompt leptons is evaluated with the MC simulation and is negligible. Details of the MC simulations are given below and are summarized in [Table 5.9](#).

The $t\bar{t}$ and single-top processes were simulated [\[113\]](#) at next-to-leading-order (NLO) accuracy in perturbative QCD using the POWHEG-BOX v2 event generator [\[88\]](#) for $t\bar{t}$, Wt , and s -channel single-top production, and using the POWHEG-BOX v1 generator for the electroweak t -channel single-top production. For these processes the spin correlations in top quark production and decay

Process	Event generator	PS and hadronization	UE tune	PDF	Cross section
$t\bar{t}$	POWHEG-BOX v2	PYTHIA 6.428	P2012	CT10	NNLO+NNLL [107]
single-top					
(Wt and s -channel)	POWHEG-BOX v2	PYTHIA 6.428	P2012	CT10	NNLO+NNLL [108, 109]
(t -channel)	POWHEG-BOX v1	PYTHIA 6.428	P2012	CT10	NNLO+NNLL [110]
Z/W +jets	SHERPA 2.2.1	SHERPA 2.2.1	Default	NNPDF3.0	NNLO [111]
Diboson	SHERPA 2.2.1	SHERPA 2.2.1	Default	NNPDF3.0	NLO
Diboson (EW/loop)	SHERPA 2.1.1	SHERPA 2.1.1	Default	CT10	NLO
$t\bar{t} + W/Z$	MG5_AMC@NLO 2.2.3	PYTHIA 8.212	A14	NNPDF2.3	NLO
$t\bar{t}^*$	MG5_AMC@NLO 2.2.3	PYTHIA 8.186	A14	NNPDF2.3	NLO+NLL [112]

Table 5.9: MC simulation details by physics process.

were preserved, and the top quark mass was set to 172.5 GeV. The matrix element was interfaced with the CT10 PDF set [114], and the parton shower (PS), fragmentation, and underlying event were simulated with PYTHIA 6.428 [81] using the CTEQ6L1 PDF set [115] and the P2012 underlying-event tuned parameters (UE tune) [77], with additional radiation simulated to the leading-logarithm approximation through p_T -ordered parton showers [116].

The Z/γ^* +jets and W +jets samples were generated at NLO [117] with the SHERPA 2.2.1 event generator [118]. Matrix elements were calculated for up to two partons at NLO and four partons at LO using Comix [119] and OpenLoops [120], and merged with the SHERPA PS [121] using the ME+PS@NLO prescription [122]. The NNPDF3.0 PDF set [123] was used in conjunction with a dedicated PS tuning developed by the SHERPA authors. Diboson samples with two, three, or four leptons were similarly generated with SHERPA 2.2.1. The diboson matrix elements contain all diagrams with four electroweak vertices, and were calculated for up to one (ZZ) or zero (WW, WZ) partons at NLO and up to three partons at LO. Electroweak- and loop-induced diboson events were simulated with SHERPA 2.1.1, using the same prescriptions as above but with the CT10 PDF set used in conjunction with the dedicated SHERPA PS tuning. The production of $t\bar{t}$ with a W or Z boson ($t\bar{t} + V$) was simulated at NLO using MADGRAPH5_aMC@NLO (MG5_AMC@NLO) 2.2.3 [124] and interfaced to PYTHIA 8.212 [75] with the CKKW-L prescription [125]. These samples are generated with the A14 UE tune [126] and NNPDF2.3 PDF set [127].

The RPV stop signal events were generated at leading order using the MG5_AMC@NLO 2.2.3 event generator with the NNPDF2.3 PDF set and interfaced to PYTHIA 8.186 [75] using the A14 UE tune. The matrix element was matched to the PS using the CKKW-L prescription, with the matching scale set to one quarter of the generated stop mass. All other supersymmetric particles are assumed to be decoupled. The signal cross sections are calculated to NLO accuracy in the strong coupling constant, adding the resummation of soft gluon emission at next-to-leading-logarithm ac-

curacy (NLO+NLL) [82–85]. The nominal cross section and the uncertainty for each mass value are taken from a combination of cross-section predictions using different PDF sets and factorization and renormalization scales, as described in Ref. [112]. Stop samples were generated at masses between 600 and 1000 GeV in increments of 100 GeV and between 1000 and 1600 GeV in increments of 50 GeV. The cross section ranges from 175 ± 23 fb for a \tilde{t} mass of 600 GeV to 0.141 ± 0.038 fb for a mass of 1600 GeV. The generated stops decay promptly through $\tilde{t} \rightarrow b\ell$ with a $1/3$ branching ratio (\mathcal{B}) for each lepton flavor. When optimizing the signal event selection, the generated events are reweighted to have $\mathcal{B}(\tilde{t} \rightarrow be) = \mathcal{B}(\tilde{t} \rightarrow b\mu) = 0.5$ and $\mathcal{B}(\tilde{t} \rightarrow b\tau) = 0$, and various weightings are used to derive limits for different branching ratio assumptions, again following the prescription in Equation 5.1.

All background samples are normalized using the available NLO or next-to-next-to-leading order (NNLO) cross sections, as indicated in Table 5.9. The modeling of c -hadron and b -hadron decays in samples generated with POWHEG-BOX or MG5_AMC@NLO was performed with EVT-GEN 1.2.0 [128]. Generated events were propagated through a full simulation of the ATLAS detector [129] based on Geant4 [130], which describes the interactions of the particles with the detector. A parameterized simulation of the ATLAS calorimeter called Atlfast-II [129] was used for faster detector simulation of signal samples, and was found to agree well with the full simulation. Multiple overlapping pp interactions (pileup) were included by overlaying simulated minimum-bias events onto the simulated hard-scatter event. Minimum-bias events were generated using PYTHIA 8.186 with the A2 UE tune [131] and MSTW2008LO PDF set [132]. The simulated events are weighted such that the distribution of the average number of pp interactions per bunch crossing agrees with data.

5.3.2 Event reconstruction

Events and individual leptons and jets are required to satisfy several quality criteria to be considered by the analysis. Events recorded during stable beam and detector conditions are required to satisfy data-quality criteria [133]. Each event is required to have a primary reconstructed vertex with two or more associated tracks with $p_T > 400$ MeV, where the primary vertex is chosen as the vertex with the highest Σp_T^2 of associated tracks. Two stages of quality and kinematic requirements are applied to leptons and jets. The looser baseline requirements are first applied, and baseline leptons and jets are used to resolve any misidentification or overlap between electrons, muons, and jets. The subsequent tighter signal requirements are then applied to identify high-quality leptons and jets in

the kinematic phase space of interest.

Electron candidates are reconstructed from energy deposits in the electromagnetic calorimeter matched to a charged-particle track in the ID. Baseline electron candidates must have $p_T > 10$ GeV, $|\eta| < 2.47$, and satisfy a loose electron likelihood identification [134]. Signal electrons must pass the baseline electron selection, have $p_T > 40$ GeV, and satisfy a tight electron likelihood identification. In addition, they must be isolated from nearby activity, satisfying a loose p_T -dependent track-based criterion [135]. Finally, their trajectory must be consistent with the primary vertex, such that their impact parameter in the transverse plane (d_0^{PV}) satisfies $|d_0^{\text{PV}}|/\sigma_{d_0^{\text{PV}}} < 5$, where $\sigma_{d_0^{\text{PV}}}$ is the uncertainty in d_0^{PV} . Each signal electron must have a longitudinal impact parameter with respect to the primary vertex (z_0^{PV}) that satisfies $|z_0^{\text{PV}} \sin\theta| < 0.5$ mm.

Muon candidates are reconstructed by combining tracks in the ID with tracks in the MS. Baseline muon candidates must have $p_T > 10$ GeV, $|\eta| < 2.7$, and satisfy the medium muon identification criteria [136]. Signal muons must pass the baseline muon selection, have $p_T > 40$ GeV, $|\eta| < 2.5$, $|z_0^{\text{PV}} \sin\theta| < 0.5$ mm, and $|d_0^{\text{PV}}|/\sigma_{d_0^{\text{PV}}} < 3$. As with electrons, muons must satisfy the p_T -dependent loose track-based isolation criteria. Events containing a poorly measured signal muon, as determined by having incompatible momentum measurements in the ID and the MS, are rejected. Absolute requirements of $|z_0^{\text{PV}}| < 1$ mm and $|d_0^{\text{PV}}| < 0.2$ mm on the impact parameters of signal muons are applied to reject cosmic muons.

Jets are reconstructed using the anti- k_t algorithm [50, 51] with a radius parameter $R = 0.4$ from clusters of energy deposits in the calorimeters [137]. Jets are corrected for pileup contamination on an event-by-event basis using the jet area subtraction method [99, 138]. Jets are further calibrated to account for the predicted detector response in MC simulation, and a residual calibration of jets in data is derived through *in situ* measurements [139]. Baseline jet candidates are required to have $p_T > 20$ GeV and $|\eta| < 2.8$. Jets with $p_T < 60$ GeV and $|\eta| < 2.4$ are required to satisfy pileup-rejection criteria based on charged-particle tracks and implemented through the jet vertex tagger algorithm [138]. Signal jets must pass the baseline jet selection and have $p_T > 60$ GeV. Events are rejected if they contain a jet that fails the loose quality criteria [140], reducing contamination from noise bursts and non-collision backgrounds. Jets within $|\eta| < 2.5$ that are initiated by b -quarks are identified using the multivariate MV2c10 b -tagging algorithm [141, 142], which exploits the impact parameters of charged-particle tracks, the parameters of reconstructed secondary vertices, and the topology of b - and c -hadron decays inside a jet. The working point is chosen to provide a b -tagging efficiency of 77% per b -jet in simulated $t\bar{t}$ events with a rejection factor of approximately 130 for jets initiated by gluons or light-flavor quarks and 6 for jets initiated by c -quarks [142]. The choice of this

working point was motivated to optimize sensitivity in the signal regions; a discussion of this choice can be found in Appendix A. Correction factors are applied to events to compensate for differences between data and MC simulation in the b -tagging efficiency for b -jets, c -jets, and light-flavor jets.

To avoid reconstructing a single detector signature as multiple leptons or jets, an overlap removal procedure is performed on baseline leptons and jets. The requirements are applied sequentially, and failing particles are removed from consideration in the subsequent steps. If an electron and muon share a track in the ID, the electron is removed. Any jet that is not b -tagged and is within a distance⁵ $\Delta R(\ell, \text{jet}) \leq 0.2$ of a lepton is removed. If the jet is b -tagged, the lepton is removed instead in order to suppress leptons from semileptonic decays of c - and b -hadrons. Finally, any lepton that is $\Delta R(\ell, \text{jet}) \leq 0.4$ from a jet is removed.

The trigger, reconstruction, identification, and isolation efficiencies of electrons [135] and muons [136] in MC simulation are corrected using events in data with leptonic Z and J/ψ decays. Similarly, corrections to the b -tagging efficiency and mis-tag rate in MC simulation are derived from various control regions in data [142].

5.3.3 Event selection

To identify the pair production of stops, events are required to have at least two leptons and two jets. If more than two leptons or two jets are found, the two highest- p_T leptons and jets are selected. At least one of the two leading jets must be b -tagged. The selected leptons are required to have opposite charge, and one of them must be consistent with the associated single-lepton trigger. This trigger requirement is highly efficient for signal events, with an efficiency of 93% for the $\mu\mu$ channel and 98% for the ee channel.

Two nested signal regions (SRs) are constructed to optimize the identification of signal over background events. The signal regions are optimized using MC signal and background predictions, assuming \tilde{t} decays of $\mathcal{B}(\tilde{t} \rightarrow be) = \mathcal{B}(\tilde{t} \rightarrow b\mu) = 50\%$. A primary kinematic selection of the signal regions is on $m_{b\ell}^0$, with SR800 requiring $m_{b\ell}^0 > 800$ GeV and SR1100 requiring $m_{b\ell}^0 > 1100$ GeV. By defining two signal regions the sensitivity to high-mass signals above 1100 GeV is improved, while maintaining sensitivity to lower-mass signals. Several other kinematic selections, common to both SRs, are defined to reduce the contribution from the largest backgrounds. As the \tilde{t} decay products are generally very energetic, a selection on H_T (defined in Equation 5.3) is applied, such that $H_T > 1000$ GeV. To reduce contamination from $Z/\gamma^* + \text{jets}$ events, a requirement is placed on the

⁵ The distance between two four-momenta is defined as $\Delta R = \sqrt{(\Delta y)^2 + (\Delta\phi)^2}$, where Δy is their distance in rapidity and $\Delta\phi$ is their azimuthal distance. The distance with respect to a jet is calculated from its central axis.

invariant mass of two same-flavor leptons, with $m_{\ell\ell} > 300$ GeV. A large fraction of the background from processes involving a top quark is suppressed through the requirement on $m_{b\ell}^0$ and $m_{b\ell}^{\text{asym}}$, with correctly reconstructed top quark masses falling well below the signal region requirements. However, top quark decays in which the lepton and b -jet decay products are mispaired can enter the SRs if the incorrectly reconstructed masses happen to be large. In such cases it is the rejected pairing that properly reconstructs the top quark decay, with one of the two $b\ell$ pair masses below the kinematic limit for a top quark decay. To suppress such backgrounds, events are rejected if the subleading $b\ell$ mass of the rejected pairing, $m_{b\ell}^1(\text{rej})$, is compatible with that of a reconstructed top quark, with $m_{b\ell}^1(\text{rej}) < 150$ GeV. An explanation of the choice of these SR cuts can be found in Appendix A.

The distribution of predicted signal and background events is shown for the SR800 region in Figure 5.13 for $m_{b\ell}^0$, H_T , $m_{b\ell}^{\text{asym}}$, $m_{\ell\ell}$, and $m_{b\ell}^1(\text{rej})$, demonstrating the potential for background rejection. For the model with a \tilde{t} mass of 1000 GeV (1500 GeV), the SR800 selections are 21% (24%) efficient for events with two $\tilde{t} \rightarrow b\ell$ decays, 16% (16%) for events with two $\tilde{t} \rightarrow b\mu$ decays, and 0.1% (0.3%) for events with two $\tilde{t} \rightarrow b\tau$ decays.

For each of the relevant backgrounds in the signal regions, one of two methods is used to estimate the contribution. The minor diboson, $t\bar{t} + V$, and W +jets backgrounds are estimated directly from MC simulation and the normalization is corrected to the highest-order theoretical cross section available. For the dominant $t\bar{t}$, single-top, and Z/γ^* +jets backgrounds, the expected yield in the SRs is estimated by scaling each MC prediction by a normalization factor (NF) derived from three dedicated control regions (CRs), one for each background process. Each control region is defined to be kinematically close to the SRs while inverting or relaxing specific selections to enhance the contribution from the targeted background process while reducing the contamination from other backgrounds and the benchmark signals.

To derive a background-only estimate, the normalizations of the $t\bar{t}$, single-top, and Z/γ^* +jets backgrounds are determined through a likelihood fit [103] performed simultaneously to the observed number of events in each CR. The expected yield in each region is given by the inclusive sum over all background processes in the ee , $e\mu$, and $\mu\mu$ channels. The NF for each of the $t\bar{t}$, single-top, and Z/γ^* +jets backgrounds are free parameters of the fit. The systematic uncertainties are treated as nuisance parameters in the fit and are not significantly constrained.

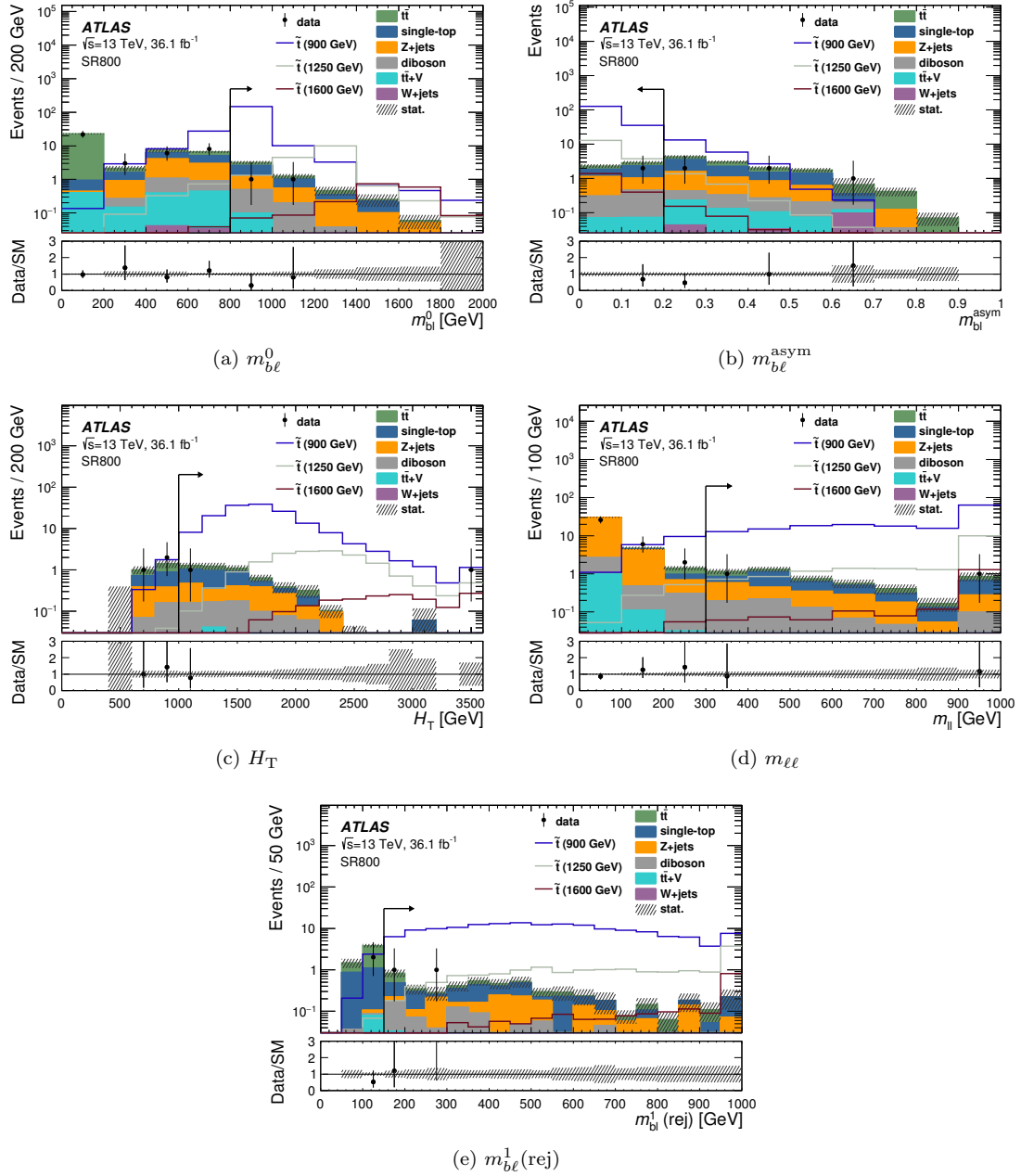


Figure 5.13: Distributions of (a) $m_{b\ell}^0$, (b) $m_{b\ell}^{\text{asym}}$, (c) H_T , (d) $m_{\ell\ell}$, and (e) $m_{b\ell}^1(\text{rej})$ in the SR800 signal region for the data and post-fit MC prediction. The SR800 event selections are applied for each distribution except the selection on the variable shown, which is indicated by an arrow. Normalization factors are derived from the background-only estimation discussed in Section 5.3.3 and are applied to the dominant $t\bar{t}$, single-top, and $Z/\gamma^* + \text{jets}$ processes. Benchmark signal models generated with \tilde{t} masses of 900, 1250, and 1600 GeV are included for comparison. The bottom panel shows the ratio between the data and the post-fit MC prediction. The hatched uncertainty band includes the statistical uncertainties in the background prediction. The last bin includes the overflow events.

Region	N_b	$m_{b\ell}^0$ [GeV]	H_T [GeV]	$m_{b\ell}^1(\text{rej})$ [GeV]	$m_{\ell\ell}$ [GeV]	m_{CT} [GeV]
SR800	≥ 1	> 800	> 1000	> 150	> 300	–
SR1100	≥ 1	> 1100	> 1000	> 150	> 300	–
CRst	$= 2$	$[200, 500]$	< 800	< 150	> 120	> 200
CRtt	≥ 1	$[200, 500]$	$[600, 800]$	< 150	> 300	$< 200^*$
CRZ	≥ 1	> 700	> 1000	–	$[76.2, 106.2]$	–
VR $m_{b\ell}^0$	≥ 1	> 500	$[600, 800]$	< 150	> 300	–
VR $m_{b\ell}^1(\text{rej})$	≥ 1	$[200, 500]$	$[600, 800]$	> 150	> 300	–
VR H_T	≥ 1	$[200, 500]$	> 800	< 150	> 300	–
VRZ	$= 0$	$[500, 800]$	> 1000	> 150	> 300	–

Table 5.10: Summary of the selections of the signal, control, and validation regions. All regions require at least two oppositely charged leptons and at least two jets. A mass asymmetry selection of $m_{b\ell}^{\text{asym}} < 0.2$ is also applied to all regions. N_b represents the requirement on the number of b -jets in each event. Each region requires at least one of the two leading jets to be b -tagged with the exception of CRst, which requires both leading jets to be b -tagged, and VRZ, which requires zero b -tagged jets in the event. The contranverse mass selection m_{CT} (Equation 5.5) is only applied to events in CRtt with exactly two b -tagged jets, as indicated by the *, ensuring the region is orthogonal to CRst.

Several validation regions (VRs) are defined to test the extrapolation from the CRs to SRs over the relevant kinematic variables. The VRs are disjoint from both the CRs and SRs, and are constructed to fall between one or more CRs and the SRs in one of the extrapolated variables. The VRs are not included in the fit, but provide a statistically independent cross-check of the background prediction in regions with a negligible signal contamination. Three VRs are constructed to test the extrapolation in the $m_{b\ell}^0$, $m_{b\ell}^1(\text{rej})$, and H_T observables. A fourth VR is constructed to validate the extrapolation of the $Z/\gamma^* + \text{jets}$ CR in $m_{\ell\ell}$. Details of the selection criteria in each CR and VR are presented below, and a summary of the selections which define all regions is provided in Table 5.10.

5.3.3.1 Single-top control region

The single-top background enters the SR through the Wt process, when the b -jet and lepton produced in the semileptonic top quark decay are incorrectly paired with the lepton from the W decay and an additional jet, respectively. The CRst control region is designed to target the Wt production in a less-energetic kinematic region or where the rejected $b\ell$ pairing correctly combines the decay products of the top quark. To separate CRst from the SRs, the H_T and $m_{b\ell}^0$ requirements are reversed such that $H_T < 800$ GeV and $200 < m_{b\ell}^0 < 500$ GeV. To target events in which the top quark is reconstructed in the rejected $b\ell$ pairing, the selection on $m_{b\ell}^1(\text{rej})$ is reversed, requiring $m_{b\ell}^1(\text{rej}) < 150$ GeV. As there is no dilepton resonance in this background process the $m_{\ell\ell}$ selection

is lowered to increase the CRst yield and improve the statistical precision of the constraint.

After these selections the control region is dominated by $t\bar{t}$ production, which has a significantly higher cross section than the Wt process. The contransverse mass (m_{CT}) [143] is introduced to discriminate between Wt and $t\bar{t}$ events and increase the Wt purity in the CRst. The m_{CT} observable attempts to reconstruct the invariant mass of pair produced particles which decay into visible and invisible decay products. For two identical decays of top quarks into two visible b -quarks b_1 and b_2 and two W bosons, each of whose decay products may include an invisible particle, m_{CT} is defined as

$$m_{\text{CT}}^2(b_1, b_2) = [E_{\text{T}}(b_1) + E_{\text{T}}(b_2)]^2 - [\mathbf{p}_{\text{T}}(b_1) - \mathbf{p}_{\text{T}}(b_2)]^2, \quad (5.5)$$

where $E_{\text{T}} = \sqrt{p_{\text{T}}^2 + m^2}$ is calculated from the kinematics of the reconstructed b -jet. For an event with two top quarks, the m_{CT} observable therefore has a kinematic endpoint at

$$m_{\text{CT}}^{\text{max}} = \frac{m_t^2 - m_W^2}{m_t}, \quad (5.6)$$

where m_t and m_W are the masses of the top quark and W boson, respectively. Requiring this variable to exceed a minimum value is effective in suppressing the $t\bar{t}$ contribution, for which m_{CT} has a kinematic endpoint of about 135 GeV, and a strict requirement of $m_{\text{CT}} > 200$ GeV is applied in CRst. The m_{CT} variable is only effective in rejecting $t\bar{t}$ events in which the b -quark decay products of both top quarks are properly identified; hence both leading jets (and only the leading jets) are required to be b -tagged in CRst, such that $N_b = 2$. The m_{CT} distribution of the backgrounds in CRst is shown in Figure 5.14a when no m_{CT} requirement is applied, and a significant single-top contribution above 55% is seen for $m_{\text{CT}} > 200$ GeV.

5.3.3.2 $t\bar{t}$ control region

The CRtt control region is constructed to target $t\bar{t}$ events with kinematics similar to the SRs. As with CRst, the H_{T} and $m_{b\ell}^0$ requirements are inverted such that $600 < H_{\text{T}} < 800$ GeV and $200 < m_{b\ell}^0 < 500$ GeV. The selection on $m_{b\ell}^1(\text{rej})$ is also inverted, requiring $m_{b\ell}^1(\text{rej}) < 150$ GeV, such that one of the two top quarks is reconstructed in the rejected $b\ell$ pairings. The distribution of $m_{b\ell}^1(\text{rej})$ in CRtt is shown in Figure 5.14b, showing the mispairing of $t\bar{t}$ events is well-modeled in MC simulation. Due to the larger cross section of the $t\bar{t}$ process, contamination from Wt events is minimal. However, to maintain orthogonality with CRst, a requirement of $m_{\text{CT}} < 200$ GeV is applied to events in which both leading jets (and only the leading jets) are b -tagged, with $N_b = 2$.

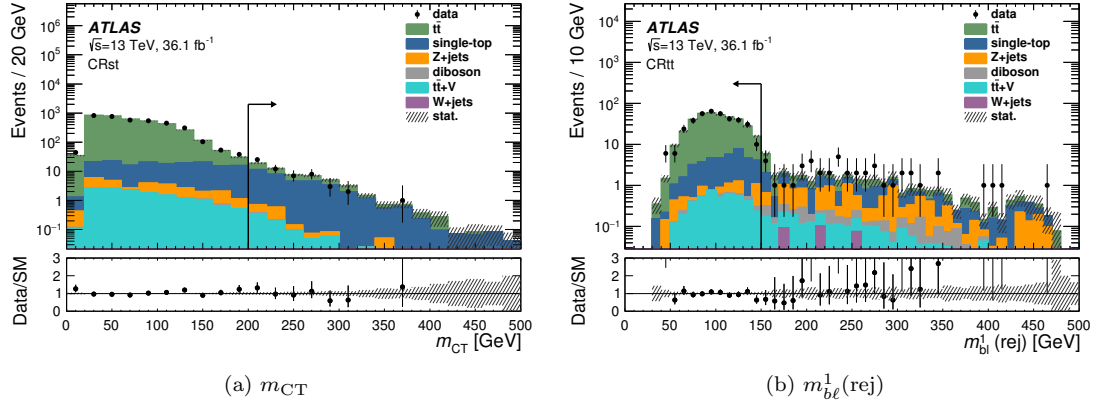


Figure 5.14: Distributions of (a) m_{CT} in CRst and (b) $m_{b\ell}^1(\text{rej})$ in CRtt for the data and post-fit MC prediction. The relevant CR event selections are applied for each distribution except the selection on the variable shown, which is indicated by an arrow. Normalization factors are derived from the background-only fit configuration and are applied to the dominant $t\bar{t}$, single-top, and $Z/\gamma^*+\text{jets}$ processes. The bottom panel shows the ratio between the data and the post-fit MC prediction. The hatched uncertainty band includes the statistical uncertainties in the background prediction. The last bin includes the overflow events.

5.3.3.3 $Z/\gamma^*+\text{jets}$ control region

The CRZ control region targets $Z/\gamma^*+\text{jets}$ events by applying a selection on the invariant mass of the dilepton pair $m_{\ell\ell}$, requiring it to be within 15 GeV of the Z mass. Both leptons are required to be of the same flavor. The $m_{\ell\ell}$ selection is effective in removing signal contamination, and the H_T selection is identical to that in the SRs, while the $m_{b\ell}^0$ selection is slightly relaxed to $m_{b\ell}^0 > 700$ GeV to enhance the event yield. This was chosen to avoid any extrapolation in H_T , since the Run 1 search had a large systematic uncertainty associated with this extrapolation.

5.3.3.4 Validation regions

Four disjoint validation regions are used to test the extrapolation of the background fit from the CRs to the SRs. A full list of the region selections is given in Table 5.10. The $\text{VR}m_{b\ell}^0$, $\text{VR}m_{b\ell}^1(\text{rej})$, and $\text{VR}H_T$ test the extrapolation from CRst and CRtt to the SRs in the $m_{b\ell}^0$, $m_{b\ell}^1(\text{rej})$, and H_T observables by requiring $m_{b\ell}^0 > 500$ GeV, $m_{b\ell}^1(\text{rej}) > 150$ GeV, and $H_T > 800$ GeV, respectively. In this way $\text{VR}m_{b\ell}^0$, $\text{VR}m_{b\ell}^1(\text{rej})$, and $\text{VR}H_T$ all lie between the SRs and both CRtt and CRst, with signal contamination below 1% for all signal mass values. No requirement is placed on m_{CT} in any VR, allowing both the $t\bar{t}$ and Wt contributions to be validated.

A fourth validation region, VRZ, is used to test the extrapolation from CRZ to the SRs in the

$m_{\ell\ell}$ observable, requiring $m_{\ell\ell} > 300$ GeV. As the $m_{\ell\ell}$ variable provides the only separation between CRZ and the SRs, the requirement on $m_{b\ell}^0$ is relaxed to $500 < m_{b\ell}^0 < 800$ GeV, and any event with a b -tagged jet is rejected, such that $N_b = 0$. The Z/γ^* +jets MC prediction is found to model the data well in both $m_{b\ell}$ and N_b , with a signal contamination in VRZ below 5% for mass values above 1000 GeV.

The observed data yield and the post-fit background prediction for each CR and VR are shown in Figure 5.15. Good agreement is seen in all validation regions, with differences between the data and SM prediction below 1σ . The modeling of the extrapolated variable for each VR is shown in Figure 5.16, demonstrating good agreement in the shape of the variables of interest.

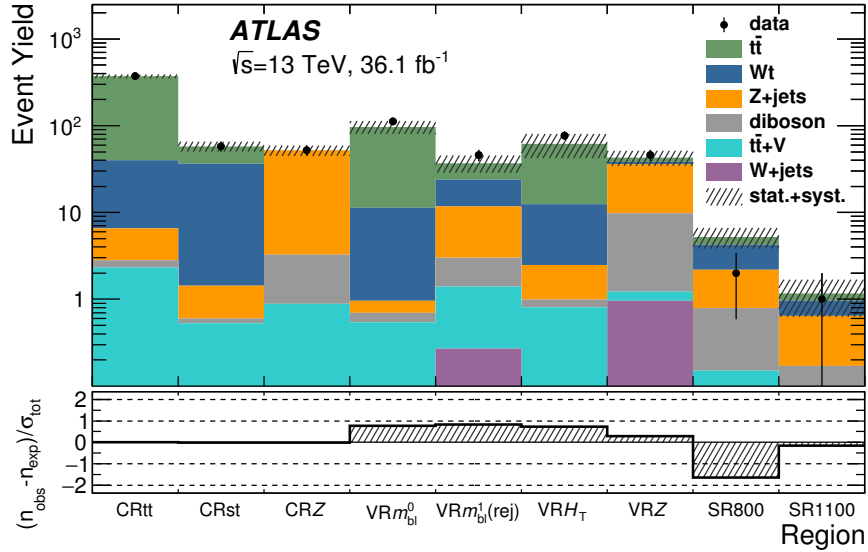


Figure 5.15: Comparison of the observed data and expected numbers of events in the CRs, VRs, and SRs. The background prediction is derived with the background-only fit configuration, and the hatched band includes the total uncertainty in the background prediction. The bottom panel shows the significance of the difference between data and the background prediction.

5.3.4 Systematic uncertainties

Systematic uncertainties in the signal and background predictions arise from theoretical uncertainties in the expected yield and MC modeling, and from experimental sources. The dominant uncertainties are summarized in Table 5.11.

Experimental uncertainties reflect the precision of the energy and momentum calibration of jets and leptons, as well as the assumptions about the identification and reconstruction efficiencies in

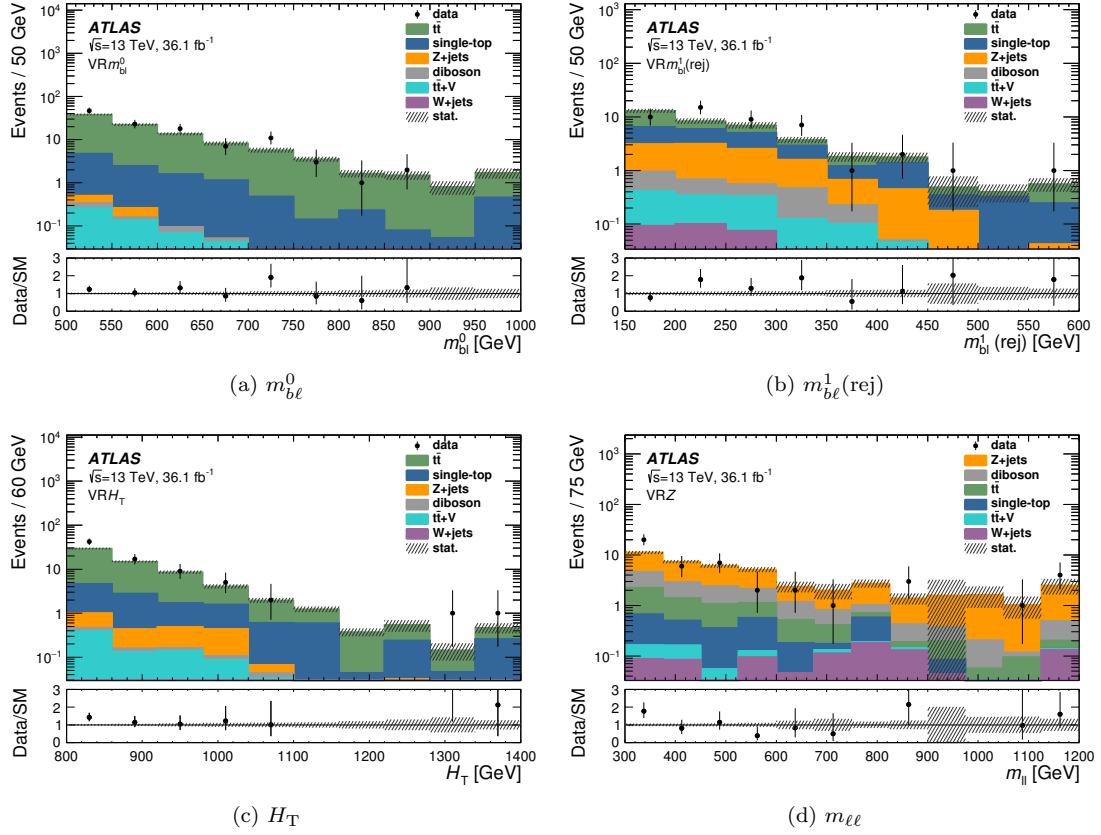


Figure 5.16: Distributions of (a) $m_{b\ell}^0$ in $VRm_{b\ell}^0$, (b) $m_{b\ell}^1(\text{rej})$ in $VRm_{b\ell}^1(\text{rej})$, (c) H_T in VRH_T , and (d) $m_{\ell\ell}$ in VRZ , for the data and post-fit MC prediction. Normalization factors are derived from the background-only fit configuration and are applied to the dominant $t\bar{t}$, single-top, and $Z/\gamma^*+\text{jets}$ processes. The bottom panel shows the ratio between the data and the post-fit MC prediction. The hatched uncertainty band includes the statistical uncertainties in the background prediction. The last bin includes the overflow events.

MC simulation. The dominant experimental uncertainties are related to jets, including those in the jet energy scale and resolution [144, 145] and the calibration of the b -tagging efficiency for b -jets, c -jets, and light-flavor jets [142]. The largest experimental uncertainties in the fitted background prediction in SR800 (SR1100) are from the b -tagging efficiency of light-flavor jets and the jet energy resolution. The experimental uncertainties associated with leptons each have a small impact on the final measurement, and include uncertainties in the energy scale and resolution of electrons [135] and muons [136], and the calibration of the lepton trigger, identification, reconstruction, and isolation efficiencies. The 3.2% uncertainty in the measured integrated luminosity also has a marginal effect on the final result.

Source \ Region	SR800	SR1100
Experimental uncertainty		
b -tagging	3%	5%
Jet energy resolution	2%	10%
Jet energy scale	1%	3%
Electrons	1%	4%
Muons	1%	3%
Theoretical modeling uncertainty		
MC statistical uncertainty	8%	17%
$t\bar{t}$	8%	45%
Single-top	21%	22%
$Z/\gamma^* + \text{jets}$	2%	4%
Diboson	4%	3%
$t\bar{t} + W/Z$	1%	1%
$W + \text{jets}$	1%	1%

Table 5.11: Summary of the dominant experimental and theoretical uncertainties in SR800 and SR1100 before the likelihood fits, quoted relative to the total pre-fit MC background predictions. The individual uncertainties can be correlated, and do not necessarily add in quadrature to the total post-fit background uncertainty.

Theoretical and MC modeling uncertainties of the $t\bar{t}$ and Wt backgrounds account for the choice of event generator, underlying-event tune, and their parameters. The uncertainties are derived separately for each background process and are treated as uncorrelated nuisance parameters. As the $t\bar{t}$ (Wt) background normalization is constrained in the likelihood fits, the uncertainties are derived on the transfer of the NF from the CR $t\bar{t}$ (CR st) to both SR800 and SR1100 by comparing CR-to-SR yield ratios in alternative models. The uncertainty in the background estimate due to the choice of MC event generator is estimated for $t\bar{t}$ and Wt by comparing the CR-to-SR yield ratios derived using MG5_AMC@NLO 2.2.3 with the one derived using POWHEG-BOX v2, both showered with Herwig++ v2.7.1 [146] using the UEEE5 UE tune [147]. The generator uncertainties are found to be conservative due to the limited statistical precision of the MG5_AMC@NLO samples. The hadronization and fragmentation modeling uncertainty is similarly estimated in both $t\bar{t}$ and Wt by comparing the nominal POWHEG + PYTHIA sample with the same POWHEG + HERWIG sample. The uncertainty due to the choice of parameters in the POWHEG + PYTHIA generator and P2012 underlying-event tune are derived by varying the parameters related to the amount of initial- and final-state radiation, the factorization and renormalization scales, and (for $t\bar{t}$ only) the p_T of the first additional emission beyond the Born level [113]. An uncertainty in the single-top yield due to the destructive interference between the $t\bar{t}$ and Wt processes is estimated by using inclusively generated

$WWbb$ events in a comparison with the combined yield of $t\bar{t}$ and Wt samples, all generated at LO with MG5_AMC@NLO 2.5.5.

The theoretical uncertainties of the Z/γ^* +jets, diboson, and $t\bar{t} + V$ samples are estimated by varying event generator parameters related to the factorization, renormalization, resummation, and CKKW matching scales. The envelope of these variations is taken as the theoretical uncertainty in the predicted yield in each SR. As the diboson and $t\bar{t} + V$ samples are not normalized in the CRs, the uncertainty in the theoretical cross section is also included. The uncertainty in the NLO cross section is taken to be 6% for the diboson process [148] and 13% for the $t\bar{t} + V$ process [124]. A 50% uncertainty is applied to the small W +jets yield in both SRs.

The stop signal model uncertainties are dominated by the cross-section uncertainty, derived from the envelope of cross-section predictions from several distinct PDF sets and varying the factorization and renormalization scales, as described in Ref. [112]. The uncertainty in the cross section varies from 13% for the 600 GeV mass value to 27% for the 1600 GeV mass value. The electron efficiency uncertainties are between 3 and 4% for the various stop masses when assuming $\mathcal{B}(\tilde{t} \rightarrow be) = \mathcal{B}(\tilde{t} \rightarrow b\mu) = 50\%$, and are between 5 and 8% when assuming $\mathcal{B}(\tilde{t} \rightarrow be) = 100\%$. Similarly, the muon efficiency uncertainties are between 2 and 4% when assuming $\mathcal{B}(\tilde{t} \rightarrow be) = \mathcal{B}(\tilde{t} \rightarrow b\mu) = 50\%$, and rise to 6% when assuming $\mathcal{B}(\tilde{t} \rightarrow b\mu) = 100\%$. The electron, muon, and jet energy scale and resolution uncertainties are generally below 1% for the stop signal models, reaching 1% for masses near the $m_{b\ell}$ threshold of 800 GeV for SR800 and 1100 GeV for SR1100. The b -tagging efficiency uncertainties are between 1 and 3%, reaching the largest value for the 600 GeV signal model.

5.3.5 Results

The observed yields and fitted background predictions in SR800 and SR1100 are shown in Table 5.12. One event is observed in SR1100 and two are observed in SR800, in agreement with the SM prediction. The SR1100 event is included in SR800 by definition, and both events are found in the $\mu\mu$ channel. The observed and predicted $m_{b\ell}^0$, H_T , $m_{b\ell}^{\text{asym}}$, $m_{\ell\ell}$, and $m_{b\ell}^1(\text{rej})$ distributions in SR800 are shown in Figure 5.13.

For each SR, model-independent upper limits are derived on the visible cross section of potential BSM processes at a 95% confidence level (CL). A likelihood fit is performed to the number of observed events in all three CRs and the target SR, and a generic BSM process is assumed to contribute to the SR only. No theoretical or systematic uncertainties are considered for the signal model except the luminosity uncertainty. The observed (S_{obs}^{95}) and expected (S_{exp}^{95}) limits on the number of BSM

	SR800				SR1100			
	inclusive	ee	$e\mu$	$\mu\mu$	inclusive	ee	$e\mu$	$\mu\mu$
Observed yield	2	0	0	2	1	0	0	1
Total post-fit bkg yield	5.2 ± 1.4	1.8 ± 0.5	2.1 ± 0.8	1.35 ± 0.32	$1.2^{+0.6}_{-0.5}$	$0.51^{+0.22}_{-0.20}$	$0.44^{+0.39}_{-0.33}$	0.22 ± 0.13
Post-fit single-top yield	2.0 ± 1.3	0.6 ± 0.4	1.1 ± 0.7	0.32 ± 0.20	0.32 ± 0.29	0.11 ± 0.10	0.21 ± 0.19	–
Post-fit Z/γ^* +jets yield	1.40 ± 0.33	0.80 ± 0.24	0.01 ± 0.01	0.59 ± 0.14	0.47 ± 0.15	0.28 ± 0.10	–	0.19 ± 0.11
Post-fit $t\bar{t}$ yield	1.0 ± 0.5	0.27 ± 0.14	0.54 ± 0.25	0.21 ± 0.10	$0.21^{+0.55}_{-0.21}$	$0.06^{+0.16}_{-0.06}$	$0.13^{+0.34}_{-0.13}$	$0.01^{+0.03}_{-0.01}$
Post-fit diboson yield	0.64 ± 0.23	0.14 ± 0.05	0.31 ± 0.12	0.19 ± 0.08	0.13 ± 0.05	0.06 ± 0.03	0.07 ± 0.03	0.01 ± 0.01
Post-fit $t\bar{t} + V$ yield	0.12 ± 0.03	0.01 ± 0.01	0.07 ± 0.02	0.04 ± 0.02	0.03 ± 0.01	–	0.01 ± 0.01	0.01 ± 0.01
Post-fit W +jets yield	0.03 ± 0.03	–	0.04 ± 0.04	–	$0.01^{+0.02}_{-0.01}$	–	$0.01^{+0.02}_{-0.01}$	–
Total MC bkg yield	4.9 ± 1.2	1.7 ± 0.4	2.0 ± 0.7	1.23 ± 0.28	$1.1^{+0.6}_{-0.5}$	$0.46^{+0.21}_{-0.19}$	$0.43^{+0.40}_{-0.33}$	0.18 ± 0.10
MC single-top yield	1.9 ± 1.0	0.57 ± 0.34	1.0 ± 0.6	0.29 ± 0.17	0.29 ± 0.25	0.10 ± 0.08	0.19 ± 0.17	–
MC Z/γ^* +jets yield	1.15 ± 0.21	0.65 ± 0.17	0.01 ± 0.01	0.48 ± 0.09	0.38 ± 0.10	0.23 ± 0.07	–	0.15 ± 0.09
MC $t\bar{t}$ yield	1.1 ± 0.5	0.29 ± 0.14	0.57 ± 0.26	0.22 ± 0.10	$0.22^{+0.57}_{-0.22}$	$0.07^{+0.18}_{-0.07}$	$0.14^{+0.36}_{-0.14}$	$0.01^{+0.03}_{-0.01}$
MC diboson yield	0.64 ± 0.23	0.14 ± 0.05	0.31 ± 0.12	0.19 ± 0.08	0.13 ± 0.05	0.06 ± 0.03	0.07 ± 0.03	0.01 ± 0.01
MC $t\bar{t} + V$ yield	0.12 ± 0.03	0.01 ± 0.01	0.07 ± 0.02	0.04 ± 0.02	0.03 ± 0.01	–	0.01 ± 0.01	0.01 ± 0.01
MC W +jets yield	0.03 ± 0.03	–	0.04 ± 0.04	–	$0.01^{+0.02}_{-0.01}$	–	$0.01^{+0.02}_{-0.01}$	–
S_{exp}^{95}	$6.4^{+3.0}_{-1.9}$	$4.1^{+1.8}_{-1.1}$	$4.0^{+2.2}_{-0.9}$	$3.9^{+1.6}_{-0.7}$	$3.9^{+2.4}_{-0.5}$	$3.0^{+1.3}_{-0.0}$	$3.0^{+1.3}_{-0.0}$	$3.1^{+0.6}_{-0.1}$
S_{obs}^{95}	4.0	3.0	3.0	4.8	3.9	3.0	3.1	4.1
$\sigma_{\text{vis}}[\text{fb}]$	0.11	0.08	0.08	0.13	0.11	0.08	0.08	0.11

Table 5.12: The observed and expected background yields in SR800 and SR1100. Both the MC background expectation before the fit and the background-only post-fit yields are shown, with each broken down into single-top, Z/γ^* +jets, $t\bar{t}$, diboson, $t\bar{t} + V$ and W +jets background processes. Model-independent upper limits are set at a 95% CL on the visible number of expected (S_{exp}^{95}) and observed (S_{obs}^{95}) events and on the visible cross section (σ_{vis}) of a generic BSM process. Results are shown in each flavor channel and inclusively. The background estimates and their uncertainties are derived from a background-only fit configuration.

events are derived at 95% CL in each flavor channel and inclusively, and are shown in the lower rows of Table 5.12. Also shown are the observed limits on the visible cross section σ_{vis} , defined as S_{obs}^{95} normalized to the integrated luminosity, and representing the product of the production cross section, acceptance, and selection efficiency of a generic BSM signal. Limits on σ_{vis} are set between 0.08 and 0.13 fb, with the weaker limit set in the $\mu\mu$ channel due to the two observed events.

Exclusion limits are derived at 95% CL for the \tilde{t} signal samples. Limits are obtained through a profile log-likelihood ratio test using the CL_s prescription [104], following the simultaneous fit to the CRs and a target SR [103]. The signal contributions in both the SR and CRs are accounted for in the fit, although they are negligible in the latter. Exclusion fits are performed separately for various branching ratio assumptions, sampling values of $\mathcal{B}(\tilde{t} \rightarrow be)$, $\mathcal{B}(\tilde{t} \rightarrow b\mu)$, and $\mathcal{B}(\tilde{t} \rightarrow b\tau)$ whose sum is unity in steps of 5%, and reweighting events in the signal samples according to the generated decays. For both SR800 and SR1100, limits are derived in the ee , $e\mu$, $\mu\mu$, and inclusive channels. Observed limits are reported for the SR and channel combination with the lowest expected CL_s value, and therefore best expected sensitivity, at a given mass value and branching ratio. The inclusive channel typically has the stronger expected sensitivity when $\mathcal{B}(\tilde{t} \rightarrow be)$ and $\mathcal{B}(\tilde{t} \rightarrow b\mu)$ are both above 15%,

while the ee channel is more sensitive when $\mathcal{B}(\tilde{t} \rightarrow b\mu)$ is below 15%, and vice versa. The inclusive channel is always more sensitive than the $e\mu$ channel because a substantial fraction of signal events have two leptons of the same flavor, regardless of individual branching ratios.

The expected and observed exclusion contours for the branching ratios are shown in Figure 5.17 for each simulated \tilde{t} mass. The limits are strongest at low values of $\mathcal{B}(\tilde{t} \rightarrow b\tau)$, where the expected number of events with electrons or muons in the final state is largest. Expected limits are slightly stronger for increasing $\mathcal{B}(\tilde{t} \rightarrow be)$, reflecting a higher trigger efficiency for electrons than for muons. Stops with $\mathcal{B}(\tilde{t} \rightarrow b\tau)$ up to 80% or more are excluded for masses between 600 and 1000 GeV while those with larger $\mathcal{B}(\tilde{t} \rightarrow be)$ or $\mathcal{B}(\tilde{t} \rightarrow b\mu)$ may be excluded up to 1500 GeV. Observed limits are stronger than expected for \tilde{t} masses of 1100 GeV or below, reflecting the lower-than-expected event yield in SR800 in the ee channel and inclusively. Exclusion contours reflecting the highest \tilde{t} mass excluded at a 95% CL for a given point in the branching ratio plane are shown in Figure 5.18.

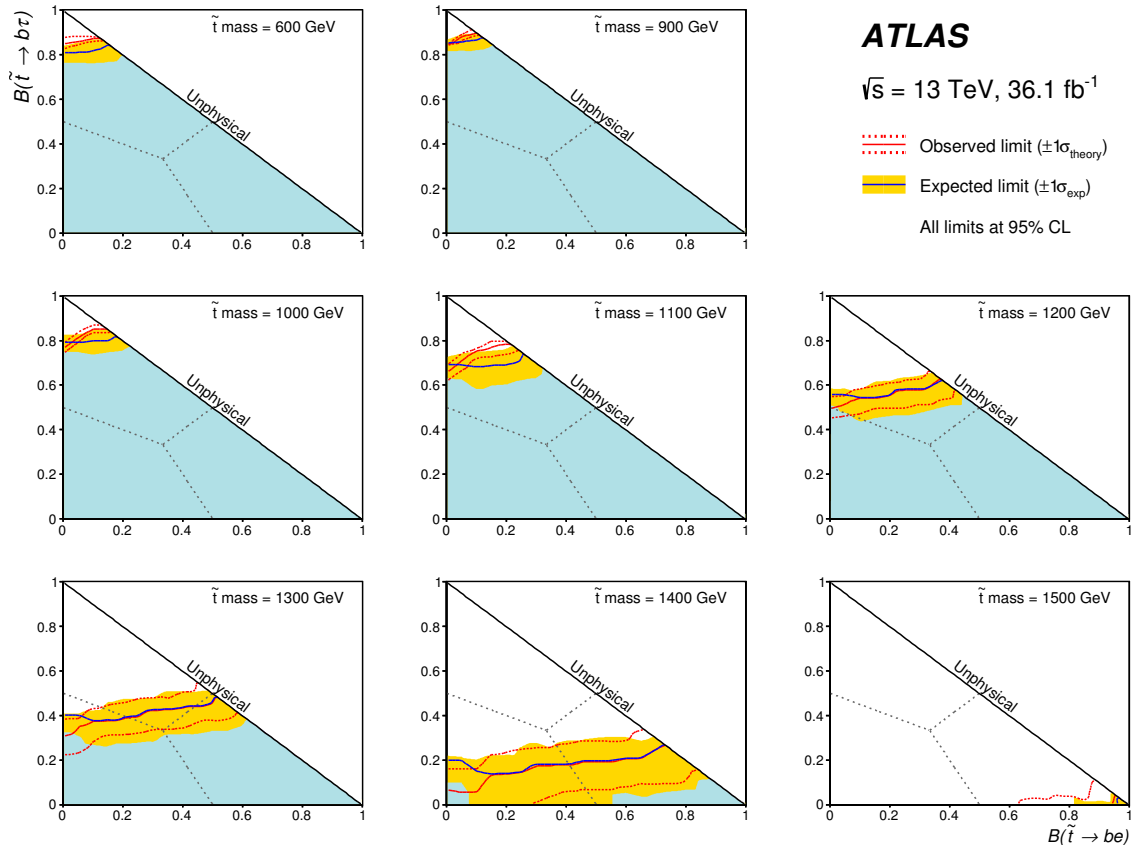


Figure 5.17: Expected (dashed blue) and observed (solid red) limit curves as a function of \tilde{t} branching ratios for various mass values between 600 and 1500 GeV. The sum of $\mathcal{B}(\tilde{t} \rightarrow be)$, $\mathcal{B}(\tilde{t} \rightarrow b\mu)$, and $\mathcal{B}(\tilde{t} \rightarrow b\tau)$ is assumed to be unity everywhere, and points of equality are marked by a dotted gray line. The yellow band reflects the $\pm 1\sigma$ uncertainty of the expected limit due to theoretical, experimental, and MC statistical uncertainties. The shaded blue area represents the branching ratios that are expected to be excluded beyond 1σ . The dotted red lines correspond to the $\pm 1\sigma$ cross section uncertainty of the observed limit derived by varying the signal cross section by the theoretical uncertainties.

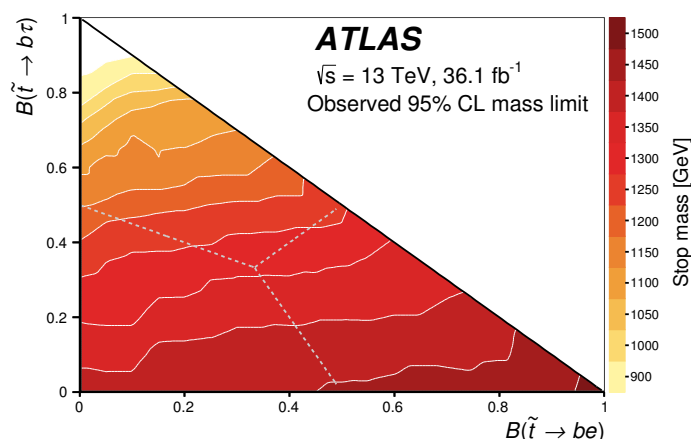


Figure 5.18: The observed lower limits on the \tilde{t} mass at 95% CL as a function of \tilde{t} branching ratios. The sum of $\mathcal{B}(\tilde{t} \rightarrow be)$, $\mathcal{B}(\tilde{t} \rightarrow b\mu)$, and $\mathcal{B}(\tilde{t} \rightarrow b\tau)$ is assumed to be unity everywhere, and points of equality are marked by a dotted gray line. The limits are obtained using the nominal \tilde{t} cross-section predictions. As the branching ratio $\mathcal{B}(\tilde{t} \rightarrow b\tau)$ increases, the expected number of events with electrons or muons in the final state decreases, reducing the mass reach of the exclusion.

5.4 Prospects

This chapter presented the first ATLAS results on the search for the pair production of stops, each decaying via an R -parity-violating coupling to a b -quark and a lepton. No significant excess of events over the Standard Model prediction is observed, and limits are set on the \tilde{t} mass at a 95% confidence level. These results significantly extend the lower-mass exclusion limits on the $B - L$ stop model from reinterpretations of Run 1 leptoquark searches. Model-independent upper limits are set on the cross section of potential BSM processes in the ee , $e\mu$, and $\mu\mu$ channels and inclusively. A scan of various \tilde{t} branching ratios is performed to set branching-ratio-dependent limits on decays to be , $b\mu$, and $b\tau$ for various \tilde{t} mass models. Limits are set on \tilde{t} masses between 600 GeV for large $b\tau$ decay branching ratios and 1500 GeV for a be branching ratio of 100%.

There are several ways to strengthen the limits on a stop LSP from this $B - L$ RPV model. Firstly, the inclusion of tau leptons would greatly improve the signal efficiency in the high $\mathcal{B}(\tilde{t} \rightarrow b\tau)$ corner of the BR plane. As mentioned before, this is covered by a leptoquark search in the exotics group. Similarly, as mentioned in Section 2.3.2, there is a possibility that the stop decays to a top quark and a neutrino rather than a b -quark and a lepton if the stop is purely right-handed. In this case the pair production of two stops would result in a final state with two top quarks and a large amount of missing energy. There are searches for RPC SUSY that have sensitivity to these decays, in particular searches for stops which then decay to a top and a stable neutralino. Both the leptoquark search and the RPC stop searches will be presented in Section 5.4.1. Moreover, limits derived from the analysis presented in this chapter can be improved with more proton-proton collision data, as well as some improvements in the analysis strategy. These improvements will be discussed in Section 5.4.2.

5.4.1 Similar searches

5.4.1.1 Third-generation leptoquark search

Many extensions to the SM predict leptoquarks [149–155] which are bosons that decay to a lepton-quark pair. It is particularly interesting to search for “third-generation leptoquarks” (LQ_3) which can be up-type or down-type analogously to SM quarks. Up-type third-generation leptoquarks (LQ_3^u) decay to either a top quark and a neutrino or a bottom quark and a tau lepton, as shown in Figure 5.19⁶. Such a search was performed with 36.1 fb^{-1} of 13 TeV proton-proton data [156],

⁶Down-type third-generation leptoquarks (LQ_3^d), which are also targeted in the leptoquark search, decay to either a top quark and a tau lepton or a bottom quark and a neutrino. Since there is no $m_{b\ell}$ resonance in these final states, they are not as similar to the RPV stop final states as LQ_3^u .

optimized for these up-type third-generation leptoquarks which decay 100% to $b\tau$, so this search is very sensitive to the RPV stop signature. This analysis uses a boosted decision tree (BDT) algorithm to improve signal to background ratio using $m_{b\ell}$ among other variables as input discriminants. In fact, the assumed leptoquark cross-sections are identical to the stop cross-sections, so the limits set in this search can be directly translated to stop limits. These limits are shown in Figure 5.20 for $\mathcal{B}(\text{LQ} \rightarrow b\tau) = 100\%$, where leptoquarks (and hence stops) below 1030 GeV are excluded, and as a function of $\mathcal{B}(\text{LQ} \rightarrow b\tau)$ in Figure 5.21.

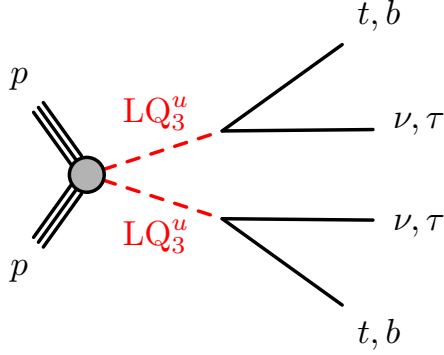


Figure 5.19: Pair production and decay of LQ_3^u [156].

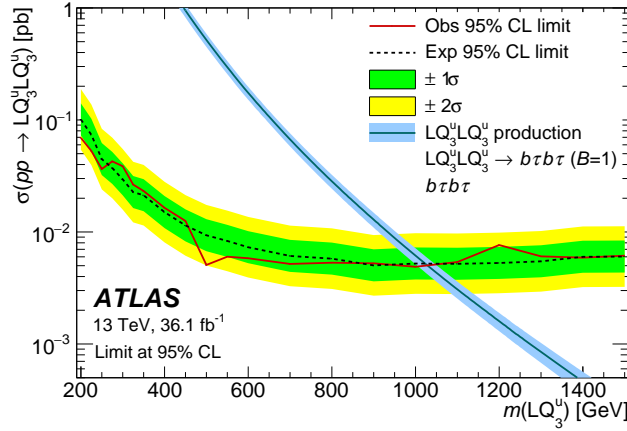


Figure 5.20: Expected and observed 95% CL upper limits on up-type third-generation leptoquark, for $\mathcal{B}(\text{LQ} \rightarrow b\tau) = 100\%$. The observed limit is shown as the solid line. The thickness of the theory curve represents the theoretical uncertainty from PDFs, renormalization and factorization scales, and the strong coupling constant α_S [156].

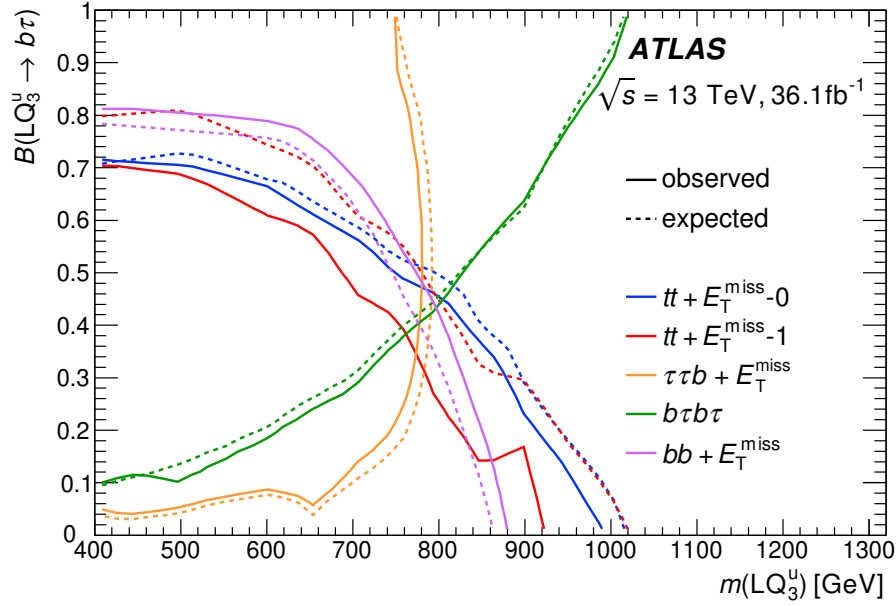


Figure 5.21: Expected and observed 95% CL upper limits on up-type third-generation leptoquark, as a function of $\mathcal{B}(\text{LQ} \rightarrow b\tau)$ versus LQ mass. The green line ($b\tau b\tau$) represents the limits derived from this dedicated search. The other lines are reinterpretations for other **SUSY** models: bottom-squark pair production ($bb + E_{\text{T}}^{\text{miss}}$) [157], top-squark pair production with one ($tt + E_{\text{T}}^{\text{miss}} - 1\ell$) [158] or zero leptons ($tt + E_{\text{T}}^{\text{miss}} - 0\ell$) [159] in the final state, and for top squarks decaying via τ -sleptons ($\tau\tau b + E_{\text{T}}^{\text{miss}}$) [160]. The region to the left of the contour lines is excluded at 95% confidence level. Since the assumed cross-sections are identical to stop pair production, these limits can be interpreted as stop limits as well [156].

5.4.1.2 RPC stop searches

As discussed in Section 2.3.2, in the $B - L$ MSSM model, if the stop is purely right-handed, it primarily decays to a top quark and a neutrino. This will look identical to **RPC** searches for stops which decay to a top and a stable neutralino when the neutralino is very light. There are several of these searches, split based on the lepton multiplicity in the final state, which is dependent on the decay of the W bosons from the tops [158, 159, 161–166]. A summary of the limits set from these searches is shown in Figure 5.22 [167]. Here it can be seen that stops which decay to a top and a very light, stable, neutral particle are excluded up to 1 TeV. It is generally interesting that there is one window that is not excluded, as shown in the insert in the upper right of the figure, but this is relevant for masses too high to be consistent with a neutrino.

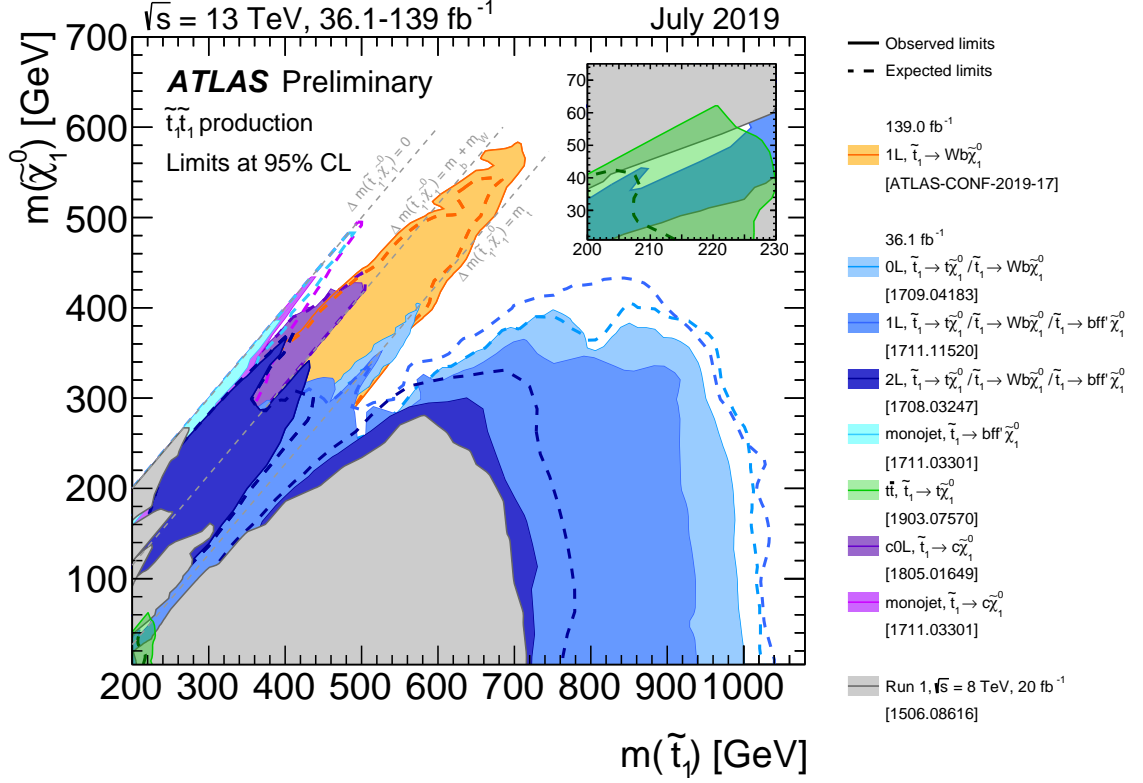


Figure 5.22: Summary of the dedicated ATLAS searches for top squark (stop) pair production based on pp collision data taken at $\sqrt{s} = 13 \text{ TeV}$. Exclusion limits at 95% CL are shown in the (lightest stop (\tilde{t}_1), lightest neutralino ($\tilde{\chi}_1^0$)) mass plane. The dashed and solid lines show the expected and observed limits, respectively, including all uncertainties except the theoretical signal cross section uncertainty (PDFs and scale). Four decay modes are considered separately with 100% BR: $\tilde{t}_1 \rightarrow t + \tilde{\chi}_1^0$ (where the \tilde{t}_1 is mostly right), $\tilde{t}_1 \rightarrow W + b + \tilde{\chi}_1^0$ (3-body decay for $m(\tilde{t}_1) < m(t) + m(\tilde{\chi}_1^0)$), $\tilde{t}_1 \rightarrow c + \tilde{\chi}_1^0$ and $\tilde{t}_1 \rightarrow f + f' + b + \tilde{\chi}_1^0$ (4-body decay). The latter two decay modes are superimposed. [167]

5.4.2 Future improvements to this search

The inclusion of more data will certainly help improve the limits on a high-mass RPV-decaying stop, up to roughly 1.7 TeV depending on the assumed lepton flavor branching ratio, as can be seen in Figure 5.23. This was estimated by interpolating the signal acceptance and efficiency of the 2015+2016 analysis with the full Run 2 luminosity, which was estimated at the time of making this plot to be 150 fb^{-1} .

In addition to the gains possible with more data, there are several ways that future versions of this analysis can be improved for higher discovery potential. Most notably, the dominant uncertainties

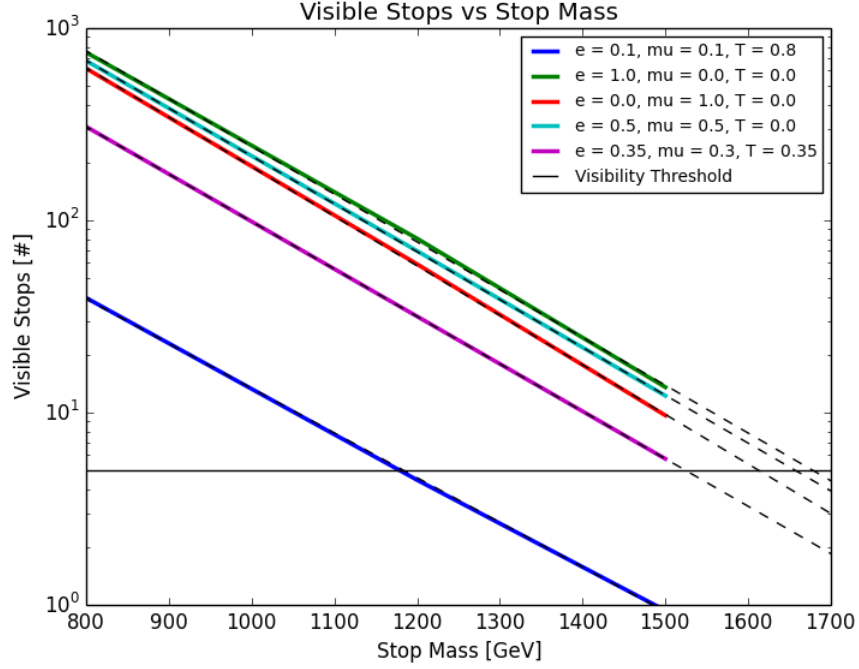


Figure 5.23: Expected number of events with “visible” stops as a function of stop mass with 150 fb^{-1} at $\sqrt{s} = 13 \text{ TeV}$, calculated using the signal acceptance and efficiency of the 2015+2016 analysis. The various colored lines represent different lepton flavor branching ratios. The expected limits for high $\mathcal{B}(\tilde{t} \rightarrow b\mu)$ are slightly worse than those for high $\mathcal{B}(\tilde{t} \rightarrow be)$ because muons have slightly lower efficiency than electrons. The solid black line demarcates 5 events, as an estimate of the number of signal events required in an SR to claim discovery. Courtesy of James Heinlein.

are the statistics of MC background samples. This is true in both the [Run 1](#) and early [Run 2](#) (2015-2016) analyses, ignoring the Run 1 H_T extrapolation uncertainty which was mitigated in the Run 2 search. It is encouraging to note that these uncertainties were smaller for the early Run 2 search than they were in Run 1; hopefully with dedicated effort to increase the statistics, this trend continues.

Additionally it would be nice to set stronger limits on the lower masses. Because the loosest early Run 2 SR had a requirement on $m_{b\ell}$ of 800 GeV, the efficiency for stops with masses smaller than this was quite low. This can be gleaned from [Figure 5.17](#) where the limits set on the 600 GeV stop mass are roughly the same as those set on the 900 GeV stop mass. Having something like a sliding window, or performing a shape fit of the $m_{b\ell}$ distribution rather than these strict cuts would greatly improve the low-mass limits. Additionally, sensitivity can potentially be gained by investigating new b -tagging working points which are targeted for high efficiency at high jet p_T , to avoid the inefficiencies due to a b -quark with a large Lorentz boost (see [Appendix A](#)).

CHAPTER 6

Search for Wino LSP Decays with a Trilepton Resonance

With no significant deviations from the [SM](#) observed, and with the large increase in integrated luminosity with the full [Run 2](#) LHC dataset, it is feasible to search for [SUSY](#) processes with smaller cross-sections. In particular, it is feasible to search for [EWK](#) production of SUSY particles. Recall there are four charginos ($\tilde{\chi}_1^\pm, \tilde{\chi}_2^\pm$) which are generally admixtures of the charged winos and higgsinos, and four neutralinos ($\tilde{\chi}_1^0, \tilde{\chi}_1^0, \tilde{\chi}_2^0, \tilde{\chi}_3^0, \tilde{\chi}_4^0$) which are generally admixtures of the neutral winos, higgsinos, and bino. The subscripts on these particle names are ordered such that smaller numbers correspond to lighter masses. As discussed in [Section 2.3.4](#), a possible channel in which to search for the $B-L$ MSSM is via charged and neutral wino [LSPs](#), which both have many possible decays whose relative [BRs](#) depend on $\tan\beta$ and the neutrino hierarchy. For the remainder of this chapter, the charged and neutral wino will be referred to simply as the chargino and the neutralino respectively.

The search presented in this chapter targets mass-degenerate chargino ($\tilde{\chi}_1^\pm$) and neutralino ($\tilde{\chi}_1^0$) LSPs which each decay via [RPV](#) couplings, produced via either chargino pair production (C1C1) or chargino-neutralino production (C1N1). In the $B-L$ model, the $\tilde{\chi}_1^\pm$ and $\tilde{\chi}_1^0$ are both almost fully wino. Therefore the other charginos and neutralinos tend to be heavier and are decoupled, so additional production modes (for example C1N2) are not considered in this search.

If the chargino decays to $Z\ell$, and the Z decays leptonically ($\tilde{\chi}_1^\pm \rightarrow Z\ell \rightarrow \ell\ell\ell$), as shown in [Figure 6.1](#), the trilepton invariant mass will reconstruct the chargino mass and leave a very distinct experimental signature. This analysis searches for a trilepton invariant mass resonance in events with at least three light leptons (electrons and muons). Taus are not used to optimize the search but leptonically decaying taus are not explicitly vetoed and so can contribute to sensitivity. Henceforth

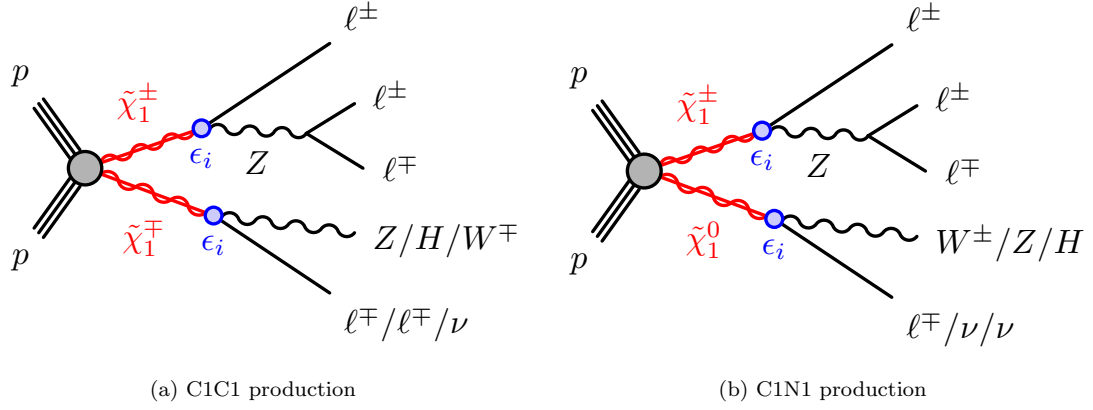


Figure 6.1: Feynman diagram for mass-degenerate chargino pair production (a) and chargino-neutralino production (b), with at least one $\tilde{\chi}_1^\pm \rightarrow Z\ell \rightarrow \ell\ell\ell$ decay.

the ℓ symbol is used to denote light leptons. While the target of this search is the trilepton resonance from a single chargino, features from the decay of the other produced chargino or neutralino are used as well to improve signal selection and background rejection.

During Run 1 there were two similar searches in ATLAS [168, 169] and one in CMS [170] which had sensitivity to this model, but none since then. Ref. [169] performed a resonance search in the $m_{Z\ell} - m_{\ell\ell}$ distribution and so is quite similar to this search. These searches respectively excluded type-III Seesaw heavy leptons with masses between 100–468 GeV [168] and below 840 GeV [170], and excluded vector-like leptons with masses between 114–176 GeV [168], depending on the theoretical scenario considered. The current lower bound on chargino and neutralino masses is taken to be 100 GeV, from the precision EWK measurements at the Large Electron-Positron Collider (LEP) [171, 172]. LEP collided electrons and positrons at center-of-mass energies up to 209 GeV and, being energetic enough to pair produce W and Z bosons, enabled precision measurements of EWK processes. No deviations from the SM were observed, so it follows that any winos must be too massive to have been produced at LEP.

There are several event reconstruction strategies depending on the physics objects in the final state, in order to most effectively select signal and reject background. These strategies are described in Section 6.1. The datasets used in this analysis are listed in Section 6.2. The event reconstruction is described in Section 6.3, the method used to estimate fake backgrounds is presented in Section 6.4, and the event selection is explained in Section 6.5. Uncertainties are explored in Section 6.6, and results and interpretations are presented in Section 6.7. Finally, prospects for future versions of this

analysis are discussed in Section 6.8.

6.1 Analysis Overview

There are hundreds of possible final states, depending how the chargino, neutralino, and subsequent bosons decay. All final states with at least one $\tilde{\chi}_1^\pm \rightarrow Z\ell \rightarrow \ell\ell\ell$ decay leg are targeted in this analysis, where ℓ denotes the light leptons (electrons and muons). In order to benefit from the many possible final states, the analysis strategy combines two main event types, called OneLeg and TwoLeg. OneLeg targets final states where only the trilepton leg decays fully visibly, and TwoLeg targets final states where both winos decay fully visibly. Specifically, TwoLeg targets final states with one trilepton leg from the chargino, and either a trilepton or a $jj\ell$ leg from the other chargino or neutralino. Nominally, these final states are:

- $C1C1 \rightarrow Z\ell Z\ell \rightarrow \ell\ell\ell \ell\ell$
- $C1C1 \rightarrow Z\ell Z\ell \rightarrow \ell\ell jj\ell$
- $C1C1 \rightarrow Z\ell H\ell \rightarrow \ell\ell\ell b\bar{b}\ell$
- $C1N1 \rightarrow Z\ell W\ell \rightarrow \ell\ell\ell jj\ell$

The OneLeg event type is designed to reconstruct only the trilepton decay leg, in final states where the other decay leg is semi-invisible or has more than a three-body decay due to cascade decays of the boson. Some of the final states that are targeted in OneLeg are:

- $C1C1 \rightarrow Z\ell Z\ell \rightarrow \ell\ell\ell \nu\nu\ell$
- $C1C1 \rightarrow Z\ell H\ell \rightarrow \ell\ell\ell WW\ell$
- $C1C1 \rightarrow Z\ell W\nu \rightarrow \ell\ell\ell jj\nu$
- $C1N1 \rightarrow Z\ell Z\nu \rightarrow \ell\ell\ell jj\nu$
- $C1N1 \rightarrow Z\ell H\nu \rightarrow \ell\ell\ell WW\nu$
- $C1N1 \rightarrow Z\ell W\ell \rightarrow \ell\ell\ell \ell\nu\ell$

In practice, OneLeg also picks up final states with a fully visible non-trilepton decay leg which is not successfully reconstructed due to leptons not being reconstructed or an invariant mass not falling within the required mass window for the second boson, described below. A detailed discussion of

the truth final states that are targeted for, and reconstructed in, each category can be found in Appendix B.

Each event is assigned to either OneLeg or TwoLeg using the following algorithm, which is shown schematically in Figure 6.2. First a Z boson is reconstructed by selecting two SFOS with an invariant mass within 10 GeV of 91.2 GeV. Then if there are at least 4 remaining leptons, or at least 2 remaining leptons and at least 2 jets, the reconstruction of a second boson is attempted in the following manner. If there are at least 4 remaining leptons (for a total of 6 leptons in the final state), the attempted boson is a second leptonic Z , again with an invariant mass within 10 GeV of 91.2 GeV. If there are at least 2 remaining leptons (for a 4-lepton final state) and at least 2 jets, the attempted boson is reconstructed from a jet pair that has an invariant mass within the window [71.2 GeV, 111.2 GeV] to target hadronic W and Z decays. If at least one of these jets is b -tagged (according to the criteria which will be outlined in Section 6.3), the upper limit of the invariant mass window is extended to 150 GeV to also include Higgs decays. If a second boson is successfully reconstructed with these criteria and there are still two remaining leptons, then this event falls in the TwoLeg category. If there are multiple candidates for the second boson, the one with invariant mass closest to the true Z or Higgs mass is chosen, where the Higgs mass is only considered in addition to the Z for boson candidates with a b -jet. The leptons are then matched to the bosons in such a way to minimize the mass asymmetry, defined as

$$m_{Z\ell} \text{ asymmetry} = \frac{|m_{Z\ell} - m_{B\ell}|}{m_{Z\ell} + m_{B\ell}}. \quad (6.1)$$

Here $m_{Z\ell}$ is the invariant mass of the trilepton leg, and $m_{B\ell}$ is the invariant mass of the other leg, labeled with B because it could be a Z , H , or W boson⁷. The asymmetry should be small if the boson-lepton pairs come from two particles of the same mass. Indeed this matching scheme selects the correct lepton-boson pairs effectively.

If a second boson was not successfully reconstructed, or if there are fewer than two remaining leptons, then this event falls in the OneLeg category. If there are exactly three leptons in the event, then the third lepton is assigned to the reconstructed Z . If there are four or more leptons, there is ambiguity as to which lepton should be used for the trilepton leg. Because of the varying kinematics depending on chargino mass, there is no lepton matching choice that performs best for all mass points. Many options were studied and are documented in Appendix C. The chosen scheme uses L_T , the scalar sum of the p_T of all leptons in an event, as a proxy for the chargino mass.

⁷If both bosons are reconstructed from two leptons, meaning there are two trilepton legs in an event, the trilepton leg with the SFOS lepton pair closest to the true Z mass is labeled $Z\ell$. However this is very rare because of the small BR of Z to leptons.

If $L_T < 550$ GeV, then the lepton spatially closest to the Z (that which minimizes $\Delta R(Z, \ell)$) is assigned. This works well for low mass points because the Z and the lepton from the same chargino leg are generally collimated due to the boost of the chargino. On the other hand, if $L_T > 550$ GeV, then the lepton which maximizes $m_{Z\ell}$ is assigned. This works well for high mass points because it is unlikely that a random combination of $Z\ell$ pairs would have a large invariant mass, in both signal and background.

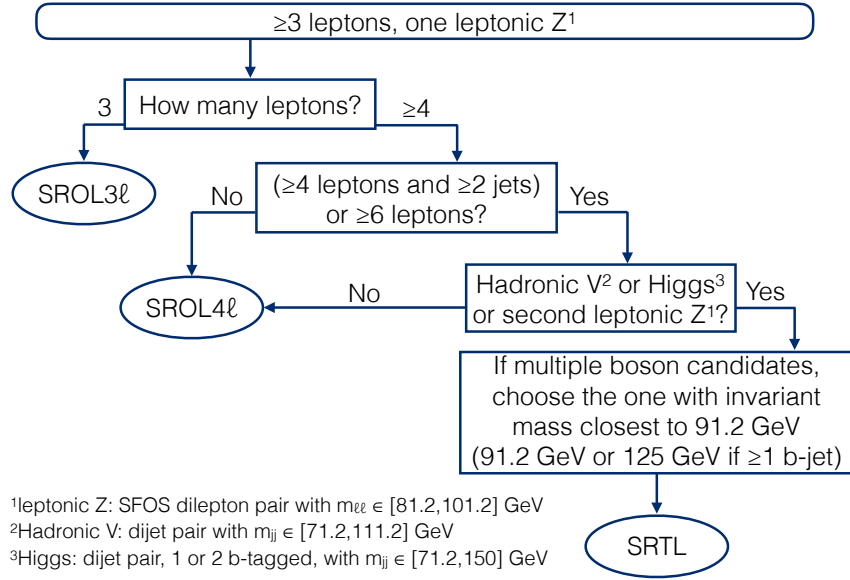


Figure 6.2: Schematic flow chart describing the object criteria for each SR.

The main backgrounds in this analysis are Standard Model processes with at least one Z boson. Most notably these are Drell-Yan ($Z/\gamma^* + \text{jets}$), WZ , ZZ , and ttZ . The yields of these processes can be minimized by applying dedicated cuts which will be described in Section 6.5. Because Drell-Yan only has two prompt leptons in the final state, to enter the 3ℓ final states, the third lepton must be either another object that was misidentified as a lepton, or a non-prompt decay product such as from a photon conversion or a B -hadron decay. These leptons are generally referred to as “fakes” even though the non-prompt leptons are real. There is a dedicated data-driven method for estimating this fake background, which is referred to as the fake factor method. The other large backgrounds are estimated using normalization factors derived in dedicated Control Regions (CRs). The fake factor method will be described in Section 6.4, and the CRs will be described in Section 6.5. Other smaller backgrounds are Higgs, Triboson, $t\bar{t}$, and other $t\bar{t} + V$ processes. These backgrounds are

estimated using MC simulation directly. The relative abundance of each of these backgrounds is very different for each of our SR types (OneLeg compared to TwoLeg, 3ℓ compared to 4ℓ).

The goal is to find a resonance in the trilepton invariant mass spectrum. To achieve this, the search is conducted using a shape fit from the HistFitter [103] statistical analysis framework. If there are two fully leptonic $Z\ell$ pairs, reconstructed from six leptons, the average of both is taken because the mass resolution of each should be similar. The masses of each are also guaranteed to be similar because of a requirement on $m_{Z\ell}$ asymmetry which will be described in Section 6.5.

The fit uses a variable bin width in the $m_{Z\ell} - m_Z + (91.2/\text{GeV})$ distribution, denoted $m_{Z\ell}^{\text{shifted}}$, as outlined in Table 6.1. The choice of this binning is explained in Appendix D. Further details on the fit procedure are given in Section 6.7.

Bin width [GeV]	$m_{Z\ell}^{\text{shifted}}$ range [GeV]
20	[90, 270)
30	[270, 360)
40	[360, 440)
140	[440, 580)
Inclusive	[580, ∞)

Table 6.1: The chosen binning for the shape fit of the $m_{Z\ell}^{\text{shifted}}$ distribution.

6.2 Dataset and Monte Carlo simulated samples

During 2015, 2016, 2017, and 2018, the ATLAS detector recorded approximately 149 fb^{-1} of pp collisions at a center-of-mass energy (\sqrt{s}) of 13 TeV, of which 139 fb^{-1} was found suitable for physics. All subdetectors were required to be operational as defined in the good runs list (GRL) provided by the Data Preparation Group.

Simulated MC samples are used to model the shape of the expected background and to define and tune the analysis. Each sample is generated according to the corresponding process and propagated through a simulation of the ATLAS detector. The primary backgrounds in this analysis are Diboson (WZ and ZZ), $Z/\gamma^* + \text{jets}$, and $t\bar{t}Z$.

Diboson, Triboson, and $V + \text{jets}$ samples are simulated with the SHERPA 2.2 [78] Monte Carlo generator. Diboson samples include fully leptonic and semileptonic decays as well as loop-induced and electroweak $VVjj$ production.

The production of $t\bar{t}$ events is modeled using the POWHEGBOX [86–89] v2 generator at NLO

with the NNPDF3.0nnlo PDF set and the h_{damp} parameter⁸ set to $1.5 m_{\text{top}}$ [173]. The events are interfaced with PYTHIA.230 [174] using the A14 tune [126] and the NNPDF2.31o PDF set [123]. The NLO $t\bar{t}$ inclusive production cross section is corrected to the theory prediction at next-to-next-to-leading order (NNLO) in QCD including the resummation of next-to-next-to-leading logarithmic (NNLL) soft-gluon terms calculated using TOP++2.0 [107, 175–180]. Single-top Wt associated production is modeled using the POWHEGBOX [86–88, 92, 181, 182] v2 generator at NLO in QCD with the NNPDF3.0nnlo parton distribution function (PDF) set. The events are interfaced with PYTHIA.230 using the A14 tune and the NNPDF2.31o PDF set. Rare top processes include $t\bar{t} + X$ (where X is a W , Z , or Higgs boson), $t\bar{t} + WZ$, $t + Z$, and $t + WZ$ production and are modeled using the MADGRAPH5_AMC@NLO v2.3.3 [124] generator at NLO with the NNPDF3.0nnlo PDF, and interfaced with PYTHIA.210 using the A14 tune and the NNPDF2.31o PDF set. Rare top also encompasses $t\bar{t} + \gamma$, $t\bar{t} + WW$, and 4-top production, which are similarly modeled using MADGRAPH5_AMC@NLO v2.2.3 interfaced with PYTHIA.186.

Higgs boson production processes are generated using POWHEGBOX v2 and interfaced with PYTHIA 8.212 using the AZNLO [183] tune and CTEQ6L1 [115] PDF set. Higgs samples are normalized with cross sections calculated at NLO [184].

MC samples are also generated to model the wino signal processes. Samples are generated in MadGraph+Pythia8 [79, 174] and detector interactions are simulated with AtIfast-II [185], except the 500 GeV mass point in the mc16d campaign, which used the normal full simulation (“FullSim”). Signal production cross sections assume a wino-like chargino and neutralino, as this is larger and more favored than higgsino in the theory model of interest [27]. Signal production cross sections for C1C1 and C1N1 are computed at NLO plus next-to-leading-log (NLL) precision in a limit of mass-degenerate wino $\tilde{\chi}_2^0$ and $\tilde{\chi}_1^\pm$, light bino $\tilde{\chi}_1^0$, and with all the other sparticles assumed to be heavy and decoupled [186, 187]. Since the benchmark model for this analysis has a wino-like $\tilde{\chi}_1^\pm$ and $\tilde{\chi}_1^0$, the cross sections calculated here are assumed to be valid for C1N1.

In C1C1, the chargino branching ratios are set to 11.1% for Ze , $Z\mu$, $Z\tau$, He , $H\mu$, and $H\tau$, as well as 33.3% for $W\nu$ to account for the three neutrino flavors. In C1N1, the charginos are forced to decay to Ze , $Z\mu$, $Z\tau$, each with 33.3% branching ratio, while the neutralinos can decay to $Z\nu$ or $H\nu$, each with 33.3% branching ratio, or We , $W\mu$, or $W\tau$, each with 11.1%. For mass points below 125 GeV, the Higgs decay is turned off and equal branching ratios are assigned to the Z and W

⁸The h_{damp} parameter controls the transverse momentum p_T of the first additional emission beyond the leading-order Feynman diagram in the parton shower and therefore regulates the high- p_T emission against which the $t\bar{t}$ system recoils.

decay modes. In both processes, a filter is applied to event generation which requires a leptonically decaying Z (here, leptons include taus) in each event to be stored in the output. C1N1 has an additional filter applied that removes any events without at least 3 light leptons, i.e. a hadronically decaying tau does not count towards this minimum. There is also a filter which requires a minimum p_T of 9 GeV and maximum $|\eta|$ of 2.8 for all leptons for C1N1, slightly looser than the baseline lepton requirements that will be described in Section 6.3.

All studies and optimization for this analysis are performed using C1C1 and the nominal event generation branching ratios, with an effective increase in $\tilde{\chi}_1^\pm \rightarrow Z\ell$ because of the generator filter. Limits are interpreted for many possible $\tilde{\chi}_1^\pm$ or $\tilde{\chi}_1^0$ branching ratios, by applying a truth-level event reweighting according to the chargino or neutralino decays in each event analogously to the reweighting applied for the stop search, given in Equation 5.1.

6.3 Event Reconstruction

Events and physics objects are required to pass a set of quality criteria to be included in the analysis. Individual events are required to pass the criteria of various sub-detector and physics performance groups for signs of data corruption, noise bursts, and detector issues [188], as well as to fire one of several single-lepton triggers. “Baseline” objects are used to calculate missing energy, and as input to overlap removal. “Signal” objects are baseline objects which pass overlap removal and satisfy tighter criteria.

Trigger selection

This analysis uses unscaled single electron and single muon triggers. The triggers for both electrons and muons for each year are shown in Table 6.2. Events are required to have at least one signal lepton matched to the trigger fired in that event. This lepton is not required to be the leading lepton in an event, but it must exceed the offline p_T threshold for the trigger. For muons, this is 1.05 times the HLT trigger threshold, which is the number listed in the trigger name (in GeV). For electrons, this is 1 GeV larger than the HLT trigger threshold. For simplicity and consistency across data years, the p_T requirement applied to the trigger-matched signal lepton corresponds to the trigger thresholds for data taken during and after 2016, except for `HLT_e120_lhloose` in which case the standard 121 GeV is used.

The trigger requirement is applied to both data and MC events. To account for differences in the data and MC trigger efficiencies, a trigger scale factor is applied to MC events. These scale factors

Electron Triggers	Muon Triggers
2015	
HLT_e24_lhmedium_L1EM20VH HLT_e60_lhmedium HLT_e120_lhloose	HLT_mu20_iloose_L1MU15 HLT_mu50
2016, 2017, 2018	
HLT_e26_lhtight_nod0_ivarloose HLT_e60_lhmedium_nod0 HLT_e140_lhloose_nod0	HLT_mu26_ivarmedium HLT_mu50

Table 6.2: Electron and muon triggers used for each year. The name of the trigger includes either “mu” or “e” which signifies whether a muon or electron candidate is required. Then the p_T cut of the trigger is specified in GeV. “L1” with some string following refers to the L1 seed; this seed is required for all triggers but it is not explicitly included in all trigger names. Text with “i” refers to the trigger-level isolation criteria, where “ivar” indicates a variable sized cone isolation requirement. Text such as “lhtight” and “lhmedium” refers to the trigger-level identification criteria, where “lh” signifies that a likelihood-based identification is used. “nod0” means there is no requirement on d_0 or $d_0/\sigma(d_0)$ [69–71].

are provided by the e/γ and muon performance groups.

Electron selection

Baseline electrons, which are used for calculating missing energy as well as input into overlap removal, have the following selection criteria. They are required to have $p_T > 10$ GeV and $|\eta| < 2.47$, with a veto for electrons that fall in the calorimeter crack, corresponding to $|\eta|$ between 1.37 and 1.52. They must also have a small longitudinal impact parameter $|z_0 \sin(\theta)| \leq 0.5$ mm. They must also pass the `LooseAndBLayerLLH` likelihood selection and `BADCLUSELECTRON` object quality selection.

Signal electrons are all baseline electrons which pass overlap removal and the following additional selection criteria. They have the tighter likelihood selection of `MediumLLH` (for a discussion of this selection, see Appendix E) and must pass the `FCTight` isolation working point, as well as a transverse impact parameter significance cut of $|d_0/\sigma(d_0)| < 5$ and a tighter p_T cut of 12 GeV.

All criteria for baseline and signal electrons are summarized in Table 6.3.

Cut	Value/description
Baseline electron	
Acceptance	$p_T > 10$ GeV, $ \eta < 2.47$, crack veto
Impact parameter	$ z_0 \sin(\theta) \leq 0.5$ mm
Identification WP	LooseAndBLayerLLH
Object quality	BADCLUSELECTRON electron veto
Signal electron	
Acceptance	$p_T > 12$ GeV
Impact parameter	$ d_0/\sigma(d_0) < 5$
Identification WP	MediumLLH
Isolation WP	FCTight

Table 6.3: Summary of electron selection criteria. Signal criteria are applied on top of baseline criteria after overlap removal.

Muon selection

Baseline muons, which are used for calculating missing energy as well as input into overlap removal, have the following selection criteria. They are required to have $p_T > 10$ GeV and $|\eta| < 2.7$. They must also have a small longitudinal impact parameter $|z_0 \sin(\theta)| \leq 0.5$ mm. They must also pass the **Medium** identification working point (for a discussion of ID WP selection, see Appendix E).

Signal muons are all baseline muons which pass overlap removal and the following additional selection criteria. They have a tighter p_T cut of 12 GeV. They must also pass the **FCTight_FixedRad** isolation working point, as well as a transverse impact parameter significance cut of $|d_0/\sigma(d_0)| < 3$. Cosmic muons are vetoed, and events with bad muons are vetoed.

All criteria for baseline and signal muons are summarized in Table 6.4.

Cut	Value/description
Baseline muon	
Acceptance	$p_T > 10$ GeV, $ \eta < 2.7$
Impact parameter	$ z_0 \sin(\theta) \leq 0.5$ mm
Identification WP	Medium
Signal muon	
Acceptance	$p_T > 12$ GeV
Impact parameter	$ d_0/\sigma(d_0) < 3$
Identification WP	Medium
Isolation WP	FCTight_FixedRad
Object quality	Cosmic muon veto, bad muon event veto

Table 6.4: Summary of muon selection criteria. Signal criteria are applied on top of baseline criteria after overlap removal.

Photon selection

While photons are not used as signal objects in this analysis, they are used as input to the missing energy calculation. Photons have a minimum transverse momentum of 25 GeV and a maximum $|\eta|$ of 2.37, with a veto for photons that fall in the calorimeter crack region, corresponding to $|\eta|$ between 1.37 and 1.52. The **BADCLUSPHOTON** object quality criteria is required, as well as an author selection.

Jet selection

Baseline jets are used to calculate missing energy and as input to overlap removal. This analysis uses **EMTopo** jets reconstructed using the anti- k_T algorithm with maximum R of 0.4. They have a minimum transverse momentum of 20 GeV and an effective maximum $|\eta|$ requirement of 4.5. All baseline jets are used in E_T^{miss} calculation and overlap removal. Baseline jets identified as being pileup by the track-based jet vertex tagger (JVT) and forward jet vertex tagger (fJVT) are labeled but not vetoed, as they are needed in the missing energy calculation. JVT is calculated for jets with $p_T < 120$ GeV and $|\eta| < 2.5$, using the **Medium** JVT working point.

Signal jets have a tighter $|\eta|$ cut of 2.8, and the JVT-tagged jets (but not fJVT) are vetoed. Like muons, if any signal jets fail the **LooseBad** working point, the event is rejected.

Jets within $|\eta| < 2.5$ are tagged by dedicated algorithms to check if they are initiated by a b -quark. The tagging is performed on all baseline jets, for use in overlap removal, but only b -tagged jets which pass all signal criteria are used in the analysis. The b -tagging working point used in this analysis is **Fixed 85%** using the **MV2c10** b -tagging MVA variable.

All criteria for baseline and signal jets are summarized in Table 6.5.

Cut	Value/description
Baseline jet	
Acceptance	$p_T > 20$ GeV
Signal jet	
Acceptance	$ \eta < 2.8$
JVT	Medium ($p_T < 120$ GeV, $ \eta < 2.5$)
Object quality	LooseBad event veto
Signal b -jet	
Acceptance	$ \eta < 2.5$
b -tagger algorithm	MV2c10
b -tagging WP	Fixed 85%

Table 6.5: Summary of jet selection criteria. Signal criteria are applied on top of baseline criteria after overlap removal.

Missing energy

The missing transverse energy is calculated with the **Tight** working point, using all calibrated baseline objects in the event (electrons, muons, jets, and photons) as well as all tracks matched to the primary vertex not associated with these objects. Baseline jets are used only if they are tagged as originating from the hard scatter, using JVT.

Overlap removal

Overlaps in the reconstruction of electrons, muons, and jets are removed with a dedicated algorithm. All objects that are rejected by overlap removal are removed from further overlap removal steps, and from future consideration in the analysis. Overlap removal follows the steps in the order outlined here:

- Electrons that share a track with another higher- p_T electron are rejected.
- Electrons that share a track with a non-calorimeter-tagged muon are rejected.
- Jets that are not b -tagged, or that are b -tagged with $p_T > 100$ GeV, and are within $\Delta R(e, \text{jet}) \leq 0.2$ of an electron are rejected.
- Electrons that are within $\Delta R(e, \text{jet}) \leq 0.4$ of a jet are rejected.
- Jets that are not b -tagged, or that are b -tagged with $p_T > 100$ GeV, and are ghost-matched to a muon (or within $\Delta R(\mu, \text{jet}) \leq 0.2$) and which satisfy $n_{\text{track}} < 3$ are rejected.
- Muons that are within $\Delta R(\mu, \text{jet}) \leq 0.4$ of a jet are rejected.

The b -jet overlap removal is p_T -dependent to maintain high efficiency for high- p_T electrons and so high- p_T b -jets that are close to a lepton are rejected. For further details regarding this choice, see Appendix F.

6.4 Fake Factor Method

The **MC** modeling of fake and non-prompt leptons (collectively labeled “fakes”) tends to be poor, because it is difficult to properly model the rates at which each source leads to a fake lepton. Additionally, on the scale of hadronic interactions, the rate of a hadron being reconstructed as a lepton, and the rate of a non-prompt lepton from a hadronic decay or from a photon conversion meeting the selection criteria of a prompt lepton, are quite rare. However on the scale of **EWK**

interactions, this rate is non-negligible, so even small effects can give rise to fakes. For this reason it is advantageous for analyses with a sizable fake background contribution to estimate this background with a data-driven method. In this analysis, this is achieved by selecting a region of phase space that is enriched in fakes and deriving the number of predicted fake events from that, using collections of “ID” and “anti-ID” leptons, which are defined by the baseline and signal lepton requirements outlined in Section 6.3. ID (or “tight”) leptons are those which satisfy all the signal requirements, and anti-ID (or “loose”) leptons are those which satisfy all the baseline requirements and explicitly fail at least one of the signal requirements. We then use data events in a dedicated data sample to calculate the fake factor F , defined as

$$F = \frac{N_T}{N_L} \quad (6.2)$$

where N_T and N_L are the number of tight and loose leptons, respectively, in the measurement region. Once measured, the fake factors can be used to estimate the fake background, in the various analysis regions. For each region, a corresponding anti-ID region is defined with identical requirements, except at least one signal lepton is replaced with an anti-ID lepton. The number of events in the analysis region with one fake lepton can then be estimated with the following equation:

$$N_T^F = N_T - N_T^R = F(N_L - N_L^R). \quad (6.3)$$

The F and R superscripts correspond to the number of events with a fake and real lepton, respectively. So for example, N_T^F is the number of events with a signal lepton that is fake. F and N_L are measured in data, while N_L^R is determined from simulation and is subtracted so that processes which have real leptons in our fake measurement region are not included in the fake estimate. This procedure can be generalized to handle any number of fake leptons in an event, by adding more terms. Ultimately the equation used in our 3ℓ analysis to determine the number of events with at least one fake lepton N_T^F is:

$$\begin{aligned} N_T^F = N_{TTT} - N_{TTT}^{\text{RRR}} = & F_1(N_{LTT} - N_{LTT}^{\text{RRR}}) + F_2(N_{TLT} - N_{TLT}^{\text{RRR}}) + F_3(N_{TTL} - N_{TTL}^{\text{RRR}}) \\ & - F_1F_2(N_{LLT} - N_{LLT}^{\text{RRR}}) - F_1F_3(N_{LTL} - N_{LTL}^{\text{RRR}}) - F_2F_3(N_{TLL} - N_{TLL}^{\text{RRR}}) \\ & + F_1F_2F_3(N_{LLL} - N_{LLL}^{\text{RRR}}), \end{aligned} \quad (6.4)$$

where F_i is the factor for the i th lepton, ordered by p_T . Similarly, this equation can be extended for 4ℓ regions as well. In any case, the grand majority of events with a fake lepton have only one.

This prediction is known to depend on the kinematics of the lepton, so the actual fake factors are binned in the lepton’s p_T^{cone} , which is the sum of the p_T of the lepton and all tracks within its

isolation cone. The p_T^{cone} variable is used instead of p_T because this is found to better reconstruct the p_T of the underlying jet which often leads to the fake lepton. In general, $p_T \approx p_T^{\text{cone}}$ for ID leptons, because isolation requirements demand little activity near a signal lepton, but for anti-ID leptons, p_T^{cone} can be much larger than p_T . By binning the fake factor in p_T^{cone} rather than p_T , fake ID leptons originating from jets can be estimated using fake anti-ID leptons originating from jets with similar momenta.

The fake factors for this analysis are derived in a region dominated by Z/γ^* +jets events with fake leptons. Events in this region, which is referred to as CRZj, must have exactly three baseline leptons. Two of these leptons, known as the “tag” leptons, must also pass the signal lepton requirements and together form a Z boson candidate (SFOS pair with $|m_{\ell\ell} - m_Z| < 10$ GeV). Additionally, one of the two tag leptons must also fire a single lepton trigger and pass its associated offline p_T cut, as described in Section 6.3. The remaining baseline lepton, known as the “probe” lepton, is used for the fake factor measurement.

To increase the Z/γ^* +jets purity and reduce prompt contamination (mostly WZ), the fake factor measurement region requires $m_T^{\text{min}} < 30$ GeV and $E_T^{\text{miss}} < 30$ GeV. To reduce the number of $Z \rightarrow 4\ell$ events (with one lost lepton), a cut of $m_{3\ell} > 105$ GeV is applied. All selections used to define this Z/γ^* +jets fake factor measurement region are summarized in Table 6.6.

Three baseline leptons
SFOS pair of signal leptons with $ m_{\ell\ell} - m_Z < 10$ GeV,
with one lepton firing a single lepton trigger and its associated offline p_T cut.
$m_T^{\text{min}} < 30$ GeV
$E_T^{\text{miss}} < 30$ GeV
$m_{3\ell} > 105$ GeV

Table 6.6: Selection criteria used to define the Z/γ^* +jets dominated fake factor measurement region.

The p_T^{cone} -binned fake factors measured in this Z/γ^* +jets enriched region are shown in Figure 6.3. These are the fake factors used for all fake estimates used in this analysis. The fake factors are cutoff at 100 (50) GeV for electrons (muons) due to a lack of statistics above these values. Events with anti-ID leptons above the cutoff have the fake factor from the highest bin applied. The data and MC fake factors are not necessarily expected to agree, since the processes giving rise to fake leptons are not well modeled by the MC.

To ensure that the fake factor method provides an accurate fake estimate in the signal regions, it is validated in an intermediate E_T^{miss} region. This region is designed to be close to the SRs while maintaining Z/γ^* +jets purity. The definition of the fake factor validation region (VRZj) is

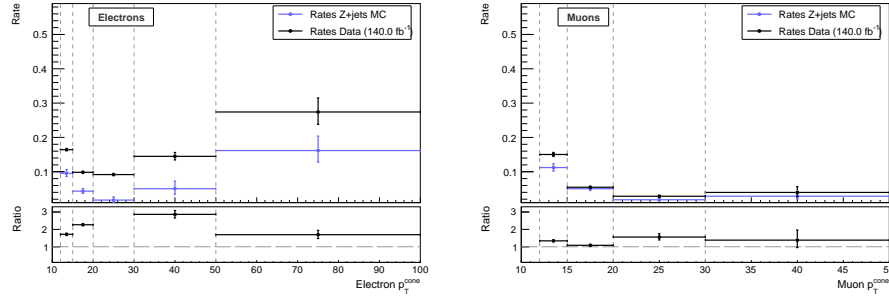


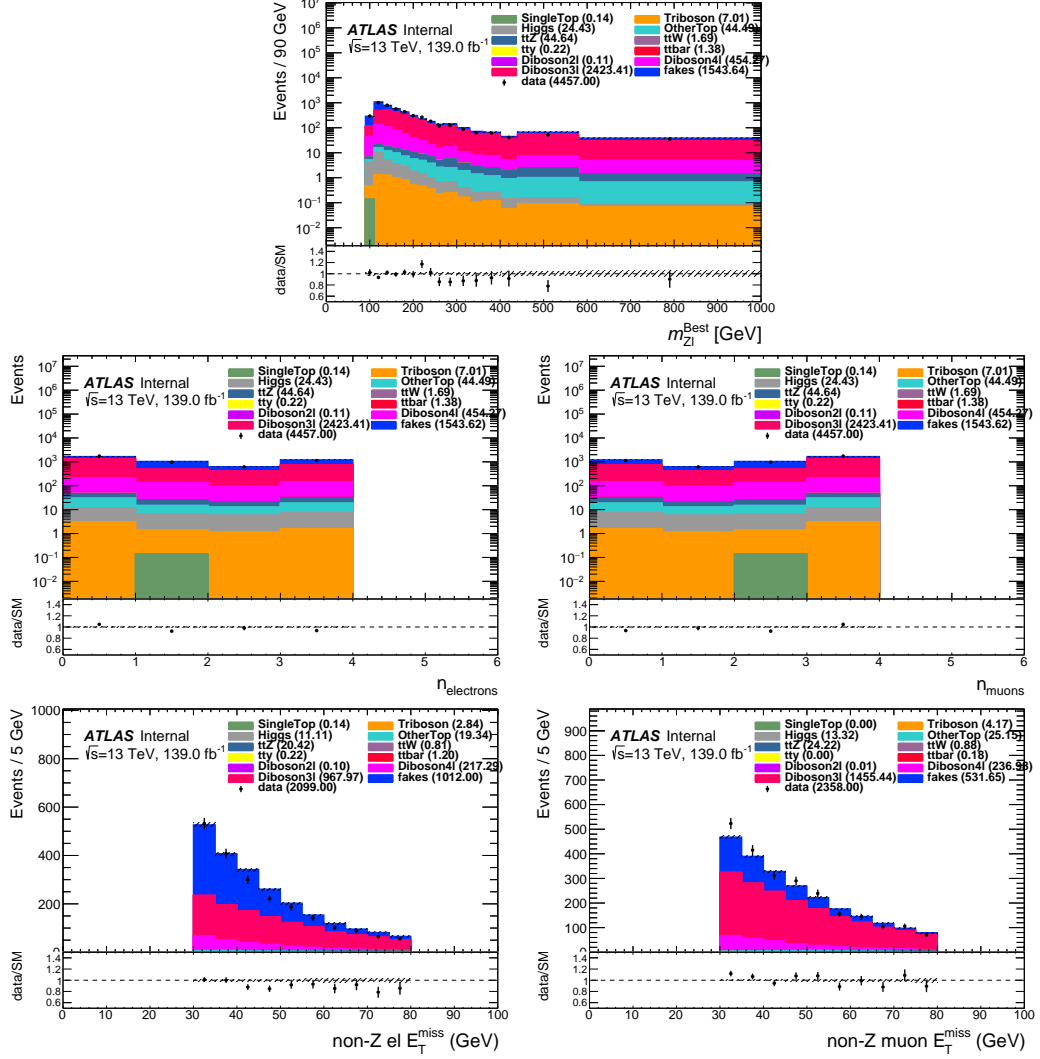
Figure 6.3: $Z/\gamma^*+\text{jets}$ fake factors for electrons (left) and muons (right), binned in p_T^{cone} .

summarized in Table 6.7. Figure 6.4 shows the data/SM agreement in VRZj in distributions of $m_{Z\ell}$, electron and muon multiplicity, and E_T^{miss} , where the latter is shown separately for fake electron and fake muon events. Good agreement is seen in all distributions so the fake estimate is performing well.

Exactly three signal leptons, no additional leptons
Same-flavor, opposite-sign pair of signal leptons with $ m_{\ell\ell} - m_Z < 10 \text{ GeV}$,
$m_T^{\text{min}} < 30 \text{ GeV}$
$30 < E_T^{\text{miss}} < 80 \text{ GeV}$

Table 6.7: Selection criteria used to define the $Z/\gamma^*+\text{jets}$ fake factor validation region.

While $Z/\gamma^*+\text{jets}$ is the largest contributor to the fake background, there are other sources as well, such as $t\bar{t}$ in 3ℓ regions and WZ in the 4ℓ regions. These are all estimated using the same fake factor. Any differences in fake factor which may arise due to these different sources are accounted for in systematic uncertainties, which will be described in Section 6.6. The relative contributions of each process to the total fake background in various analysis regions is shown in Table 6.8. Also shown is the fake background as a percent of the total background. These percentages are measured in MC.

Figure 6.4: Distributions of $m_{Z\ell}$, electron and muon multiplicity, and E_T^{miss} in VRZj.

fake process	CRWZ	VRMet	VRmTmin	CRttZ	VRttZ	SROL3l	SROL4l	SRTL
$Z/\gamma^* + \text{jets}/Z + \gamma$	74%	47%	63%	37%	23%	41%	22%	5%
WZ	-	-	-	-	-	-	45%	21%
ZZ	-	-	-	-	-	-	15%	19%
ttV	-	-	-	-	-	-	-	40%
top-like	20%	43%	28%	54%	69%	48%	3%	10%
tot. fake / tot. bkgd	4%	5%	8%	12%	11%	7%	5%	2%

Table 6.8: The relative contributions of each process to the fake and total background in various analysis regions. The “top-like” background includes $t\bar{t}$, single top, and WW . The ZZ regions are very pure in real ZZ events and are not included in the table.

6.5 Event Selection

Several regions of phase space are defined for use in this analysis. Signal regions (SRs) are the search regions, and are designed to have high signal-to-background ratios. There is one SR for events with 3 leptons, with only one leg reconstructed (SROL3 ℓ). There are two SRs for events with 4 leptons, one with only one leg reconstructed (SROL4 ℓ) and one with both legs fully reconstructed (SRTL). Additional kinematic requirements are applied in all SRs to reduce background contributions. These cuts were chosen to optimize the Z_N of signal as calculated with `RooStats::NumberCountingUtils::BinomialObsZ()`, for mass points 300 GeV and above, while still maintaining enough background events so as not to be statistics-limited. Control regions (CRs) are designed to isolate individual background processes from one another and from signal, and are used to constrain the estimate of the targeted process, in order to extrapolate this estimate to the SR. Validation regions (VRs) are kinematically between the CRs and SRs, and are used to validate the extrapolation between CRs and SRs. These regions are also constructed to have small signal yields. The CRs and VRs are split into 3 ℓ and $\geq 4\ell$ categories, with the exception of the $t\bar{t}Z$ regions which require $\geq 3\ell$ leptons.

The optimization of the CR and VR definitions targets a signal contamination of less than 5% from a given mass point, and background purity of at least 70%, to ensure a clean region to estimate the targeted SM process. However there is a caveat on the signal contamination requirements, in that the lowest mass points considered in this analysis, which have very similar kinematics as background processes, are allowed to have more sizable contamination in the CRs and VRs. The justification for this caveat is that the expected sensitivities for these low mass signals are very large. Even if a low mass signal appears in real data and has some non-negligible yield in a CR, the resultant overestimate of background processes in the SRs will not reduce the sensitivity enough to mask the signal. This is quantified in Appendix G. Therefore the analysis regions have not been tuned to reduce the contamination of these points so as to not negatively impact the sensitivity towards higher mass points.

The various regions and the variables they use are defined in the following sections and summarized in Table 6.9. The detailed studies that went into these region definitions are described in Appendices H and I, and an overview is given in the following two sections. All regions require three light leptons, two of which are SFOS and which have an invariant mass between 81.2 GeV and 101.2 GeV. Additionally, each region requires $m_{Z\ell} > 90$ GeV, to avoid the selection of soft leptons from i.e. $Z \rightarrow \ell\ell\ell$. Table 6.10 shows the expected yields in each SR, and Table 6.11 shows the ex-

pected yields in each CR and VR, compared to two signal mass points with equal wino BR to each boson and lepton flavor. The signal contamination in the CRs and VRs meets the requirements outlined above. The lowest few mass points (< 200 GeV) do have significant contamination especially in VRZZ and VRttZ, but the sensitivity is so large for these mass points that the contamination is not concerning.

Region	N_{lep}	$N_{b\text{-jet}}$	$\Delta R(b, b)^\dagger$	$E_{\text{T}}^{\text{miss}}$ [GeV]	$m_{\text{T}}^{\text{min}}$ [GeV]	Second boson	$4\ell 2Z$; $ m_{\ell\ell,2} - m_Z $ [GeV]	$m_{Z\ell}$ asymmetry
SROL3ℓ	≥ 3	-	< 1.5	> 150	> 125	-	-	-
CRWZ	≥ 3	-	< 1.5	< 80	[50,100]	-	-	-
VRMet	≥ 3	-	< 1.5	> 80	< 100	-	-	-
VRmTmin	≥ 3	-	< 1.5	< 80	> 125	-	-	-
CRZj	≥ 3	-	< 1.5	< 30	< 30	-	-	-
VRZj	≥ 3	-	< 1.5	[30,80]	< 30	-	-	-
CRttZ	≥ 3	≥ 2	> 2.5	> 40	-	-	veto; < 20	-
VRttZ	≥ 3	≥ 2	[1.5,2.5]	> 40	-	-	veto; < 20	-
SROL4ℓ	≥ 4	-	< 1.5	$> 80^*$	-	No	veto; < 20	-
SRTL	≥ 4	-	< 1.5	-	-	Yes	veto; < 20	< 0.1
CRZZ	≥ 4	-	< 1.5	-	-	-	require; < 5	-
VRZZ	≥ 4	-	< 1.5	-	-	-	require; [5,20]	-

Table 6.9: Kinematic selections for each region used in this analysis. The signal regions are emphasized with boldface. All regions require a SFOS pair of light leptons with an invariant mass between 81.2 GeV and 101.2 GeV and a third light lepton, the invariant mass of which ($m_{Z\ell}$) must be at least 90 GeV. The dagger (\dagger) indicates that this cut is only applied for events with at least 2 b -jets. The “second boson” requirement is shown to make the orthogonality between SROL4 ℓ and SRTL explicit. This second boson is usually reconstructed from two jets, but it can also be reconstructed from a SFOS lepton pair, with an invariant mass requirement that changes depending on the objects used, as described in Section 6.1. This is distinct from the $4\ell 2Z$ criterion which only applies to a leptonic Z . The asterisk (*) in the SROL4 ℓ $E_{\text{T}}^{\text{miss}}$ cut indicates that this cut is only applied for events with two pairs of SF leptons. This condition is also referred to as $E_{\text{T}}^{\text{miss,SF}}$.

6.5.1 3L regions

The major background in the 3 ℓ region is Diboson3 ℓ (which is usually WZ), an irreducible background which has a dedicated CR (CRWZ) and two dedicated VRs (VRMet and VRmTmin), each designed to validate the extrapolation of one variable used to separate CRWZ from SROL3 ℓ . All selections in SROL3 ℓ are designed to reduce both Diboson3 ℓ and fake backgrounds.

Selection requirements are applied to the following kinematic observables:

- $E_{\text{T}}^{\text{miss}}$. As explained in Section 6.1, many C1C1 and C1N1 final states which are targeted in SROL3 ℓ have missing energy from undetected neutrinos. In contrast, no significant $E_{\text{T}}^{\text{miss}}$ is expected in $Z/\gamma^* + \text{jets}$. A lower $E_{\text{T}}^{\text{miss}}$ cut of 150 GeV is applied in SROL3 ℓ , and an upper cut

	SROL3l	SROL4l	SRTL
$m_{\tilde{\chi}_1^\pm}=120$ GeV	136.98	824.81	384.02
$m_{\tilde{\chi}_1^\pm}=300$ GeV	41.32	47.97	37.11
MC exp. SM events	49.64	73.12	35.52
MC exp. Diboson3l events	31.49	0.40	0.05
MC exp. Diboson4l events	0.80	18.49	18.06
MC exp. ttZ events	6.72	15.58	11.02
MC exp. Triboson events	4.27	13.93	1.41
MC exp. Higgs events	0.47	13.84	2.79
MC exp. Fakes events	2.05	4.07	0.20
MC exp. Other events	3.79	6.76	2.00

Table 6.10: Expected pre-fit yields for all SM backgrounds and C1C1 for two benchmark mass points, in all SRs, for an integrated luminosity of 139.0 fb^{-1} .

	CRWZ	CRZZ	CRttZ	VRMet	VRmTmin	VRZZ	VRttZ
$m_{\tilde{\chi}_1^\pm}=120$ GeV	1758.88	69.60	23.54	634.17	71.93	214.39	28.63
$m_{\tilde{\chi}_1^\pm}=300$ GeV	30.40	1.77	5.51	38.54	14.58	4.38	8.84
MC exp. SM events	11131.27	1087.74	322.30	4548.60	298.04	625.84	211.40
MC exp. Diboson3l events	9769.73	0.00	57.28	3935.20	229.50	0.00	37.56
MC exp. Diboson4l events	694.55	1078.29	6.07	129.12	31.41	614.33	3.16
MC exp. ttZ events	103.98	1.20	178.52	149.67	7.11	4.56	119.09
MC exp. Triboson events	19.69	1.75	0.46	19.76	1.94	2.45	0.18
MC exp. Higgs events	31.61	0.15	5.79	26.60	0.58	0.75	3.93
MC exp. Fakes events	385.93	6.03	22.50	159.32	21.34	2.26	11.81
MC exp. Other events	125.77	0.33	51.67	128.91	6.15	1.50	35.66

Table 6.11: Expected pre-fit yields for all SM backgrounds and C1C1 for two benchmark mass points, in all CRs and VRs, for an integrated luminosity of 139.0 fb^{-1} .

of 80 GeV is applied in VRZj and CRWZ. VRMet validates the extrapolation in this variable between CRWZ and SROL3 ℓ .

- m_T^{\min} . The standard definition of transverse mass (m_T) when trying to reconstruct the W mass is

$$m_T(\ell, \nu) = \sqrt{2p_T^\ell E_T^{\text{miss}} [1 - \cos(\phi_\ell - \phi_{\text{miss}})]} \quad (6.5)$$

which should have a kinematic edge at the W mass of 80.4 GeV. In 3ℓ final states, where the assumed process is WZ , the lepton used in this equation is traditionally the one which was not already assigned to the Z . For signal, the leptonic Z reconstruction efficiency is high

(> 95%). However the same is not necessarily true for **SM** WZ , since the Z can be off-shell and a selection which minimizes $|m_{\ell\ell} - m_Z|$ may not choose the correct leptons. For this reason m_T^{\min} was introduced by an earlier 3ℓ search [189]. This definition does not automatically use the lepton left over from the Z , but rather calculates m_T for all available leptons which still leave a **SFOS** pair, and selects the minimum of these m_T calculations. A comparison of m_T and m_T^{\min} is shown in Figure H.5 (in Appendix H). Here it is clear that for signal, m_T and m_T^{\min} are often the same quantity, which is expected because of the high efficiency of selecting the leptons from the Z . Meanwhile in the background distributions, m_T^{\min} is often much lower than m_T , and is more consistent with the kinematic edge at the W mass. Because of the downward shift in background which is not present in signal, m_T^{\min} performs better as a discriminating variable than m_T . A lower m_T^{\min} cut of 125 GeV is applied in SROL3 ℓ , an upper cut of 30 GeV is applied in VRZj, and a range of [50,100] GeV is required in CRWZ. VRmTmin validates the extrapolation in this variable between CRWZ and SROL3 ℓ .

- $dR(b_0, b_1)$, the angular separation between the two hardest b -jets in an event. An upper cut of $dR(b_0, b_1) < 1.5$ is required in all regions with exactly 3 leptons, to impose orthogonality with $t\bar{t}Z$ regions which will be described in Section 6.5.2. This requirement is only applied to events with at least two b -jets.

The expected distributions of E_T^{miss} , m_T^{\min} , and $dR(b_0, b_1)$ in SROL3 ℓ are shown in Figure 6.5 before the corresponding cut is applied (commonly referred to as N-1 plots). The $m_{Z\ell}$ distribution in SROL3 ℓ is shown after these cuts in Figure 6.6.

The N-1 distributions of E_T^{miss} , m_T^{\min} , and $dR(b_0, b_1)$ are shown in Figure 6.7 for CRWZ, Figure 6.9 for VRMet, and Figure 6.11 for VRmTmin. The expected $m_{Z\ell}$ distribution after these cuts is shown in Figure 6.8 for CRWZ, Figure 6.10 for VRMet, and Figure 6.12 for VRmTmin.

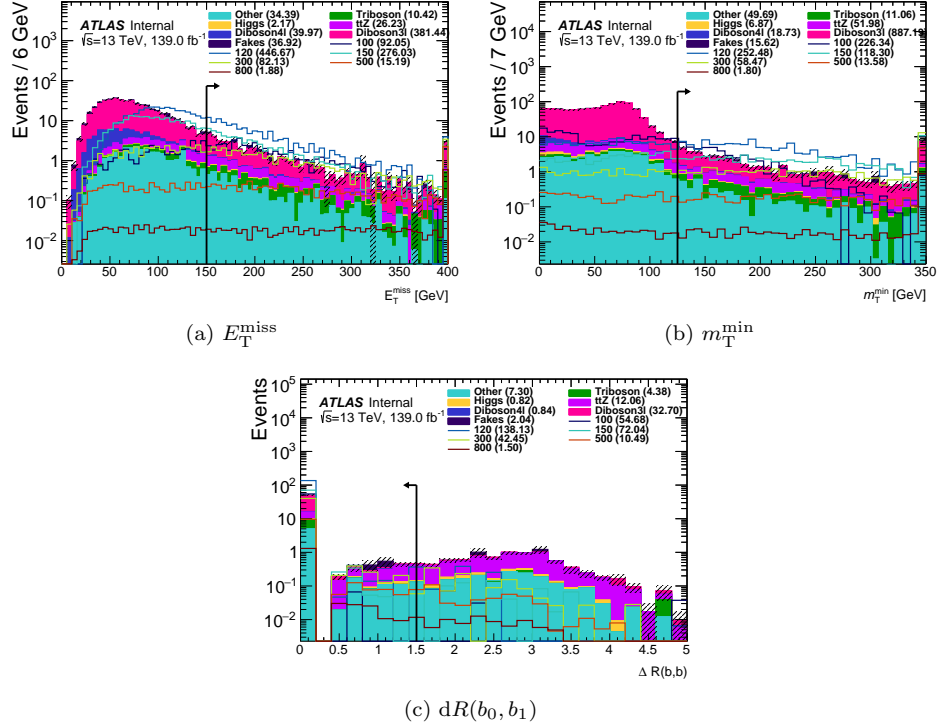


Figure 6.5: Expected distributions of E_T^{miss} (a), m_T^{min} (b), and $dR(b_0, b_1)$ (c) in SROL3 ℓ , before the corresponding cut is applied (N-1 plots). The entries in the 0 bin of the $dR(b_0, b_1)$ distribution correspond to events with < 2 b -jets. Uncertainties are statistical only.

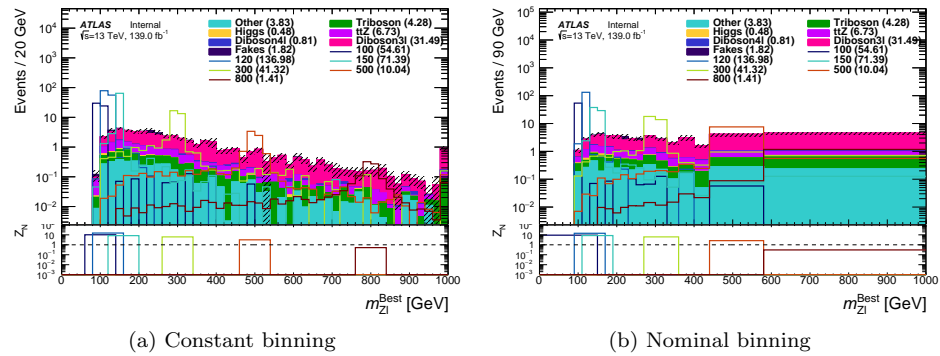


Figure 6.6: $m_{Z\ell}$ after m_T^{min} , E_T^{miss} and $dR(b_0, b_1)$ cuts in SROL3 ℓ , with constant bin widths (a) and the nominal binning used in exclusion and discovery fits (b). Lower panel: Estimated sensitivity for each mass point obtained with a 30 GeV window around the true gaugino mass, with a flat 20% uncertainty, as calculated with `RooStats::NumberCountingUtils::BinomialObsZ()`. Uncertainties are statistical only.

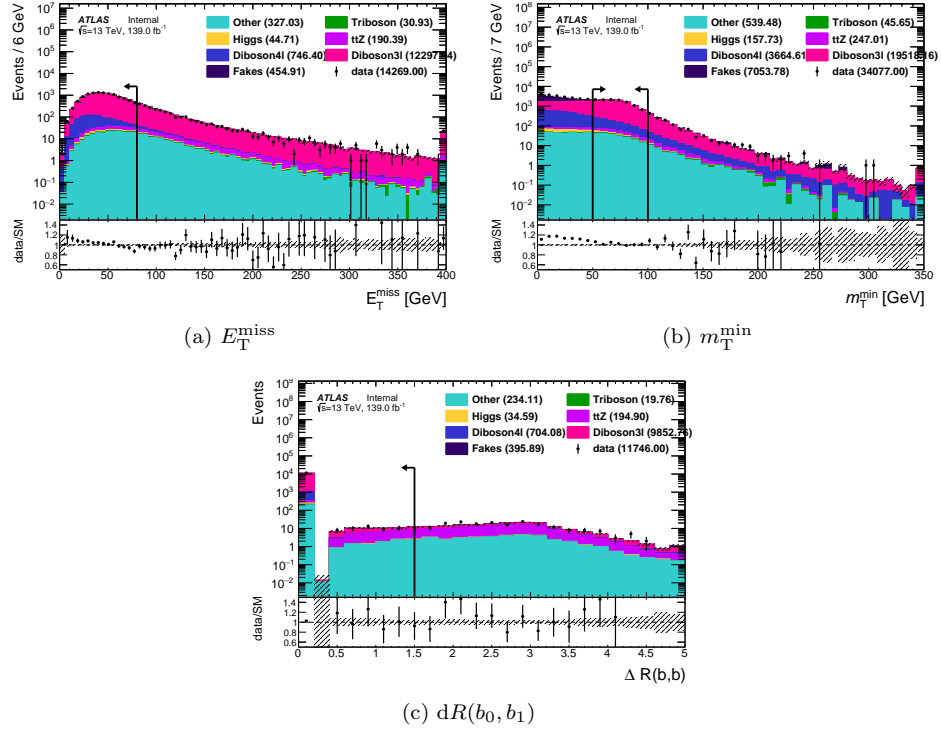


Figure 6.7: Expected distributions of E_T^{miss} (a), m_T^{min} (b), and $dR(b_0, b_1)$ (c) in CRWZ, before the corresponding cut is applied (N-1 plots). The entries in the 0 bin of the $dR(b_0, b_1)$ distribution correspond to events with < 2 b -jets. Uncertainties are statistical only.

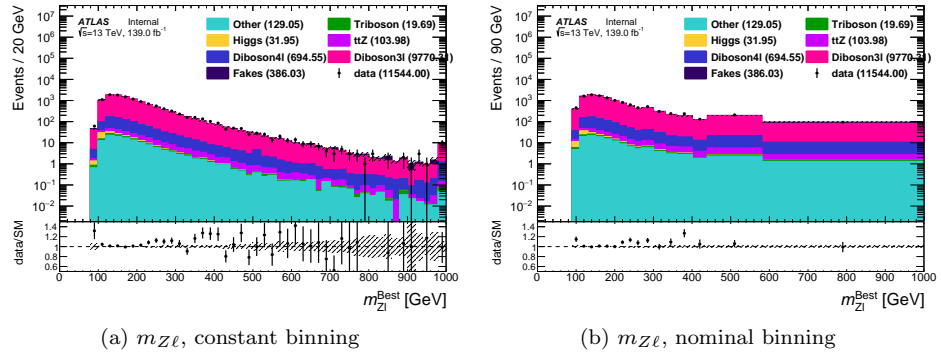


Figure 6.8: Data-MC comparisons of $m_{Z\ell}$ with constant bin widths (a) and the nominal binning used in exclusion and discovery fits (b) in CRWZ. The plots are shown before the background is normalized to the data. Uncertainties are statistical only.

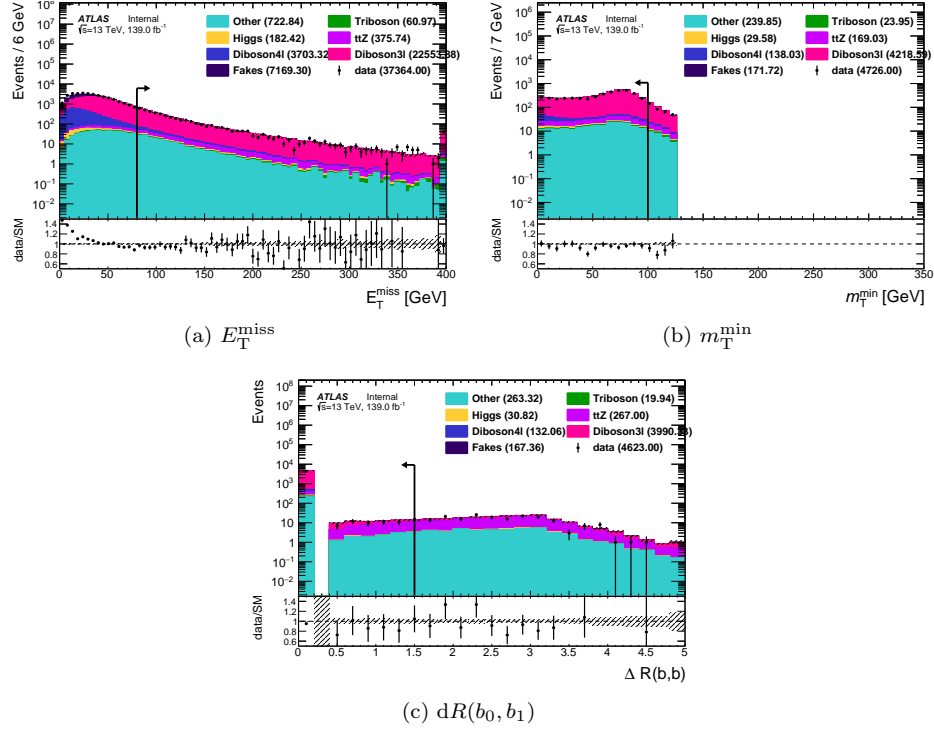


Figure 6.9: Expected distributions of E_T^{miss} (a), m_T^{min} (b), and $dR(b_0, b_1)$ (c) in VRMet, before the corresponding cut is applied (N-1 plots). The m_T^{min} distribution is cut off at 125 GeV to maintain orthogonality with SROL3 ℓ . The entries in the 0 bin of the $dR(b_0, b_1)$ distribution correspond to events with < 2 b -jets. Uncertainties are statistical only.

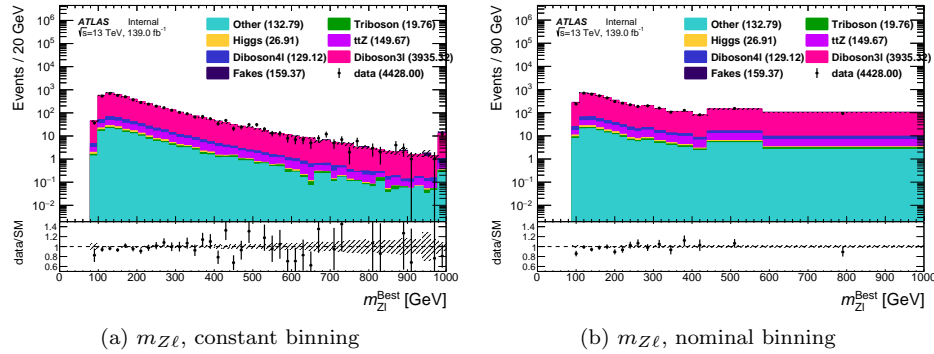


Figure 6.10: Data-MC comparisons of $m_{Z\ell}$ with constant bin widths (a) and the nominal binning used in exclusion and discovery fits (b) in VRMet. The plots are shown before the background is normalized to the data. Uncertainties are statistical only.

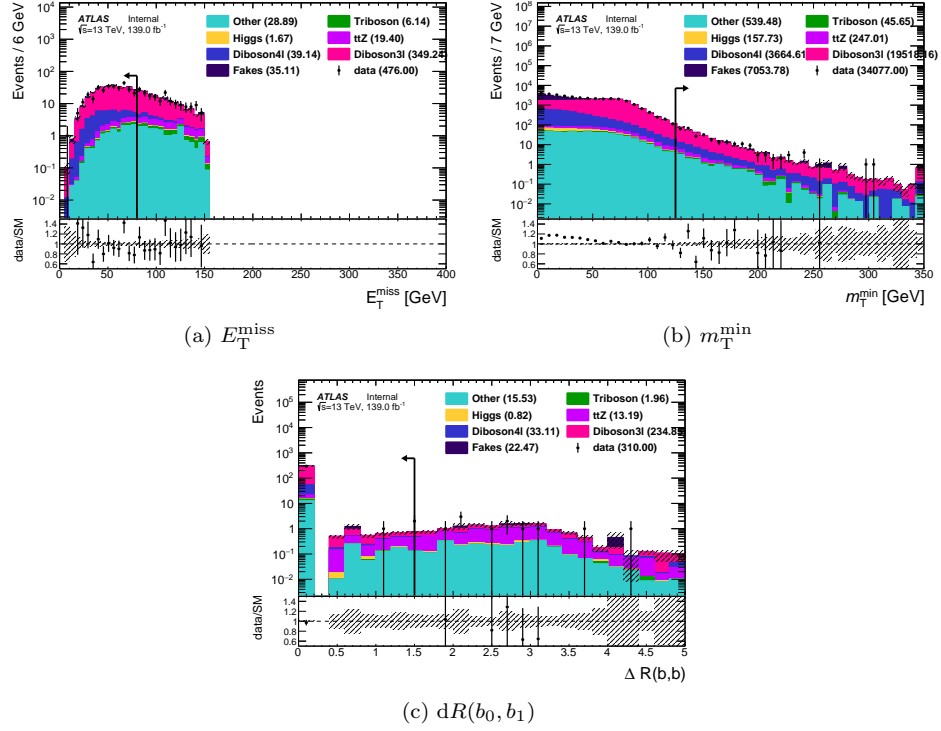


Figure 6.11: Expected distributions of E_T^{miss} (a), m_T^{min} (b), and $dR(b_0, b_1)$ (c) in VRmTmin, before the corresponding cut is applied (N-1 plots). The E_T^{miss} distribution is cut off at 150 GeV to maintain orthogonality with SROL3 ℓ . The entries in the 0 bin of the $dR(b_0, b_1)$ distribution correspond to events with < 2 b -jets.

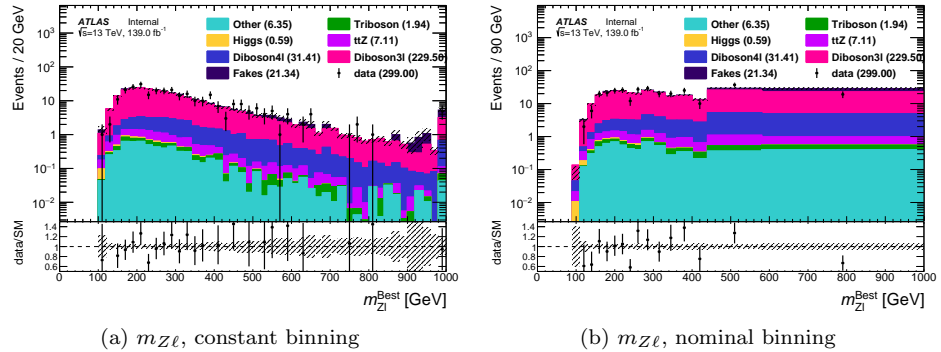


Figure 6.12: Data-MC comparisons of $m_{Z\ell}$ with constant bin widths (a) and the nominal binning used in exclusion and discovery fits (b) in VRmTmin. The plots are shown before the background is normalized to the data.

6.5.2 4L regions

Diboson 4ℓ (predominantly ZZ) is the dominant background in both SROL 4ℓ and SRTL. $t\bar{t}Z$ also contributes a significant amount in SRTL. All selections in these SRs are designed to reduce these backgrounds, and dedicated CRs and VRs are also created to normalize them and validate these normalizations.

Selection requirements are applied to the following kinematic observables in all regions with 4 or more leptons:

- The $4\ell 2Z$ criterion. This is applied to events with exactly 4 leptons and 2 pairs of SFOS leptons with invariant mass requirements described below. It is designed to separate ZZ events from other processes; it is applied as a selection in the ZZ control and validation regions (defined below) and as a veto in all other regions. One SFOS pair is required to be within 10 GeV of the Z mass, as per the Preselection requirements described at the start of this chapter. The mass requirement on the second SFOS pair varies for each region. Several mass windows were tested for the second Z candidate requirement, which is labeled $m_{\ell\ell,2}$; more details on these studies can be found in Appendix I. In CRZZ, $m_{\ell\ell,2}$ must be within 5 GeV of the Z mass, to preserve good purity in this region. Because the second Z candidate is by definition farther from the Z mass than the first, the 5 GeV requirement is indirectly imposed on the first Z candidate as well. In VRZZ, to maintain orthogonality with CRZZ, $m_{\ell\ell,2}$ is required to be between 5 and 20 GeV away from the Z mass, i.e. either between 71.2 and 86.2 GeV, or between 96.2 and 111.2 GeV. In all other regions, the $m_{\ell\ell}$ window for the second Z candidate is extended to 20 GeV around the Z mass, to maximize the amount of ZZ rejected.
- $dR(b_0, b_1)$, the angular separation between the leading and subleading b -jet in the event. This cut is introduced to improve purity in the $t\bar{t}Z$ CR, and is designed to reject events with b -jets from Higgs decays, which tend to be more collimated than b -jets from $t\bar{t}$ decays. A cut of $dR(b_0, b_1) > 2.5$ is chosen to optimize $t\bar{t}Z$ purity and statistics in the region. To achieve orthogonality, in VR $t\bar{t}Z$ a window of $1.5 < dR(b_0, b_1) < 2.5$ is chosen, and in all other regions $dR(b_0, b_1) < 1.5$ is imposed.

Some additional selection criteria are applied to individual regions as described below.

As in SROL 3ℓ , many of the targeted final states in SROL 4ℓ have missing energy from undetected neutrinos, whereas no significant E_T^{miss} is expected in ZZ , the largest background in this region even after the $4\ell 2Z$ rejection. To directly target ZZ and reduce the number of signal events rejected, a

cut on E_T^{miss} is applied only for events with two SF lepton pairs. This requirement is henceforth referred to as $E_T^{\text{miss,SF}}$. The expected distributions of $E_T^{\text{miss,SF}}$, $m_{\ell\ell,2}$, and $dR(b_0, b_1)$ in SROL4 ℓ are shown in Figure 6.13 before the corresponding cut is applied (commonly referred to as N-1 plots). The $m_{Z\ell}$ distribution in SROL4 ℓ is shown after these cuts in Figure 6.14.

For SRTL, the signal is fully reconstructed and E_T^{miss} thus provides little discrimination. However, in SRTL the $m_{Z\ell}$ asymmetry which was defined in Equation 6.1 can be calculated and provides excellent discrimination against backgrounds. The $m_{Z\ell}$ asymmetry is peaked at small values for signal and is flat for backgrounds. The expected distributions of $m_{Z\ell}$ asymmetry, $m_{\ell\ell,2}$, and $dR(b_0, b_1)$ in SRTL are shown in Figure 6.15 before the corresponding cut is applied (commonly referred to as N-1 plots). The $m_{Z\ell}$ distribution in SRTL is shown after these cuts in Figure 6.16.

The CRZZ and VRZZ require exactly 4 leptons which satisfy the 4 ℓ 2Z criterion. The expected $dR(b_0, b_1)$ distribution, before the cut on this variable, is shown in Figure 6.17 for CRZZ and in Figure 6.19 for VRZZ. The expected $m_{Z\ell}$ distribution after all cuts is shown in Figure 6.18 for CRZZ and in Figure 6.20 for VRZZ.

In CRttZ and VRttZ, at least 2 b -jets are required. A cut of $E_T^{\text{miss}} \geq 40$ GeV is also required to increase purity against $Z/\gamma^* + \text{jets}$. The N-1 distributions of E_T^{miss} , $m_{\ell\ell,2}$, and b -jet multiplicity are shown in Figure 6.21 for CRttZ and in Figure 6.23 for VRttZ. The expected $m_{Z\ell}$ distribution after all cuts is shown in Figure 6.22 for CRttZ and in Figure 6.24 for VRttZ.

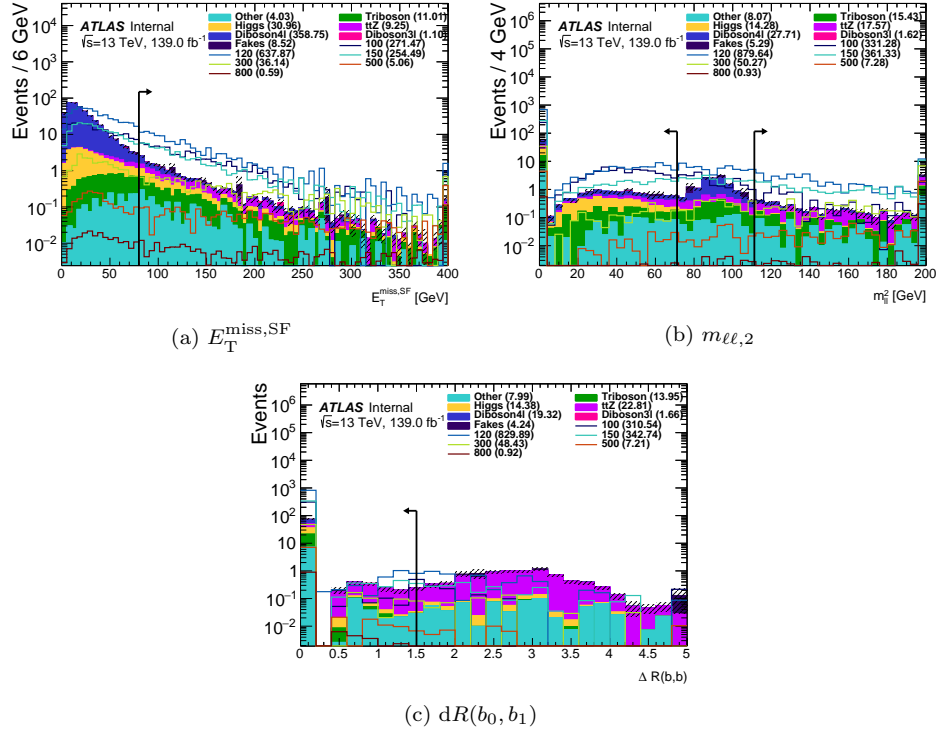


Figure 6.13: Expected distributions of $E_T^{\text{miss,SF}}$ (a), $m_{\ell\ell,2}$ (b), and $dR(b_0, b_1)$ (c) in SROL4 ℓ , before the corresponding cut is applied (N-1 plots). The entries in the 0 bin of the $dR(b_0, b_1)$ distribution correspond to events with < 2 b -jets. Uncertainties are statistical only.

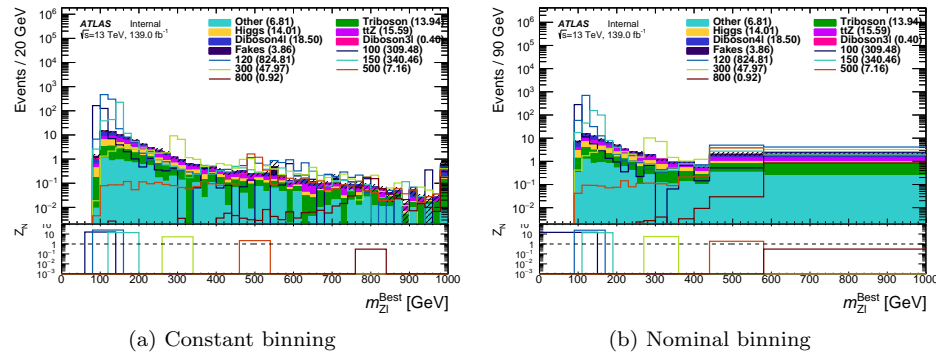


Figure 6.14: $m_{Z\ell}$ after $4\ell 2Z$, $E_T^{\text{miss,SF}}$ and $dR(b_0, b_1)$ cuts in SROL4 ℓ , with constant bin widths (a) and the nominal binning used in exclusion and discovery fits (b). Lower panel: Estimated sensitivity for each mass point obtained with a 40 GeV window around the true gaugino mass, with a flat 20% uncertainty, as calculated with `RooStats::NumberCountingUtils::BinomialObsZ()`. Uncertainties are statistical only.

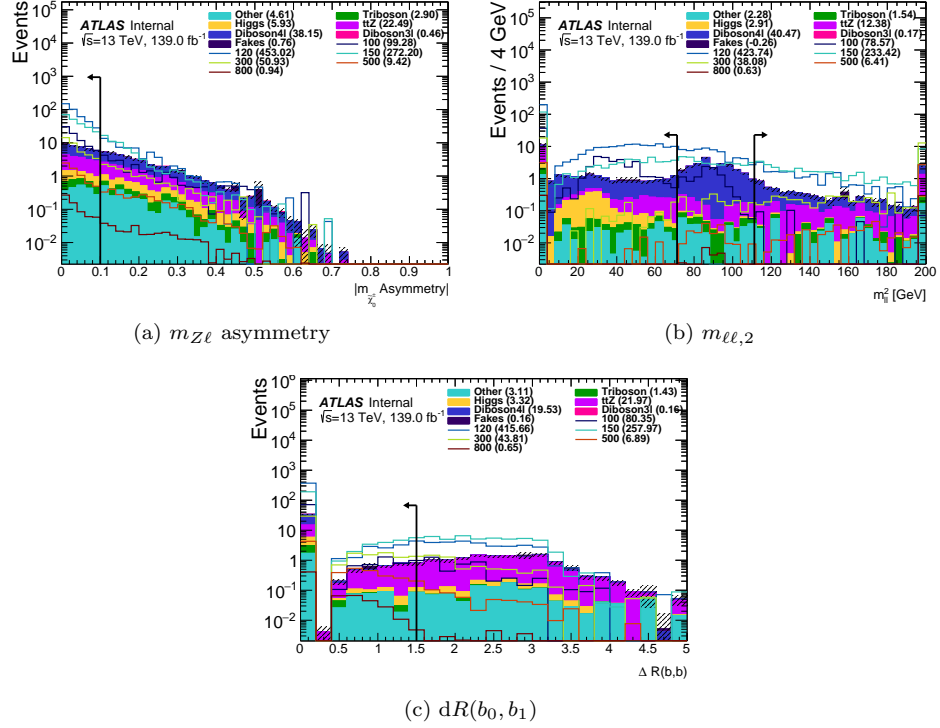


Figure 6.15: Expected distributions of $m_{Z\ell}$ asymmetry (a), $m_{\ell\ell,2}$ (b), and $dR(b_0, b_1)$ (c) in SRTL, before the corresponding cut is applied (N-1 plots). The entries in the 0 bin of the $dR(b_0, b_1)$ distribution correspond to events with < 2 b-jets. Uncertainties are statistical only.

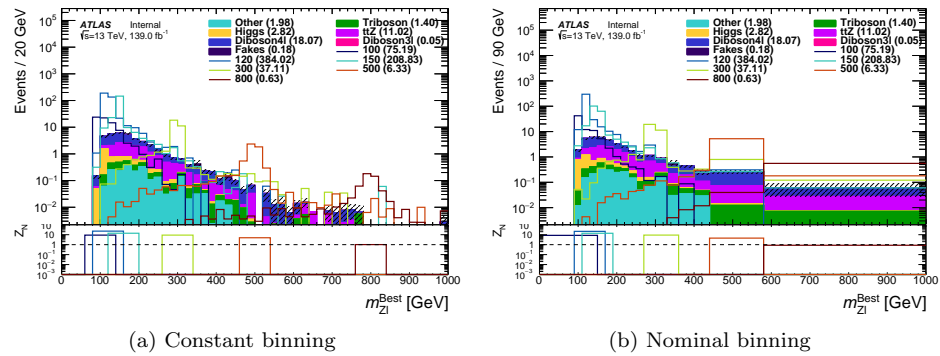


Figure 6.16: $m_{Z\ell}$ after $4\ell 2Z$, $m_{Z\ell}$ asymmetry and $dR(b_0, b_1)$ cuts in SRTL, with constant bin widths (a) and the nominal binning used in exclusion and discovery fits (b). Lower panel: Estimated sensitivity for each mass point obtained with a 40 GeV window around the true gaugino mass, with a flat 20% uncertainty, as calculated with `RooStats::NumberCountingUtils::BinomialObsZ()`. Uncertainties are statistical only.

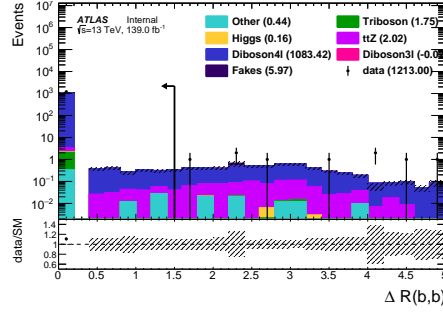


Figure 6.17: Expected $dR(b_0, b_1)$ distribution in CRZZ, before the corresponding cut is applied (N-1 plots). The entries in the 0 bin of the $dR(b_0, b_1)$ distribution correspond to events with < 2 b -jets. Uncertainties are statistical only.

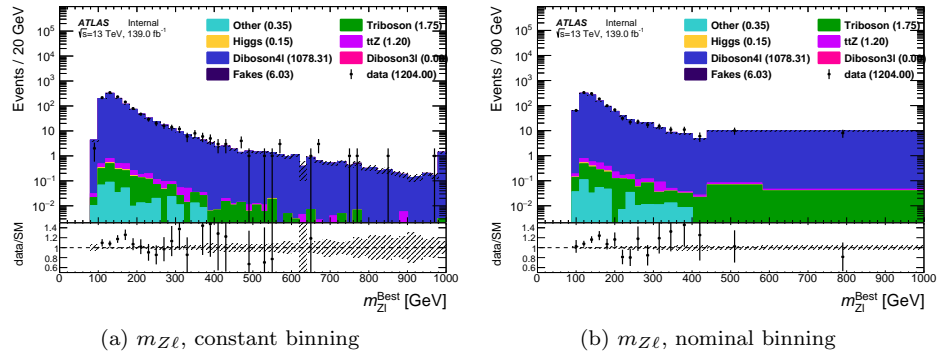


Figure 6.18: Data-MC comparisons of $m_{Z\ell}$ with constant bin widths (a) and the nominal binning used in exclusion and discovery fits (b) in CRZZ. The plots are shown before the background is normalized to the data. Uncertainties are statistical only.

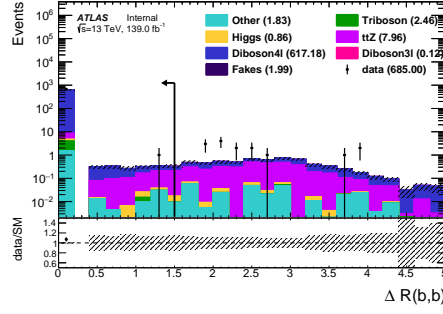


Figure 6.19: Expected $dR(b_0, b_1)$ distribution in VRZZ, before the corresponding cut is applied (N-1 plots). The entries in the 0 bin of the $dR(b_0, b_1)$ distribution correspond to events with < 2 b -jets.

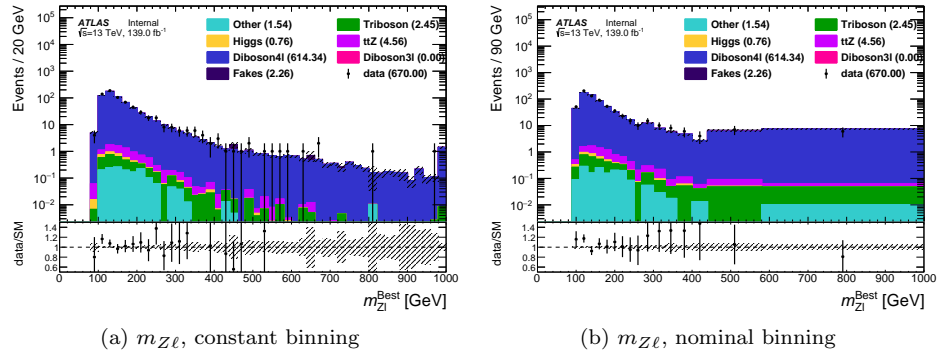


Figure 6.20: Data-MC comparisons of $m_{Z\ell}$ with constant bin widths (a) and the nominal binning used in exclusion and discovery fits (b) in VRZZ. The plots are shown before the background is normalized to the data.

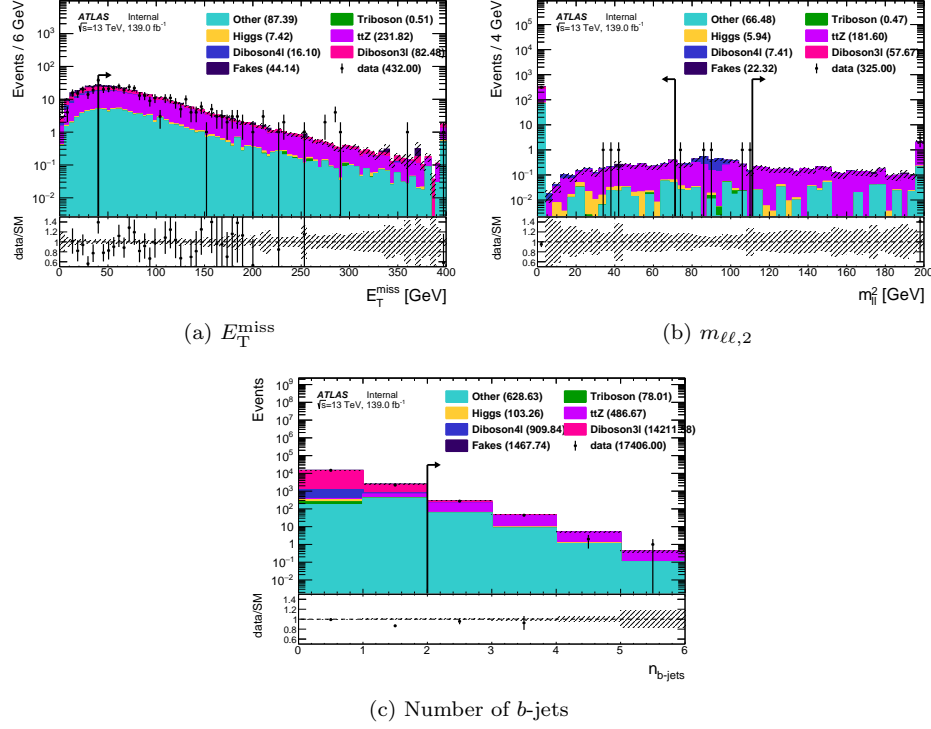


Figure 6.21: Expected distributions of E_T^{miss} (a), $m_{\ell\ell,2}$ (b) and b -jet multiplicity (c) in CRttZ, before the corresponding cut is applied (N-1 plots). Uncertainties are statistical only.

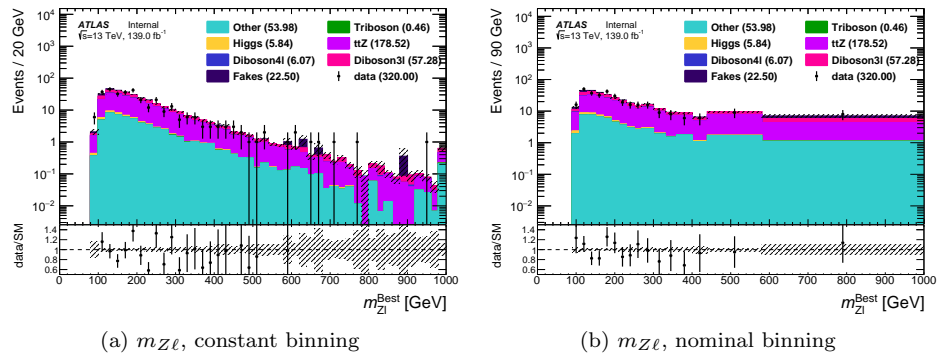


Figure 6.22: Data-MC comparisons of $m_{Z\ell}$ with constant bin widths (a) and the nominal binning used in exclusion and discovery fits (b) in CRttZ. The plots are shown before the background is normalized to the data. Uncertainties are statistical only.

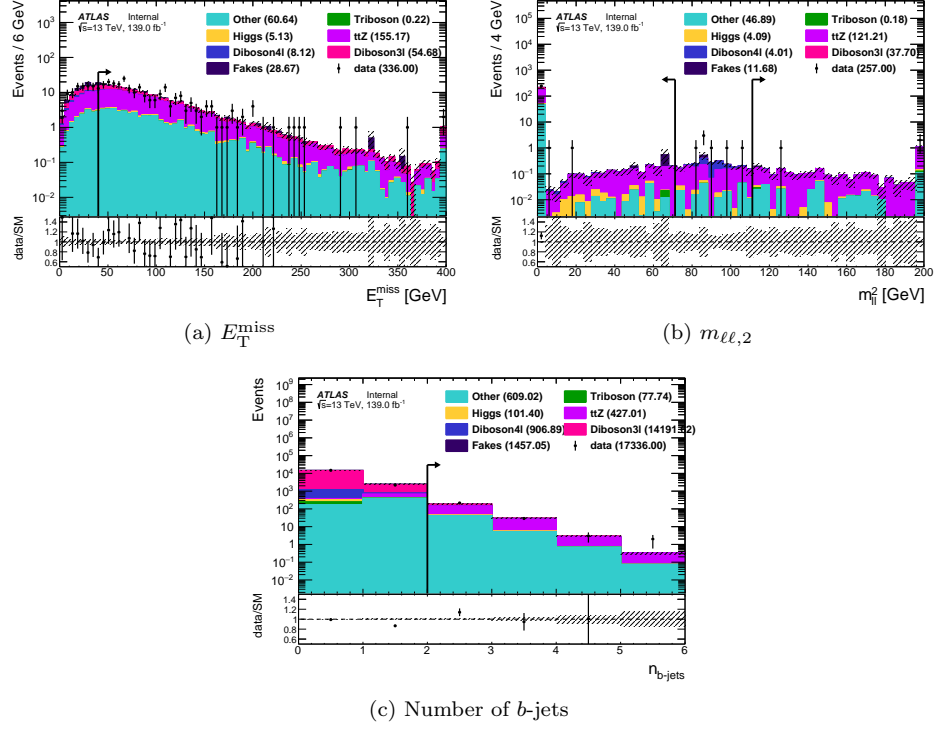


Figure 6.23: Expected distributions of E_T^{miss} (a), $m_{\ell\ell,2}$ (b) and b -jet multiplicity (c) in VRttZ, before the corresponding cut is applied (N-1 plots). Uncertainties are statistical only.

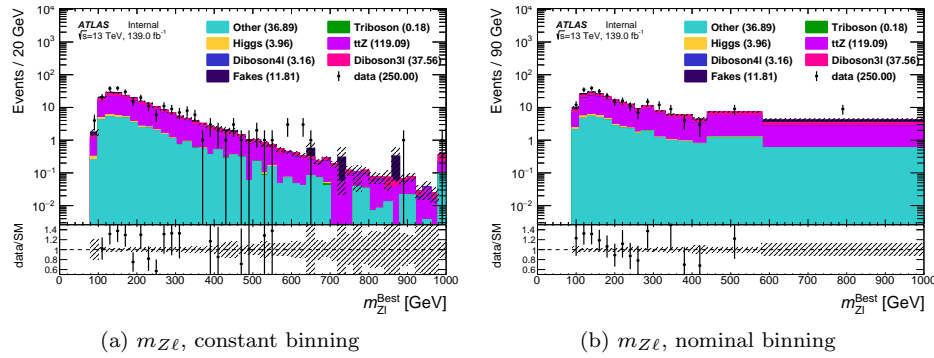


Figure 6.24: Data-MC comparisons of $m_{Z\ell}$ with constant bin widths (a) and the nominal binning used in exclusion and discovery fits (b) in VRttZ. The plots are shown before the background is normalized to the data. Uncertainties are statistical only.

6.6 Systematic Uncertainties

Systematic uncertainties are applied to the signal and background predictions to account for experimental and theoretical sources. The dominant uncertainties in each SR are shown in Tables 6.12 and 6.14. These tables are still currently missing the theory systematics as well as most fake systematics, which will be described below.

Experimental uncertainties reflect the limited precision of our object measurements, typically affecting energy scales and resolutions, or the measured efficiency of object selection criteria such as lepton identification or reconstruction. The dominant uncertainties are related to E_T^{miss} and jets, including jet energy scale and resolution [144, 145] and the calibration of the b -tagging efficiency for b -jets, c -jets, and light-flavor jets [142], as well as the pileup-tagging efficiency. The experimental uncertainties associated with leptons include uncertainties in the energy scale and resolution of electrons [135] and muons [136], and the calibration of the lepton trigger, identification, reconstruction, and isolation efficiencies. As all physics objects are propagated through the E_T^{miss} calculation, a new E_T^{miss} is derived for each systematic variation. Dedicated uncertainties on the E_T^{miss} soft term are also derived [190]. The 1.7% uncertainty in the measured integrated luminosity is derived following a methodology similar to that detailed in Ref. [106], and using the LUCID-2 detector for the baseline luminosity measurements [191], from calibration of the luminosity scale using x-y beam-separation scans. This uncertainty also has a marginal effect on the final result.

Theoretical uncertainties reflect mismodeling in the yield or shape of the MC simulation used in the background estimation. Cross-section uncertainties exist for all backgrounds, but are less important for those fitted by HistFitter as the cross-section uncertainty would completely cancel out in the normalization procedure. Conservative cross-section uncertainties are applied on the minor backgrounds, as well as on the signals during limit setting. Shape uncertainties are also derived to account for the chosen renormalization (μ_R) and factorization (μ_F) scales, α_S , and PDFs. All of these may affect the cross-section differently in various regions of phase-space, and can change the amount of initial and final state radiation. The choice of MC generator for matrix element calculations and for parton showering may also have a sizable effect. The strategy for calculating theoretical systematics may change depending on the SM process, and the uncertainties are generally derived following the recommendations of Ref. [192].

The following general procedure is used for estimation of the theoretical uncertainties of $t\bar{t}Z$

Uncertainty of $m_{Z\ell}^{\text{shifted}}$ range [GeV]	[90, 270]	[270, 360]	[360, 440]	[440, 580]	> 580
Total background expectation	28.58	8.64	4.76	4.21	4.61
Total statistical ($\sqrt{N_{\text{exp}}}$)	± 5.35	± 2.94	± 2.18	± 2.05	± 2.15
Total background systematic	± 1.52 [5.33%]	± 0.55 [6.42%]	± 0.63 [13.32%]	± 0.45 [10.73%]	± 0.39 [8.40%]
mu_ttZ	± 0.57	± 0.14	± 0.06	± 0.05	± 0.04
gamma_stat_SROL3l_0_all_mymZlMinusmZPlusZmass_bin_2	± 0.55	± 0.00	± 0.00	± 0.00	± 0.00
gamma_stat_SROL3l_0_all_mymZlMinusmZPlusZmass_bin_6	± 0.54	± 0.00	± 0.00	± 0.00	± 0.00
gamma_stat_SROL3l_0_all_mymZlMinusmZPlusZmass_bin_5	± 0.48	± 0.00	± 0.00	± 0.00	± 0.00
gamma_stat_SROL3l_0_all_mymZlMinusmZPlusZmass_bin_7	± 0.48	± 0.00	± 0.00	± 0.00	± 0.00
gamma_stat_SROL3l_0_all_mymZlMinusmZPlusZmass_bin_3	± 0.46	± 0.00	± 0.00	± 0.00	± 0.00
alpha_MET_SoftTrk_Scale	± 0.45	± 0.14	± 0.05	± 0.06	± 0.05
gamma_stat_SROL3l_0_all_mymZlMinusmZPlusZmass_bin_1	± 0.37	± 0.00	± 0.00	± 0.00	± 0.00
alpha_MET_SoftTrk_ResoPerp	± 0.21	± 0.09	± 0.05	± 0.03	± 0.06
alpha_MET_SoftTrk_ResoPara	± 0.17	± 0.09	± 0.01	± 0.00	± 0.05
alpha_JET_JER_EffectiveNP_3_1up	± 0.16	± 0.01	± 0.02	± 0.01	± 0.06
alpha_JET_JER_EffectiveNP_2_1up	± 0.15	± 0.01	± 0.01	± 0.00	± 0.05
alpha_EL_EFF_ID_TOTAL_1NPCOR_PLUS_UNCOR	± 0.08	± 0.02	± 0.01	± 0.01	± 0.06
alpha_JET_JER_EffectiveNP_7restTerm_1up	± 0.04	± 0.02	± 0.03	± 0.00	± 0.05
alpha_EG_RESOLUTION_ALL	± 0.02	± 0.09	± 0.11	± 0.00	± 0.00
alpha_MUON_SCALE	± 0.01	± 0.05	± 0.08	± 0.00	± 0.00
alpha_JET_JER_DataVsMC_1up	± 0.01	± 0.01	± 0.03	± 0.00	± 0.05
gamma_stat_SROL3l_4_all_mymZlMinusmZPlusZmass_bin_0	± 0.00	± 0.00	± 0.00	± 0.00	± 0.35
gamma_stat_SROL3l_2_all_mymZlMinusmZPlusZmass_bin_0	± 0.00	± 0.00	± 0.56	± 0.00	± 0.00
gamma_stat_SROL3l_2_all_mymZlMinusmZPlusZmass_bin_1	± 0.00	± 0.00	± 0.22	± 0.00	± 0.00
gamma_stat_SROL3l_1_all_mymZlMinusmZPlusZmass_bin_1	± 0.00	± 0.31	± 0.00	± 0.00	± 0.00
gamma_stat_SROL3l_1_all_mymZlMinusmZPlusZmass_bin_0	± 0.00	± 0.29	± 0.00	± 0.00	± 0.00
gamma_stat_SROL3l_1_all_mymZlMinusmZPlusZmass_bin_2	± 0.00	± 0.21	± 0.00	± 0.00	± 0.00
gamma_stat_SROL3l_3_all_mymZlMinusmZPlusZmass_bin_0	± 0.00	± 0.00	± 0.00	± 0.44	± 0.00

Table 6.12: Breakdown of the dominant systematic uncertainties on background estimates in the SROL3 ℓ signal regions. Note that the individual uncertainties can be correlated, and do not necessarily add up quadratically to the total background uncertainty. The percentages show the size of the uncertainty relative to the total expected background, and the grayscale shows the relative contribution for each region. Theory and most fake systematics are not included. Systematics which contribute less than 1% of the total uncertainty in all regions shown in this table are excluded.

and multiboson (including WZ and ZZ , as well as triboson processes). Uncertainties on the renormalization and factorization (QCD) scales, α_S , and PDF error set are propagated to the samples as internal weights. Following PDF4LHC recommendations [193], a new background prediction is derived in the $m_{Z\ell}^{\text{shifted}}$ distribution of every SR for each of the variations. In each bin of $m_{Z\ell}^{\text{shifted}}$, the uncertainties are derived as follows.

- **QCD:** Six variations are considered, which each scale μ_R and μ_F by factors of 0.5 and 2, avoiding opposite factors. These variations are treated as correlated nuisance parameters among regions, and as uncorrelated across samples.
- α_S : Half the difference in event yield between the up and down variations, which each represent ± 0.001 shifts in α_S .
- **PDF error set:** The standard deviation of the 100 PDF variations, treating positive and negative variations separately.

Uncertainty of $m_{Z\ell}^{\text{shifted}}$ range [GeV]	[90, 270]	[270, 360]	[360, 440]	[440, 580]	> 580
Total background expectation	65.13	4.12	1.58	2.05	2.09
Total statistical ($\sqrt{N_{\text{exp}}}$)	± 8.07	± 2.03	± 1.26	± 1.43	± 1.45
Total background systematic	± 2.82 [4.33%]	± 0.25 [6.17%]	± 0.13 [8.26%]	± 0.32 [15.59%]	± 0.33 [15.56%]
mu_ttZ	± 1.67	± 0.15	± 0.06	± 0.06	± 0.06
alpha_EL_EFF_ID_TOTAL_1NPCOR_PLUS_UNCOR	± 1.17	± 0.05	± 0.02	± 0.03	± 0.04
alpha_JET_GroupedNP_1	± 0.86	± 0.05	± 0.01	± 0.04	± 0.03
alpha_JET_GroupedNP_2	± 0.73	± 0.05	± 0.00	± 0.05	± 0.03
Lumi	± 0.57	± 0.04	± 0.01	± 0.02	± 0.02
alpha_FT_EFF_B_systematics	± 0.41	± 0.03	± 0.02	± 0.02	± 0.03
alpha_JET_Flavor_Response	± 0.28	± 0.01	± 0.00	± 0.03	± 0.01
alpha_JET_JER_EffectiveNP_1_1up	± 0.13	± 0.01	± 0.03	± 0.02	± 0.04
alpha_JET_JER_EffectiveNP_2_1up	± 0.12	± 0.03	± 0.02	± 0.01	± 0.04
alpha_MUON_EFF_RECO_SYS	± 0.04	± 0.01	± 0.01	± 0.02	± 0.02
gamma_stat_SROL4l.4_all_mymZlMinusmZPlusZmass_bin.0	± 0.00	± 0.00	± 0.00	± 0.00	± 0.30
gamma_stat_SROL4l.3_all_mymZlMinusmZPlusZmass_bin.0	± 0.00	± 0.00	± 0.00	± 0.30	± 0.00
gamma_stat_SROL4l.1_all_mymZlMinusmZPlusZmass_bin.0	± 0.00	± 0.11	± 0.00	± 0.00	± 0.00
gamma_stat_SROL4l.1_all_mymZlMinusmZPlusZmass_bin.1	± 0.00	± 0.09	± 0.00	± 0.00	± 0.00
gamma_stat_SROL4l.1_all_mymZlMinusmZPlusZmass_bin.2	± 0.00	± 0.08	± 0.00	± 0.00	± 0.00
gamma_stat_SROL4l.2_all_mymZlMinusmZPlusZmass_bin.1	± 0.00	± 0.00	± 0.06	± 0.00	± 0.00
gamma_stat_SROL4l.2_all_mymZlMinusmZPlusZmass_bin.0	± 0.00	± 0.00	± 0.08	± 0.00	± 0.00

Table 6.13: Breakdown of the dominant systematic uncertainties on background estimates in the SROL4 ℓ signal regions. Note that the individual uncertainties can be correlated, and do not necessarily add up quadratically to the total background uncertainty. The percentages show the size of the uncertainty relative to the total expected background, and the grayscale shows the relative contribution for each region. Theory and most fake systematics are not included. Systematics which contribute less than 1% of the total uncertainty in all regions shown in this table are excluded.

The α_S and PDF uncertainties are derived separately for all samples and regions then added in quadrature into a single uncertainty, and are treated as uncorrelated nuisance parameters across samples and regions. Then, the predictions from two samples using different MC generators or tunes are compared. This typically accounts for differences in the modeling of the hard-scatter calculation, parton shower, or amount of ISR. To derive the uncertainty on these effects, the event yield in the CRs and SRs is calculated for each sample. These are calculated at truth-level with samples that have enhanced statistics. The transfer factor (TF) is then calculated by comparing this varied yield ratio with the nominal one, providing an uncertainty on the normalization factor. For the radiation (ISR/FSR) variations, the TF uncertainty is derived as

$$\text{TF} = \frac{(\frac{\text{SR}}{\text{CR}})_{\text{up}} - (\frac{\text{SR}}{\text{CR}})_{\text{down}}}{(\frac{\text{SR}}{\text{CR}})_{\text{up}} + (\frac{\text{SR}}{\text{CR}})_{\text{down}}}. \quad (6.6)$$

For the one-sided comparisons against other MC generators, the TF uncertainty is derived as

$$\text{TF} = \frac{(\frac{\text{SR}}{\text{CR}})_{\text{shifted}} - (\frac{\text{SR}}{\text{CR}})_{\text{nominal}}}{(\frac{\text{SR}}{\text{CR}})_{\text{nominal}}}. \quad (6.7)$$

A conservative, flat uncertainty is applied to less dominant background processes, such as Higgs and top processes.

Uncertainty of $m_{Z\ell}^{\text{shifted}}$ range [GeV]	[90, 270]	[270, 360]	[360, 440]	[440, 580]	> 580
Total background expectation	33.96	2.58	0.75	0.31	0.07
Total statistical ($\sqrt{N_{\text{exp}}}$)	± 5.83	± 1.61	± 0.86	± 0.55	± 0.27
Total background systematic	± 2.40 [7.07%]	± 0.34 [13.26%]	± 0.11 [15.17%]	± 0.05 [17.87%]	± 0.06 [87.16%]
<hr/>					
alpha_JET_GroupedNP_1	± 1.30	± 0.10	± 0.04	± 0.01	± 0.02
mu_ttZ	± 1.26	± 0.11	± 0.03	± 0.01	± 0.00
alpha_JET_GroupedNP_2	± 1.09	± 0.10	± 0.03	± 0.00	± 0.02
mu_Diboson4l	± 0.53	± 0.03	± 0.01	± 0.01	± 0.00
alpha_JET_Flavor_Response	± 0.52	± 0.01	± 0.00	± 0.01	± 0.01
gamma_stat_SRTL_0_all_mymZMinusmZPlusZmass_bin_3	± 0.42	± 0.00	± 0.00	± 0.00	± 0.00
alpha_FT_EFF_B_systematics	± 0.42	± 0.05	± 0.01	± 0.00	± 0.00
gamma_stat_SRTL_0_all_mymZMinusmZPlusZmass_bin_2	± 0.38	± 0.00	± 0.00	± 0.00	± 0.00
alpha_JET_JER_EffectiveNP_2_1up	± 0.31	± 0.10	± 0.01	± 0.02	± 0.03
alpha_JET_JER_EffectiveNP_6_1up	± 0.30	± 0.12	± 0.02	± 0.02	± 0.00
alpha_JET_JER_EffectiveNP_5_1up	± 0.25	± 0.04	± 0.04	± 0.02	± 0.00
alpha_JET_JER_EffectiveNP_4_1up	± 0.23	± 0.05	± 0.02	± 0.00	± 0.01
alpha_JET_JER_EffectiveNP_1_1up	± 0.19	± 0.10	± 0.00	± 0.02	± 0.03
alpha_JET_JER_EffectiveNP_3_1up	± 0.17	± 0.07	± 0.02	± 0.00	± 0.00
alpha_EL_EFF_ID_TOTAL_1NPCOR_PLUS_UNCOR	± 0.15	± 0.01	± 0.00	± 0.00	± 0.00
alpha_JET_JER_EffectiveNP_7restTerm_1up	± 0.15	± 0.05	± 0.01	± 0.01	± 0.01
alpha_JET_JER_DataVsMC_1up	± 0.04	± 0.02	± 0.01	± 0.01	± 0.00
alpha_MUON_EFF_RECO_SYS	± 0.02	± 0.00	± 0.00	± 0.00	± 0.00
alpha_EG_RESOLUTION_ALL	± 0.02	± 0.00	± 0.00	± 0.00	± 0.00
alpha_FT_EFF_Light_systematics	± 0.02	± 0.02	± 0.00	± 0.00	± 0.00
alpha_EG_SCALE_ALL	± 0.01	± 0.00	± 0.00	± 0.00	± 0.00
alpha_MUON_MS	± 0.01	± 0.01	± 0.00	± 0.00	± 0.00
alpha_MUON_SAGITTA_RESBIAS	± 0.00	± 0.00	± 0.00	± 0.00	± 0.00
alpha_JET_EtaIntercalibration_NonClosure_posEta	± 0.00	± 0.00	± 0.00	± 0.00	± 0.00
alpha_MUON_ID	± 0.00	± 0.00	± 0.01	± 0.01	± 0.00
alpha_JET_GroupedNP_3	± 0.00	± 0.03	± 0.01	± 0.00	± 0.00
alpha_FT_EFF_extrapolation	± 0.00	± 0.00	± 0.01	± 0.00	± 0.00
gamma_stat_SRTL_2_all_mymZMinusmZPlusZmass_bin_0	± 0.00	± 0.00	± 0.05	± 0.00	± 0.00
gamma_stat_SRTL_2_all_mymZMinusmZPlusZmass_bin_1	± 0.00	± 0.00	± 0.06	± 0.00	± 0.00
gamma_stat_SRTL_3_all_mymZMinusmZPlusZmass_bin_0	± 0.00	± 0.00	± 0.00	± 0.03	± 0.00
gamma_stat_SRTL_4_all_mymZMinusmZPlusZmass_bin_0	± 0.00	± 0.00	± 0.00	± 0.00	± 0.03
gamma_stat_SRTL_1_all_mymZMinusmZPlusZmass_bin_2	± 0.00	± 0.16	± 0.00	± 0.00	± 0.00
gamma_stat_SRTL_1_all_mymZMinusmZPlusZmass_bin_1	± 0.00	± 0.07	± 0.00	± 0.00	± 0.00
gamma_stat_SRTL_1_all_mymZMinusmZPlusZmass_bin_0	± 0.00	± 0.08	± 0.00	± 0.00	± 0.00

Table 6.14: Breakdown of the dominant systematic uncertainties on background estimates in the SRTL signal regions. Note that the individual uncertainties can be correlated, and do not necessarily add up quadratically to the total background uncertainty. The percentages show the size of the uncertainty relative to the total expected background, and the grayscale shows the relative contribution for each region. Theory and most fake systematics are not included. Systematics which contribute less than 1% of the total uncertainty in all regions shown in this table are excluded.

For SUSY signal samples, several uncertainties are considered by generating private samples with the relevant variations. An uncertainty on the cross-section is also considered.

Fake background uncertainties are derived independently by this analysis, accounting for the specialized methods and the unique challenges of this search. Unique systematic uncertainties are derived on the fake factor method that account for various features below.

- **Fake factor statistical uncertainties:** The uncertainties on each bin of the fake factor method account for the limited precision in the fake-enriched region. They are treated as uncorrelated and each is propagated to the final result independently.

- **Magnitude of prompt subtraction:** As described in Section 6.4, the fake estimate is determined by subtracting off the contribution from MC events with at least one real lepton that is tagged as anti-ID. The cross-section uncertainty of this MC is propagated through the derivation and application of the fake factors.
- **Parameterization:** The fake factors are parameterized with respect to p_T^{cone} , but could depend on other kinematic variables, such as $N_{b\text{-jets}}$ or η . The fake estimate is recalculated in the measurement region with various 2D parameterizations, and the effect on the fake factor is treated as an uncertainty.
- **Closure:** This uncertainty is designed to account for any difference between the fake estimate and the amount of fakes in real data. It is estimated using the total VRZj yield, such that this uncertainty, added in quadrature with MC and data statistical uncertainties, covers any difference between data and total SM yields.
- **Composition:** This uncertainty is designed to account for differences in fake source (in particular light-flavor versus heavy-flavor jets) across regions, which can lead to different fake factors and therefore fake estimates. This uncertainty is derived by calculating the fake factors in MC separately for each source, and then applying a weighted fake estimate depending on the relative contribution from each source. This relative contribution is calculated inclusively, not for each bin in p_T^{cone} , to avoid issues due to low statistics.

6.7 Results

To estimate the background contributions in the signal regions, and search for an excess, the HistFitter package [103] is used to perform a simultaneous fit of the control and signal regions. HistFitter is a flexible statistical tool used in many ATLAS SUSY analyses. The simultaneous fit accounts for any expected contributions in the control regions due to the target signal model. First estimates of the expected background contributions are extracted from MC estimates. The various background processes were grouped as described in Section 6.2. The normalization for the WZ , ZZ , and $t\bar{t}Z$ samples are allowed to float when performing the fit, while the normalization for the other background processes are fixed to their theoretical cross-section, with the exception of the fake background (primarily $Z/\gamma^* + \text{jets}$) which is estimated via the fake factor method as described in Section 6.4.

The number of events passing each of the control and signal region selections is used to constrain the normalization of the background and signal processes, providing a best fit to the data. These best-fit normalization factors are then used to estimate the background and signal contribution in the signal region. The systematic uncertainties discussed in Section 6.6 are treated as nuisance parameters. All results shown in this section are preliminary as the theory and fake systematics are not yet included. The effect of these uncertainties is estimated with a flat 30% uncertainty applied to all backgrounds. The normalization factors obtained for WZ , ZZ , and $t\bar{t}Z$ are shown in Table 6.15.

μ_{WZ}	1.0300 ± 0.018
μ_{ZZ}	1.1068 ± 0.037
$\mu_{t\bar{t}Z}$	1.0228 ± 0.127

Table 6.15: Normalization factors obtained from the background-only fit using detector systematics with 139.0 fb^{-1} , for each of the three main backgrounds.

The results of the fit are summarized in Figure 6.25 for the CRs and VRs and in Figure 6.26 for the SRs. Tables with a breakdown of each region are provided in Tables 6.16 and 6.17 for all CRs and VRs, and in Table 6.18, Table 6.19, and Table 6.20 for all SRs. For each region the observed, fitted, and MC expectation event yields are shown. The post-fit CR yields agree by design, since this is the region where the normalization factors are derived. VRmTmin and VRZZ exhibit very good agreement between data and SM predictions, while VRMet and VRttZ show decent agreement compared to SM predictions. There are a few SR bins with small deficits and excesses but nothing significant is observed.

6.7.1 Model-dependent exclusion fit

Model-dependent exclusion limits on the generated SUSY $\tilde{\chi}_1^\pm$ and $\tilde{\chi}_1^0$ signal samples are derived at 95% confidence level (CL) through the profile log-likelihood ratio test using the CL_S prescription [104]. For each signal model, a simultaneous fit is performed to the control regions and the signal regions, fitting to the number of events passing each selection criteria. Each bin of the $m_{Z\ell}^{\text{shifted}} = m_{Z\ell} - m_Z + (91.2/\text{GeV})$ distribution in each SR is fit independently, so there are effectively 48 SRs being fit simultaneously. The modified frequentist CL_S technique is then used to determine the expected mass limit, which is selected as the point where CL_S = 0.05.

The C1C1 and C1N1 events are combined and limits are set simultaneously for both production mechanisms. Since the charged and neutral winos in the $B - L$ model have several possible decays,

table.results.yields channel	CRWZ	VRMet	VRmTmin
Observed events	11544	4428	299
Fitted bkg events	11545.491 ± 149.685	5542.893 ± 1784.281	364.872 ± 106.396
Fitted Diboson3l events	9940.555 ± 407.401	4878.653 ± 1789.392	284.648 ± 104.554
Fitted Diboson4l events	937.618 ± 380.111	176.867 ± 72.277	42.958 ± 17.582
Fitted ttZ events	102.746 ± 51.286	148.085 ± 73.998	7.065 ± 3.548
Fitted Triboson events	19.715 ± 5.886	19.776 ± 5.944	1.946 ± 0.587
Fitted Higgs events	31.947 ± 9.552	26.948 ± 8.098	0.594 ± 0.179
Fitted Fakes events	383.845 ± 114.945	159.319 ± 47.796	21.344 ± 6.403
Fitted Other events	129.066 ± 38.612	133.245 ± 40.100	6.316 ± 1.913
MC exp. SM events	11134.887	4552.780	298.243
MC exp. Diboson3l events	9769.730	3935.204	229.502
MC exp. Diboson4l events	694.546	129.123	31.414
MC exp. ttZ events	103.982	149.671	7.110
MC exp. Triboson events	19.694	19.761	1.935
MC exp. Higgs events	31.948	26.910	0.590
MC exp. Fakes events	385.935	159.319	21.344
MC exp. Other events	129.052	132.792	6.347

Table 6.16: Expected and fitted results for all 3ℓ CRs and VRs, for an integrated luminosity of 139.0 fb^{-1} . The results are obtained from the control regions using the discovery fit (see text for details). Nominal MC expectations (normalized to MC cross-sections) are given for comparison. The errors shown are the statistical plus detector systematic uncertainties. Uncertainties on the fitted yields are symmetric by construction, where the negative error is truncated when reaching to zero event yield.

table.results.yields channel	CRZZ	CRttZ	VRZZ	VRttZ
Observed events	1204	320	670	250
Fitted bkg events	1205.602 ± 39.842	321.317 ± 17.980	852.626 ± 342.338	220.915 ± 58.661
Fitted Diboson3l events	0.000 ± 0.000	68.346 ± 27.772	0.000 ± 0.000	46.433 ± 18.689
Fitted Diboson4l events	1196.143 ± 40.016	8.177 ± 3.625	841.074 ± 342.877	4.293 ± 1.940
Fitted ttZ events	1.188 ± 0.594	163.470 ± 38.868	4.525 ± 2.257	117.505 ± 58.414
Fitted Triboson events	1.749 ± 0.522	0.454 ± 0.173	2.449 ± 0.737	0.167 ± 0.078
Fitted Higgs events	0.147 ± 0.044	5.820 ± 1.752	0.759 ± 0.228	3.941 ± 1.194
Fitted Fakes events	6.023 ± 1.796	22.307 ± 6.691	2.257 ± 0.677	11.811 ± 3.543
Fitted Other events	0.353 ± 0.109	52.743 ± 15.982	1.562 ± 0.482	36.765 ± 11.160
MC exp. SM events	1087.764	324.652	625.888	212.659
MC exp. Diboson3l events	0.000	57.281	0.000	37.555
MC exp. Diboson4l events	1078.292	6.070	614.329	3.165
MC exp. ttZ events	1.196	178.523	4.558	119.093
MC exp. Triboson events	1.746	0.457	2.446	0.183
MC exp. Higgs events	0.147	5.838	0.761	3.961
MC exp. Fakes events	6.028	22.503	2.257	11.811
MC exp. Other events	0.354	53.980	1.539	36.891

Table 6.17: Expected and fitted results for ZZ and ttZ CRs and VRs, for an integrated luminosity of 139.0 fb^{-1} . The results are obtained from the control regions using the discovery fit (see text for details). Nominal MC expectations (normalized to MC cross-sections) are given for comparison. The errors shown are the statistical plus detector systematic uncertainties. Uncertainties on the fitted yields are symmetric by construction, where the negative error is truncated when reaching to zero event yield.

Yield of $m_{Z\ell}^{\text{shifted}}$ range [GeV]	[90, 270]	[270, 360]	[360, 440]	[440, 580]	> 580
Observed events	35	8	3	7	8
Fitted bkg events	33.867 ± 4.778	9.204 ± 1.903	4.781 ± 1.261	5.332 ± 1.319	6.000 ± 1.479
Fitted Diboson3l events	21.123 ± 5.106	6.314 ± 1.911	3.724 ± 1.235	4.229 ± 1.313	4.947 ± 1.485
Fitted Diboson4l events	0.613 ± 0.252	0.219 ± 0.093	0.096 ± 0.043	0.090 ± 0.039	0.087 ± 0.038
Fitted ttZ events	4.443 ± 2.209	1.077 ± 0.537	0.457 ± 0.233	0.419 ± 0.216	0.328 ± 0.166
Fitted Triboson events	2.518 ± 0.766	0.756 ± 0.232	0.303 ± 0.098	0.300 ± 0.094	0.393 ± 0.120
Fitted Higgs events	0.433 ± 0.132	0.031 ± 0.011	0.008 ± 0.003	0.012 ± 0.004	0.005 ± 0.002
Fitted Fakes events	2.201 ± 0.653	0.132 ± 0.041	0.002 ± 0.001	0.001 ± 0.000	0.001 ± 0.000
Fitted Other events	2.535 ± 0.757	0.675 ± 0.209	0.191 ± 0.065	0.280 ± 0.088	0.240 ± 0.075
MC exp. SM events	28.171	8.476	4.650	4.112	4.493
MC exp. Diboson3l events	15.749	5.607	3.591	3.054	3.488
MC exp. Diboson4l events	0.449	0.159	0.071	0.064	0.062
MC exp. ttZ events	4.415	1.106	0.473	0.413	0.321
MC exp. Triboson events	2.530	0.762	0.312	0.294	0.382
MC exp. Higgs events	0.428	0.031	0.008	0.012	0.005
MC exp. Fakes events	2.144	0.132	0.002	0.001	0.001
MC exp. Other events	2.456	0.679	0.194	0.273	0.233

Table 6.18: Expected and fitted results for SROL3 ℓ signal regions, for an integrated luminosity of 139.0 fb^{-1} . The results are obtained from the control regions using the discovery fit (see text for details). Nominal MC expectations (normalized to MC cross-sections) are given for comparison. The errors shown are the statistical plus detector systematic uncertainties. Uncertainties on the fitted yields are symmetric by construction, where the negative error is truncated when reaching to zero event yield.

Yield of $m_{Z\ell}^{\text{shifted}}$ range [GeV]	[90, 270]	[270, 360]	[360, 440]	[440, 580]	> 580
Observed events	81	4	1	2	1
Fitted bkg events	76.267 ± 7.522	4.327 ± 0.710	1.624 ± 0.294	2.161 ± 0.446	2.136 ± 0.454
Fitted Diboson3l events	0.458 ± 0.173	0.041 ± 0.015	0.019 ± 0.007	0.003 ± 0.001	0.004 ± 0.002
Fitted Diboson4l events	26.306 ± 8.679	0.889 ± 0.369	0.302 ± 0.128	0.415 ± 0.179	0.539 ± 0.234
Fitted ttZ events	13.984 ± 6.778	1.135 ± 0.573	0.456 ± 0.226	0.485 ± 0.250	0.450 ± 0.234
Fitted Triboson events	12.319 ± 3.420	0.986 ± 0.298	0.398 ± 0.124	0.437 ± 0.147	0.534 ± 0.184
Fitted Higgs events	13.588 ± 3.749	0.809 ± 0.244	0.242 ± 0.075	0.205 ± 0.068	0.116 ± 0.039
Fitted Fakes events	3.813 ± 1.112	0.003 ± 0.001	0.002 ± 0.001	0.272 ± 0.090	0.256 ± 0.085
Fitted Other events	5.800 ± 1.710	0.464 ± 0.166	0.206 ± 0.085	0.343 ± 0.124	0.237 ± 0.103
MC exp. SM events	63.802	4.094	1.571	2.034	2.062
MC exp. Diboson3l events	0.369	0.033	0.015	0.003	0.003
MC exp. Diboson4l events	16.903	0.646	0.221	0.305	0.421
MC exp. ttZ events	13.034	1.155	0.456	0.483	0.460
MC exp. Triboson events	11.559	0.982	0.402	0.433	0.563
MC exp. Higgs events	12.634	0.810	0.245	0.206	0.120
MC exp. Fakes events	3.747	0.003	0.002	0.274	0.266
MC exp. Other events	5.556	0.465	0.230	0.330	0.230

Table 6.19: Expected and fitted results for SROL4 ℓ signal regions, for an integrated luminosity of 139.0 fb^{-1} . The results are obtained from the control regions using the discovery fit (see text for details). Nominal MC expectations (normalized to MC cross-sections) are given for comparison. The errors shown are the statistical plus detector systematic uncertainties. Uncertainties on the fitted yields are symmetric by construction, where the negative error is truncated when reaching to zero event yield.

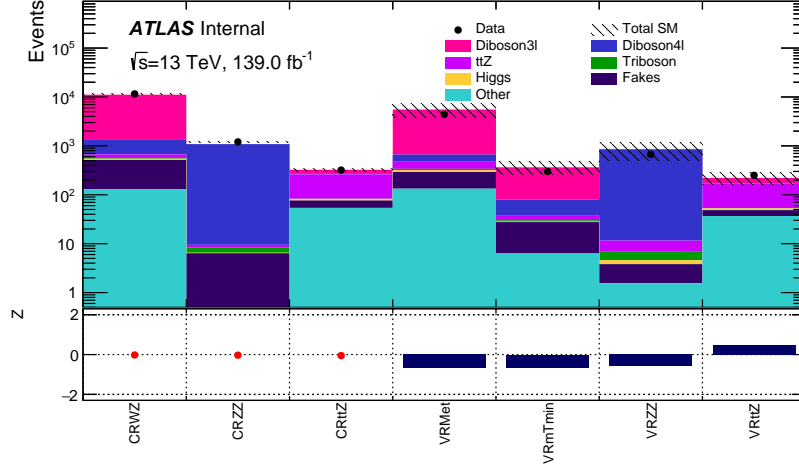


Figure 6.25: Data/SM agreement in all CRs and VRs. The bottom panel shows the significance in each bin.

limits are set in each signal region as a function of the branching ratio of the $\tilde{\chi}_1^\pm$ into $Z\ell$, $H\ell$, and $W\nu$ and of the $\tilde{\chi}_1^0$ into $Z\nu$, $H\nu$, and $W\ell$. Signal events are reweighted according to the truth decay of the wino to effectively set limits on each decay separately. This is achieved by using a truth reweighting of the signals analogous to the reweighting used in the stop search and defined in Equation 5.1. A scan is performed over each charged lepton flavor (electron, muon, and tau) and over each possible boson type (Z , W , and Higgs). The considered points in the lepton flavor scan are $(\mathcal{B}(\tilde{\chi}_1 \rightarrow Be), \mathcal{B}(\tilde{\chi}_1 \rightarrow B\mu), \mathcal{B}(\tilde{\chi}_1 \rightarrow B\tau)) = (1,0,0)$, $(0,1,0)$, $(0,0,1)$, and $(0.33,0.33,0.34)$, where B is a W boson for C1N1 events, and can be either a Z or a Higgs for C1C1. Then for each of these points, a finer granularity scan is performed over the possible boson types of the wino decay. Limits are set as a function of $\mathcal{B}(\tilde{\chi}_1 \rightarrow H)$ versus $\mathcal{B}(\tilde{\chi}_1 \rightarrow Z)$, separately for each considered wino-to-lepton branching ratio point. $\mathcal{B}(\tilde{\chi}_1 \rightarrow W)$ is implicitly included on the 2D plots since the sum of the three BRs must equal 1. Because of the generator-level filter which favors $\tilde{\chi}_1^\pm \rightarrow Z\ell \rightarrow \ell\ell\ell$, limits are not set for $\mathcal{B}(\tilde{\chi}_1 \rightarrow Z)=0$.

To increase sensitivity for the $\mathcal{B}(\tilde{\chi}_1 \rightarrow Be)=100\%$ and $\mathcal{B}(\tilde{\chi}_1 \rightarrow B\mu)=100\%$ scenarios in the lepton flavor scan, additional SR selections are applied on the flavor of the third lepton which is assumed to come directly from the C1 or N1 decay (that which is assigned to the $Z\ell$ leg but which is not assigned to the Z). For $\mathcal{B}(\tilde{\chi}_1 \rightarrow Be)=100\%$ limits, this lepton is required to be an electron, and for $\mathcal{B}(\tilde{\chi}_1 \rightarrow B\mu)=100\%$ limits, this lepton is required to be a muon. SRTL events require that all

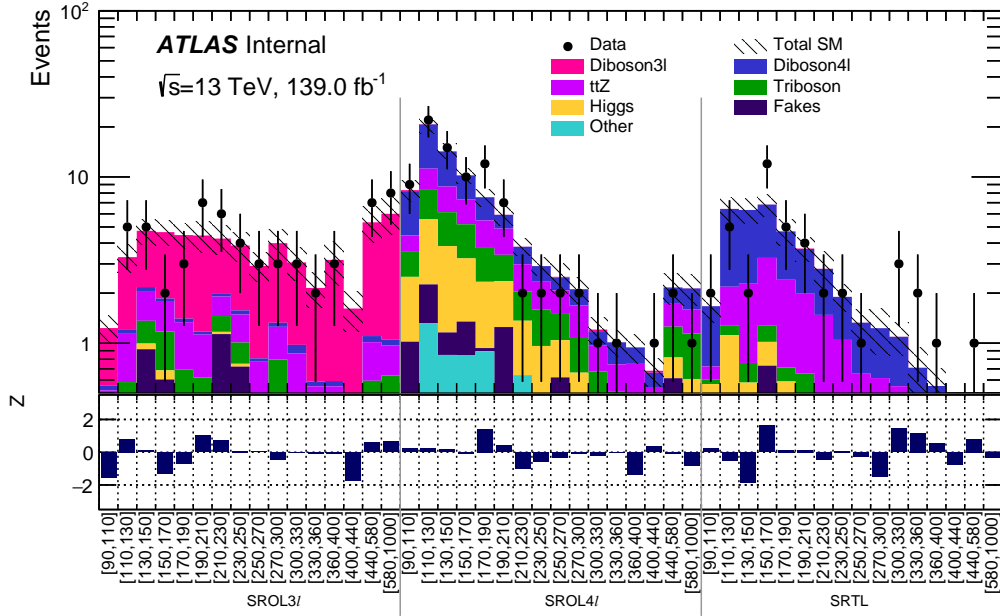


Figure 6.26: Data/SM agreement in all SRs. The bottom panel shows the significance in each bin.

leptons assigned directly to the C1 or N1 decay (and not to a boson) must have the required flavor. This imposes the requirement that both winos decay to the same lepton flavor, as predicted in the $B - L$ model because the wino-to-lepton BR is dictated by the neutrino hierarchy and hence should be the same for charginos and neutralinos. SROL4 ℓ events are agnostic to the fourth lepton flavor. The reasoning for this, as opposed to the agreement between the third and fourth leptons which is required in SRTL, is because in SROL4 ℓ the fourth lepton can often come from the second boson decay and hence its flavor is random compared to the lepton directly from the wino decay. The other two points in the lepton flavor scan (fully tau and flavor democratic) allow all lepton flavors.

Some examples of these limits set as a function of $\mathcal{B}(\tilde{\chi}_1 \rightarrow H)$ versus $\mathcal{B}(\tilde{\chi}_1 \rightarrow Z)$ can be seen in Figure 6.27 for $\mathcal{B}(\tilde{\chi}_1 \rightarrow B\tau)=100\%$. These represent the weakest limits achieved in this scan; lower wino masses and smaller values of $\mathcal{B}(\tilde{\chi}_1 \rightarrow B\tau)$ have stronger exclusion limits and are not shown here. At the time of writing this thesis, higher mass points are in the process of being generated in order to set limits across the full boson BR plane. These contours will then be combined to show the masses excluded as a function of $\mathcal{B}(\tilde{\chi}_1 \rightarrow H)$ versus $\mathcal{B}(\tilde{\chi}_1 \rightarrow Z)$, for each lepton BR point.

Yield of $m_{Z\ell}^{\text{shifted}}$ range [GeV]	[90, 270]	[270, 360]	[360, 440]	[440, 580]	> 580
Observed events	35	5	1	1	0
Fitted bkg events	35.675 ± 4.901	3.032 ± 0.713	0.827 ± 0.226	0.389 ± 0.123	$0.065^{+0.073}_{-0.065}$
Fitted Diboson3l events	0.070 ± 0.065	0.000 ± 0.000	0.000 ± 0.000	0.000 ± 0.000	0.000 ± 0.000
Fitted Diboson4l events	19.578 ± 5.902	1.503 ± 0.617	0.491 ± 0.204	0.276 ± 0.117	$0.032^{+0.061}_{-0.032}$
Fitted ttZ events	9.878 ± 4.621	0.891 ± 0.472	0.187 ± 0.107	0.062 ± 0.038	0.019 ± 0.014
Fitted Triboson events	1.124 ± 0.358	0.173 ± 0.066	0.033 ± 0.015	0.047 ± 0.025	0.014 ± 0.012
Fitted Higgs events	2.694 ± 0.838	0.077 ± 0.034	0.008 ± 0.004	0.002 ± 0.001	0.000 ± 0.000
Fitted Fakes events	0.672 ± 0.197	0.135 ± 0.051	0.031 ± 0.012	0.001 ± 0.000	0.000 ± 0.000
Fitted Other events	1.660 ± 0.538	0.253 ± 0.101	0.076 ± 0.037	0.000 ± 0.000	0.000 ± 0.000
MC exp. SM events	32.589	2.503	0.716	0.289	0.071
MC exp. Diboson3l events	0.047	0.000	0.000	0.000	0.000
MC exp. Diboson4l events	16.458	1.025	0.363	0.190	0.034
MC exp. ttZ events	9.837	0.898	0.204	0.057	0.020
MC exp. Triboson events	1.147	0.157	0.036	0.039	0.017
MC exp. Higgs events	2.740	0.073	0.008	0.002	0.000
MC exp. Fakes events	0.646	0.121	0.031	0.001	0.000
MC exp. Other events	1.714	0.230	0.074	0.000	0.000

Table 6.20: Expected and fitted results for SRTL signal regions, for an integrated luminosity of 139.0 fb^{-1} . The results are obtained from the control regions using the discovery fit (see text for details). Nominal MC expectations (normalized to MC cross-sections) are given for comparison. The errors shown are the statistical plus detector systematic uncertainties. Uncertainties on the fitted yields are symmetric by construction, where the negative error is truncated when reaching to zero event yield.

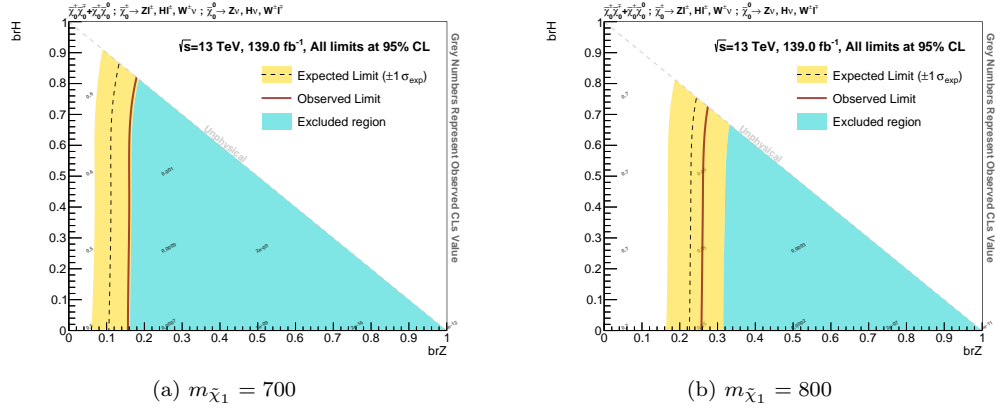


Figure 6.27: Expected (dashed blue) and observed (solid red) 95% CL limit curves as a function of $\mathcal{B}(\tilde{\chi}_1 \rightarrow H)$ versus $\mathcal{B}(\tilde{\chi}_1 \rightarrow Z)$ for 700 and 800 GeV wino masses, for $\mathcal{B}(\tilde{\chi}_1 \rightarrow \tau)=100\%$. The yellow band reflects the $\pm 1\sigma$ uncertainty of the expected limit due to theoretical, fake, experimental, and MC statistical uncertainties although the theory and fake uncertainties are at the moment estimated with a flat 30% uncertainty. The shaded blue area represents the branching ratios that are expected to be excluded beyond 1σ . The grey numbers represent the observed CL_S value.

6.7.2 Model-independent fit

It is also possible to set limits at 95% CL on the visible cross-section ($\langle\epsilon\sigma_{\text{obs}}^{95}\rangle$) and the observed (S_{obs}^{95}) and expected (S_{exp}^{95}) number of events for new physics processes, independent of what that process may be. This fit considers one SR at a time, to avoid any assumption on relative signal contributions across SRs and $m_{Z\ell}^{\text{shifted}}$ bins. Hence, this analysis has 48 discovery regions which are fit independently, corresponding to the 16 bins in each of the three SR types described in Section 6.5. Figure 6.28 shows the model-dependent p-value and significance, as a function of $m_{Z\ell}^{\text{shifted}}$ for each of the SR types. It can be seen there is no significance above 2σ , and in fact most bins have significance below 1σ .

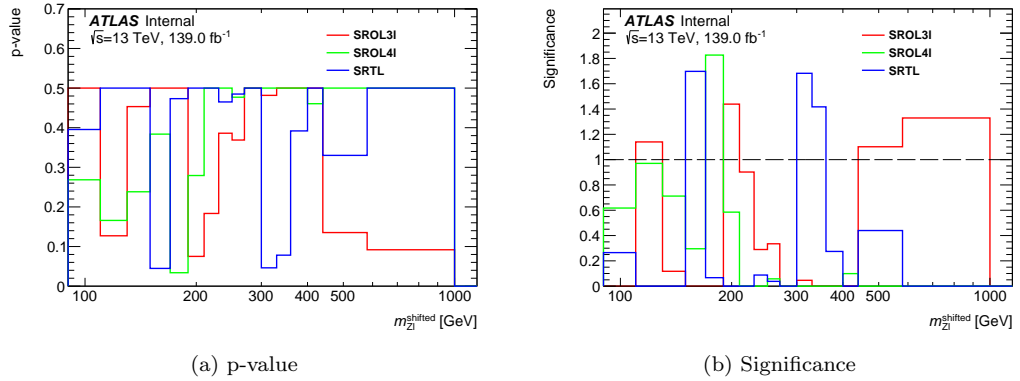


Figure 6.28: Model-independent p-value and significance for any [BSM](#) processes in each $m_{Z\ell} - m_Z + (91.2/\text{GeV})$ ($m_{Z\ell}^{\text{shifted}}$) bin. No significance above 2σ is observed, and most bins have significance below 1σ .

6.8 Prospects

Beyond the obvious gain in sensitivity that will be achieved with additional data, another way to greatly improve the sensitivity in a realistic way for the model used to motivate this search is to optimize on the Higgs decays rather than the Z decays. As shown in Figures 2.12 and 2.13 (in Chapter 2), many more points in the parameter scan have a large Higgs [BR](#) than a large Z BR. For this reason it could be beneficial to use final states with Higgs bosons when searching for a $B - L$ MSSM wino LSP. To maximize signal efficiency, it is reasonable to focus on Higgs decays to two b -quarks, since almost 60% of Higgs decay this way. Then the search could be performed in an analogous way to the trilepton search, but with a resonance in the invariant mass spectrum of $b\bar{b}\ell$

objects. Of course the mass resolution will not be as sharply peaked, since jet energy resolution is inherently larger than lepton energy resolution. Analogously to the trilepton search, several final states could be targeted depending on the decay of the non- bbl wino leg. It would be reasonable to again split these reconstruction strategies into OneLeg and TwoLeg, where TwoLeg in this case would be a $2\ell, 4b$ final state, where two b -jet pairs each reconstruct a Higgs boson. This would be very interesting since there are few SM processes which could lead to the same final state, and the very rare SM di-Higgs production has not yet been observed at the time of this writing [194, 195]. However it would be more challenging to successfully match the b -jet pairs than it is to match lepton pairs to reconstruct a Z , due to the worse energy resolution and the fact that there are no SFOS pairs to exploit. One could also consider including $2\ell, 2b, 2j$ final states in the TwoLeg category, to additionally accept $\tilde{\chi}_1^\pm \rightarrow Z\ell \rightarrow jj\ell$ and $\tilde{\chi}_1^0 \rightarrow W\ell \rightarrow jj\ell$ events. The backgrounds for this final state would be more numerous, since it is relatively common for any physics process to have extra jets from ISR or FSR, although the requirement that they have an invariant mass near the W or Z mass would greatly decrease these backgrounds. Additionally, any SM processes with missing energy from undetected neutrinos, such as $t\bar{t}$ or $t\bar{t} + V$, could be effectively reduced by requiring small E_T^{miss} significance analogously to the Run 1 stop search, since any signal falling in the TwoLeg reconstruction should have no missing energy.

Then it would again be reasonable to split the OneLeg events by lepton multiplicity. The major backgrounds in the $1\ell 2b$ final state will be SM processes with semi-leptonic b decays as well as W +jets and VH processes, which could be reduced by requiring large missing energy, while the major backgrounds in the $2\ell 2b$ final state will be the same as the backgrounds in the stop search. Both of these final states present challenges, but there is one feature that could certainly help. The decay products of a high-mass wino will be high-energy and so the b -jets from the Higgs will be collimated. These two collimated jets could be reconstructed as a single large-radius jet which has measurable substructure that can be used to tag the jet as being from a Higgs. This could certainly help to reject many low-energy backgrounds. It might also be worthwhile to check the sensitivity of splitting the OneLeg category by b -jet multiplicity, but this may be less effective because requiring additional b -jets would only target events where the non- bbl leg is $\tilde{\chi}_1^0 \rightarrow H(Z)\nu \rightarrow bb\nu$, or $\tilde{\chi}_1^\pm \rightarrow H(Z)\ell \rightarrow bbl$ when the lepton was not reconstructed. This may be less effective than splitting by lepton multiplicity, which can increase by a number of boson decay chains and so can target many $\tilde{\chi}_1^\pm$ and $\tilde{\chi}_1^0$ decays, and which decreases SM background rates more effectively.

CHAPTER 7

Conclusion

This dissertation has presented efforts in the [TRT](#) group to maintain good tracking and electron identification in high pileup conditions, as well as several searches for [SUSY](#) particles with R-parity-violating decays which are predicted by the $B - L$ MSSM, using $\sqrt{s} = 8$ and 13 TeV [LHC](#) data collected by the ATLAS experiment from 2012 to 2018.

Chapter 4 presented some recent studies and improvements in the TRT software. The [local track occupancy](#) was introduced as a new metric of detector activity surrounding a TRT track, and as a proxy for pileup. The exact definition of this variable was optimized to provide an accurate representation of the detector activity while requiring as little CPU and memory as possible. This variable proved useful in tracking and [PID](#) studies and calibrations alike, and was implemented as a discriminant in the PID as well as for use in the [HLT](#). Additionally, the observed drop in TRT track extension efficiency at high pileup was mitigated by reoptimizing the [PHF](#) cut, with little observed difference in the resultant track momentum resolution.

Chapter 5 presented searches for pair production of scalar top quarks (stops) which subsequently decay to a b -quark and a charged lepton. Depending on the stop [BR](#) to lepton flavor, limits are set on the stop mass between 500 and 1000 GeV for the [Run 1](#) analysis, and between 900 and 1500 GeV for the [Run 2](#) analysis. In both analyses, the best limits are achieved for $\mathcal{B}(\tilde{t} \rightarrow be) > 95\%$. Chapter 6 presented a search for charged and neutral wino production, searching for a trilepton mass resonance and utilizing several reconstruction techniques to have sensitivity to many different chargino and neutralino decays. Stringent limits are set on the wino mass for many possible lepton and boson branching ratios. This represents the first trilepton resonance search in [Run 2](#).

While no deviations from the [SM](#) have been observed, there are many ways presented in these pages that these analyses can be improved to raise their discovery potential. Beyond these improve-

ments, ATLAS and CMS will continue to collect pp collisions from the LHC in the years to come, as well as to explore more corners of phase space that have not yet been probed. There is still plenty of discovery potential at the LHC as well as at future colliders like the High-Luminosity LHC. If SUSY is a true theory of nature and is accessible at these energies, it is very possible that it will be discovered at the LHC, and many of the outstanding issues in the SM, and in particle physics as a whole, would be resolved.

Appendices

APPENDIX A

13 TeV Stop Search: Signal Region Optimization

This appendix illustrates some methods used to optimize the region definitions for the Run 2 stop search. The SR selections are optimized to maximize sensitivity while reducing statistical uncertainties associated with the number of generated MC events which pass the SR requirements. The sensitivity can be estimated using the number of signal events divided by the square root of total background events (S/\sqrt{B}), or by simply comparing the signal and background efficiency of a given cut. As described in Section 5.3.4, the dominating uncertainties are statistical so in order to avoid too severely reducing background statistics, several selections are looser than would have been chosen based on sensitivity alone.

First we will consider one example of using efficiency to choose an optimal cut. Figure A.1 shows the effect of varying cuts on $m_{b\ell}^1(\text{rej})$ on several signal and background processes. Figure A.1a shows the efficiency as a function of the $m_{b\ell}^1(\text{rej})$ cut, and Figure A.1b shows the consequential raw MC yield. It can be seen that the processes with a real top ($t\bar{t}$ and single-top) have a rapid drop in efficiency between a cut on $m_{b\ell}^1(\text{rej})$ of 50 GeV to 150 GeV, above which the decrease in efficiency is not as steep. The efficiency for $Z/\gamma^*+\text{jets}$ is higher than for top processes because the $b\ell$ pairings are completely random in this process, so there is no kinematic edge. The efficiency of top processes at a $m_{b\ell}^1(\text{rej})$ cut of 150 GeV is roughly 20%, and the efficiency for $Z/\gamma^*+\text{jets}$ is roughly 45%. Meanwhile the signal efficiency of the $m_{b\ell}^1(\text{rej})$ cut is much higher than background for all \tilde{t} mass points shown, and is $> 85\%$ efficient for a $m_{b\ell}^1(\text{rej})$ cut at 150 GeV.

The expected sensitivities for the 1000 GeV stop mass point, as estimated from S/\sqrt{B} , are shown for the variables which define SR800 in Figure A.2, and the corresponding plots for SR1100,

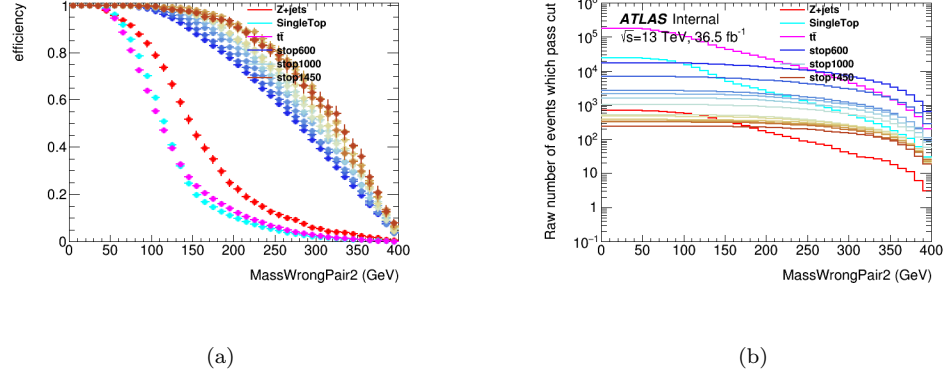


Figure A.1: Efficiency and raw MC yield as a function of cut on $m_{b\ell}^1(\text{rej})$ (“MassWrongPair2”). Distributions shown here are before any other selections except 2 leptons and 2 jets, at least one of which is b -tagged.

at the 1300 GeV stop mass point, are shown in Figure A.3. These distributions are shown before the corresponding cuts are applied (N-2 plots). These figures demonstrate how the SRs would have higher S/\sqrt{B} if they had tighter selections, particularly in $m_{\ell\ell}$ and H_T . However, Table A.1 shows the raw number of MC events after all cuts are applied in both SRs. Here it can be seen that the raw number of MC background events is very small with the chosen cuts (in the SRs: $H_T > 1000$ GeV, $m_{b\ell}^1(\text{rej}) > 150$ GeV, $m_{\ell\ell} > 300$ GeV, and $m_{b\ell} > 800$ or 1100 GeV as defined in Table 5.10). Applying selections any tighter than these would reduce the raw number of events to near 0. The chosen selections optimize for both of these effects.

Selection	SR800	SR1100
$m_{\tilde{t}} = 1000$ GeV	9722	901
$m_{\tilde{t}} = 1200$ GeV	4092	3336
$m_{\tilde{t}} = 1400$ GeV	4200	3867
Total background	192	54
$t\bar{t}$	26	3
Single top	45	6
$Z/\gamma^* + \text{jets}$	97	41
$W + \text{jets}$	4	2
Other	20	2

Table A.1: Raw number of Monte Carlo events in SR800 and SR1100, for the selections defined in Table 5.10. Expected number of events are shown in Section 5.3.3.

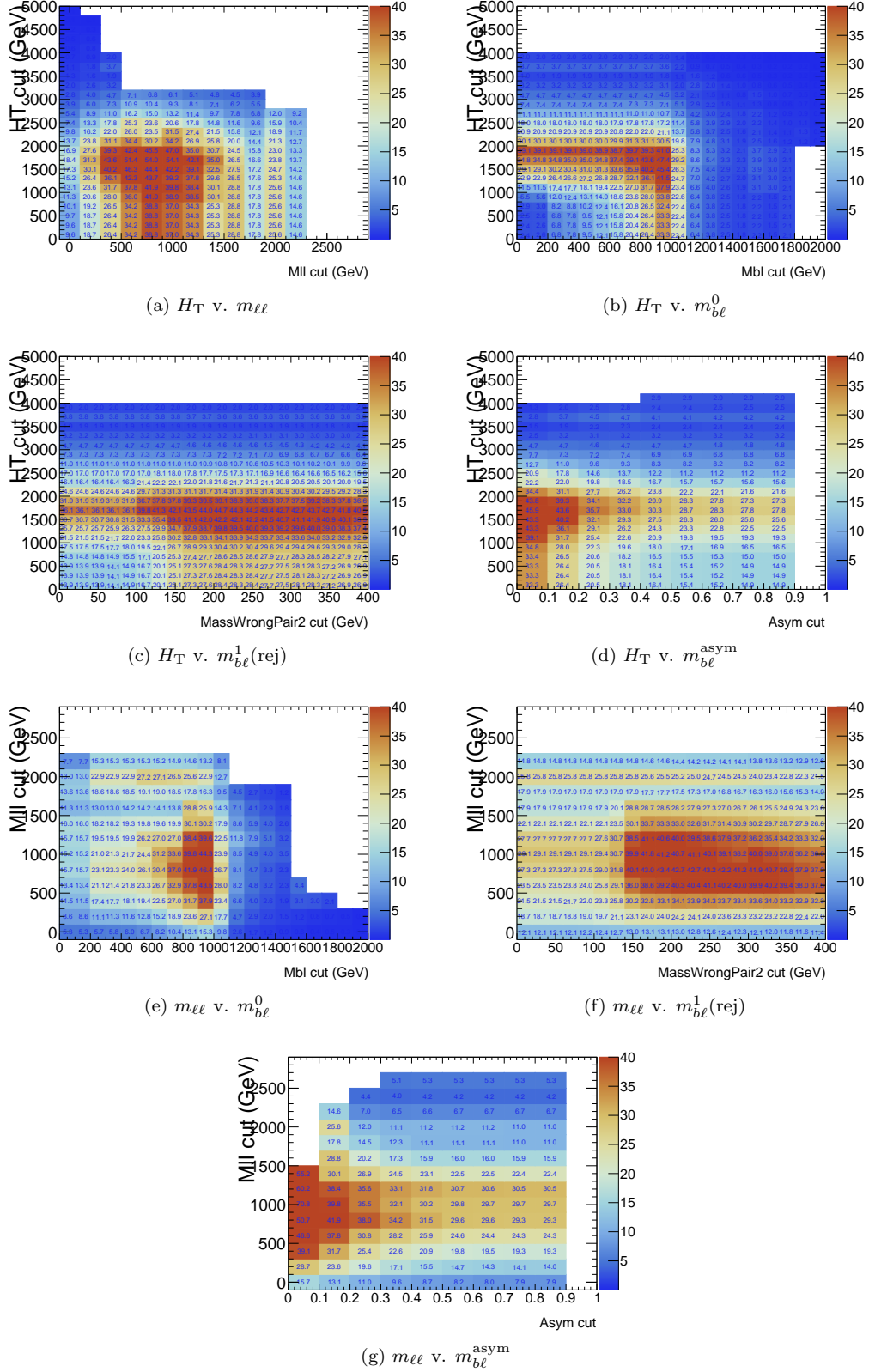


Figure A.2: S/\sqrt{B} for $m_{\tilde{t}} = 1000$ GeV in the H_T v. $m_{\ell\ell}$ (a), H_T v. $m_{b\ell}$ (b), H_T v. $m_{b\ell}^1(\text{rej})$ (c), H_T v. $m_{b\ell}^{\text{asym}}$ (d), $m_{\ell\ell}$ v. $m_{b\ell}$ (e), $m_{\ell\ell}$ v. $m_{b\ell}^1(\text{rej})$ (f), and $m_{\ell\ell}$ v. $m_{b\ell}^{\text{asym}}$ (g) planes, in SR800. The distribution of all these variables are shown before the corresponding cuts are applied (commonly referred to as N-2 plots).

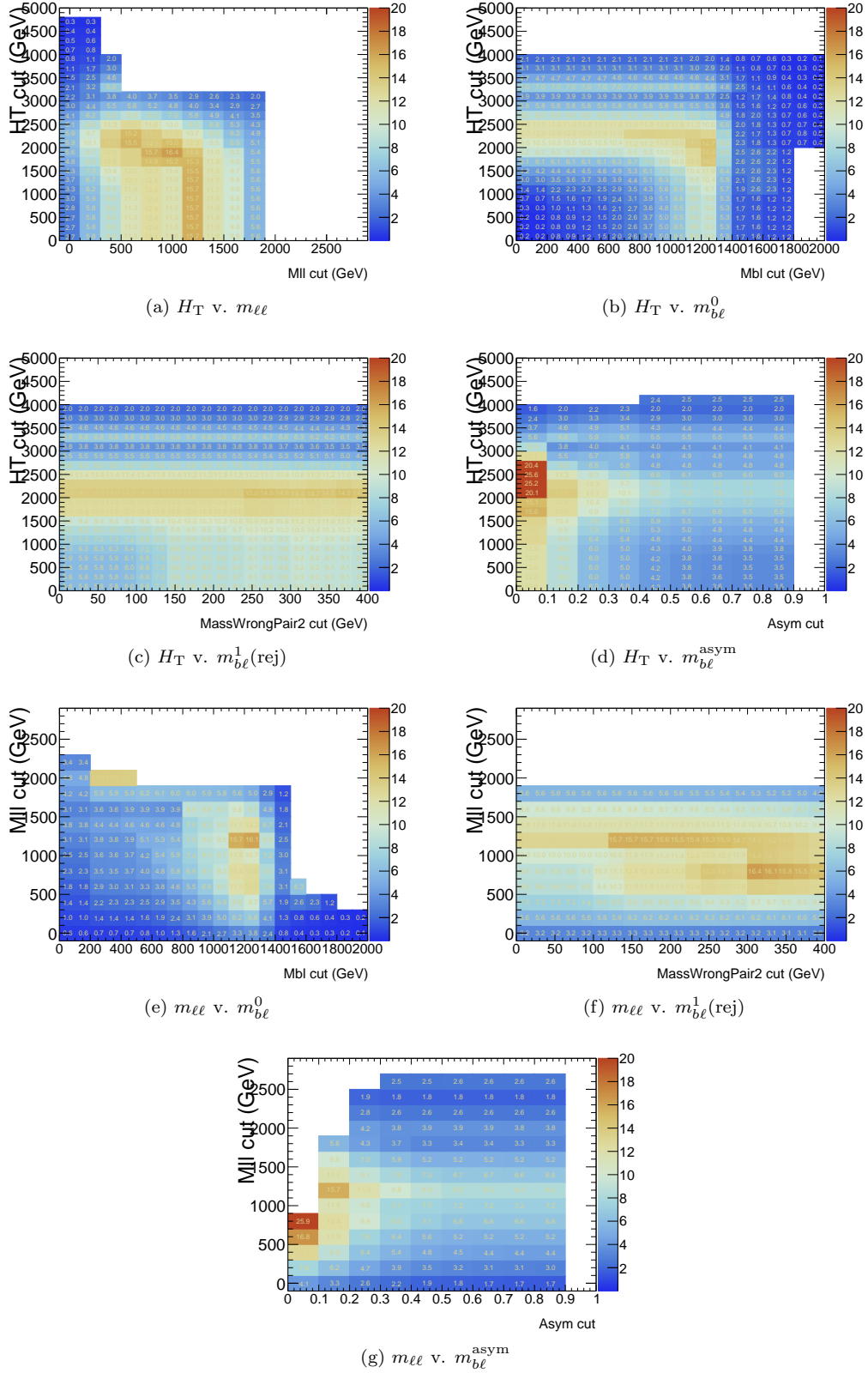


Figure A.3: S/\sqrt{B} for $m_{\tilde{t}} = 1300$ GeV mass point in the H_T v. $m_{\ell\ell}$ (a), H_T v. $m_{b\ell}$ (b), H_T v. $m_{b\ell}^1(\text{rej})$ (c), H_T v. $m_{b\ell}^{\text{asym}}$ (d), $m_{\ell\ell}$ v. $m_{b\ell}$ (e), $m_{\ell\ell}$ v. $m_{b\ell}^1(\text{rej})$ (f), and $m_{\ell\ell}$ v. $m_{b\ell}^{\text{asym}}$ (g) planes, in SR1100. The distribution of all these variables are shown before the corresponding cuts are applied (commonly referred to as N-2 plots).

The b -tagging working point can also affect the sensitivity and statistics of an analysis, and hence should also be considered when optimizing the analysis selections. There are several b -tagging working points defined by the flavor tagging group [196] which have different signal efficiencies and background rejection. These typically have the nominal signal efficiency included in the name; for example the **Fixed 77%** working point has a nominal signal efficiency of 77%. There is a trade-off between efficiency and fake positive rate (where light flavor-initiated jets are b -tagged). Higher signal efficiency comes with higher rates of misidentification, and vice versa. The flavor tagging working group additionally supplies several different types of working points, because of the unique difficulties of b -tagging. It is a known effect that b -tagging efficiency decreases as the b -jet p_T increases, because the large Lorentz boost of the B hadron translates to a decay further into the detector and so the displaced vertex might be too far to pass the criteria of b -tagging. An example of this drop in efficiency can be seen in Figure A.4. In an effort to mitigate this effect, a campaign of working points were introduced called “**Flat**” working points, as opposed to the standard “**Fixed**”. The goal of these working points was to maintain a constant (flat) efficiency as a function of jet p_T . Both sets of working points will be compared in this section in terms of sensitivity and raw MC yields.

Several b -tagging working points, both **Flat** and **Fixed**, are compared in terms of their impact on S/\sqrt{B} and raw number of background events. Table A.2 summarizes the significance for each considered working point, at various stop mass points, in both SR800 and SR1100. Tables A.3 and A.4 respectively report the number of raw MC signal and background statistics for each working point, and Tables A.5 and A.6 show the expected number of events in both SRs for signal and background, respectively. In general the **Flat** working points lead to a larger raw yield than the **Fixed**. This is especially true for background processes, which have a larger difference between **Flat** and **Fixed** than signal processes. This means that the **Fixed** working points have lower backgrounds and better sensitivity than **Flat**, for a given working point. Similarly, for increasing working point efficiencies, the increase in background yields grows more rapidly than the corresponding increase in signal yields. Hence the sensitivity is best for the tightest working points.

The **Fixed** and **Flat** 70% working points are rejected immediately because of their low statistics, and the **Fixed** and **Flat** 85% working points are also rejected due to their low significance. **Flat** 77% is slightly preferred over **Fixed** 77% because it has larger background statistics with relatively little difference in significance. The selected working point is **Fixed 77%**.

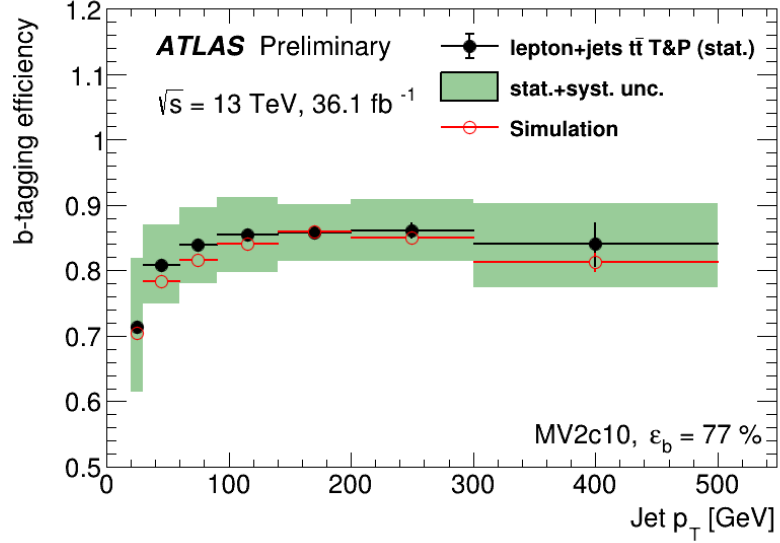


Figure A.4: The b -tagging efficiencies as a function of jet p_T for the Fixed 77% working point. The b -tagging efficiencies for the predictions extracted from the simulation are shown as a red line while the efficiencies measured in data are shown as black dots. The vertical error bars represent the statistical uncertainty on the measurement. The green band indicates the total statistical and systematic uncertainties on the measurement. [197]

	$m_{\tilde{t}} = 1000 \text{ GeV}$		$m_{\tilde{t}} = 1200 \text{ GeV}$		$m_{\tilde{t}} = 1400 \text{ GeV}$	
	SR800	SR1100	SR800	SR1100	SR800	SR1100
Fixed 70%	32.0	7.6	7.7	16.8	2.0	4.9
Flat 70%	31.6	6.4	8.2	14.1	2.3	4.4
Fixed 77%	31.7	6.6	7.9	14.6	2.1	4.6
Flat 77%	29.0	5.5	7.7	11.9	2.1	3.7
Fixed 85%	28.9	5.7	7.6	12.7	2.1	3.9
Flat 85%	25.6	5.0	6.8	10.7	1.9	3.4

Table A.2: S/\sqrt{B} for various b -tagging working points, in SR800 and SR1100. The chosen working point is Fixed 77% and is shown in bold.

	$m_{\tilde{t}} = 1000$ GeV		$m_{\tilde{t}} = 1200$ GeV		$m_{\tilde{t}} = 1400$ GeV	
	SR800	SR1100	SR800	SR1100	SR800	SR1100
Fixed 70%	8488	762	278	2827	3465	3193
Flat 70%	10210	1001	4489	3720	4827	4491
Fixed 77%	9722	901	4092	3336	4200	3867
Flat 77%	11015	1099	4909	4054	5268	4895
Fixed 85%	11041	1079	4845	3962	5108	4733
Flat 85%	11823	1204	5313	4369	5781	5368

Table A.3: Raw number of signal Monte Carlo events for various b -tagging working points, in SR800 and SR1100. The chosen working point is Fixed 77% and is shown in bold.

	$t\bar{t}$		Single top		Z/γ^* +jets		W +jets		Other	
	SR800	SR1100	SR800	SR1100	SR800	SR1100	SR800	SR1100	SR800	SR1100
Fixed 70%	19	1	34	1	65	26	2	2	14	2
Flat 70%	28	5	53	10	127	49	4	2	23	3
Fixed 77%	26	3	45	6	97	41	4	2	20	2
Flat 77%	39	9	63	12	183	76	7	4	40	8
Fixed 85%	35	6	63	13	193	69	8	3	30	6
Flat 85%	62	15	72	14	363	139	13	5	67	19

Table A.4: Raw number of background Monte Carlo events for various b -tagging working points, in SR800 and SR1100. The chosen working point is Fixed 77% and is shown in bold.

	$m_{\tilde{t}} = 1000$ GeV		$m_{\tilde{t}} = 1200$ GeV		$m_{\tilde{t}} = 1400$ GeV	
	SR800	SR1100	SR800	SR1100	SR800	SR1100
Fixed 70%	60.751	5.432	14.616	11.997	3.790	3.507
Flat 70%	74.528	7.346	19.405	16.091	5.358	4.997
Fixed 77%	70.139	6.483	17.508	14.338	4.631	4.278
Flat 77%	80.201	8.068	21.282	17.581	5.839	5.439
Fixed 85%	80.320	7.801	21.149	17.268	5.749	5.350
Flat 85%	86.343	8.867	23.033	18.874	6.433	5.985

Table A.5: Expected number of signal Monte Carlo events for various b -tagging working points, in SR800 and SR1100. The chosen working point is Fixed 77% and is shown in bold.

	$t\bar{t}$		Single top		Z/γ^* +jets		W +jets		Other	
	SR800	SR1100	SR800	SR1100	SR800	SR1100	SR800	SR1100	SR800	SR1100
Fixed 70%	0.757	0.037	1.415	0.038	0.881	0.315	-0.003	-0.003	0.562	0.121
Flat 70%	1.200	0.183	2.325	0.436	1.341	0.456	0.013	-0.008	0.696	0.243
Fixed 77%	1.103	0.116	1.984	0.298	1.236	0.434	0.022	-0.002	0.561	0.116
Flat 77%	1.640	0.397	2.805	0.509	1.914	0.692	0.042	0.010	1.260	0.582
Fixed 85%	1.531	0.256	2.833	0.572	2.583	0.774	0.070	0.009	0.687	0.243
Flat 85%	2.474	0.589	3.102	0.601	4.188	1.146	0.126	0.035	1.520	0.723

Table A.6: Expected number of background Monte Carlo events for various b -tagging working points, in SR800 and SR1100. The chosen working point is Fixed 77% and is shown in bold.

APPENDIX B

Wino Search: Truth Final States

This section shows a breakdown of the final states which typically fall into each reconstruction algorithm (OneLeg or TwoLeg).

Figure B.1 shows the acceptance of each truth final state in each signal region, before any SR cuts except lepton multiplicity and ZZ rejection via the $4\ell 2Z$ criterion. Each truth final state is represented by a bin on the x -axis, where the bins are defined below. It is clear from Figure B.1 that usually the majority of truth final states in a given SR are the targeted final states. This is shown more explicitly in Figure B.2, which collapses the 100+ bins in Figure B.1 into four: targeted final states for each signal region, and “not targeted” for the final states that are not explicitly targeted in any of the signal regions. This includes, for example, final states with a tau instead of a light lepton on the $\tilde{\chi}_1^\pm \rightarrow Z\ell \rightarrow \ell\ell\ell$ leg (leptonically decaying taus are also considered to be “not targeted”).

While the majority of final states in each SR are the targeted final states, there is a noticeable amount of “final state migration”, i.e. when a final state that is targeted for one SR falls in another. This can usually be explained by one of two situations. The first is when objects are not reconstructed or do not pass selection criteria, due to an acceptance and efficiency lower than unity. This situation explains why final states targeted for SROL4 ℓ or SRTL fall in SROL3 ℓ , and why final states targeting SRTL fall in SROL4 ℓ . The second situation that explains final state migration is that the decay products of taus or Higgs are used as signal objects in the event. For example, final states targeting SROL3 ℓ can be reconstructed in SROL4 ℓ or SRTL if the fourth lepton is a tau that decays leptonically, or if a Higgs decays to WW and one of these bosons subsequently decays leptonically.

The following list of truth final states defines the bins used in Figure B.1. In these definitions, the capitalized characters are the bosons from each wino decay leg. The following characters are

the decay products of each respective boson, and the final character (or the last character before the next boson) is the other direct wino daughter. In this notation, “t” denotes a tau lepton. Note that tau and Higgs decay products (aside from $b\bar{b}$) are essentially ignored, so there could be more leptons in a given final state than the notation here suggests.

C1C1

Zℓ Zℓ

ZlllZlll=1, ZlllZjjl=2, ZlllZvvl=3, ZlllZttl=4, ZlllZllt=5, ZlllZjjt=6, ZlllZvvt=7, ZlllZttt=8, ZlltZjjl=9, ZlltZvvl=10, ZlltZttl=11, ZlltZllt=12, ZlltZjjt=13, ZlltZvvt=14, ZlltZttt=15, ZttlZjjl=16, ZttlZvvl=17, ZttlZttl=18, ZttlZjjt=19, ZttlZvvt=20, ZttlZttt=21, ZtttZjjl=22, ZtttZvvl=23, ZtttZjjt=24, ZtttZvvt=25, ZtttZttt=26,

Zℓ Hℓ

ZlllHbb=27, ZlllHWW=28, ZlllHother=29, ZlllHbbt=30, ZlllHWWt=31, ZlllHother=32, ZlltHbb=33, ZlltHWW=34, ZlltHother=35, ZlltHbbt=36, ZlltHWWt=37, ZlltHother=38, ZttlHbb=39, ZttlHWW=40, ZttlHother=41, ZttlHbbt=42, ZttlHWWt=43, ZttlHother=44, ZtttHbb=45, ZtttHWW=46, ZtttHother=47, ZtttHbbt=48, ZtttHWWt=49, ZtttHother=50,

Zℓ Wν

ZlllWjjv=51, ZlllWlvv=52, ZlllWtvv=53, ZlltWjjv=54, ZlltWlvv=55, ZlltWtvv=56, ZttlWjjv=57, ZttlWlvv=58, ZttlWtvv=59, ZtttWjjv=60, ZtttWlvv=61, ZtttWtvv=62,

C1N1

Zℓ Wℓ

ZlllWjjl=63, ZlllWlvl=64, ZlllWtv=65, ZlltWjjl=66, ZlltWlvl=67, ZlltWtv=68, ZttlWjjl=69, ZttlWlvl=70, ZttlWtv=71, ZtttWjjl=72, ZtttWlvl=73, ZtttWtv=74,

ZlllWjjt=75, ZlllWlvt=76, ZlllWtv=77, ZlltWjjt=78, ZlltWlvt=79, ZlltWtv=80, ZttlWjjt=81, ZttlWlvt=82, ZttlWtv=83, ZtttWjjt=84, ZtttWlvt=85, ZtttWtv=86,

Zℓ Zν

ZlllZllv=87, ZlllZjjv=88, ZlllZvvv=89, ZlllZttv=90, ZlltZllv=91, ZlltZjjv=92, ZlltZvvv=93, ZlltZttv=94, ZttlZllv=95, ZttlZjjv=96, ZttlZvvv=97, ZttlZttv=98, ZtttZllv=99, ZtttZjjv=100, ZtttZvvv=101, ZtttZttv=102,

Zℓ Hν

ZlllHbbv=103, ZlllHWWv=104, ZlllHotherv=105, ZlltHbbv=106, ZlltHWWv=107, ZlltHotherv=108, ZttlHbbv=109, ZttlHWWv=110, ZttlHotherv=111, ZtttHbbv=112, ZtttHWWv=113, ZtttHotherv=114,

lostLeg=115 (when some truth decay information was lost),

other=0 (unwanted final states, where leptonic Z came from Higgs decay)

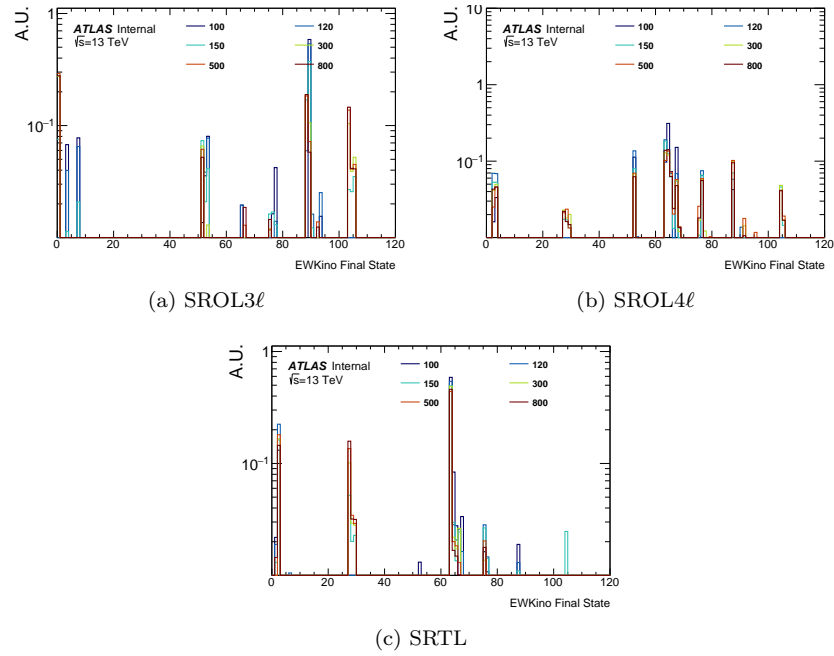


Figure B.1: Acceptance of each truth final state in SROL3 ℓ (a), SROL4 ℓ (b), and SRTL (c), for several wino mass points.

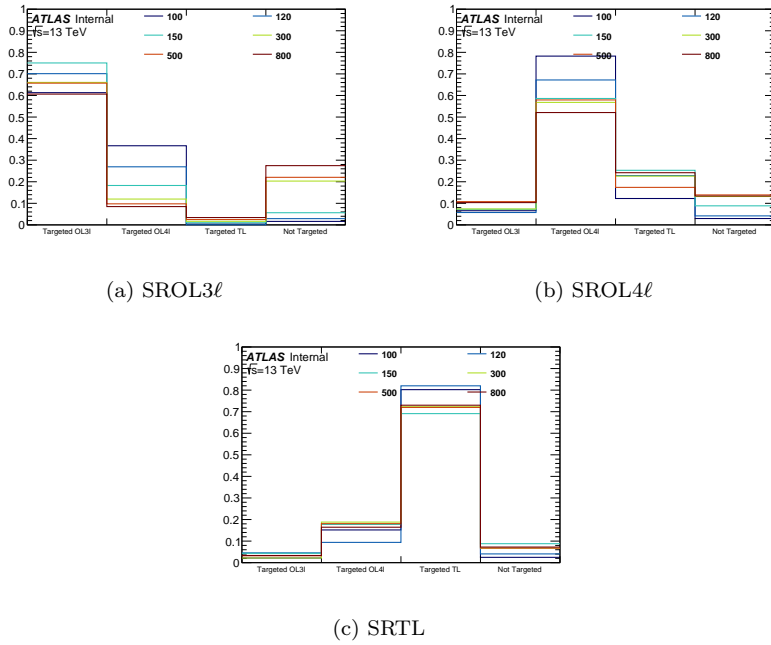


Figure B.2: Acceptance of targeted truth final states in SROL3 ℓ (a), SROL4 ℓ (b), and SRTL (c), for several wino mass points.

APPENDIX C

Wino Search: SROL4 ℓ Object Matching

This section describes the optimization that went into matching leptons to reconstruct the trilepton leg in SROL4 ℓ .

C.1 OL4 ℓ m_{Zl} optimization

Reconstructing the chargino mass is particularly challenging in the OL4 ℓ region. While the two leptons from the Z decay are relatively easy to identify via the SFOS and $m_{\ell\ell}$ window requirements, it is difficult to choose the correct lepton to pair with the Z to reconstruct the chargino. A particular matching scheme may work well for some range of chargino masses but poorly for another. For example, choosing the third lepton via minimizing $\Delta R(Z, \ell)$ has a high efficiency at low chargino mass when the winos are boosted, but a low efficiency at high mass when the winos are nearly at rest in the lab frame.

While many schemes were studied, the most promising was a “hybrid” method, which involves using different schemes depending on the value of some proxy for the chargino mass. Ultimately, the scalar sum of the all lepton transverse momenta, L_T , was chosen as this mass proxy. The L_T distributions in the OL4 ℓ region are shown in Figure C.1 for a range of chargino masses. Below some L_T value, the third lepton is chosen via minimizing $\Delta R(Z, \ell)$. Above, the third lepton is chosen via maximizing $m_{Z\ell}$.

Figure C.2 shows the efficiency for choosing the correct three leptons for a range of chargino masses and L_T cuts. When calculating this correct lepton selection efficiency, events are only considered if they have reconstructed all three leptons from a single chargino. This way, the hybrid matching scheme actually has a chance of choosing the correct leptons.

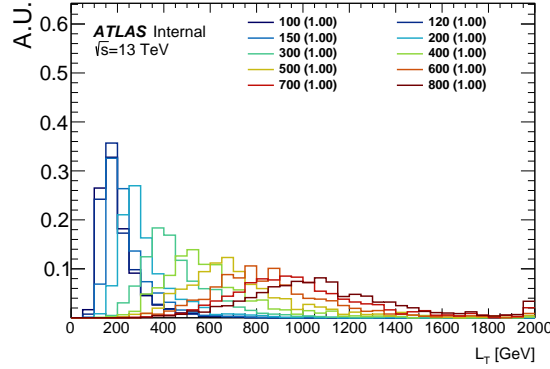


Figure C.1: The unit-normalized L_T distributions for various wino masses in C1C1 OL4 ℓ event types (as defined in Figure 6.2, before any of the event selections in Table 6.9 applied).

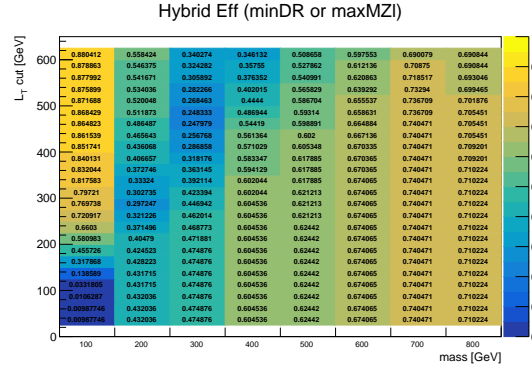


Figure C.2: The correct lepton selection efficiency as a function of L_T cut and wino mass in C1C1 OL4 ℓ event types (as defined in Figure 6.2, before any of the event selections in Table 6.9 applied). The efficiency only considers events where all three leptons from a chargino decay are present at reconstruction level and pass the signal lepton requirements. Below the L_T cut on the y -axis, the third lepton is chosen by minimizing $\Delta R(Z, \ell)$. Otherwise, the third lepton is chosen by maximizing $m_{Z\ell}$.

While informative, Figure C.2 does not indicate which value of the L_T cut maximizes sensitivity. Choosing the correct three leptons more often will increase the size of the $m_{Z\ell}$ resonance if the signal is present, but the background must also be considered. A particular matching scheme may have a lower efficiency for choosing the three correct leptons, but a higher signal significance if it pushes the background away from the signal resonance. Also, events with incorrect $Z\ell$ pairings and therefore non-resonant $m_{Z\ell}$ values still contribute to the sensitivity in a shape fit. As a result, the optimal matching scheme (and in the case of the hybrid method, the optimal L_T cut) must be chosen using the statistical power of HistFitter.

C.2 HistFitter-based OL4 ℓ optimization

With no clear OL4 ℓ lepton matching choice that gives the best performance for all mass points, it is useful to compare the exclusion limit potential of each choice by running through the full HistFitter machinery. This was performed in SROL4 ℓ for each C1C1 mass point for the following lepton matching schemes:

- minDR: choose lepton closest in ΔR to Z
- min: choose lepton to minimize $m_{Z\ell}$
- max: choose lepton to maximize $m_{Z\ell}$
- hybrid: if $L_T < L_T$ cut, use minDR, else use max $m_{Z\ell}$
- hybrid_minmax: if $L_T < L_T$ cut, use min $m_{Z\ell}$, else use max $m_{Z\ell}$

Different values are also tested for the L_T cut, from 200 to 800 GeV. The results from these comparisons can be seen in Figure C.3, which shows the 95% CL upper limit on the C1C1 signal strength $\sigma/\sigma_{\text{SUSY}}$ for each of these schemes and for a range of wino mass points. There are two sets of error bars on each point: one for $\pm 1\sigma$ and one for $\pm 2\sigma$. Errors only include statistical uncertainties. On each plot there is one filled point for each mass point. This filled point marks the lowest limit achieved for this mass point, and is labeled “min” on the legend.

It can be seen that for a given mass point, the lepton matching scheme gives very little difference in the upper limit, except for a few cases for the low mass points. As before, the optimal lepton

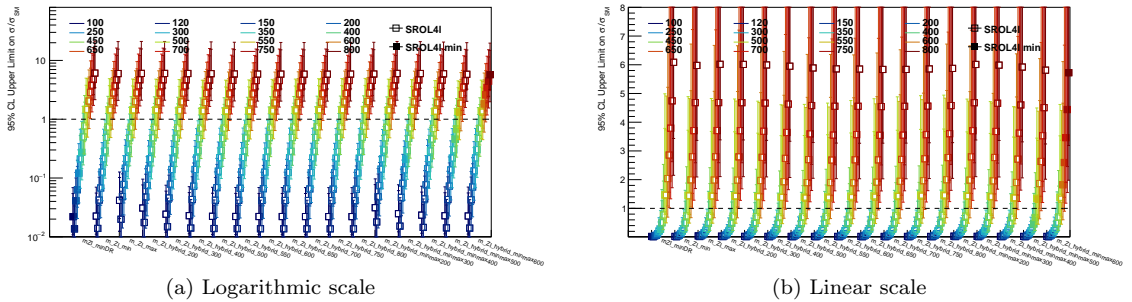


Figure C.3: 95% CL upper limit on the signal strength $\sigma/\sigma_{\text{SUSY}}$ for each C1C1 mass point in SROL4 ℓ , for various lepton matching schemes. The numbers in the bin labels represent the L_T cut used for this scheme. On each plot there is one filled point for each mass point. This filled point marks the lowest limit achieved for this mass point, and is labeled “min” on the legend.

matching scheme is different for the low masses and the high masses. For this reason we additionally consider the relative difference between each scheme and the best-performing scheme for each mass point, to see if, for all mass points, one scheme performs similarly to each mass point’s preferred scheme. This relative difference is shown in Figure C.4, where it is clear that for all mass points, the limits achieved by hybrid550 are $< 10\%$ larger than the limits achieved by each mass point’s optimal scheme. Consequentially hybrid550 is chosen as the lepton matching scheme for SROL4 ℓ .

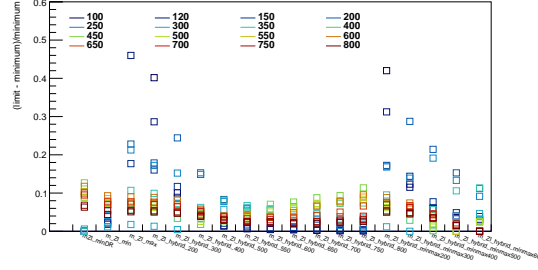


Figure C.4: Relative difference between each lepton matching scheme and the best-performing scheme (“minimum”) for each C1C1 mass point.

APPENDIX D

Wino Search: Bin Size Optimization

It is crucial to optimize the bin width used in the $m_{Z\ell}$ distribution, to ensure that the discovery potential of the shape fit used in this analysis is maximized. As explained in Appendix A, it is important to balance the maximization of sensitivity against the assurance that there are enough background statistics to avoid large uncertainties. Additionally, the full sensitivity can only be appreciated by running a simultaneous fit of the signal and background in all SRs through the full HistFitter machinery, to take into account correlations across SR types and $m_{Z\ell}$ bins. This, however, is computationally time consuming and therefore would be very laborious to use as the main procedure for optimizing bin width. For this reason the optimization is performed in two steps: A first-pass optimization is performed by considering the sensitivity in individual $m_{Z\ell}$ bins, which will be explained in Appendix D.1. Then the final optimization is chosen by comparing sensitivities achieved in HistFitter, as explained in Appendix D.2.

D.1 Optimization Based On Individual Bins

The sensitivity metric Z_N is computed in each bin of the $m_{Z\ell}$ distribution in each SR independently, as shown using a 60 GeV binning in Figure D.1. It is reasonable to expect that this fixed binning does not provide the best sensitivity, as it does not take advantage of the changing resolution of the mass peak across the full $m_{Z\ell}$ range.

Figure D.2 shows the sensitivity that can be achieved by using a variable bin width. The histograms are switched to a finer binning to better see the shapes of the signal. The Z_N is then maximized for each mass point by using the standard optimization function contained in the SciPy software package [198]. It can be seen that in general, low mass points prefer narrower bins and

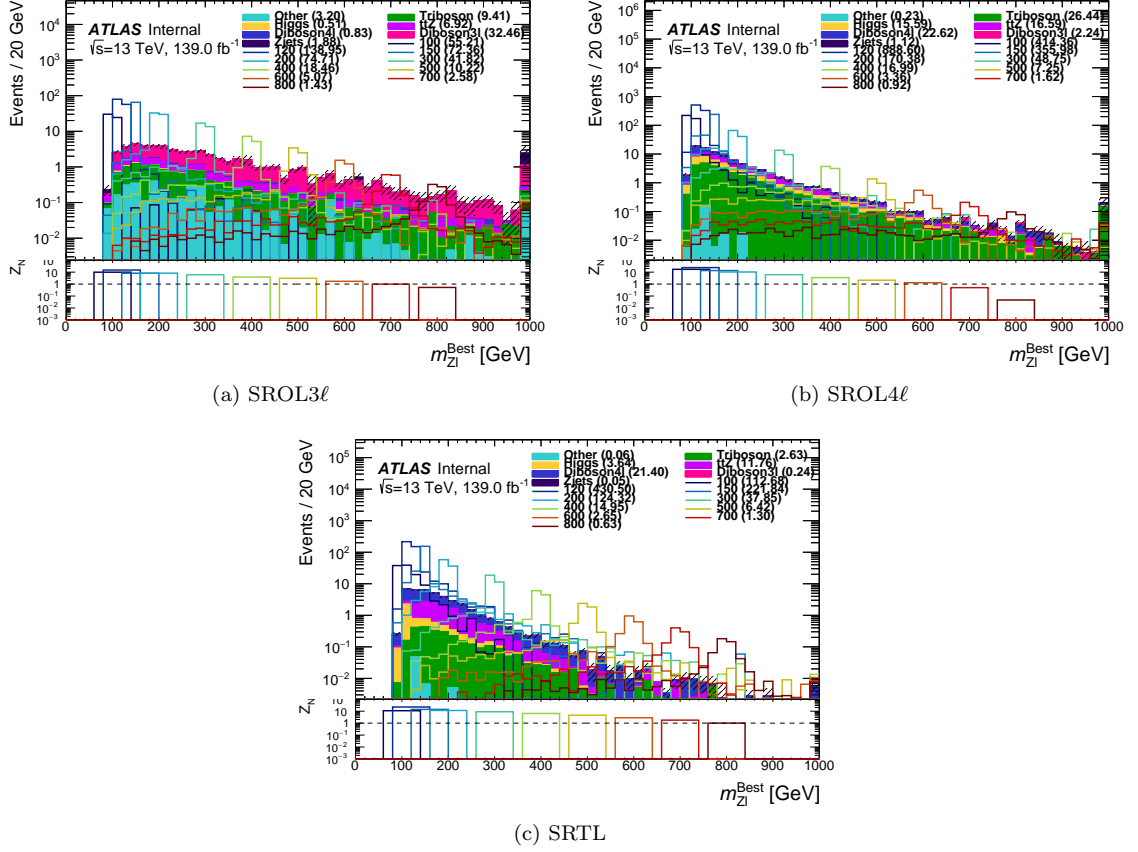


Figure D.1: $m_{Z\ell}$ distributions with corresponding Z_N ratio plots in each of the signal regions. This Z_N is computed using a 60 GeV window centered at the generated mass for each signal mass point.

high mass points prefer wider bins.

D.2 Optimization Based On HistFitter

It is useful to further optimize the bin sizes using the full statistical treatment from HistFitter. This is particularly true because it is possible that a mass peak falls in two $m_{Z\ell}$ bins, and only a statistical combination of these bins will show the true sensitivity of a signal. A comparison of C1C1 exclusion limits was performed for each mass point using several bin width options. The bin width that provides the best exclusion limit for a given $m_{Z\ell}$ range was then chosen. Because each SR can have its own optimal binning (mostly driven by the varying amount of statistics), each SR is optimized separately. Additionally, since the optimal binning for high $m_{Z\ell}$ will be coarse, fine granularity bin widths are tested up to some reasonable maximum value as shown in Table D.1.

Figure D.3 shows the upper limit on C1C1 signal strength $\sigma/\sigma_{\text{SUSY}}$ for each mass point in each SR. There are two sets of error bars on each point: one for $\pm 1\sigma$ and one for $\pm 2\sigma$. Errors only include statistical uncertainties. On each plot there is one filled point for each mass point. This filled point marks the lowest limit achieved for this mass point, and is labeled “min” on the legend. These

distributions clearly show that the exclusion potential is much better by using a shape fit rather than a single bin fit, which is effectively shown in the limits to the far right of each distribution. Additionally, the lower mass points benefit from a finer binning because of their finer resolution, whereas the higher mass points prefer a coarser binning, due to the small amount of background statistics in the regions where they dominate. It can also be seen that the relative performance of each binning choice does not change much from SR to SR, so one binning scheme can be chosen for all SRs.

There are some fluctuations between 15 and 20 GeV for the low mass points' optimal bin width. To avoid using a bin width smaller than the mass resolution of these points, the 20 GeV width is chosen between 90 and 270 GeV. A 30 GeV width is chosen between 270 and 360 GeV, to cover the optimal width for the 300 and 350 GeV mass points, and similarly a 40 GeV width is chosen between 360 and 440 GeV.

Beyond 440 GeV, a second scan is performed over the full nominal $m_{Z\ell}$ distribution, to avoid the changing maximum value performed in this scan as listed in Table D.1. The results of this scan be seen in Figure D.4. This uses the chosen binning for $m_{Z\ell} < 440$ GeV, so the bin widths shown here are only valid between 440 and 1000 GeV. Since the chosen binning in this range will predominantly affect the limits for the middle and high mass points, this scan compared upper limits set for masses 350 GeV and above.

These plots show that the lowest mass points in each SR and the high mass points in SRTL are agnostic to bin width. The mid-range mass points achieve the best limits with a bin width around 140 GeV. The chosen high- $m_{Z\ell}$ binning is therefore 140 GeV between 440 and 580 GeV, and inclusive after that. The final $m_{Z\ell}$ binning is shown in Table D.2.

Bin width [GeV]	$m_{Z\ell}$ range [GeV]
20	[90, 270)
30	[270, 360)
40	[360, 440)
140	[440, 580)
Inclusive	[580, ∞)

Table D.2: The chosen binning for the shape fit of the $m_{Z\ell}$ distribution.

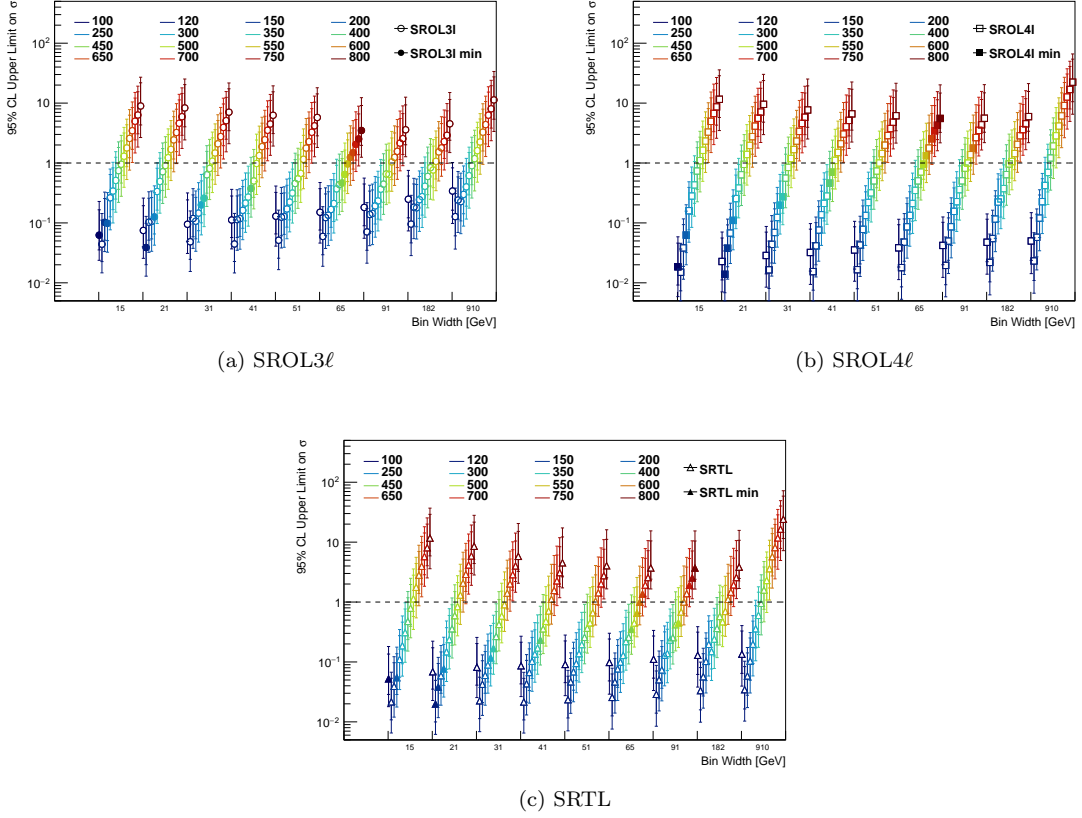


Figure D.3: Upper limit on C1C1 $\sigma/\sigma_{\text{SUSY}}$ as a function of bin width, for each mass point in each SR. Each tested bin spans an $m_{Z\ell}$ range from 90 GeV to the maximum given in Table D.1. There are two sets of error bars on each point: one for $\pm 1\sigma$ and one for $\pm 2\sigma$. Errors only include statistical uncertainties. On each plot there is one filled point for each mass point. This filled point marks the lowest limit achieved for this mass point, and is labeled “min” on the legend. In SROL4 ℓ , the lepton closest in ΔR to the leptonic Z is assigned to the $m_{Z\ell}$ leg.

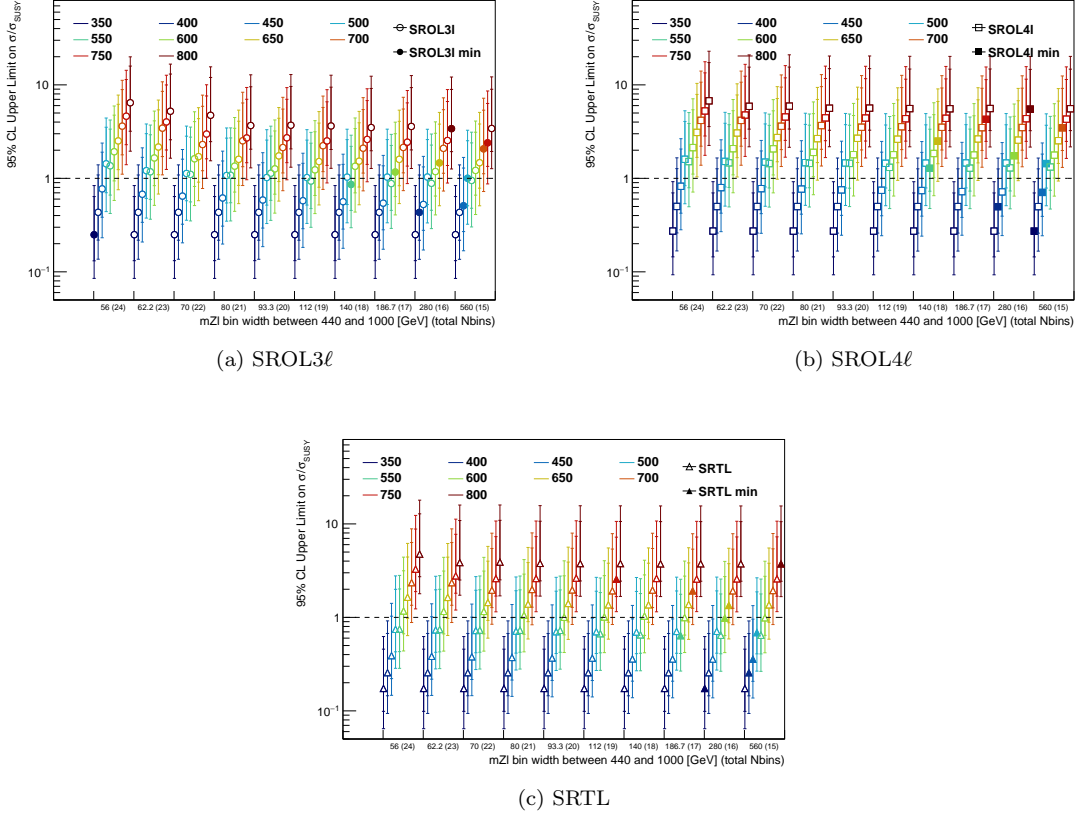


Figure D.4: Upper limit on C1C1 $\sigma/\sigma_{\text{SUSY}}$ as a function of bin width, for mass points 350 GeV and above in each SR. Each tested bin spans an $m_{Z\ell}$ range from 440 to 1000 GeV. Below this, the binning chosen from the first scan is used. The x -axis labels also show the total number of bins in each SR given each high-mass bin width. There are two sets of error bars on each point: one for $\pm 1\sigma$ and one for $\pm 2\sigma$. Errors only include statistical uncertainties. On each plot there is one filled point for each mass point. This filled point marks the lowest limit achieved for this mass point, and is labeled “min” on the legend. In SROL4 ℓ , the lepton closest in ΔR to the leptonic Z is assigned to the $m_{Z\ell}$ leg.

APPENDIX E

Wino Search: Lepton ID Working Point Comparison

In the wino search, several lepton ID working points (WPs) were considered to optimize signal efficiency as well as true and fake lepton multiplicities. In this section, for ease and simplicity of CPU, samples with each tested WP were only processed with mc16d, and only the largest backgrounds (Z/γ^* +jets, WZ , and ZZ). Additionally, jobs scanned both electron and muon WPs at the same time. In order to separate these effects, the distributions shown in the electron section have a muon veto. The distributions in the muon section do not have an electron veto, because jobs were rerun with the chosen electron WP. All distributions shown are in the preselection region.

E.1 Electrons

Medium and Tight likelihood electron WPs are compared here. Because of a difference in muon WP between the job sets, distributions in this section have a muon veto.

Figure E.1 shows the truth and fake electron multiplicities for both Medium and Tight likelihood WPs. The numbers in the legend show the mean of each distribution. Because of the muon veto, all the distributions here are shifted to higher values (because there are no events with fewer than 3 electrons, whether real or fake). Here it is clear that there are very small differences ($< 1\%$) between Medium and Tight WPs in terms of average truth and fake electrons per event, so there is no preference for one WP over the other.

Figure E.2 shows the signal efficiency in preselection for both Medium and Tight likelihood electron WPs. Here the efficiency with the Medium WP is a few percent higher than that with the Tight WP. Since there is no difference in the truth and fake electron multiplicities, this is a

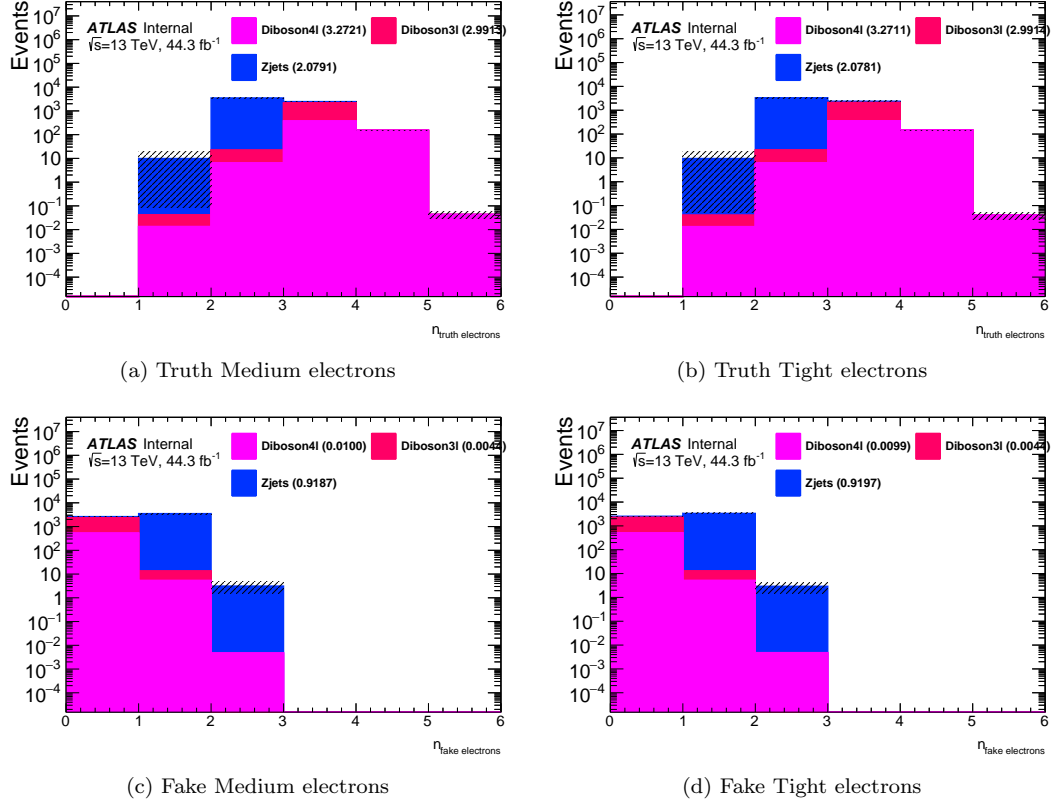


Figure E.1: True and fake electron multiplicity for each WP choice. The numbers in the legend show the mean of each distribution. There is no large difference in the truth or fake electron multiplicity depending on WP scheme.

reasonable motivation to prefer the Medium likelihood WP over Tight.

E.2 Muons

Medium and HighPt likelihood muon WPs are compared here. The Medium electron WP is used in both sets of jobs, so there is no electron veto in these distributions.

Figure E.3 shows the truth and fake muon multiplicities for both Medium and HighPt WPs. The numbers in the legend show the mean of each distribution. Medium has roughly 20-25% more truth muons per event than HighPt in all three major backgrounds. Medium also has roughly 25% more fake muons per event than HighPt in $Z/\gamma^* + \text{jets}$ (but the mean is still only 0.25), and for WZ and ZZ the averages are identical for both Medium and HighPt. This suggests a preference for Medium, since the $Z/\gamma^* + \text{jets}$ yields in our SRs are actually quite small.

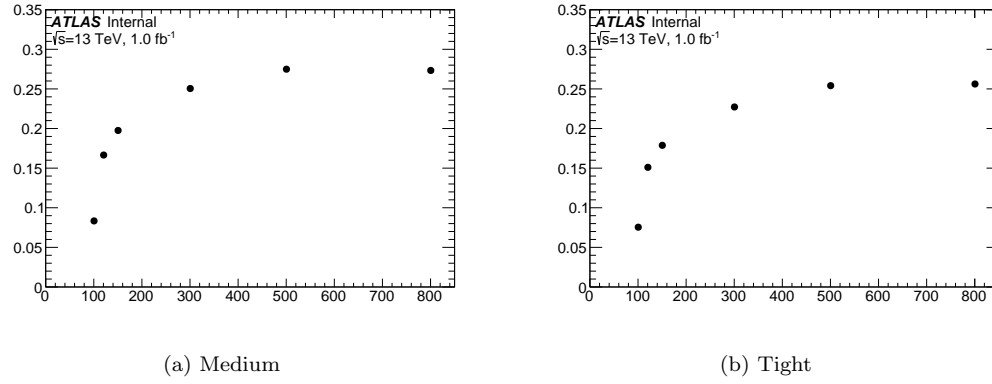


Figure E.2: Signal efficiency as a function of signal mass (in GeV) for each WP choice in the preselection region. There is a few-percent improvement in efficiency by using the Medium WP.

Figure E.4 shows the signal efficiency in preselection for both Medium and HighPt muon WPs. Here the efficiency with the Medium WP is significantly higher than that with the HighPt WP, across all chargino masses. This further confirms our decision to choose the Medium WP.

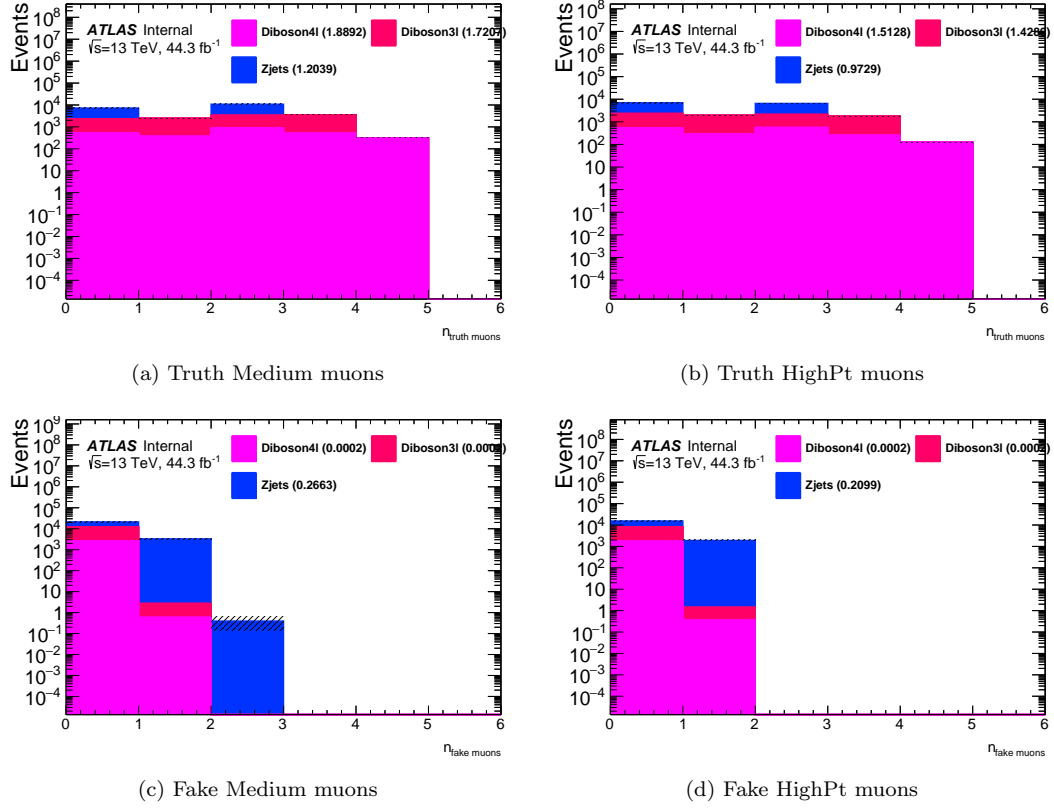


Figure E.3: True and fake muon multiplicity for each WP choice. The numbers in the legend show the mean of each distribution. The mean number of truth muons is 20-25% larger in Medium than in HighPt for all three major backgrounds, and the mean number of fake muons is 25% larger in Medium than in HighPt only for $Z/\gamma^* + \text{jets}$ (where the mean is still only 0.25), and identical for WZ and ZZ .

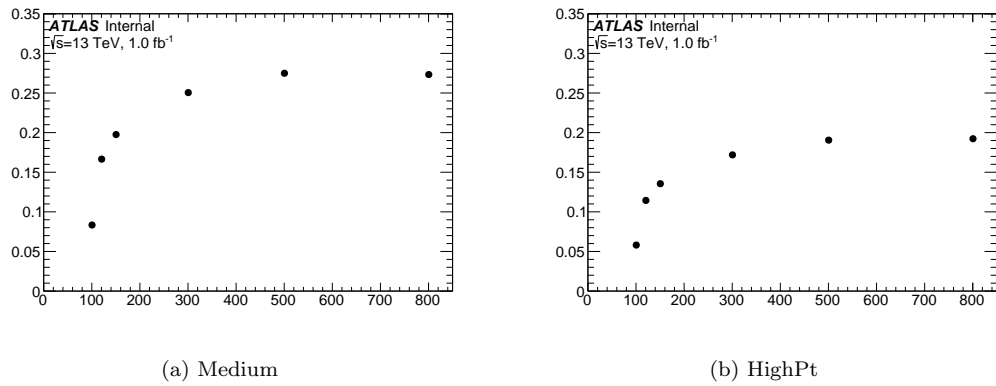


Figure E.4: Signal efficiency as a function of signal mass (in GeV) for each WP choice in the preselection region. There is a large improvement in efficiency by using the Medium WP.

APPENDIX F

Wino Search: Overlap Removal

This section explains the decision to apply a p_T -dependent heavy-flavor-aware overlap removal scheme. In Release 20.7 it was standard to remove electrons and muons within $\Delta R(\ell, b\text{-jet}) \leq 0.2$ of a b -jet, since they were likely products of a semi-leptonic b -decay. However in Release 21, a large drop in real electron efficiency at $p_T > 100$ GeV was found to be due to this overlap removal scheme, so it became standard to remove all jets within 0.2 of a lepton to regain electron efficiency. An alternative proposal for analyses with real b -jets was a p_T -dependent overlap removal scheme, which favors b -jets with p_T below 100 GeV and turns off the heavy-flavor dependency for b -jets with larger p_T . Since the wino signal can have real b -jets (from either a Higgs or Z decay), it is worthwhile to compare these overlap removal schemes in terms of b -jet multiplicity, true and fake electrons, and signal efficiency.

In this section, for ease and simplicity of CPU, samples with each OR scheme were only processed with data17 and mc16d, and only the largest backgrounds ($Z/\gamma^* + \text{jets}$, WZ , and ZZ). All distributions shown are in the preselection region.

The following nomenclature is used in this section. “HFS” refers to the “heavy-flavor selecting” scheme, which rejects all leptons within 0.2 of a b -jet. “HFR” refers to the “heavy-flavor rejecting” scheme, which rejects all jets (heavy flavor or otherwise) within 0.2 of a lepton. “pTD” refers to the p_T -dependent scheme: if the b -jet has $p_T < 100$ GeV, do HFS; else do HFR.

Figure F.1 shows the b -jet multiplicity for each OR scheme. The numbers in the legend show the mean of each distribution for ease of comparison. The differences in average b -jet multiplicity are small at $< 5\%$ (usually closer to 3%). In terms of b -jet multiplicity, there is no strong preference for any of these OR schemes.

Figure F.2 shows the p_T distribution of the leading electron for each OR scheme. Here the drop

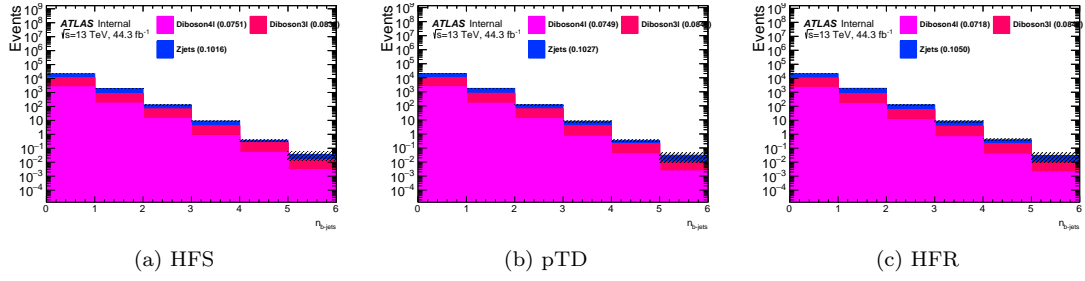


Figure F.1: b -jet multiplicity for each OR scheme. The numbers in the legend show the mean of each distribution. There is no large difference in the b -jet multiplicity depending on OR scheme.

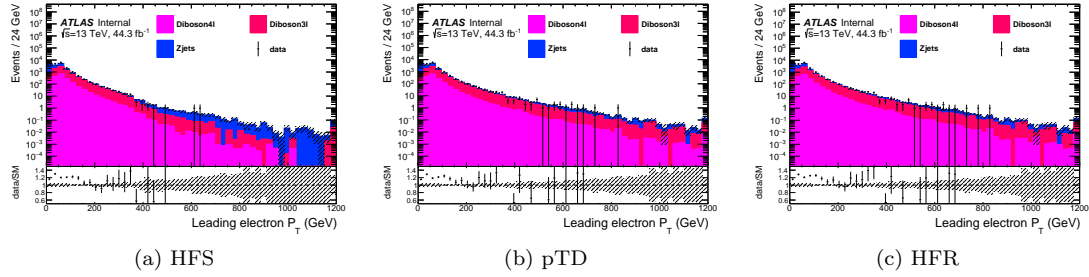


Figure F.2: Leading electron p_T for each OR scheme. The inefficiency from HFS is clearly visible.

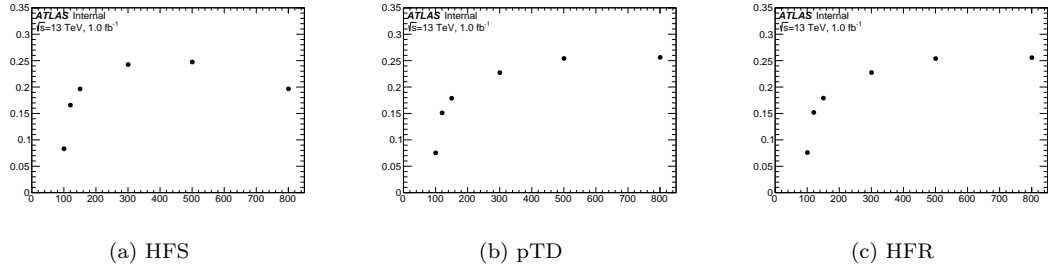


Figure F.3: Signal efficiency as a function of chargino mass (in GeV) for each OR scheme. The inefficiency from HFS is clearly visible.

in efficiency at high electron p_T using HFS is clearly visible, which gives strong motivation to move away from this scheme.

Figure F.3 shows the signal efficiency for each OR scheme. Here the drop in efficiency at high electron p_T using HFS is again clearly visible in the high mass points, which gives strong motivation to move away from this scheme. There is no visible difference in efficiency between pTD and HFR.

Figure F.4 shows the true electron multiplicity for each OR scheme. The numbers in the legend

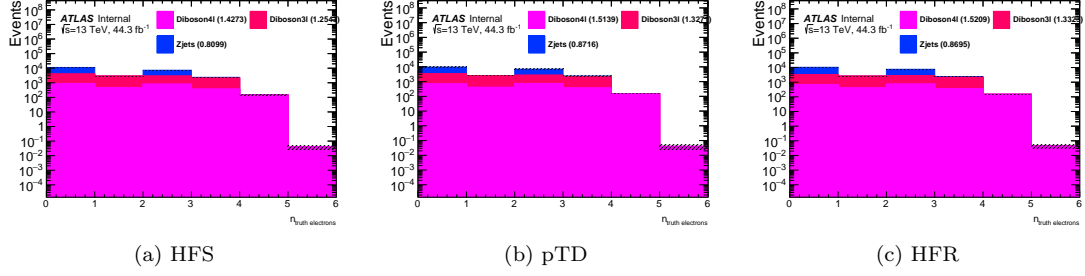


Figure F.4: True electron multiplicity for each OR scheme. The numbers in the legend show the mean of each distribution.

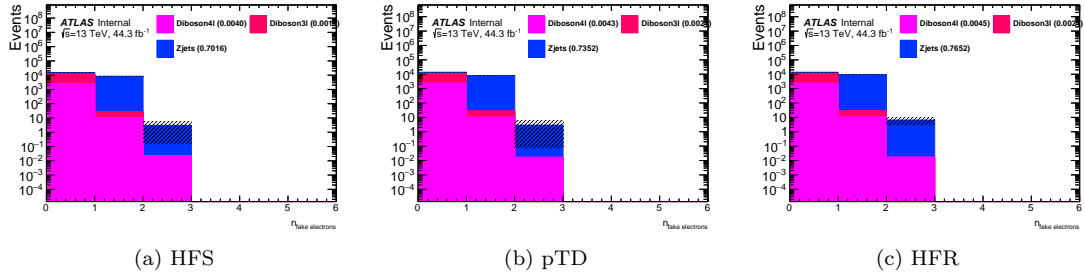


Figure F.5: Fake electron multiplicity for each OR scheme. The numbers in the legend show the mean of each distribution.

show the mean of each distribution. On average, HFR has roughly 6 or 7% more true electrons per event than HFS, and $< 1\%$ more than pTD.

Figure F.5 shows the fake electron multiplicity for each OR scheme. The numbers in the legend show the mean of each distribution. On average, HFR has roughly 10% more fake electrons per event than HFS, and 4 or 5% more than pTD.

There is little difference in the performance of pTD and HFR, except in the fake electron multiplicity distributions where pTD has slightly fewer fakes than HFR. For this reason pTD is chosen as the overlap removal scheme in this analysis.

APPENDIX G

Wino Search: Signal Contamination

This section describes the method by which a certain level of signal contamination is deemed acceptable in the CRs. The largest concern related to this effect is if a real low-mass signal appears in data and contaminates a CR. In this case the normalization factor (NF) derived in this CR will increase proportionately to the signal contamination ($\text{NF} \rightarrow \text{NF}(1 + S_{\text{CR}}/B_{\text{CR}})$), and the targeted process will consequently be overestimated in each SR. The total background estimate in an SR will then increase by roughly $B \rightarrow B(1 + P * S_{\text{CR}}/B_{\text{CR}})$, where P is the relative SR contribution of the background process being normalized. Then, if we estimate the sensitivity by S/\sqrt{B} , the sensitivity decreases by roughly $S/\sqrt{B} \rightarrow S/\sqrt{B}(1 + P * S_{\text{CR}}/B_{\text{CR}})^{-1/2}$.

This estimate only considers the dominant background in a given SR and ignores the fact that in each SR, the NFs will be combined from several estimated processes. However this effect should be small since WZ is small in the 4ℓ SRs, and ZZ is small in $\text{SROL}3\ell$.

Tables [G.1](#) and [G.2](#) show this effect for C1C1 signal contamination of several mass points, scaling the Z_N reported by RooStats according to the scheme above. It can be seen that there are no large differences in the expected sensitivity for any mass point in any signal region because of signal contamination in CRWZ or CRZZ. For signal mass points of 300 GeV or larger, the contamination is small enough that the sensitivity does not change.

Signal mass [GeV]	S_{CR}	$S_{\text{CR}}/B_{\text{CR}}$	SROL3 ℓ ($P=62.1\%$ WZ)		SROL4 ℓ ($P=5.1\%$ WZ)		SRTL ($P=1.3\%$ WZ)	
			Old Z_N estimate	New Z_N estimate	Old Z_N estimate	New Z_N estimate	Old Z_N estimate	New Z_N estimate
100	2156.480	0.153	6.89	6.58	17.03	16.96	12.37	12.36
120	2340.440	0.166	9.32	8.87	22.29	22.19	22.48	22.46
150	784.930	0.056	4.78	4.70	12.89	12.88	14.80	14.79
300	38.000	0.003	4.32	4.32	6.25	6.25	9.94	9.94

Table G.1: Effect of signal contamination on estimated sensitivity in CRWZ. The total background yield B_{CR} is 14060.

Signal mass [GeV]	S_{CR}	$S_{\text{CR}}/B_{\text{CR}}$	SROL3 ℓ ($P=3.5\%$ ZZ)		SROL4 ℓ ($P=28.9\%$ ZZ)		SRTL ($P=41.7\%$ ZZ)	
			Old Z_N estimate	New Z_N estimate	Old Z_N estimate	New Z_N estimate	Old Z_N estimate	New Z_N estimate
100	172.100	0.125	6.89	6.87	17.03	16.73	12.37	12.06
120	97.780	0.071	9.32	9.31	22.29	22.06	22.48	22.16
150	39.860	0.029	4.78	4.77	12.89	12.84	14.80	14.71
300	2.230	0.002	4.32	4.32	6.25	6.25	9.94	9.94

Table G.2: Effect of signal contamination on estimated sensitivity in CRZZ. The total background yield B_{CR} is 1382.

APPENDIX H

Wino search: 3ℓ Region Optimization

This section describes how the regions with 3 leptons were defined and optimized. All signal distributions in this section show C1C1 production with the nominal $\tilde{\chi}_1^\pm$ BR.

Figure H.1 shows the expected yields of each background, assuming 140 fb^{-1} , in SROL 3ℓ before any cuts. It is clear that $Z/\gamma^* + \text{jets}$ and Diboson 3ℓ , which is usually standard model WZ , are the major 3ℓ backgrounds. All the selections described in the following sections are designed to reject these major backgrounds.

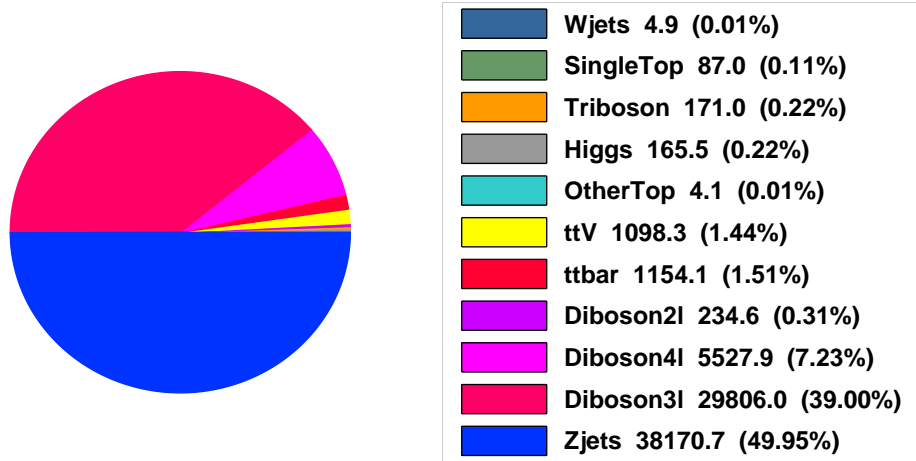


Figure H.1: Expected yields of each background in SROL 3ℓ , before any cuts, assuming 140 fb^{-1} . No normalization factors are applied.

Table H.1 shows the raw MC yields in each 3ℓ region for each background, given the cuts that will be described in this section. CRttZ and VRttZ are shown here as well as the corresponding 4ℓ table in Appendix I. The important processes have enough raw events in each region such that the

Process	CRWZ	CRttZ	VRMet	VRmTmin	VRttZ	SROL3 ℓ
WZ	1441584	12392	889417	59138	8239	6574
$t\bar{t}Z$	95786	174498	147251	6827	120151	6904
$Z/\gamma^* + \text{jets}$	3413	388	1680	884	187	33
ZZ	511479	6046	119830	34040	3337	832
Triboson	30632	825	36939	4355	543	10662
Higgs	355970	13647	119140	5205	9956	3700
Other	3016	2921	4793	397	2137	477

Table H.1: Raw MC yields for each background process in each 3ℓ region. CRttZ and VRttZ are shown here as well as the corresponding 4ℓ table in Appendix I.

Wino mass [GeV]	CRWZ	CRttZ	VRMet	VRmTmin	VRttZ
100	14	4.8	19	3.7	8.1
120	16	9.0	14	24	17
150	5.3	10	5.0	24	24
200	1.8	6.9	2.7	16	16
300	0.27	2.1	0.8	4.8	5.1
400	0.07	0.7	0.3	1.9	1.6
500	0.02	0.3	0.1	0.8	0.6
600	0.00	0.1	0.0	0.3	0.3
700	0.00	0.1	0.0	0.1	0.1
800	0.00	0.0	0.0	0.0	0.0

Table H.2: Signal contamination as a percentage of total background yield in each 3ℓ CR and VR.

analysis won't be statistics limited. Table H.2 shows the amount of signal contamination in each 3ℓ CR and VR, including CRttZ and VRttZ which are again repeated in the corresponding 4ℓ table. The signal contamination is shown as a percentage of the total background yield in each region.

H.1 SROL3 ℓ

The major 3ℓ backgrounds are $Z/\gamma^* + \text{jets}$ and Diboson3l, so all selections in SROL3 ℓ are designed to reduce these backgrounds. Figure H.2 shows the E_T^{miss} and m_T^{min} distributions, which show reasonable promise in background rejection. In the E_T^{miss} distribution the background is predominantly at lower values, as the expected E_T^{miss} is not large in $Z/\gamma^* + \text{jets}$ or WZ processes. In contrast, there is a large amount of expected E_T^{miss} in OneLeg processes, which can be seen in Figure H.3 which shows E_T^{miss} as a function of truth final state for each event that was reconstructed as OL3 ℓ for several mass points. Moreover, Figure H.4 shows that the resolution of $m_{Z\ell}$ improves at higher E_T^{miss} values, suggesting that a harder cut on E_T^{miss} favors events with a correctly reconstructed gaugino mass.

The Diboson3l distribution in m_T^{\min} has the expected edge near the W mass, and the $Z/\gamma^* + \text{jets}$ distribution is predominantly at very small values of m_T^{\min} , presumably because of the low E_T^{miss} . There is no such edge in the signal m_T^{\min} distribution, so this is also a promising variable. It was explained in Section 6.5 why m_T^{\min} is preferable to the standard m_T definition. This can be seen quantitatively in Figure H.5 which compares the two values for signal and background separately. For signal, m_T and m_T^{\min} are often the same quantity, whereas for background, m_T^{\min} more reliably shows the expected kinematic edge at the W mass. An alternative m_T^{\min} definition was tested, which selects the minimum m_T calculation in the same way as the standard m_T definition, with the additional requirement that there is a leftover SFOS lepton pair with $m_{\ell\ell}$ below 101 GeV. The reasoning behind this definition is to leave a more plausibly physical lepton pair for the Z candidate. However the sensitivity of this variable is not as high as the standard m_T sensitivity, since the background distribution shifts to higher values whereas the signal stays more or less the same (since m_T^{\min} is already usually the same as m_T in signal as in Figure H.5). A comparison of this alternate m_T^{\min} and the standard m_T^{\min} can be seen in Figure H.6.

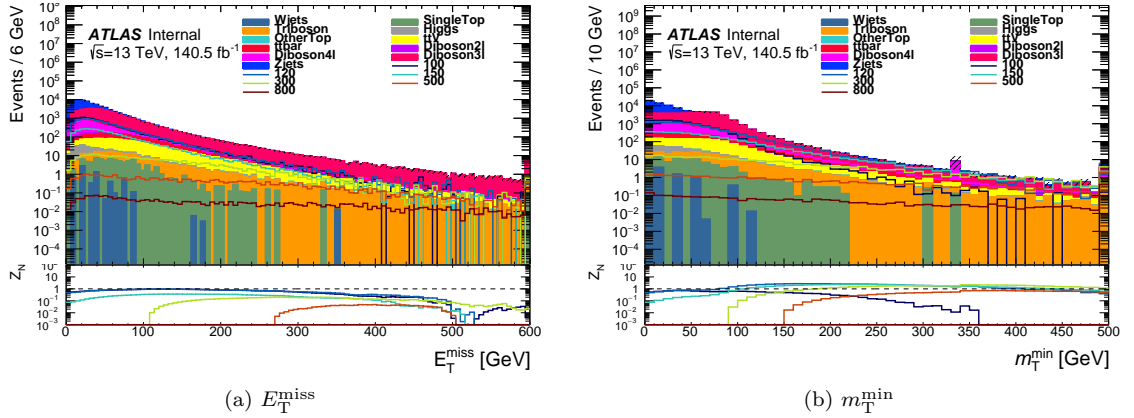


Figure H.2: Upper panel: E_T^{miss} (a) and m_T^{\min} (b) distributions for signal and background. Lower panel: Estimated sensitivity for each mass point obtained by the given lower cut on E_T^{miss} (a) and m_T^{\min} (b) with a flat 20% uncertainty.

Cuts on E_T^{miss} and m_T^{\min} were chosen to optimize sensitivity while preserving enough statistics for each signal and background. The distributions vary significantly as a function of chargino mass, so a compromise was chosen that would work well for high masses without cutting out too much of the low masses.

Figure H.7 shows S/\sqrt{B} as a function of lower cuts on m_T^{\min} and E_T^{miss} for several mass points. S/\sqrt{B} , where S is signal yield and B is background yield, is used as an estimate for sensitivity in

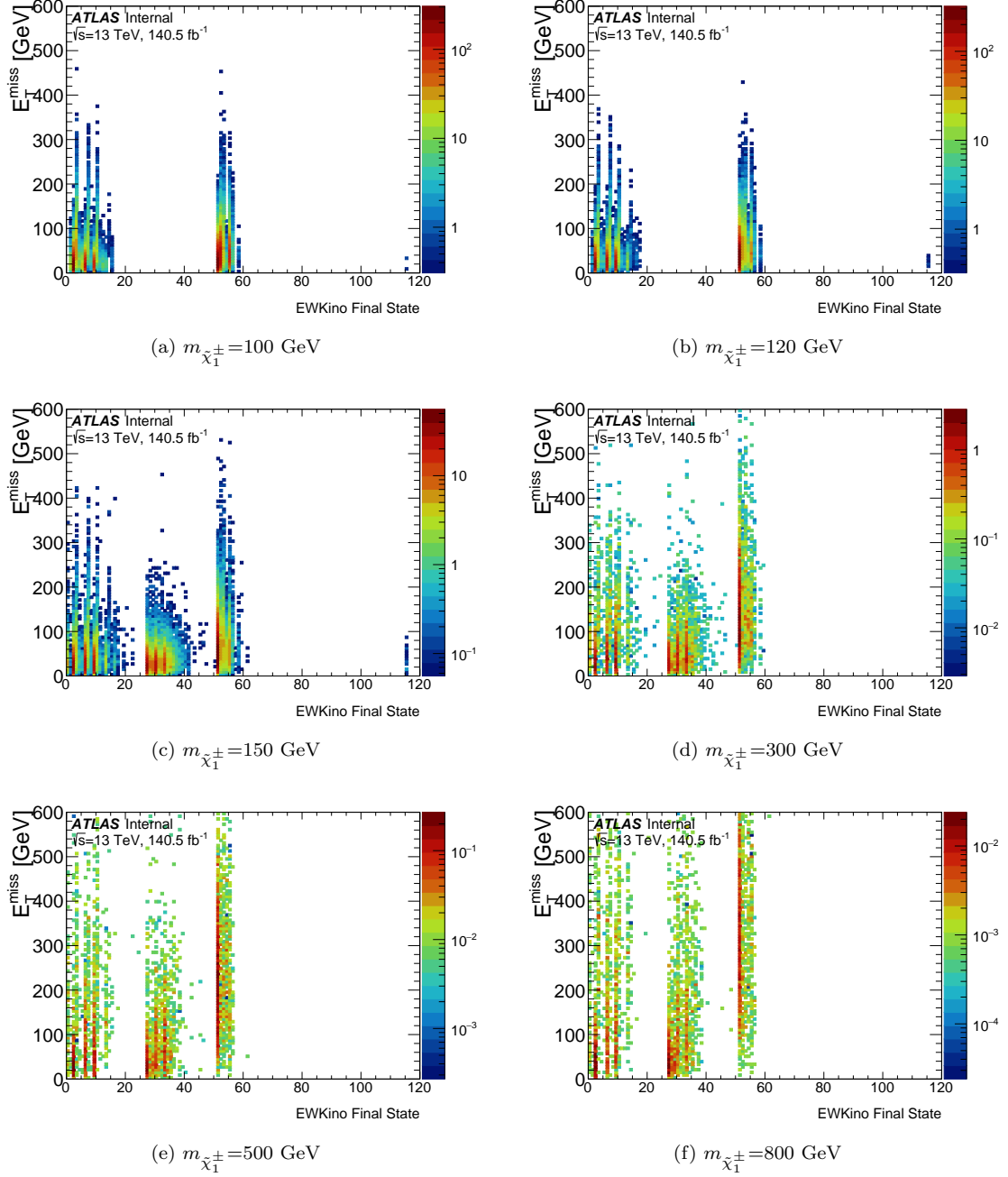


Figure H.3: E_T^{miss} distribution as a function of truth final state for each event that was reconstructed as OL3 ℓ , for several C1C1 mass points. The definitions of the truth final states can be found in Appendix B. Most of the final states that are targeted in OL3 ℓ have real E_T^{miss} .

these distributions. Note also that ultimately the sensitivity of this search will be determined by the $m_{Z\ell}$ distributions, which is not accounted for in these 2D distributions. These are simply used to determine the optimal cuts to remove background and maintain signal yields, with the understanding that the final sensitivity may be different than the values obtained here. Here it is clear that the maximum sensitivity for each mass point is achieved by very different cuts on m_T^{min} and E_T^{miss} , so some compromise is necessary. The selections $m_T^{\text{min}} > 125$ GeV and $E_T^{\text{miss}} > 150$ GeV were chosen as such a compromise, since they still have quite high sensitivities for the lower mass points, provide maximum sensitivities for the mid-range mass points, and leave enough raw background events to have enough statistics.

Since $m_{Z\ell}$ is the final discriminating variable of interest, it is interesting to compare the $m_{Z\ell}$ distributions before and after these m_T^{min} and E_T^{miss} cuts. Figure H.8 shows this comparison. After these cuts, the $m_{Z\ell}$ resolution in signal seems slightly improved, and the sensitivity is significantly improved. Figure H.9 also shows the background composition after these cuts. It is clear that WZ is now the dominant background, with ZZ and $t\bar{t}Z$ subdominant.

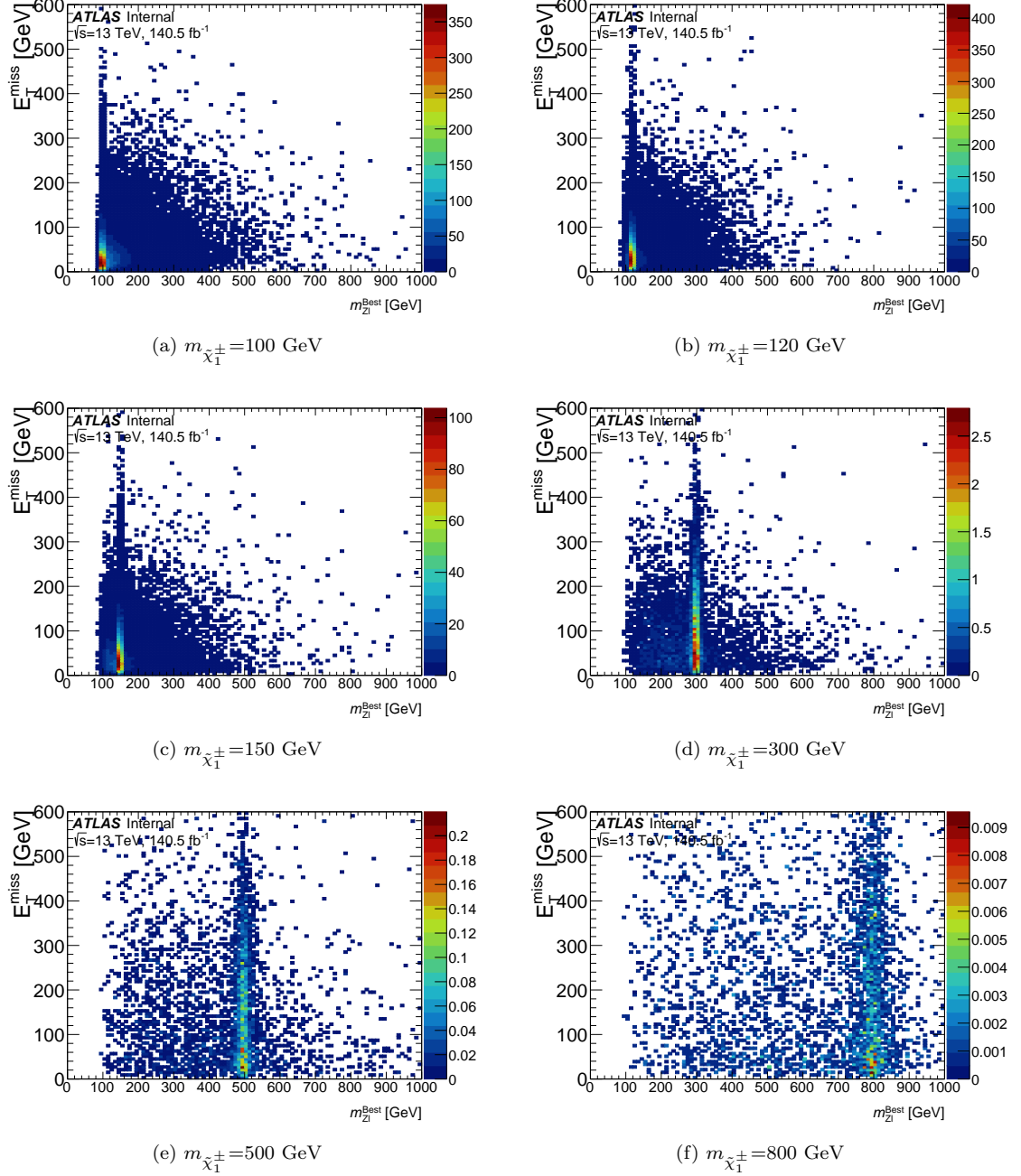


Figure H.4: E_T^{miss} as a function of $m_{Z\ell}$ for several mass points. The resolution of $m_{Z\ell}$ improves at higher values of E_T^{miss} , especially for lower mass points.

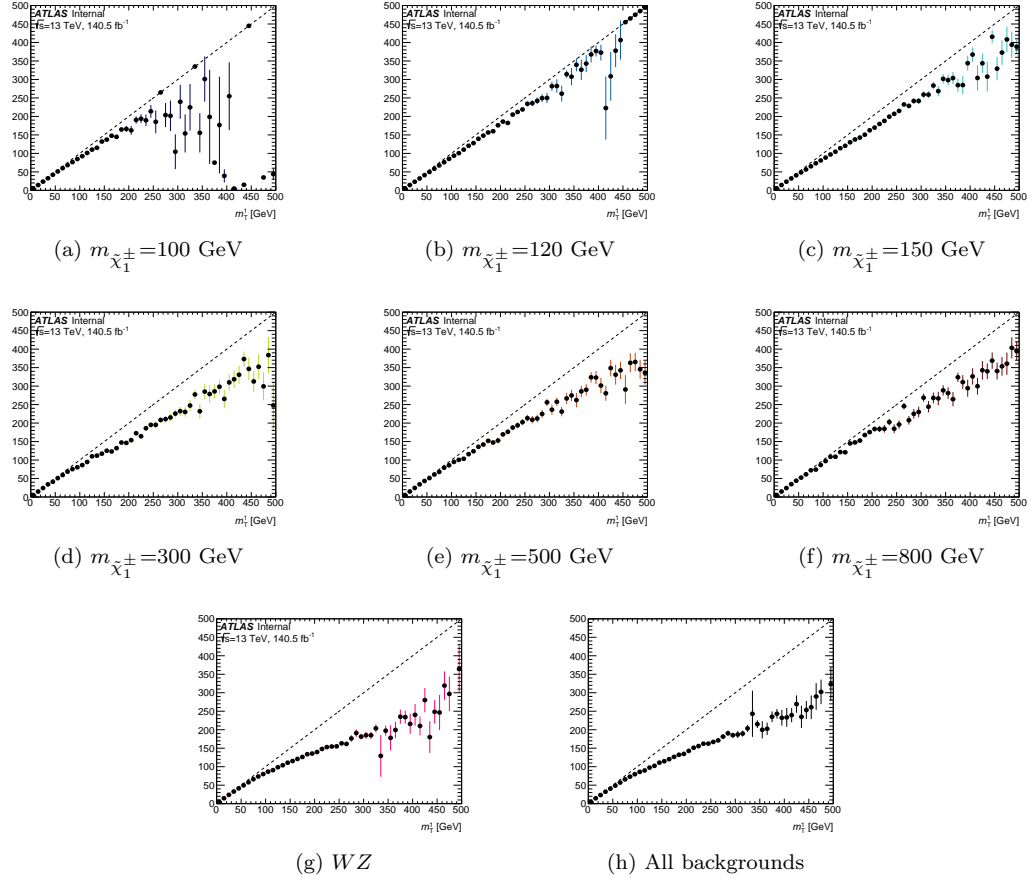


Figure H.5: m_T^{\min} versus m_T for various chargino mass points (a) - (f), as well as for standard model WZ (g) and all backgrounds (h).

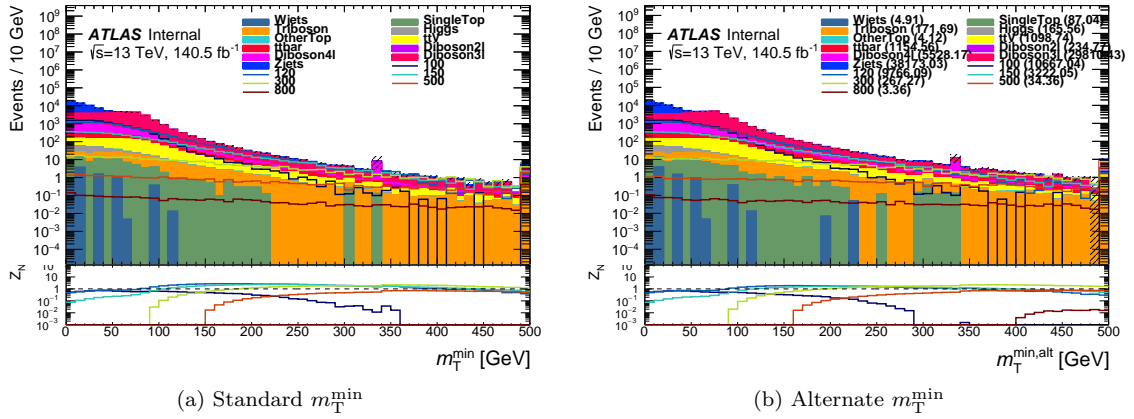


Figure H.6: Upper panel: Standard m_T^{\min} (a) and an alternate m_T^{\min} (b) distributions for signal and background. Lower panel: Estimated sensitivity for each mass point obtained by the given lower cut on standard (a) and alternate (b) m_T^{\min} with a flat 20% uncertainty.

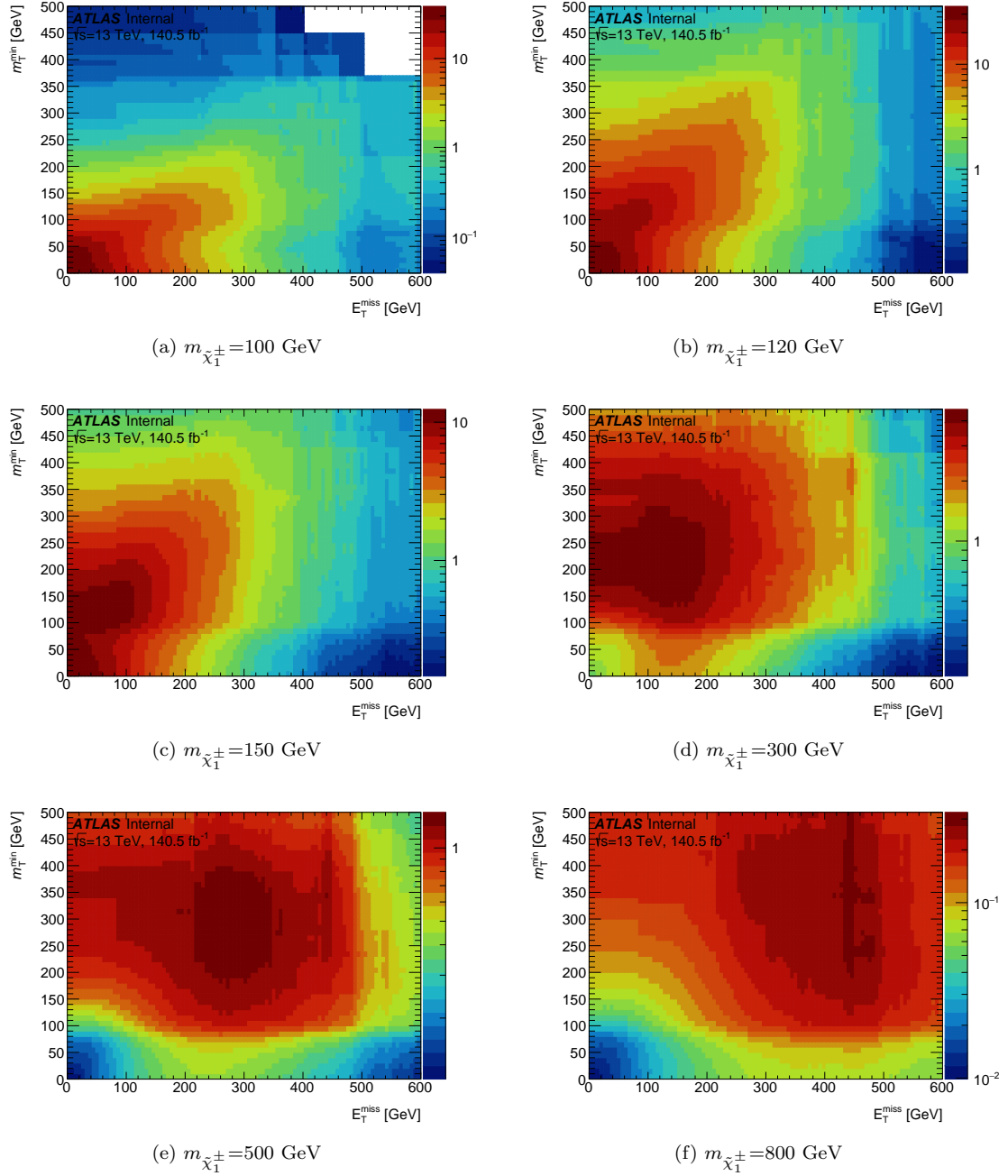


Figure H.7: S/\sqrt{B} , where S is signal yield and B is background yield, with the given lower cuts on m_T^{\min} and E_T^{miss} , for several mass points. No normalization factors are applied to the background yields.

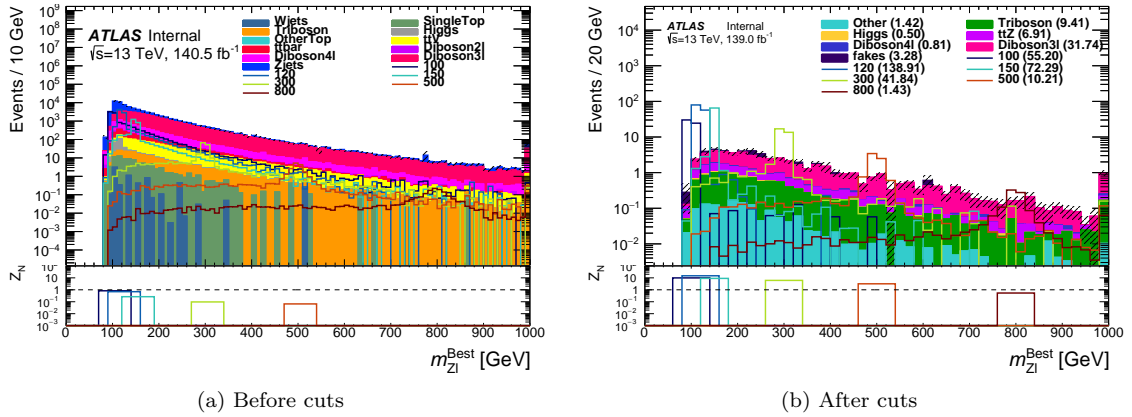


Figure H.8: A comparison of m_{Zl} distributions before (a) and after (b) m_T^{\min} and E_T^{miss} cuts. Lower panel: Estimated sensitivity for each mass point obtained with a 30 GeV window around the true gaugino mass, with a flat 20% uncertainty.

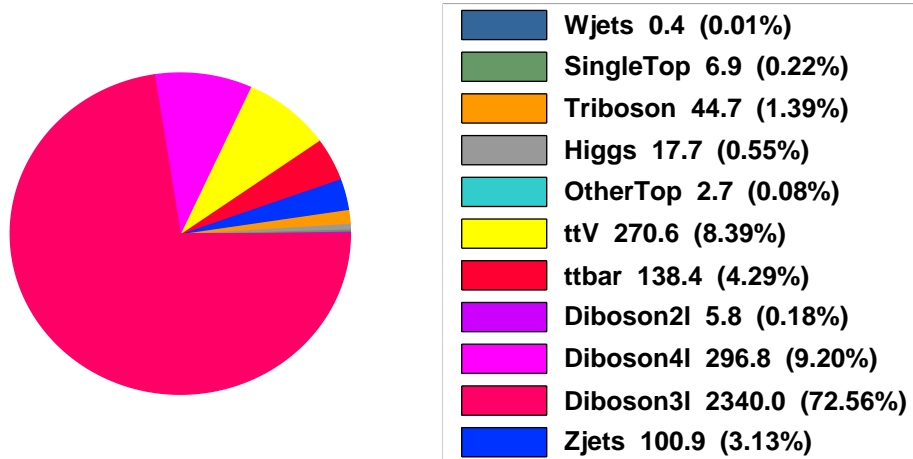


Figure H.9: Expected yields of each background in SROL3l, assuming 140 fb^{-1} . No normalization factors are applied.

H.2 CRWZ

As WZ is one of the main 3ℓ backgrounds, it has a dedicated control region to constrain its predictions using the method described in Section 6.7.

Referring again to Figure H.2, there is a clear region in m_T^{\min} where WZ dominates. Applying the cuts $m_T^{\min} > 50$ GeV and $m_T^{\min} < 100$ GeV already gives a region that has quite high WZ purity. To increase this purity and reduce signal contamination, an additional cut of $E_T^{\text{miss}} > 80$ GeV is applied. These cuts result in a WZ yield of 1441584 raw events, so there are plenty of statistics to have a reliable normalization in this region. The resulting background yields can be seen in Figure H.10, and the signal contamination can be seen in Table 6.11 (in Section 6.5). The maximum C1C1, nominal $\tilde{\chi}_1^\pm$ BR signal contamination comes from the 120 GeV mass point and has roughly 1777 expected events, which corresponds to 16% of the total background yield in this region.

It is possible to reduce the signal contamination in CRWZ by applying additional selections, most notably $dR(Z, \ell)$, the spatial separation between the leptonic Z and the third lepton. This distribution can be seen for signal and background in Figure H.11. The lower panel on this plot shows the signal contamination achieved by the given cut. While a cut of $\Delta R(Z, \ell) > 2.75$ can result in a maximum signal contamination of roughly 8%, it is not necessary to reduce the contamination by this much because the SR sensitivity is still decent given the current signal contamination, as discussed in Appendix G. So it was decided not to apply this cut since it will unnecessarily move the CR away from the phase space of the SR.

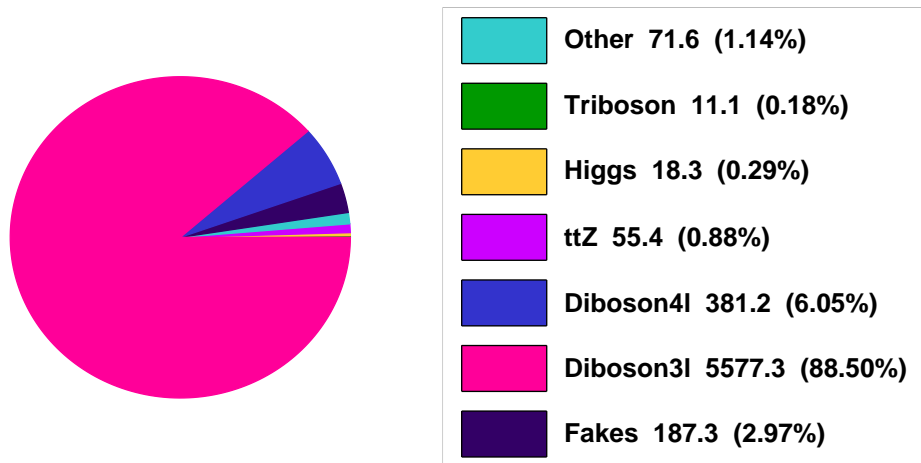


Figure H.10: Expected yields of each background in CRWZ, assuming 140 fb^{-1} . No normalization factors are applied.

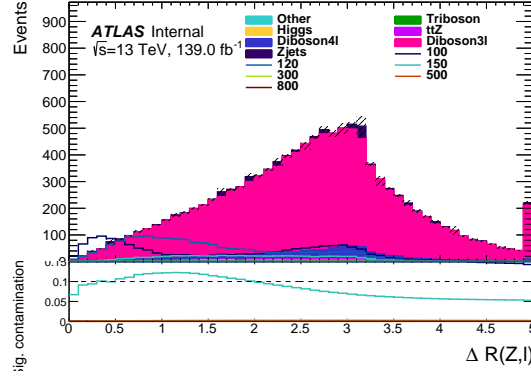


Figure H.11: Upper panel: Distribution of $\Delta R(Z, \ell)$ for signal and background in CRWZ. Lower panel: signal contamination for a given cut on $dR(Z, \ell)$.

H.3 VRMet and VRmTmin

Since SROL 3ℓ and CRWZ are separated by both E_T^{miss} and m_T^{min} cuts, it is useful to have regions to validate the extrapolation in each of these variables. VRMet is the region used to extrapolate E_T^{miss} , and requires $E_T^{\text{miss}} > 80$ GeV and $m_T^{\text{min}} < 100$ GeV. VRmTmin is the region used to extrapolate m_T^{min} , and requires $E_T^{\text{miss}} < 80$ GeV and $m_T^{\text{min}} > 125$ GeV. WZ is the dominant process in both of these regions, as can be seen in Figure H.12.

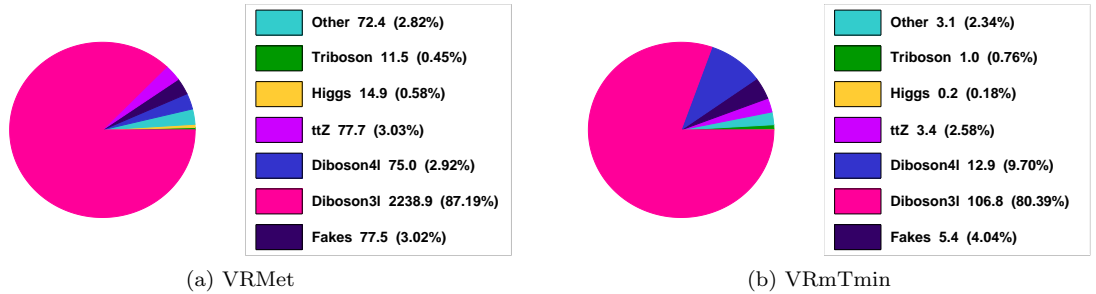


Figure H.12: Expected yields of each background in VRMet and VRmTmin, assuming 140 fb^{-1} . No normalization factors are applied.

APPENDIX I

Wino search: 4ℓ Region Optimization

This section describes how the regions with 4 leptons were defined and optimized. All signal distributions in this section show C1C1 production with the nominal $\tilde{\chi}_1^\pm$ BR.

Figure I.1 shows the expected yields of each background, assuming 140 fb^{-1} , in each signal region before any cuts. Diboson4 ℓ , which is usually standard model ZZ , and $t\bar{t}Z$ are the major backgrounds for final states with four or more leptons. All the selections described in the following sections are designed to reject these major backgrounds.

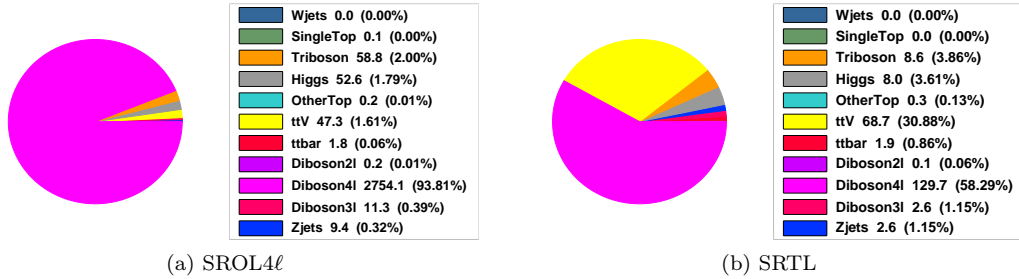


Figure I.1: Expected yields of each background in SROL4 ℓ (a), and SRTL (b), before any cuts, assuming 140 fb^{-1} . No normalization factors are applied.

Table I.1 shows the raw MC yields in each 4ℓ region for each background, given the cuts that will be described in this section. CRttZ and VRttZ are shown here as well as the corresponding 3ℓ table in Appendix H. The important processes have enough raw events in each region such that the analysis won't be statistics limited. Table I.2 shows the amount of C1C1 nominal $\tilde{\chi}_1^\pm$ BR signal contamination in each 4ℓ CR and VR, including CRttZ and VRttZ which are again repeated in the corresponding 3ℓ table. The signal contamination is shown as a percentage of the total background

Process	CRZZ	CRttZ	VRZZ	VRttZ	SROL4 ℓ	SRTL
WZ	12	12392	33	8239	490	88
$t\bar{t}Z$	1122	174498	4607	120151	12680	12094
$Z/\gamma^* + \text{jets}$	1	388	3	187	7	2
ZZ	786343	6046	450368	3337	16213	26622
Triboson	23846	825	16990	543	32169	8043
Higgs	2684	13647	3898	9956	70141	50804
Other	0	2921	3	2137	23	11

Table I.1: Raw MC yields for each background process in each 4ℓ region. CRttZ and VRttZ are shown here as well as the corresponding 3ℓ table in Appendix H.

Wino mass [GeV]	CRZZ	CRttZ	VRZZ	VRttZ
100	12	4.8	16	8.1
120	6.4	9.0	34	17
150	2.5	10	16	24
200	1.0	6.9	5.8	16
300	0.2	2.1	0.7	5.1
400	0.0	0.7	0.1	1.6
500	0.0	0.3	0.1	0.6
600	0.0	0.1	0.0	0.3
700	0.0	0.1	0.0	0.1
800	0.0	0.0	0.0	0.0

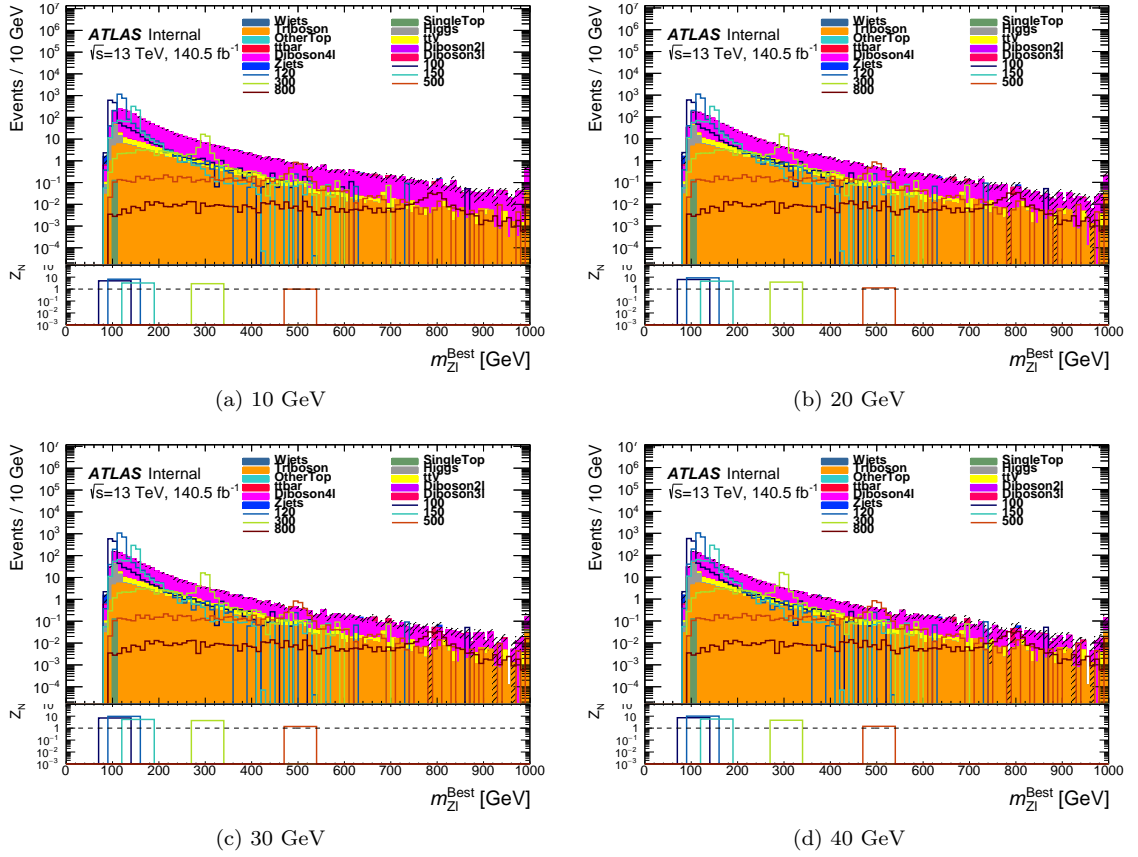
Table I.2: Signal contamination as a percentage of total background yield in each 4ℓ CR and VR.

yield in each region.

I.1 $4\ell 2Z$ optimization

One criterion that is applied (either as a selection or veto) to all regions with 4 or more leptons is the $4\ell 2Z$ criterion which was defined in Section 6.5. Several $m_{\ell\ell}$ window sizes were compared for the Z candidate requirement, to optimize this criterion in terms of signal sensitivities and background yields in the SRs, and background and signal yields in CRZZ. The windows compared are 10, 20, 30, and 40 GeV wide and centered at 91 GeV (i.e. the 10 GeV window has a range of 86 GeV to 96 GeV).

The $m_{Z\ell}$ distributions for each $m_{\ell\ell}$ window are shown for SROL4 ℓ in Figure I.2. Here it can be seen that the size of the $m_{\ell\ell}$ window does little to change the $m_{Z\ell}$ sensitivity, but the sensitivity is slightly higher for the larger $m_{\ell\ell}$ windows. Predictably, the signal and background yields also decrease as $m_{\ell\ell}$ increases, since more events pass the $4\ell 2Z$ criterion and are vetoed from this SR.

Figure I.2: $m_{Z\ell}$ distributions for each tested $m_{\ell\ell}$ window in SROL4 ℓ .

The background yields for each $m_{\ell\ell}$ window are shown for SROL4 ℓ in Figure I.3. Here it can be seen that ZZ dominates regardless of the $m_{\ell\ell}$ window, but its dominance decreases slightly with larger $m_{\ell\ell}$ windows since more events pass the $4\ell 2Z$ criterion.

The corresponding $m_{Z\ell}$ distributions and background yields for each $m_{\ell\ell}$ window in SRTL are shown respectively in Figures I.4 and I.5. The overall lesson is the same here as it is in SROL4 ℓ ; the choice of $m_{\ell\ell}$ window does not change the sensitivities or yields by much. To reject as much ZZ as possible from the SRs, the largest $m_{\ell\ell}$ window is chosen. Any event with a second Z candidate within the $m_{\ell\ell}$ window [71,111] GeV is rejected from the SRs. This same criterion is now applied to all regions with at least 4 leptons, except those in which ZZ is the targeted process.

The background yields for each $m_{\ell\ell}$ window are shown for CRZZ in Figure I.6. Here it is clear that ZZ totally dominates regardless of the chosen $m_{\ell\ell}$ window. Not shown here, but the signal contamination in CRZZ increases with $m_{\ell\ell}$ window, for the same reason that the yields decreased

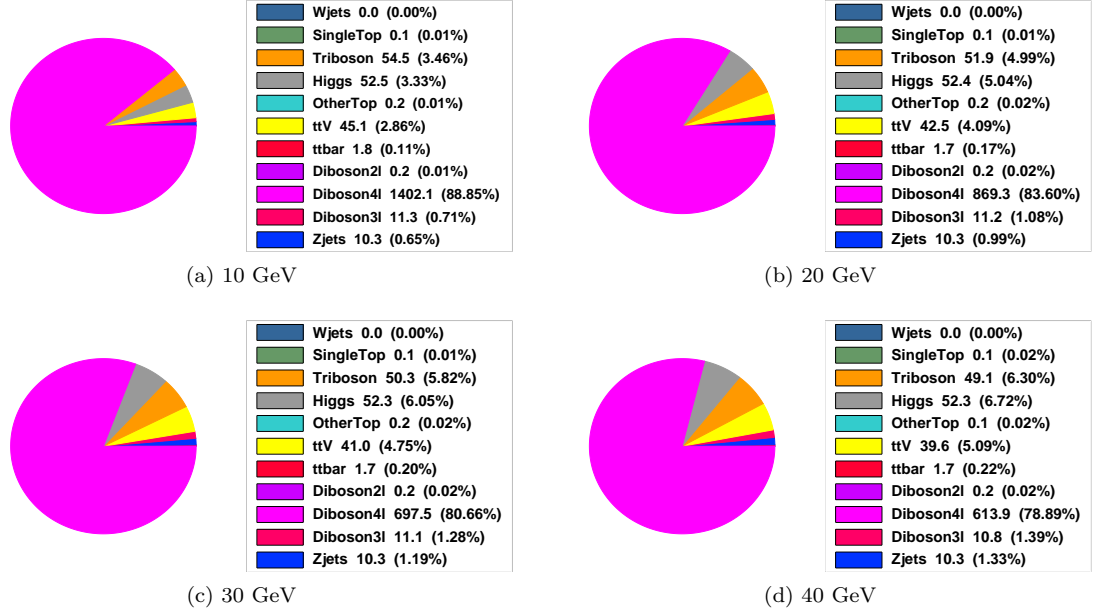


Figure I.3: Expected background yields for each tested $m_{\ell\ell}$ window in SROL4 ℓ . No normalization factors are applied.

in the SRs.

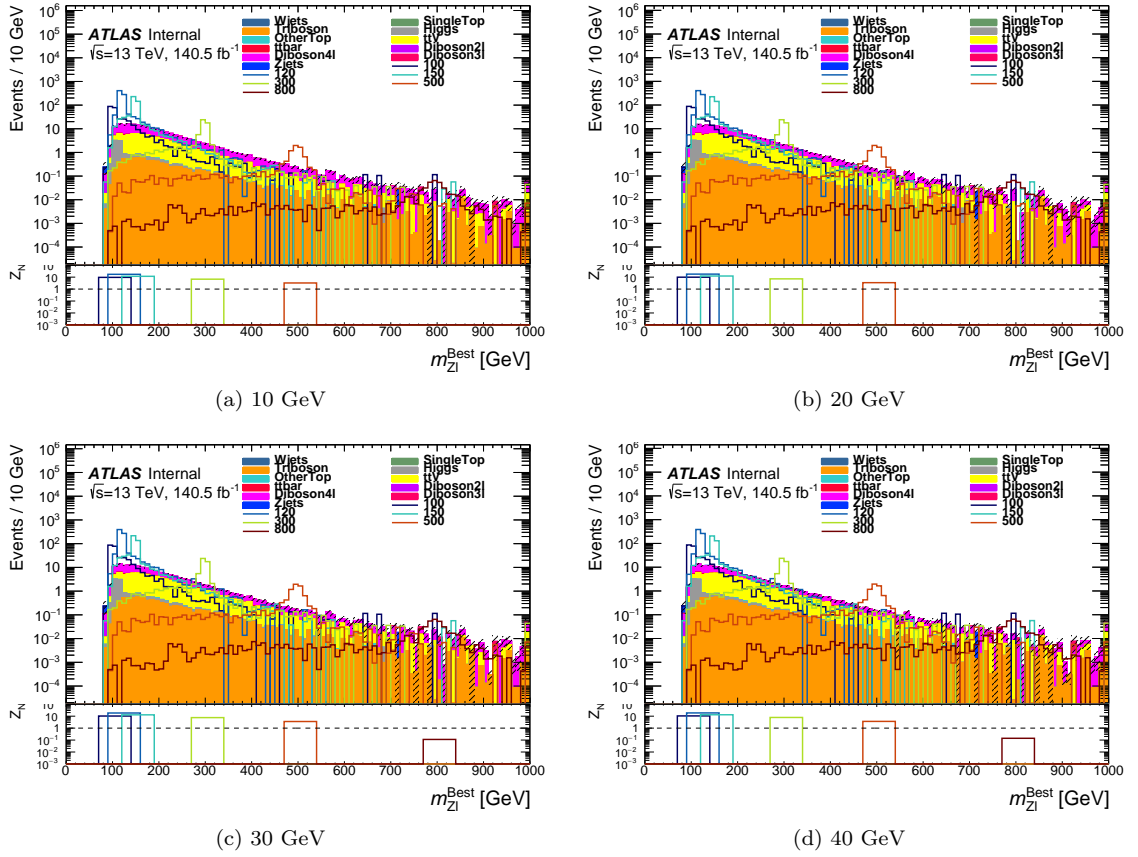
In VRZZ, to maintain similarity with the SRs, the upper limit on the $m_{\ell\ell}$ mass window is again 40 GeV, i.e. the Z candidate must be within [71,111] GeV. To maintain orthogonality with CRZZ, VRZZ has an additional lower limit on the $m_{\ell\ell}$ mass window, meaning there is some minimum value below which $|m_{\ell\ell,2} - m_Z|$ is not accepted. The background yields for tested $|m_{\ell\ell,2} - m_Z|$ minima are shown for VRZZ in Figure I.7. Here it can be seen that the total yields are quite small for all choices of $m_{\ell\ell,2}$ window, except that with a 10 GeV window minimum (with $m_{\ell\ell}$ values < 86 GeV or > 96 GeV). For this reason the accepted values for the second Z candidate in VRZZ are [71,86] GeV and [96,111] GeV. In other words, the $m_{\ell\ell,2}$ window in VRZZ is set to be [5,20] GeV.

I.2 SROL4 ℓ

Diboson4l (ZZ) is by far the dominant background in SROL4 ℓ so the selections in SROL4 ℓ are primarily designed to reduce this background.

The effect of the $4\ell 2Z$ veto in this region can be seen in Figure I.8. More than 50% of ZZ is rejected, but other processes (including signal) are rarely rejected by this veto.

Another variable with discrimination power in SROL4 ℓ is E_T^{miss} , as can be seen in Figure I.9,

Figure I.4: $m_{Z\ell}$ distributions for each tested $m_{\ell\ell}$ window in SRTL.

which shows the E_T^{miss} distribution after the $4\ell 2Z$ veto. ZZ usually has small E_T^{miss} while many signal final states that are targeted in SROL4 ℓ have true E_T^{miss} . This is demonstrated for several mass points in Figure I.10 which shows the E_T^{miss} for individual truth final states, and summarized in Figure I.11 which shows the E_T^{miss} of all events targeted for, and reconstructed in, SROL4 ℓ . In SROL4 ℓ , the E_T^{miss} cut is only applied to events with two pairs of same-flavor leptons, to effectively target ZZ rejection. The breakdown of the flavor and sign of the two leptons which are not assigned to the Z is shown in Figure I.12. This distribution is shown before (Figure I.12a) and after (Figure I.12b) the E_T^{miss} cut which is only applied to events with two SF pairs, henceforth referred to as $E_T^{\text{miss,SF}}$. The $E_T^{\text{miss,SF}}$ distribution before applying this cut is shown in Figure I.9b. Requiring $E_T^{\text{miss,SF}} > 80$ GeV corresponds roughly to the maximum sensitivity for the low mass points and it still provides reasonable raw MC statistics in SROL4 ℓ for the major backgrounds.

Since $m_{Z\ell}$ is the final discriminating variable of interest, it is interesting to compare the $m_{Z\ell}$

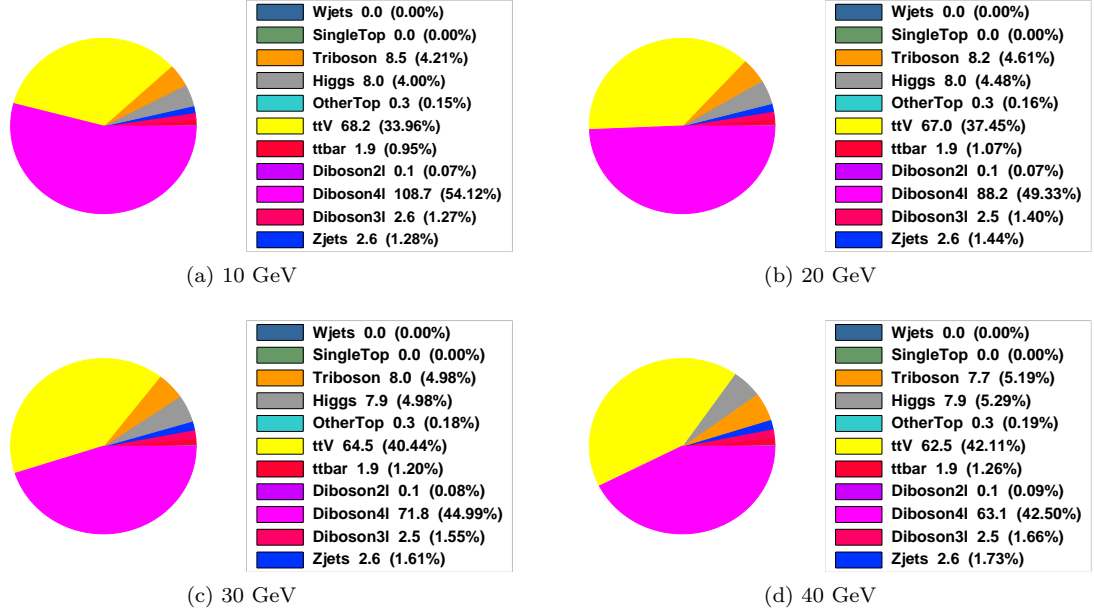


Figure I.5: Expected background yields for each tested $m_{\ell\ell}$ window in SRTL. No normalization factors are applied.

distributions before and after these $4\ell 2Z$ and $E_T^{\text{miss}, \text{SF}}$ requirements. Figure I.13 shows this comparison. After these cuts, the $m_{Z\ell}$ resolution in signal seems slightly improved, and the sensitivity is significantly improved. Figure I.14 also shows the background composition after these cuts. It is clear that ZZ is still the dominant background, with $t\bar{t}Z$ and Triboson subdominant.

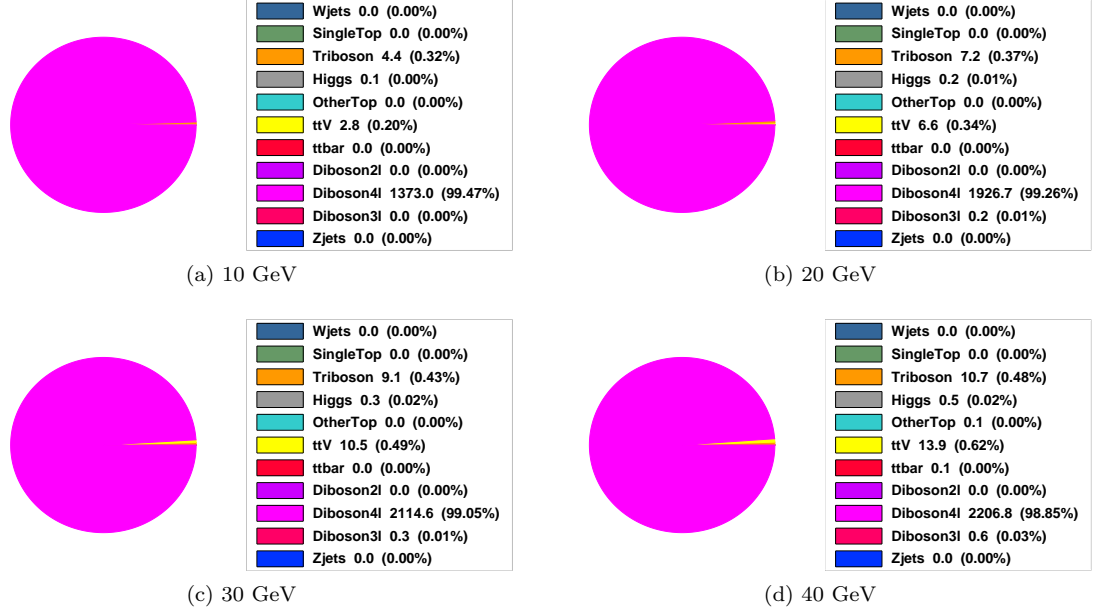


Figure I.6: Expected background yields for each tested $m_{\ell\ell}$ window in CRZZ. No normalization factors are applied.

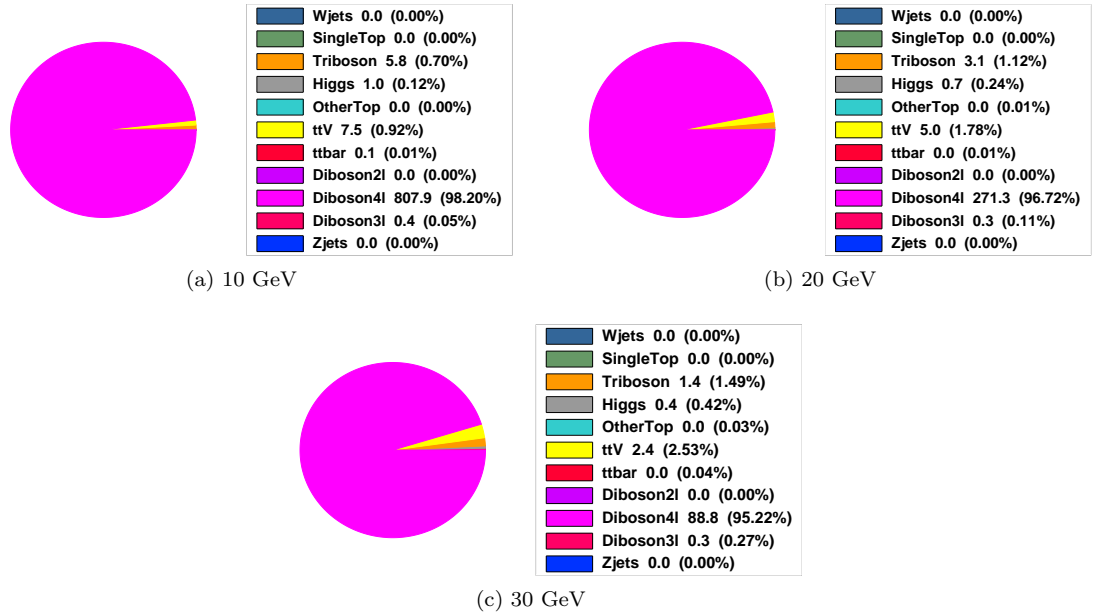


Figure I.7: Expected background yields for each tested $m_{\ell\ell}$ window in VRZZ. No normalization factors are applied.

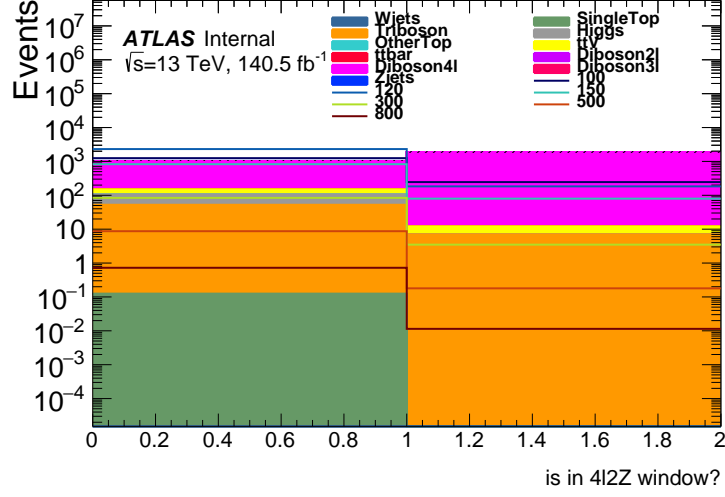


Figure I.8: Boolean describing if event satisfies $4\ell 2Z$ criterion in SROL 4ℓ , before any cuts. 0 is false, 1 is true. A $4\ell 2Z$ veto rejects more than half the ZZ events in this region.

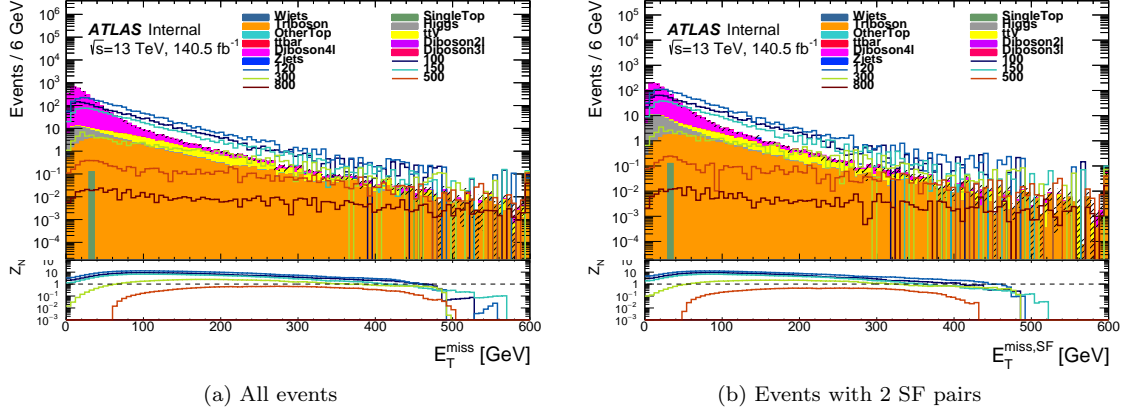


Figure I.9: E_T^{miss} distribution for SROL 4ℓ events after $4\ell 2Z$ veto.

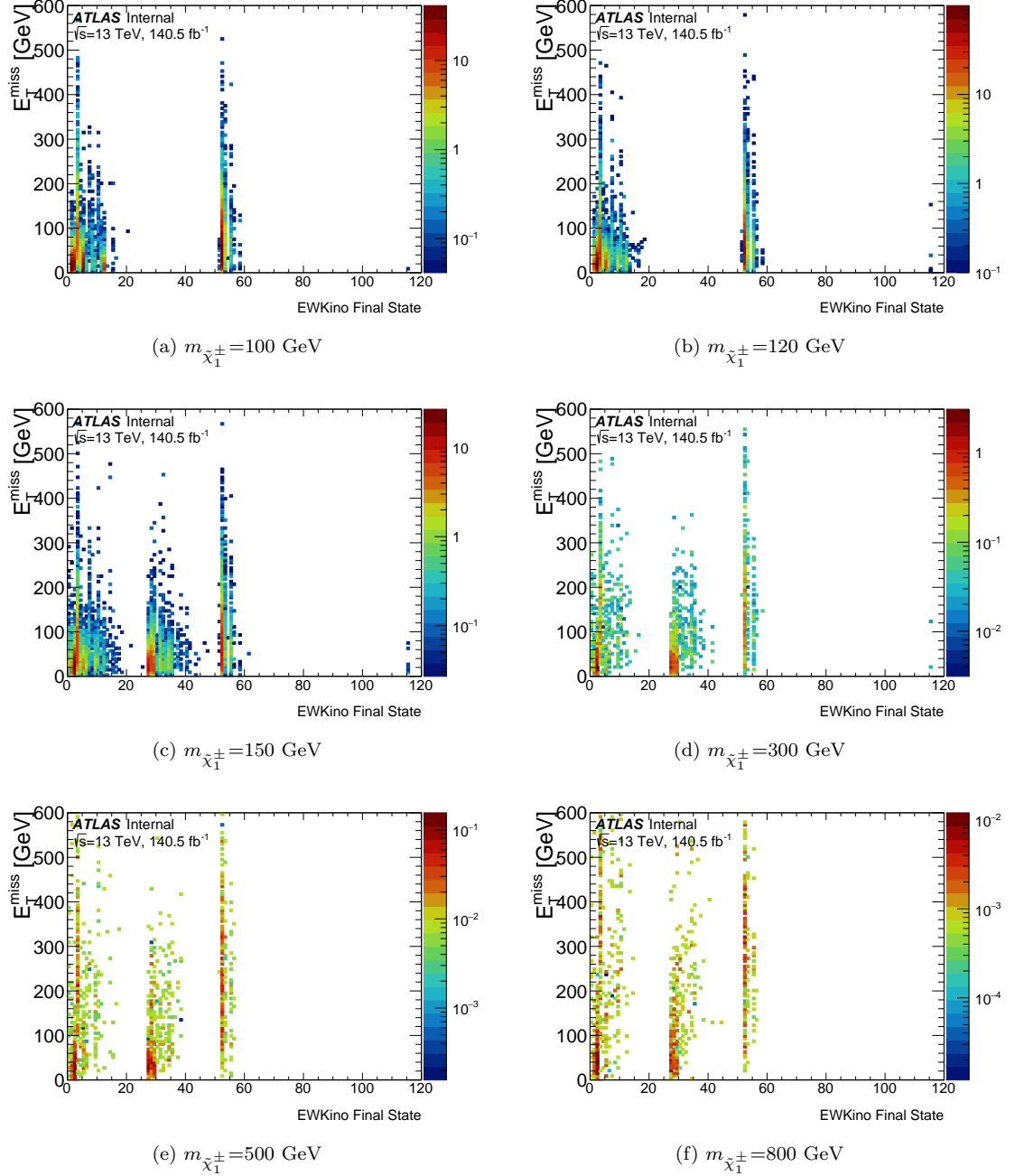


Figure I.10: E_T^{miss} distribution as a function of truth C1C1 final state for each event that was reconstructed as OL4 ℓ . The definitions of the truth final states can be found in Appendix B. Most of the final states that are targeted in OL4 ℓ have real E_T^{miss} .

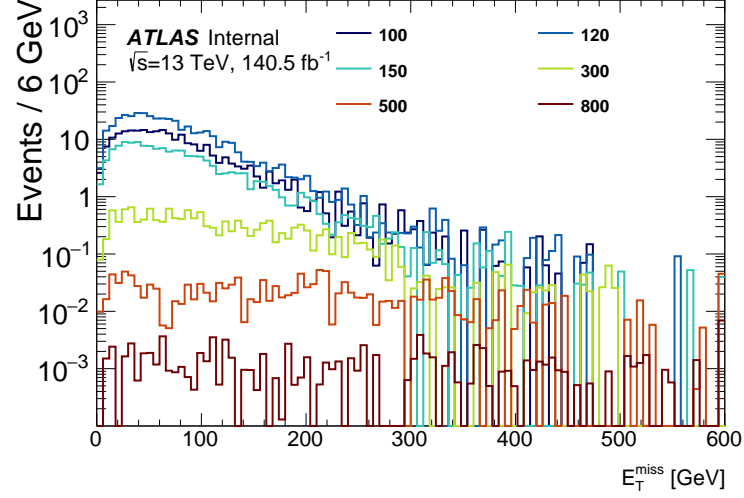


Figure I.11: E_T^{miss} distribution for C1C1 final states which are targeted for, and reconstructed in, SROL4 ℓ .

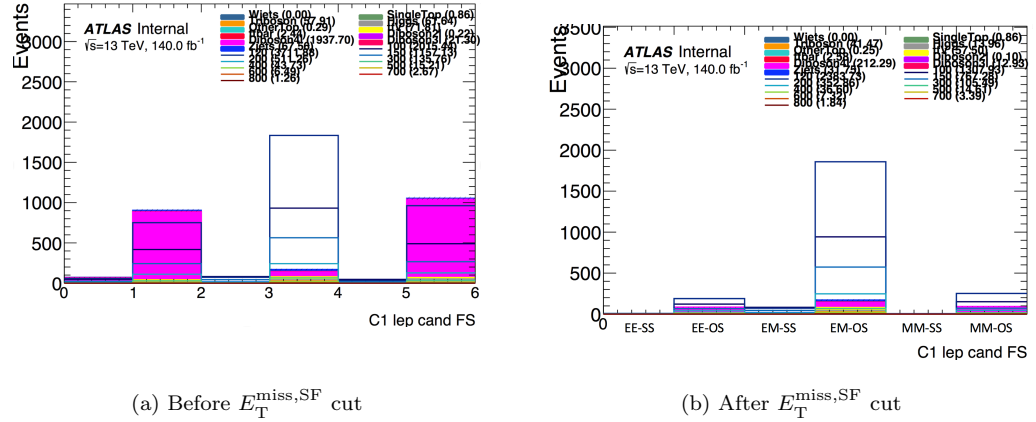


Figure I.12: Flavor and sign breakdown for all SROL4 ℓ events after $4\ell 2Z$ veto, for the two leptons that are not assigned to the Z . The x -axis bins are the same for both distributions and are labeled in Figure I.12b.

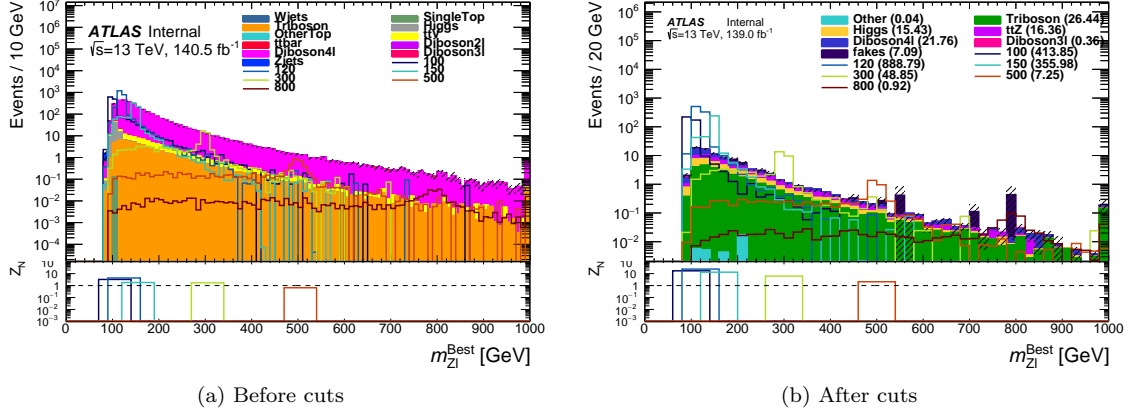


Figure I.13: A comparison of $m_{Z\ell}$ distributions before (a) and after (b) $E_T^{\text{miss,SF}}$ cut and $4\ell 2Z$ veto in SROL4 ℓ . Lower panel: Estimated sensitivity for each mass point obtained with a 30 GeV window around the true gaugino mass, with a flat 20% uncertainty.

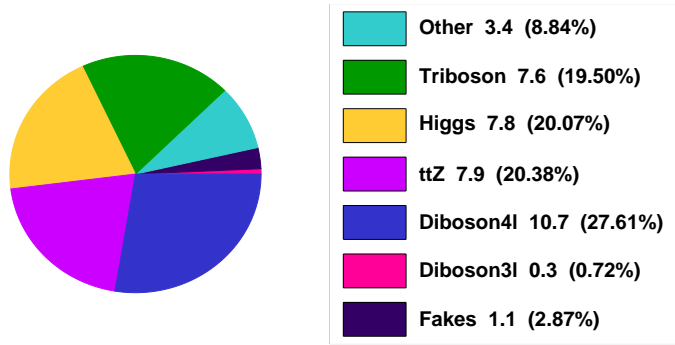


Figure I.14: Expected yields of each background in SROL4 ℓ , assuming 140 fb^{-1} . No normalization factors are applied.

I.3 SRTL

Diboson4l (ZZ) is by far the dominant background in SRTL so the selections in SRTL are primarily designed to reduce this background.

The effect of the $4\ell 2Z$ veto in this region can be seen in Figure I.15. ZZ is the process with the largest fraction of events that pass the $4\ell 2Z$ criteria, so this veto performs well in SRTL.

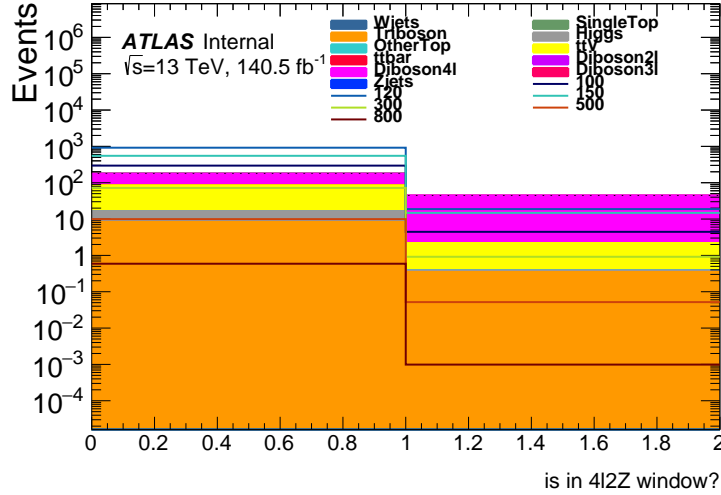
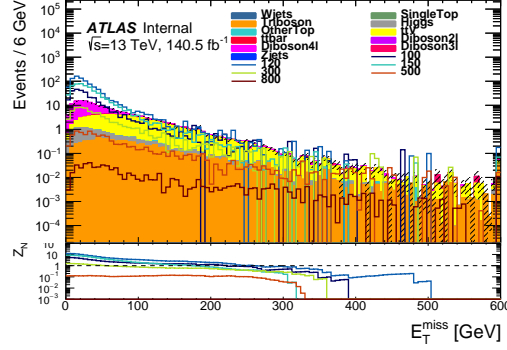
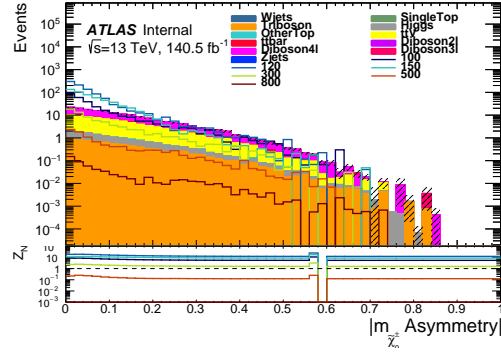


Figure I.15: Boolean describing if event satisfies $4\ell 2Z$ criterion in SRTL, before any cuts. 0 is false, 1 is true.

While E_T^{miss} is a powerful discriminating variable in the OneLeg SRs, its performance is not as strong in SRTL because there is not real E_T^{miss} in the signal final states which are targeted for SRTL. The E_T^{miss} distribution for signal and background, and the corresponding sensitivity for various E_T^{miss} cuts, is shown in Figure I.16.

Alternatively, the $m_{Z\ell}$ asymmetry which was defined in Equation 6.1 is expected to be small for signal and more or less flat in background. This is indeed the case, as can be seen in Figure I.17. Here, since signal is expected to be small and background to be flat, the sensitivity shown in the lower panel is obtained by applying scanning values of upper cuts on the asymmetry, rather than the standard lower cut. The upper cut that achieves maximum sensitivity is more or less independent of mass point, and is chosen to be 0.1 as a compromise between sensitivity and MC statistics.

Since $m_{Z\ell}$ is the final discriminating variable of interest, it is interesting to compare the $m_{Z\ell}$ distributions before and after these $4\ell 2Z$ and $m_{Z\ell}$ asymmetry requirements. Figure I.18 shows this comparison. After these cuts, the $m_{Z\ell}$ resolution in signal seems slightly improved, and the

Figure I.16: E_T^{miss} distribution for SRTL events after $4\ell 2Z$ veto.Figure I.17: $m_{Z\ell}$ asymmetry distribution for SRTL events after $4\ell 2Z$ veto.

sensitivity is significantly improved. Figure I.19 also shows the background composition after these cuts. It is clear that ZZ is still the dominant background, with $t\bar{t}Z$ subdominant.

I.4 CRZZ

The only criterion for the ZZ CR is the $4\ell 2Z$ criterion, which is used as a selection in this region. This selection has very high ZZ purity, which is shown in Figure I.20 (identical to Figure I.6b), and results in a ZZ yield of 786343 raw MC events, so there are plenty of statistics to have a reliable normalization in this region. It also has a maximum C1C1 nominal BR signal contamination of roughly 128 events which corresponds to 12% of the background yield, from the 100 GeV mass point (see Table 6.11 in Section 6.5 and Table I.2).

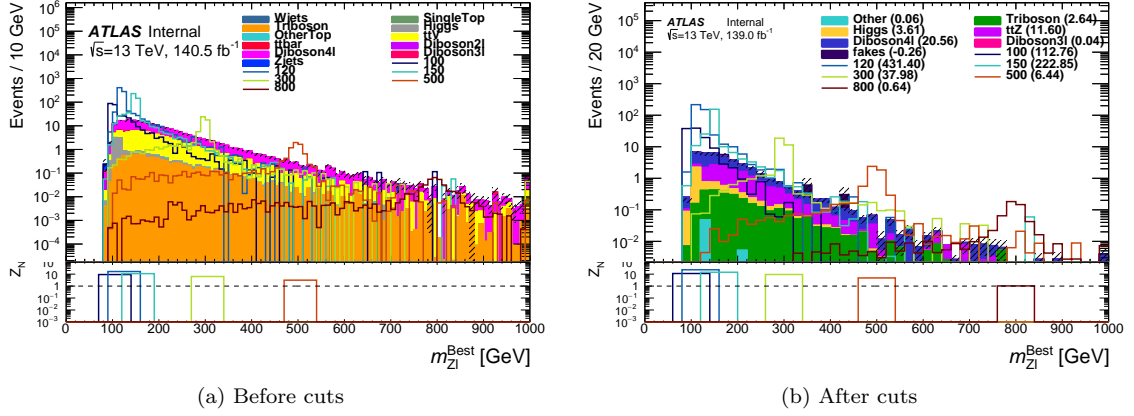


Figure I.18: A comparison of $m_{Z\ell}$ distributions before (a) and after (b) $m_{Z\ell}$ asymmetry cut and $4\ell 2Z$ veto in SRTL. Lower panel: Estimated sensitivity for each mass point obtained with a 30 GeV window around the true gaugino mass, with a flat 20% uncertainty.

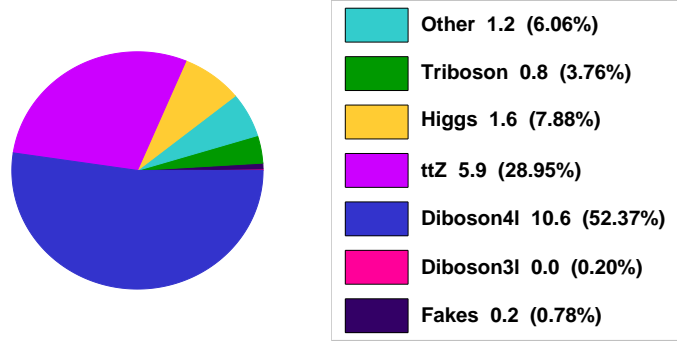


Figure I.19: Expected yields of each background in SRTL, assuming 140 fb^{-1} . No normalization factors are applied.

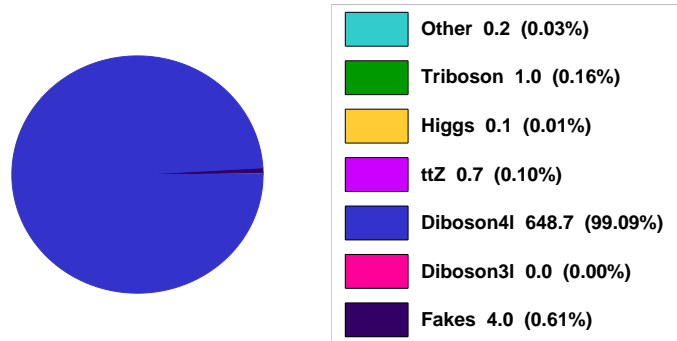


Figure I.20: Expected yields of each background in CRZZ, assuming 140 fb^{-1} . No normalization factors are applied.

I.5 VRZZ

The only criterion for the ZZ VR is the $4\ell 2Z$ criterion, which is used as a selection in this region. This selection has very high ZZ purity, which is shown in Figure I.21 (identical to Figure I.7a). It also has a maximum C1C1 nominal BR signal contamination of roughly 220 events which corresponds to 34% of the background yield, from the 120 GeV mass point (see Table 6.11 in Section 6.5 and Table I.2).

I.6 CRttZ

With the effective rejection of ZZ from the $4\ell 2Z$ criterion, $t\bar{t} + V$ becomes a significant background in the 4ℓ SRs. The composition of the $t\bar{t} + V$ background is predominantly $t\bar{t}Z$ as shown in the pie chart in Figure I.22. Most $t\bar{t}Z$ events have 2 b -jets from the top decays, so $n_{b\text{-jet}} \geq 2$ is required for this region. A cut of $E_T^{\text{miss}} \geq 50$ GeV is also required to increase $t\bar{t}Z$ purity against $Z/\gamma^* + \text{jets}$. To reject signal events from this region, a selection is applied to the variable $dR(b_0, b_1)$, which is the angular separation between the leading and subleading b -jets in an event. This cut is designed to reject events with b -jets from Higgs decays, which tend to be more collimated than b -jets from $t\bar{t}$ decays. A cut of $dR(b_0, b_1) > 2.5$ is chosen to optimize $t\bar{t}Z$ purity and statistics in the region. The background yields and $m_{Z\ell}$ distribution, with corresponding signal contamination ratio plot, in CRttZ are shown in Figures I.23 and I.24 respectively.

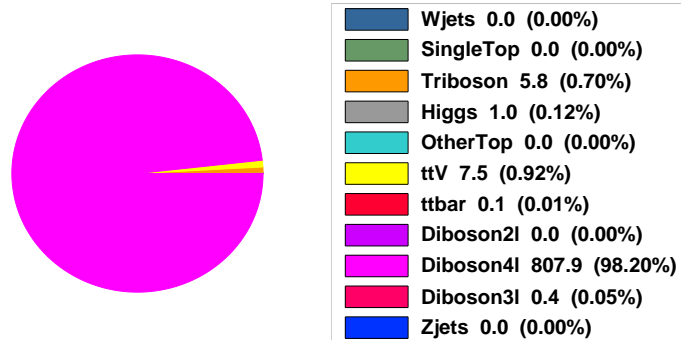
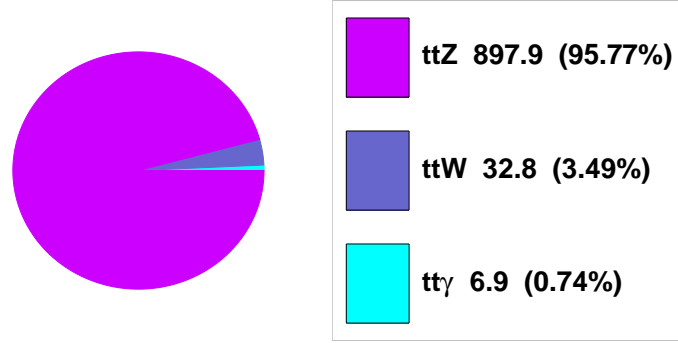
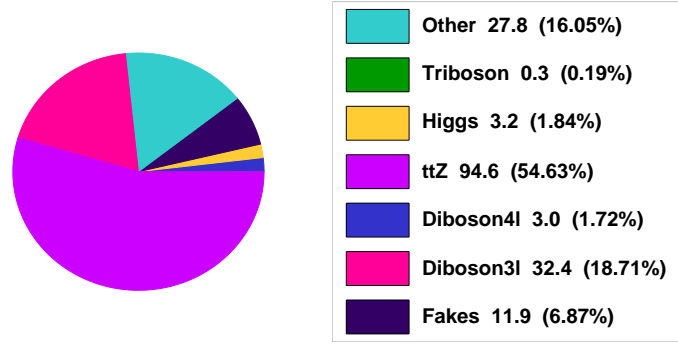
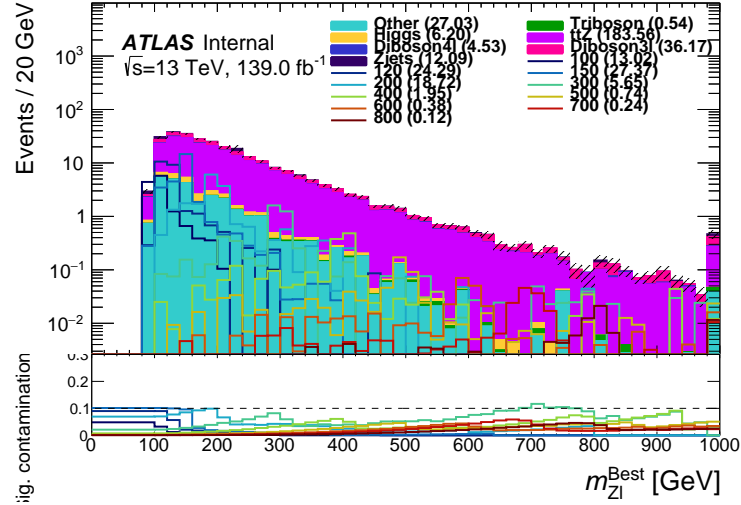


Figure I.21: Expected yields of each background in VRZZ, assuming 140 fb^{-1} . No normalization factors are applied.

Figure I.22: Expected $t\bar{t} + V$ yields split into $t\bar{t}Z$, $t\bar{t}W$, and $t\bar{t}\gamma$, at preselection.Figure I.23: Expected background yields in the CRttZ region, assuming 140 fb^{-1} . No normalization factors are applied.Figure I.24: $m_{Z\ell}$ distribution in the CRttZ region with corresponding signal contamination ratio plot, assuming 140 fb^{-1} . No normalization factors are applied.

I.7 VRttZ

VRttZ utilizes cuts on the same variables as those used in CRttZ. A cut of $n_{b\text{-jets}} \geq 2$ is applied to VRttZ to maintain good purity in this region. $E_T^{\text{miss}} \geq 50$ GeV is also required to reduce $Z/\gamma^* + \text{jets}$. A $dR(b_0, b_1)$ window of $2.0 < dR(b_0, b_1) < 2.5$ is applied in order to be kinematically between CRttZ and the SRs, while maintaining good purity. The background yields and $m_{Z\ell}$ distribution, with corresponding signal contamination ratio plot, in VRttZ are shown in Figures I.25 and I.26 respectively.

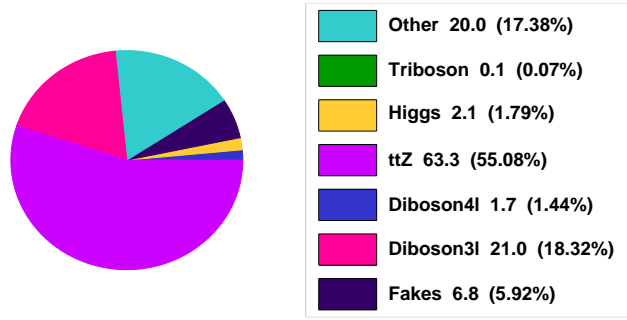


Figure I.25: Expected background yields in the VRttZ region, assuming 140 fb^{-1} . No normalization factors are applied.

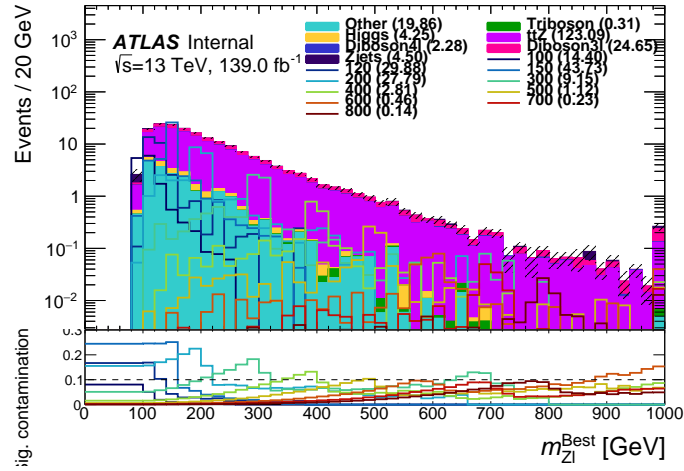


Figure I.26: $m_{Z\ell}$ distribution in the VRttZ region with corresponding signal contamination ratio plot, assuming 140 fb^{-1} . No normalization factors are applied.

Bibliography

- [1] ATLAS Collaboration, *A search for $B - L$ R -parity-violating scalar top decays in $\sqrt{s} = 8$ TeV pp collisions with the ATLAS experiment*, ATLAS-CONF-2015-015, 2015, <https://cds.cern.ch/record/2002885>. Cited on pages xx and 65.
- [2] L. Schaefer, B. Jackson, E. Thomson, J. Kroll, and Z. Marshall, *Prospects for a search for stop pair production with R -Parity violating decay at 13 TeV*, <https://indico.cern.ch/event/314048/contributions/1688977/>. Cited on page xxi.
- [3] ATLAS Collaboration, *Search for $B - L$ R -parity-violating top squarks in $\sqrt{s} = 13$ TeV pp collisions with the ATLAS experiment*, *Phys. Rev. D* **97** (2018) 032003, [arXiv:1710.05544](https://arxiv.org/abs/1710.05544) [hep-ex]. Cited on pages xxiii and 65.
- [4] L. Schaefer, G. Lerner, J. Dandoy, K. Suruliz, E. Thomson, B. Jackson, I. Vivarelli, and I. Dyckes, *A search for B - L R -parity-violating scalar top decays in $\sqrt{s} = 13$ TeV pp collisions with the ATLAS experiment*, <https://indico.fnal.gov/event/11999/session/10/contribution/203>. Cited on page xxiii.
- [5] L. Schaefer, *SEARCH FOR B - L R -PARITY-VIOLATING TOP SQUARK DECAYS AT $\sqrt{s}=13$ TeV WITH THE ATLAS DETECTOR*, <https://cds.cern.ch/record/2282868>. Cited on page xxiii.
- [6] M. E. Peskin and D. V. Schroeder, *An Introduction to Quantum Field Theory*. Addison-Wesley, 1995. Cited on pages 3 and 5.
- [7] S. Weinberg, *The Quantum Theory of Fields, Volume 1: Foundations*. Cambridge University Press, 1995. Cited on page 3.
- [8] M. Thomson, *Modern Particle Physics*. Cambridge University Press, 2013. Cited on page 3.
- [9] Bernie Hobbs, *The Standard Model of particle physics is brilliant and completely flawed*, <https://www.abc.net.au/news/science/2017-07-15/the-standard-model-of-particle-physics-explained/7670338>. Cited on page 4.
- [10] ATLAS Collaboration, *Standard Model Summary Plots Spring 2019*, Tech. Rep. ATL-PHYS-PUB-2019-010, CERN, Geneva, Mar, 2019. <https://cds.cern.ch/record/2668559>. Cited on page 6.

- [11] S. P. Martin, *A Supersymmetry primer*, [arXiv:hep-ph/9709356 \[hep-ph\]](#), [Adv. Ser. Direct. High Energy Phys.18,1(1998)]. Cited on pages 5, 7, and 8.
- [12] G. R. Farrar and P. Fayet, *Phenomenology of the Production, Decay, and Detection of New Hadronic States Associated with Supersymmetry*, *Phys. Lett. B* **76** (1978) 575–579. Cited on page 7.
- [13] G. 't Hooft, *Symmetry Breaking through Bell-Jackiw Anomalies*, *Phys. Rev. Lett.* **37** (1976) 8–11, <https://link.aps.org/doi/10.1103/PhysRevLett.37.8>. Cited on page 8.
- [14] P. Fileviez Perez and S. Spinner, *Spontaneous R-Parity breaking and left-right symmetry*, *Phys. Lett. B* **673** (2009) 251–254, [arXiv:0811.3424 \[hep-ph\]](#). Cited on page 9.
- [15] V. Barger, P. Fileviez Perez, and S. Spinner, *Minimal Gauged $U(1)_{B-L}$ Model with Spontaneous R-Parity Violation*, *Phys. Rev. Lett.* **102** (2009) 181802, [arXiv:0812.3661 \[hep-ph\]](#). Cited on page 9.
- [16] P. Fileviez Perez and S. Spinner, *Spontaneous R-Parity Breaking in SUSY Models*, *Phys. Rev. D* **80** (2009) 015004, [arXiv:0904.2213 \[hep-ph\]](#). Cited on page 9.
- [17] L. L. Everett, P. Fileviez Perez, and S. Spinner, *The right side of TeV scale spontaneous R-Parity violation*, *Phys. Rev. D* **80** (2009) 055007, [arXiv:0906.4095 \[hep-ph\]](#). Cited on page 9.
- [18] S. P. Martin, *Some simple criteria for gauged R parity*, *Phys. Rev. D* **46** (1992) R2769–R2772, <https://link.aps.org/doi/10.1103/PhysRevD.46.R2769>. Cited on page 9.
- [19] V. Braun, Y.-H. He, B. A. Ovrut, and T. Pantev, *A heterotic standard model*, *Phys. Lett. B* **618** (2005) 252–258, [arXiv:hep-th/0501070](#). Cited on page 9.
- [20] B. A. Ovrut, A. Purves, and S. Spinner, *The minimal SUSY BL model: from the unification scale to the LHC*, *JHEP* **06** (2015) 182, [arXiv:1503.01473 \[hep-ph\]](#). Cited on page 9.
- [21] Deen, Rehan and Ovrut, Burt A. and Purves, Austin, *The minimal SUSY B – L model: simultaneous Wilson lines and string thresholds*, *JHEP* **07** (2016) 043, [arXiv:1604.08588 \[hep-ph\]](#). Cited on page 9.
- [22] P. F. Pérez and S. Spinner, *Fate of R parity*, *Phys. Rev. D* **83** (2011) 035004, <https://link.aps.org/doi/10.1103/PhysRevD.83.035004>. Cited on page 10.
- [23] V. Braun, Y.-H. He, B. A. Ovrut, and T. Pantev, *The exact MSSM spectrum from string theory*, *Journal of High Energy Physics* **2006** (2006) 043–043, <https://doi.org/10.1088%2F1126-6708%2F2006%2F05%2F043>. Cited on page 9.
- [24] V. Braun, Y.-H. He, and B. A. Ovrut, *Supersymmetric hidden sectors for heterotic standard models*, *Journal of High Energy Physics* **2013** (2013) 8, [https://doi.org/10.1007/JHEP09\(2013\)008](https://doi.org/10.1007/JHEP09(2013)008). Cited on page 9.
- [25] M. Evans and B. A. Ovrut, *The World Sheet Supergravity of the Heterotic String*, *Phys. Lett. B* **171** (1986) 177. Cited on page 9.
- [26] A. Lukas, B. A. Ovrut, K. Stelle, and D. Waldram, *The Universe As a Domain Wall*, *Phys. Rev. D* **59** (1999) 086001, [arXiv:hep-th/9803235 \[hep-th\]](#). Cited on page 9.

- [27] S. Dumitru, B. A. Ovrut, and A. Purves, *The R-parity violating decays of charginos and neutralinos in the B-L MSSM*, *Journal of High Energy Physics* **2019** (2019) 124, [https://doi.org/10.1007/JHEP02\(2019\)124](https://doi.org/10.1007/JHEP02(2019)124). Cited on pages 10, 11, 14, and 115.
- [28] Z. Marshall, B. A. Ovrut, A. Purves, and S. Spinner, *Spontaneous R-Parity breaking, stop LSP decays and the neutrino mass hierarchy*, *Phys. Lett. B* **732** (2014) 325–329, [arXiv:1401.7989 \[hep-ph\]](https://arxiv.org/abs/1401.7989). Cited on pages 11, 14, and 64.
- [29] Z. Marshall, B. A. Ovrut, A. Purves, and S. Spinner, *LSP squark decays at the LHC and the neutrino mass hierarchy*, *Phys. Rev. D* **90** (2014) 015034, [arXiv:1402.5434 \[hep-th\]](https://arxiv.org/abs/1402.5434). Cited on pages 11, 13, 14, and 64.
- [30] S. Dumitru, B. A. Ovrut, and A. Purves, *R-parity Violating Decays of Wino Chargino and Wino Neutralino LSPs and NLSPs at the LHC*, *JHEP* **06** (2019) 100, [arXiv:1811.05581 \[hep-ph\]](https://arxiv.org/abs/1811.05581). Cited on pages 11, 14, 15, 16, 17, 18, 19, and 20.
- [31] LHC Physics, *SUSY Cross Sections*, <https://twiki.cern.ch/twiki/bin/view/LHCPhysics/SUSYCrossSections>. Cited on page 12.
- [32] L. R. Evans and P. Bryant, *LHC Machine*, *JINST* **3** (2008) S08001, <https://cds.cern.ch/record/1129806>, This report is an abridged version of the LHC Design Report (CERN-2004-003). Cited on page 21.
- [33] ATLAS Collaboration, *The ATLAS Experiment at the CERN Large Hadron Collider*, *JINST* **3** (2008) S08003. Cited on pages 21, 25, 26, 30, and 31.
- [34] CMS Collaboration, *The CMS experiment at the CERN LHC*, *JINST* **3** (2008) S08004. Cited on page 21.
- [35] ALICE Collaboration, *The ALICE experiment at the CERN LHC*, *Journal of Instrumentation* **3** (2008) S08002–S08002. Cited on page 21.
- [36] LHCb Collaboration, *The LHCb Detector at the LHC*, *Journal of Instrumentation* **3** (2008) S08005–S08005. Cited on page 21.
- [37] J. Haffner, *The CERN accelerator complex*, <http://cds.cern.ch/record/1621894>, General Photo. Cited on page 22.
- [38] ATLAS Collaboration, *LuminosityPublicResultsRun2*, <https://twiki.cern.ch/twiki/bin/view/AtlasPublic/LuminosityPublicResultsRun2>. Cited on pages 23 and 24.
- [39] ATLAS Collaboration, *EventDisplayRun2Physics*, <https://twiki.cern.ch/twiki/bin/view/AtlasPublic/EventDisplayRun2Physics>. Cited on page 25.
- [40] ATLAS Collaboration, *ATLAS Insertable B-Layer Technical Design Report*, Atlas-tdr-19, 2010, <https://cds.cern.ch/record/1291633>. Cited on page 27.
- [41] ATLAS Collaboration, *Performance of the ATLAS track reconstruction algorithms in dense environments in LHC Run 2*, *Eur. Phys. J. C* **77** (2017) 673, [arXiv:1704.07983 \[hep-ex\]](https://arxiv.org/abs/1704.07983). Cited on pages 28, 34, and 38.

- [42] J. Pequenaio and P. Schaffner, *How ATLAS detects particles: diagram of particle paths in the detector*, Jan, 2013. Cited on page 33.
- [43] R. Fruhwirth, *Application of Kalman filtering to track and vertex fitting*, *Nucl. Instrum. Meth.* **A262** (1987) 444–450. Cited on page 34.
- [44] T. Cornelissen, M. Elsing, I. Gavrilenko, W. Liebig, E. Moyse, and A. Salzburger, *The new ATLAS track reconstruction (NEWT)*, *J. Phys.: Conf. Ser.* **119** (2008) 032014, <https://cds.cern.ch/record/1176900>. Cited on pages 34 and 38.
- [45] ATLAS Collaboration, *Reconstruction of primary vertices at the ATLAS experiment in Run 1 proton–proton collisions at the LHC*, *Eur. Phys. J. C* **77** (2017) 332, [arXiv:1611.10235](https://arxiv.org/abs/1611.10235) [hep-ex]. Cited on page 34.
- [46] ATLAS Collaboration, *Performance of primary vertex reconstruction in proton–proton collisions at $\sqrt{s} = 7$ TeV in the ATLAS experiment*, ATLAS-CONF-2010-069, 2010, <https://cds.cern.ch/record/1281344>. Cited on page 34.
- [47] ATLAS Collaboration, *Topological cell clustering in the ATLAS calorimeters and its performance in LHC Run 1*, *Eur. Phys. J. C* **77** (2017) 490, [arXiv:1603.02934](https://arxiv.org/abs/1603.02934) [hep-ex]. Cited on page 34.
- [48] ATLAS Collaboration, *Electron reconstruction and identification in the ATLAS experiment using the 2015 and 2016 LHC proton-proton collision data at $\sqrt{s} = 13$ TeV*, *Eur. Phys. J. C* **79** (2019) 639, [arXiv:1902.04655](https://arxiv.org/abs/1902.04655) [physics.ins-det]. Cited on page 34.
- [49] ATLAS Collaboration, *Measurement of the photon identification efficiencies with the ATLAS detector using LHC Run 2 data collected in 2015 and 2016*, *Eur. Phys. J. C* **79** (2019) 205, [arXiv:1810.05087](https://arxiv.org/abs/1810.05087) [hep-ex]. Cited on page 34.
- [50] M. Cacciari, G. P. Salam, and G. Soyez, *The anti- k_t jet clustering algorithm*, *JHEP* **04** (2008) 063, [arXiv:0802.1189](https://arxiv.org/abs/0802.1189) [hep-ph]. Cited on pages 34, 72, and 89.
- [51] M. Cacciari, G. P. Salam, and G. Soyez, *FastJet user manual*, *Eur. Phys. J. C* **72** (2012) 1896, [arXiv:1111.6097](https://arxiv.org/abs/1111.6097) [hep-ph]. Cited on pages 34 and 89.
- [52] ATLAS Collaboration, *Measurements of b-jet tagging efficiency with the ATLAS detector using $t\bar{t}$ events at $\sqrt{s} = 13$ TeV*, *JHEP* **08** (2018) 089, [arXiv:1805.01845](https://arxiv.org/abs/1805.01845) [hep-ex]. Cited on page 34.
- [53] ATLAS Collaboration, *Performance of missing transverse momentum reconstruction with the ATLAS detector using proton–proton collisions at $\sqrt{s} = 13$ TeV*, [arXiv:1802.08168](https://arxiv.org/abs/1802.08168) [hep-ex]. Cited on page 34.
- [54] ATLAS Collaboration, *Performance of the ATLAS Trigger System in 2015*, *Eur. Phys. J. C* **77** (2017) 317, [arXiv:1611.09661](https://arxiv.org/abs/1611.09661) [hep-ex]. Cited on page 35.
- [55] ATLAS Collaboration, *The ATLAS Data Acquisition and High Level Trigger system*, *Journal of Instrumentation* **11** (2016) P06008–P06008. Cited on page 35.
- [56] E. Abat et al., *The ATLAS TRT electronics*, *Journal of Instrumentation* **3** (2008) P06007–P06007. Cited on page 36.

- [57] A. Alonso, *Transition Radiation Tracker calibration, searches beyond the Standard Model and multiparticle correlations in ATLAS*, Apr, 2012. <https://cds.cern.ch/record/1452211>. Presented 20 May 2012. Cited on page 38.
- [58] ATLAS Collaboration, *Particle Identification Performance of the ATLAS Transition Radiation Tracker*, ATLAS-CONF-2011-128, 2011, <https://cds.cern.ch/record/1383793>. Cited on page 40.
- [59] ATLAS Collaboration, *Basic ATLAS TRT performance studies of Run 1*, ATL-INDET-PUB-2014-001, 2014, <https://cds.cern.ch/record/1669603>. Cited on page 40.
- [60] ATLAS Collaboration, *Performance of the ATLAS Inner Detector Track and Vertex Reconstruction in High Pile-Up LHC Environment*, ATLAS-CONF-2012-042, 2012, <https://cds.cern.ch/record/1435196>. Cited on page 41.
- [61] ATLAS Collaboration, *Tracking CP Recommendations for ICHEP 2016/20.7: Track Selection*, https://twiki.cern.ch/twiki/bin/view/AtlasProtected/TrackingCPICHEP2016#Track_Selection. Cited on page 58.
- [62] ATLAS Collaboration, *Tracking CP Recommendations for ICHEP 2016/20.7: Truth Definitions*, https://twiki.cern.ch/twiki/bin/view/AtlasProtected/TrackingCPICHEP2016#Truth_definitions. Cited on page 58.
- [63] ATLAS Collaboration, *Search for scalar leptoquarks in pp collisions at $\sqrt{s} = 13$ TeV with the ATLAS experiment*, *New J. Phys.* **18** (2016) 093016, [arXiv:1605.06035](https://arxiv.org/abs/1605.06035) [hep-ex]. Cited on page 64.
- [64] ATLAS Collaboration, *Searches for scalar leptoquarks in pp collisions at $\sqrt{s} = 8$ TeV with the ATLAS detector*, *Eur. Phys. J. C* **76** (2016) 5, [arXiv:1508.04735](https://arxiv.org/abs/1508.04735) [hep-ex]. Cited on page 64.
- [65] CMS Collaboration, *Search for third-generation scalar leptoquarks and heavy right-handed neutrinos in final states with two tau leptons and two jets in proton–proton collisions at $\sqrt{s} = 13$ TeV*, *JHEP* **07** (2017) 121, [arXiv:1703.03995](https://arxiv.org/abs/1703.03995) [hep-ex]. Cited on page 64.
- [66] CMS Collaboration, *Search for pair production of first and second generation leptoquarks in proton–proton collisions at $\sqrt{s} = 8$ TeV*, *Phys. Rev. D* **93** (2016) 032004, [arXiv:1509.03744](https://arxiv.org/abs/1509.03744) [hep-ex]. Cited on page 64.
- [67] B. Jackson, *A Search For $B - L$ R-Parity-Violating Scalar Top Decays in $\sqrt{s} = 8$ TeV pp Collisions With The ATLAS Experiment*, Jul, 2015. <https://cds.cern.ch/record/2050572>. Presented 08 Jul 2015. Cited on page 65.
- [68] G. Lerner, *Search for third generation scalar quarks in events with b-tagged jets with the ATLAS detector*, 2018. <https://cds.cern.ch/record/2644859>. Presented 22 Jun 2018. Cited on page 65.
- [69] ATLAS Collaboration, *Performance of the ATLAS Electron and Photon Trigger in pp Collisions at $\sqrt{s} = 7$ TeV in 2011*, ATLAS-CONF-2012-048, 2012, <https://cds.cern.ch/record/1450089>. Cited on pages 67 and 117.
- [70] ATLAS Collaboration, *Performance of electron and photon triggers in ATLAS during LHC Run 2*, [arXiv:1909.00761](https://arxiv.org/abs/1909.00761) [hep-ex]. Cited on pages 67 and 117.

- [71] ATLAS Collaboration, *Performance of the ATLAS muon trigger in pp collisions at $\sqrt{s} = 8$ TeV*, *Eur. Phys. J. C* **75** (2015) 120, [arXiv:1408.3179 \[hep-ex\]](#). Cited on pages 67 and 117.
- [72] ATLAS Collaboration, *Improved Luminosity Determination in pp Collisions at $\sqrt{s} = 7$ TeV Using the ATLAS Detector at the LHC*, *Eur. Phys. J. C* **73** (2013) 2518, [arXiv:1302.4393 \[hep-ex\]](#). Cited on page 70.
- [73] GEANT4 Collaboration, S. Agostinelli et al., *GEANT4: A Simulation Toolkit*, *Nucl. Instrum. Meth. A* **506** (2003) 250–303. Cited on page 70.
- [74] ATLAS Collaboration, *The ATLAS Simulation Infrastructure*, *European Physical Journal C* **70** (2010) 823–874, [arXiv:1005.4568 \[physics.ins-det\]](#). Cited on page 70.
- [75] T. Sjöstrand, S. Mrenna, and P. Z. Skands, *A brief introduction to PYTHIA 8.1*, *Comput. Phys. Commun.* **178** (2008) 852, [arXiv:0710.3820 \[hep-ph\]](#). Cited on pages 70 and 87.
- [76] ATLAS Collaboration, *New ATLAS event generator tunes to 2010 data*, ATL-PHYS-PUB-2011-008, 2011, <https://cds.cern.ch/record/1345343>. Cited on page 70.
- [77] P. Z. Skands, *Tuning Monte Carlo generators: The Perugia tunes*, *Phys. Rev. D* **82** (2010) 074018, [arXiv:1005.3457 \[hep-ph\]](#). Cited on pages 70 and 87.
- [78] T. Gleisberg, S. Hoeche, F. Krauss, M. Schonherr, S. Schumann, et al., *Event Generation with SHERPA 1.1*, *J. High Energy Phys.* **0902** (2009) 007, [arXiv:0811.4622 \[hep-ph\]](#). Cited on pages 70, 71, and 114.
- [79] J. Alwall, M. Herquet, F. Maltoni, O. Mattelaer, and T. Stelzer, *MadGraph 5 : Going Beyond*, *J. High Energy Phys.* **1106** (2011) 128, [arXiv:1106.0522 \[hep-ph\]](#). Cited on pages 70 and 115.
- [80] P. M. Nadolsky, H.-L. Lai, Q.-H. Cao, J. Huston, J. Pumplin, et al., *Implications of CTEQ Global Analysis for Collider Observables*, *Phys. Rev. D* **78** (2008) 013004, [arXiv:0802.0007 \[hep-ph\]](#). Cited on pages 70 and 71.
- [81] T. Sjöstrand, S. Mrenna, and P. Z. Skands, *PYTHIA 6.4 physics and manual*, *JHEP* **05** (2006) 026, [arXiv:hep-ph/0603175](#). Cited on pages 70 and 87.
- [82] W. Beenakker, M. Krämer, T. Plehn, M. Spira, and P. Zerwas, *Stop production at hadron colliders*, *Nucl. Phys. B* **515** (1998) 3–14, [arXiv:hep-ph/9710451](#). Cited on pages 70 and 88.
- [83] W. Beenakker et al., *Supersymmetric top and bottom squark production at hadron colliders*, *JHEP* **08** (2010) 098, [arXiv:1006.4771 \[hep-ph\]](#). Cited on pages 70 and 88.
- [84] W. Beenakker et al., *Squark and Gluino Hadroproduction*, *Int. J. Mod. Phys. A* **26** (2011) 2637–2664, [arXiv:1105.1110 \[hep-ph\]](#). Cited on pages 70 and 88.
- [85] M. Krämer et al., *Supersymmetry production cross sections in pp collisions at $\sqrt{s} = 7$ TeV*, [arXiv:1206.2892 \[hep-ph\]](#). Cited on pages 70 and 88.
- [86] P. Nason, *A New Method for Combining NLO QCD with Shower Monte Carlo Algorithms*, *J. High Energy Phys.* **0411** (2004) 040, [arXiv:hep-ph/0409146 \[hep-ph\]](#). Cited on pages 71, 114, and 115.

- [87] S. Frixione, P. Nason, and C. Oleari, *Matching NLO QCD Computations with Parton Shower Simulations: the POWHEG Method*, *J. High Energy Phys.* **0711** (2007) 070, [arXiv:0709.2092 \[hep-ph\]](#). Cited on pages 71, 114, and 115.
- [88] S. Alioli, P. Nason, C. Oleari, and E. Re, *A general framework for implementing NLO calculations in shower Monte Carlo programs: the POWHEG BOX*, *JHEP* **06** (2010) 043, [arXiv:1002.2581 \[hep-ph\]](#). Cited on pages 71, 86, 114, and 115.
- [89] S. Frixione, P. Nason, and G. Ridolfi, *A Positive-Weight Next-to-Leading-Order Monte Carlo for Heavy Flavour Hadroproduction*, *J. High Energy Phys.* **0709** (2007) 126, [arXiv:0707.3088 \[hep-ph\]](#). Cited on pages 71 and 114.
- [90] ATLAS Collaboration, *Measurements of Top Quark Pair Relative Differential Cross-Sections with ATLAS in pp Collisions at $\sqrt{s} = 7$ TeV*, *Eur. Phys. J.* **C73** (2013) 2261, [arXiv:1207.5644 \[hep-ex\]](#). Cited on page 71.
- [91] ATLAS Collaboration, *Measurements of Normalized Differential Cross Sections for $t\bar{t}$ Production in pp Collisions at $\sqrt{s} = 7$ TeV Using the ATLAS Detector*, *Phys. Rev.* **D90** (2014) 072004, [arXiv:1407.0371 \[hep-ex\]](#). Cited on page 71.
- [92] S. Alioli, P. Nason, C. Oleari, and E. Re, *NLO Single-Top Production Matched with Shower in POWHEG: s- and t-Channel Contributions*, *J. High Energy Phys.* **0909** (2009) 111, [arXiv:0907.4076 \[hep-ph\]](#). Cited on pages 71 and 115.
- [93] B. P. Kersevan and E. Richter-Was, *The Monte Carlo Event Generator AcerMC Versions 2.0 to 3.8 with Interfaces to PYTHIA 6.4, HERWIG 6.5 and ARIADNE 4.1*, *Comput. Phys. Commun.* **184** (2013) 919–985, [arXiv:hep-ph/0405247 \[hep-ph\]](#). Cited on page 71.
- [94] ATLAS Collaboration, *Electron and photon energy calibration with the ATLAS detector using LHC Run 1 data*, *Eur. Phys. J.* **C74** (2014) 3071, [arXiv:1407.5063 \[hep-ex\]](#). Cited on page 71.
- [95] ATLAS Collaboration, *Measurement of the Muon Reconstruction Performance of the ATLAS Detector Using 2011 and 2012 LHC Proton-Proton Collision Data*, *Eur. Phys. J.* **C74** (2014) 3130, [arXiv:1407.3935 \[hep-ex\]](#). Cited on page 71.
- [96] M. Cacciari and G. P. Salam, *Dispelling the N^3 Myth for the k_t Jet-Finder*, *Phys. Lett. B* **641** (2006) 57–61, [arXiv:hep-ph/0512210](#). Cited on page 72.
- [97] ATLAS Collaboration, *Jet Energy Measurement with the ATLAS Detector in Proton-Proton Collisions at $\sqrt{s} = 7$ TeV*, *Eur. Phys. J.* **C 73** (2013) 2304, [arXiv:1112.6426 \[hep-ex\]](#). Cited on page 72.
- [98] ATLAS Collaboration, *Single Hadron Response Measurement and Calorimeter Jet Energy Scale Uncertainty with the ATLAS Detector at the LHC*, *Eur.Phys.J.* **C73** (2013) 2305, [arXiv:1203.1302 \[hep-ex\]](#). Cited on page 72.
- [99] M. Cacciari and G. P. Salam, *Pileup subtraction using jet areas*, *Phys. Lett. B* **659** (2008) 119, [arXiv:0707.1378 \[hep-ph\]](#). Cited on pages 72 and 89.
- [100] ATLAS Collaboration, *Calibration of b-tagging using dileptonic top pair events in a combinatorial likelihood approach with the ATLAS experiment*, ATLAS-CONF-2014-004, 2014, <https://cds.cern.ch/record/1664335>. Cited on page 72.

- [101] ATLAS Collaboration, *Calibration of the performance of b -tagging for c and light-flavour jets in the 2012 ATLAS data*, ATLAS-CONF-2014-046, 2014, <https://cds.cern.ch/record/1741020>. Cited on page 72.
- [102] ATLAS Collaboration, *Performance of Missing Transverse Momentum Reconstruction in ATLAS studied in Proton-Proton Collisions recorded in 2012 at $\sqrt{s} = 8$ TeV*, ATLAS-CONF-2013-082, 2013, <https://cds.cern.ch/record/1570993>. Cited on page 73.
- [103] M. Baak, G. J. Besjes, D. Cte, A. Koutsman, J. Lorenz, and D. Short, *HistFitter software framework for statistical data analysis*, *Eur. Phys. J. C* **75** (2015) 153, [arXiv:1410.1280 \[hep-ex\]](#). Cited on pages 74, 80, 82, 91, 100, 114, and 145.
- [104] A. L. Read, *Presentation of search results: The $CL(s)$ technique*, *J. Phys. G* **28** (2002) 2693–2704. Cited on pages 82, 100, and 146.
- [105] ATLAS Collaboration, *Search for Third Generation Scalar Leptoquarks in pp Collisions at $\sqrt{s} = 7$ TeV with the ATLAS Detector*, *J. High Energy Phys.* **1306** (2013) 033, [arXiv:1303.0526 \[hep-ex\]](#). Cited on page 83.
- [106] ATLAS Collaboration, *Luminosity determination in pp collisions at $\sqrt{s} = 8$ TeV using the ATLAS detector at the LHC*, *Eur. Phys. J. C* **76** (2016) 653, [arXiv:1608.03953 \[hep-ex\]](#). Cited on pages 86 and 141.
- [107] M. Czakon and A. Mitov, *Top++: A program for the calculation of the top-pair cross-section at hadron colliders*, *Comput. Phys. Commun.* **185** (2014) 2930, [arXiv:1112.5675 \[hep-ph\]](#). Cited on pages 87 and 115.
- [108] N. Kidonakis, *Two-loop soft anomalous dimensions for single top quark associated production with a W - or H -*, *Phys. Rev. D* **82** (2010) 054018, [arXiv:1005.4451 \[hep-ph\]](#). Cited on page 87.
- [109] N. Kidonakis, *NNLL resummation for s -channel single top quark production*, *Phys. Rev. D* **81** (2010) 054028, [arXiv:1001.5034 \[hep-ph\]](#). Cited on page 87.
- [110] N. Kidonakis, *Next-to-next-to-leading-order collinear and soft gluon corrections for t -channel single top quark production*, *Phys. Rev. D* **83** (2011) 091503, [arXiv:1103.2792 \[hep-ph\]](#). Cited on page 87.
- [111] S. Catani, L. Cieri, G. Ferrera, D. de Florian, and M. Grazzini, *Vector boson production at hadron colliders: a fully exclusive QCD calculation at NNLO*, *Phys. Rev. Lett.* **103** (2009) 082001, [arXiv:0903.2120 \[hep-ph\]](#). Cited on page 87.
- [112] C. Borschensky, M. Kramer, A. Kulesza, M. Mangano, S. Padhi, T. Plehn, and X. Portell, *Squark and gluino production cross sections in pp collisions at $\sqrt{s} = 13, 14, 33$ and 100 TeV*, *Eur. Phys. J. C* **74** (2014) 3174, [arXiv:1407.5066 \[hep-ph\]](#). Cited on pages 87, 88, and 99.
- [113] ATLAS Collaboration, *Simulation of top-quark production for the ATLAS experiment at $\sqrt{s} = 13$ TeV*, ATLAS-PHYS-PUB-2016-004, 2016, <https://cds.cern.ch/record/2120417>. Cited on pages 86 and 98.
- [114] H.-L. Lai, M. Guzzi, J. Huston, Z. Li, P. M. Nadolsky, J. Pumplin, and C. P. Yuan, *New parton distributions for collider physics*, *Phys. Rev. D* **82** (2010) 074024, [arXiv:1007.2241 \[hep-ph\]](#). Cited on page 87.

- [115] J. Pumplin, D. R. Stump, J. Huston, H. L. Lai, P. M. Nadolsky, and W. K. Tung, *New generation of parton distributions with uncertainties from global QCD analysis*, **JHEP** **07** (2002) 012, [arXiv:hep-ph/0201195](#). Cited on pages 87 and 115.
- [116] R. Corke and T. Sjöstrand, *Improved parton showers at large transverse momenta*, **Eur. Phys. J. C** **69** (2010) 1, [arXiv:1003.2384 \[hep-ph\]](#). Cited on page 87.
- [117] ATLAS Collaboration, *Monte Carlo Generators for the Production of a W or Z/γ^* Boson in Association with Jets at ATLAS in Run 2*, ATL-PHYS-PUB-2016-003, 2016, <https://cds.cern.ch/record/2120133>. Cited on page 87.
- [118] T. Gleisberg, S. Hoeche, F. Krauss, M. Schonherr, S. Schumann, et al., *Event generation with SHERPA 1.1*, **JHEP** **02** (2009) 007, [arXiv:0811.4622 \[hep-ph\]](#). Cited on page 87.
- [119] T. Gleisberg and S. Hoeche, *Comix, a new matrix element generator*, **JHEP** **12** (2008) 039, [arXiv:0808.3674 \[hep-ph\]](#). Cited on page 87.
- [120] F. Cascioli, P. Maierhofer, and S. Pozzorini, *Scattering amplitudes with Open Loops*, **Phys. Rev. Lett.** **108** (2012) 111601, [arXiv:1111.5206 \[hep-ph\]](#). Cited on page 87.
- [121] S. Schumann and F. Krauss, *A Parton shower algorithm based on Catani-Seymour dipole factorisation*, **JHEP** **03** (2008) 038, [arXiv:0709.1027 \[hep-ph\]](#). Cited on page 87.
- [122] S. Hoeche, F. Krauss, M. Schonherr, and F. Siegert, *QCD matrix elements + parton showers: The NLO case*, **JHEP** **04** (2013) 027, [arXiv:1207.5030 \[hep-ph\]](#). Cited on page 87.
- [123] NNPDF Collaboration, R. D. Ball et al., *Parton distributions for the LHC Run II*, **JHEP** **04** (2015) 040, [arXiv:1410.8849 \[hep-ph\]](#). Cited on pages 87 and 115.
- [124] J. Alwall, R. Frederix, S. Frixione, V. Hirschi, F. Maltoni, O. Mattelaer, H. S. Shao, T. Stelzer, P. Torrielli, and M. Zaro, *The automated computation of tree-level and next-to-leading order differential cross sections, and their matching to parton shower simulations*, **JHEP** **07** (2014) 079, [arXiv:1405.0301 \[hep-ph\]](#). Cited on pages 87, 99, and 115.
- [125] L. Lönnblad and S. Prestel, *Matching Tree-Level Matrix Elements with Interleaved Showers*, **JHEP** **03** (2012) 019, [arXiv:1109.4829 \[hep-ph\]](#). Cited on page 87.
- [126] ATLAS Collaboration, *ATLAS Pythia 8 tunes to 7 TeV data*, ATL-PHYS-PUB-2014-021, 2014, <https://cds.cern.ch/record/1966419>. Cited on pages 87 and 115.
- [127] R. D. Ball et al., *Parton distributions with LHC data*, **Nucl. Phys. B** **867** (2013) 244–289, [arXiv:1207.1303 \[hep-ph\]](#). Cited on page 87.
- [128] D. J. Lange, *The EvtGen particle decay simulation package*, **Nucl. Instrum. Meth. A** **462** (2001) 152–155. Cited on page 88.
- [129] ATLAS Collaboration, *The ATLAS Simulation Infrastructure*, **Eur. Phys. J. C** **70** (2010) 823, [arXiv:1005.4568 \[physics.ins-det\]](#). Cited on page 88.
- [130] GEANT4 Collaboration, S. Agostinelli et al., *GEANT4: A simulation toolkit*, **Nucl. Instrum. Meth. A** **506** (2003) 250. Cited on page 88.
- [131] ATLAS Collaboration, *Summary of ATLAS Pythia 8 tunes*, ATL-PHYS-PUB-2012-003, 2012, <https://cds.cern.ch/record/1474107>. Cited on page 88.

- [132] A. D. Martin, W. J. Stirling, R. S. Thorne, and G. Watt, *Parton distributions for the LHC*, *Eur. Phys. J. C* **63** (2009) 189–285, [arXiv:0901.0002 \[hep-ph\]](#). Cited on page 88.
- [133] ATLAS Collaboration, P. Laycock, M. A. Chelstowska, T. Cuhadar Donszelmann, J. Guenther, A. M. Nairz, R. Nicolaïdou, E. Shabalina, J. Strandberg, A. Taffard, and S.-M. Wang, *ATLAS Data Preparation in Run 2*, Feb, 2017, <https://cds.cern.ch/record/2253427>. Cited on page 88.
- [134] ATLAS Collaboration, *Electron and photon energy calibration with the ATLAS detector using data collected in 2015 at $\sqrt{s} = 13$ TeV*, ATL-PHYS-PUB-2016-015, 2016, <https://cds.cern.ch/record/2203514>. Cited on page 89.
- [135] ATLAS Collaboration, *Electron efficiency measurements with the ATLAS detector using the 2015 LHC proton–proton collision data*, ATLAS-CONF-2016-024, 2016, <https://cds.cern.ch/record/2157687>. Cited on pages 89, 90, 97, and 141.
- [136] ATLAS Collaboration, *Muon reconstruction performance of the ATLAS detector in proton–proton collision data at $\sqrt{s} = 13$ TeV*, *Eur. Phys. J. C* **76** (2016) 292, [arXiv:1603.05598 \[hep-ex\]](#). Cited on pages 89, 90, 97, and 141.
- [137] ATLAS Collaboration, *Topological cell clustering in the ATLAS calorimeters and its performance in LHC Run 1*, *Eur. Phys. J. C* **77** (2017) 490, [arXiv:1603.02934 \[hep-ex\]](#). Cited on page 89.
- [138] ATLAS Collaboration, *Performance of pile-up mitigation techniques for jets in pp collisions at $\sqrt{s} = 8$ TeV using the ATLAS detector*, *Eur. Phys. J. C* **76** (2016) 581, [arXiv:1510.03823 \[hep-ex\]](#). Cited on page 89.
- [139] ATLAS Collaboration, *Jet energy scale measurements and their systematic uncertainties in proton–proton collisions at $\sqrt{s} = 13$ TeV with the ATLAS detector*, [arXiv:1703.09665 \[hep-ex\]](#). Cited on page 89.
- [140] ATLAS Collaboration, *Selection of jets produced in 13 TeV proton–proton collisions with the ATLAS detector*, ATLAS-CONF-2015-029, 2015, <https://cds.cern.ch/record/2037702>. Cited on page 89.
- [141] ATLAS Collaboration, *Performance of b-jet identification in the ATLAS experiment*, *JINST* **11** (2016) P04008, [arXiv:1512.01094 \[hep-ex\]](#). Cited on page 89.
- [142] ATLAS Collaboration, *Optimisation of the ATLAS b-tagging performance for the 2016 LHC Run*, ATL-PHYS-PUB-2016-012, 2016, <https://cds.cern.ch/record/2160731>. Cited on pages 89, 90, 97, and 141.
- [143] D. R. Tovey, *On measuring the masses of pair-produced semi-invisibly decaying particles at hadron colliders*, *JHEP* **04** (2008) 034, [arXiv:0802.2879 \[hep-ph\]](#). Cited on page 94.
- [144] ATLAS Collaboration, *Jet energy resolution in proton–proton collisions at $\sqrt{s} = 7$ TeV recorded in 2010 with the ATLAS detector*, *Eur. Phys. J. C* **73** (2013) 2306, [arXiv:1210.6210 \[hep-ex\]](#). Cited on pages 97 and 141.
- [145] ATLAS Collaboration, *Jet Calibration and Systematic Uncertainties for Jets Reconstructed in the ATLAS Detector at $\sqrt{s} = 13$ TeV*, ATL-PHYS-PUB-2015-015, 2015, <https://cds.cern.ch/record/2037613>. Cited on pages 97 and 141.

- [146] G. Marchesini, B. R. Webber, G. Abbiendi, I. G. Knowles, M. H. Seymour, and L. Stanco, *HERWIG: A Monte Carlo event generator for simulating hadron emission reactions with interfering gluons. Version 5.1 - April 1991*, *Comput. Phys. Commun.* **67** (1992) 465–508. Cited on page 98.
- [147] S. Gieseke, C. Rohr, and A. Siodmok, *Colour reconnections in Herwig++*, *Eur. Phys. J. C* **72** (2012) 2225, [arXiv:1206.0041](https://arxiv.org/abs/1206.0041) [hep-ph]. Cited on page 98.
- [148] ATLAS Collaboration, *Multi-boson simulation for 13 TeV ATLAS analyses*, ATL-PHYS-PUB-2016-002, 2016, <https://cds.cern.ch/record/2119986>. Cited on page 99.
- [149] S. Dimopoulos and L. Susskind, *Mass without scalars*, *Nuclear Physics B* **155** (1979) 237 – 252, <http://www.sciencedirect.com/science/article/pii/055032137990364X>. Cited on page 104.
- [150] S. Dimopoulos, *Technicoloured signatures*, *Nuclear Physics B* **168** (1980) 69 – 92, <http://www.sciencedirect.com/science/article/pii/0550321380902771>. Cited on page 104.
- [151] E. Eichten and K. Lane, *Dynamical breaking of weak interaction symmetries*, *Physics Letters B* **90** (1980) 125 – 130, <http://www.sciencedirect.com/science/article/pii/0370269380900659>. Cited on page 104.
- [152] V. Angelopoulos, J. Ellis, H. Kowalski, D. Nanopoulos, N. Tracas, and F. Zwirner, *Search for new quarks suggested by the superstring*, *Nuclear Physics B* **292** (1987) 59 – 92, <http://www.sciencedirect.com/science/article/pii/0550321387906377>. Cited on page 104.
- [153] W. Buchmüller and D. Wyler, *Constraints on SU(5)-type leptoquarks*, *Physics Letters B* **177** (1986) 377 – 382, <http://www.sciencedirect.com/science/article/pii/0370269386907719>. Cited on page 104.
- [154] J. C. Pati and A. Salam, *Lepton number as the fourth "color"*, *Phys. Rev. D* **10** (1974) 275–289, <https://link.aps.org/doi/10.1103/PhysRevD.10.275>. Cited on page 104.
- [155] H. Georgi and S. L. Glashow, *Unity of All Elementary-Particle Forces*, *Phys. Rev. Lett.* **32** (1974) 438–441, <https://link.aps.org/doi/10.1103/PhysRevLett.32.438>. Cited on page 104.
- [156] ATLAS Collaboration, *Searches for third-generation scalar leptoquarks in $\sqrt{s} = 13$ TeV pp collisions with the ATLAS detector*, *Journal of High Energy Physics* **2019** (2019) 144, [https://doi.org/10.1007/JHEP06\(2019\)144](https://doi.org/10.1007/JHEP06(2019)144). Cited on pages 104, 105, and 106.
- [157] ATLAS Collaboration, *Search for supersymmetry in events with b-tagged jets and missing transverse momentum in pp collisions at $\sqrt{s} = 13$ TeV with the ATLAS detector*, *JHEP* **11** (2017) 195, [arXiv:1708.09266](https://arxiv.org/abs/1708.09266) [hep-ex]. Cited on page 106.
- [158] ATLAS Collaboration, *Search for top-squark pair production in final states with one lepton, jets, and missing transverse momentum using 36 fb^{-1} of $\sqrt{s} = 13$ TeV pp collision data with the ATLAS detector*, [arXiv:1711.11520](https://arxiv.org/abs/1711.11520) [hep-ex]. Cited on page 106.

- [159] ATLAS Collaboration, *Search for a scalar partner of the top quark in the jets plus missing transverse momentum final state at $\sqrt{s} = 13$ TeV with the ATLAS detector*, *JHEP* **12** (2017) 085, [arXiv:1709.04183 \[hep-ex\]](#). Cited on page 106.
- [160] ATLAS Collaboration, *Search for top squarks decaying to tau sleptons in pp collisions at $\sqrt{s} = 13$ TeV with the ATLAS detector*, [arXiv:1803.10178 \[hep-ex\]](#). Cited on page 106.
- [161] ATLAS Collaboration, *Search for direct top squark pair production in final states with two leptons in $\sqrt{s} = 13$ TeV pp collisions with the ATLAS detector*, *Eur. Phys. J. C* **77** (2017) 898, [arXiv:1708.03247 \[hep-ex\]](#). Cited on page 106.
- [162] ATLAS Collaboration, *Search for dark matter and other new phenomena in events with an energetic jet and large missing transverse momentum using the ATLAS detector*, *JHEP* **01** (2018) 126, [arXiv:1711.03301 \[hep-ex\]](#). Cited on page 106.
- [163] ATLAS Collaboration, *Measurements of top-quark pair spin correlations in the $e\mu$ channel at $\sqrt{s} = 13$ TeV using pp collisions in the ATLAS detector*, Submitted to: *Eur. Phys. J.* (2019), [arXiv:1903.07570 \[hep-ex\]](#). Cited on page 106.
- [164] ATLAS Collaboration, *Search for supersymmetry in final states with charm jets and missing transverse momentum in 13 TeV pp collisions with the ATLAS detector*, *JHEP* **09** (2018) 050, [arXiv:1805.01649 \[hep-ex\]](#). Cited on page 106.
- [165] ATLAS Collaboration, *ATLAS Run 1 searches for direct pair production of third-generation squarks at the Large Hadron Collider*, *Eur. Phys. J. C* **75** (2015) 510, [arXiv:1506.08616 \[hep-ex\]](#). Cited on page 106.
- [166] ATLAS Collaboration, *Search for direct top squark pair production in the 3-body decay mode with a final state containing one lepton, jets, and missing transverse momentum in $\sqrt{s} = 13$ TeV pp collision data with the ATLAS detector*, Tech. Rep. ATLAS-CONF-2019-017, CERN, Geneva, May, 2019. <https://cds.cern.ch/record/2676594>. Cited on page 106.
- [167] ATLAS Collaboration, *SUSY July 2019 Summary Plot Update*, Tech. Rep. ATL-PHYS-PUB-2019-022, CERN, Geneva, Jul, 2019. <http://cds.cern.ch/record/2682063>. Cited on pages 106 and 107.
- [168] ATLAS Collaboration, *Search for type-III seesaw heavy leptons in pp collisions at $\sqrt{s} = 8$ TeV with the ATLAS Detector*, *Phys. Rev. D* **92** (2015) 032001, [arXiv:1506.01839 \[hep-ex\]](#). Cited on page 110.
- [169] ATLAS Collaboration, *Search for heavy lepton resonances decaying to a Z boson and a lepton in pp collisions at $\sqrt{s} = 8$ TeV with the ATLAS detector*, *JHEP* **09** (2015) 108, [arXiv:1506.01291 \[hep-ex\]](#). Cited on page 110.
- [170] CMS Collaboration, *Search for Evidence of the Type-III Seesaw Mechanism in Multilepton Final States in Proton-Proton Collisions at $\sqrt{s} = 13$ TeV*, *Phys. Rev. Lett.* **119** (2017) 221802, [arXiv:1708.07962 \[hep-ex\]](#). Cited on page 110.
- [171] S. Mele, *Z Z cross-section measurements*, pp. , 674–676. 2000. [arXiv:hep-ex/0009004 \[hep-ex\]](#). Cited on page 110.
- [172] A. Lipniacka, *Understanding SUSY limits from LEP*, [arXiv:hep-ph/0210356 \[hep-ph\]](#). Cited on page 110.

- [173] ATLAS Collaboration, *Studies on top-quark Monte Carlo modelling for Top2016*, ATL-PHYS-PUB-2016-020, 2016, <https://cds.cern.ch/record/2216168>. Cited on page 115.
- [174] T. Sjöstrand, S. Ask, J. R. Christiansen, R. Corke, N. Desai, P. Ilten, S. Mrenna, S. Prestel, C. O. Rasmussen, and P. Z. Skands, *An Introduction to PYTHIA 8.2*, *Comput. Phys. Commun.* **191** (2015) 159, [arXiv:1410.3012](https://arxiv.org/abs/1410.3012) [[hep-ph](#)]. Cited on page 115.
- [175] M. Beneke, P. Falgari, S. Klein, and C. Schwinn, *Hadronic top-quark pair production with NNLL threshold resummation*, *Nucl. Phys. B* **855** (2012) 695–741, [arXiv:1109.1536](https://arxiv.org/abs/1109.1536) [[hep-ph](#)]. Cited on page 115.
- [176] M. Cacciari, M. Czakon, M. Mangano, A. Mitov, and P. Nason, *Top-pair production at hadron colliders with next-to-next-to-leading logarithmic soft-gluon resummation*, *Phys. Lett. B* **710** (2012) 612–622, [arXiv:1111.5869](https://arxiv.org/abs/1111.5869) [[hep-ph](#)]. Cited on page 115.
- [177] P. Bärnreuther, M. Czakon, and A. Mitov, *Percent Level Precision Physics at the Tevatron: First Genuine NNLO QCD Corrections to $q\bar{q} \rightarrow t\bar{t} + X$* , *Phys. Rev. Lett.* **109** (2012) 132001, [arXiv:1204.5201](https://arxiv.org/abs/1204.5201) [[hep-ph](#)]. Cited on page 115.
- [178] M. Czakon and A. Mitov, *NNLO corrections to top-pair production at hadron colliders: the all-fermionic scattering channels*, *JHEP* **12** (2012) 054, [arXiv:1207.0236](https://arxiv.org/abs/1207.0236) [[hep-ph](#)]. Cited on page 115.
- [179] M. Czakon and A. Mitov, *NNLO corrections to top pair production at hadron colliders: the quark-gluon reaction*, *JHEP* **1301** (2013) 080, [arXiv:1210.6832](https://arxiv.org/abs/1210.6832) [[hep-ph](#)]. Cited on page 115.
- [180] M. Czakon, P. Fiedler, and A. Mitov, *The total top quark pair production cross-section at hadron colliders through $O(\alpha_s^4)$* , *Phys. Rev. Lett.* **110** (2013) 252004, [arXiv:1303.6254](https://arxiv.org/abs/1303.6254) [[hep-ph](#)]. Cited on page 115.
- [181] R. Frederix, E. Re, and P. Torrielli, *Single-top t -channel hadroproduction in the four-flavour scheme with POWHEG and aMC@NLO*, *JHEP* **09** (2012) 130, [arXiv:1207.5391](https://arxiv.org/abs/1207.5391) [[hep-ph](#)]. Cited on page 115.
- [182] E. Re, *Single-top Wt -channel production matched with parton showers using the POWHEG method*, *Eur. Phys. J. C* **71** (2011) 1547, [arXiv:1009.2450](https://arxiv.org/abs/1009.2450) [[hep-ph](#)]. Cited on page 115.
- [183] ATLAS Collaboration, *Measurement of the Z/γ^* boson transverse momentum distribution in pp collisions at $\sqrt{s} = 7$ TeV with the ATLAS detector*, *JHEP* **09** (2014) 145, [arXiv:1406.3660](https://arxiv.org/abs/1406.3660) [[hep-ex](#)]. Cited on page 115.
- [184] LHC Higgs Cross Section Working Group Collaboration, D. de Florian et al., *Handbook of LHC Higgs Cross Sections: 4. Deciphering the Nature of the Higgs Sector*, *FERMILAB-FN-1025-T*, *CERN-2017-002-M* (2016), [arXiv:1610.07922](https://arxiv.org/abs/1610.07922) [[hep-ph](#)]. Cited on page 115.
- [185] ATLAS Collaboration, *The simulation principle and performance of the ATLAS fast calorimeter simulation FastCaloSim*, ATL-PHYS-PUB-2010-013, 2010, <https://cds.cern.ch/record/1300517>. Cited on page 115.

- [186] B. Fuks, M. Klasen, D. R. Lamprea, and M. Rothering, *Gaugino production in proton-proton collisions at a center-of-mass energy of 8 TeV*, *JHEP* **10** (2012) 081, [arXiv:1207.2159 \[hep-ph\]](#). Cited on page 115.
- [187] B. Fuks, M. Klasen, D. R. Lamprea, and M. Rothering, *Precision predictions for electroweak superpartner production at hadron colliders with Resummino*, *Eur. Phys. J. C* **73** (2013) 2480, [arXiv:1304.0790 \[hep-ph\]](#). Cited on page 115.
- [188] ATLAS Collaboration, *Data Preparation Check List For Physics Analysis*, <https://twiki.cern.ch/twiki/bin/viewauth/Atlas/DataPreparationCheckListForPhysicsAnalysis>. Accessed: 2016-10-11. Cited on page 116.
- [189] ATLAS Collaboration, *Search for electroweak production of supersymmetric particles in final states with two or three leptons at $\sqrt{s} = 13$ TeV with the ATLAS detector*, [arXiv:1803.02762 \[hep-ex\]](#). Cited on page 128.
- [190] E. Tolley, D. Schaefer, T. J. Khoo, M. H. Klein, M. Petrov, M. Testa, F.-y. Tsai, M. Valente, C. J. Young, M. Scornajenghi, M. Saito, T. Eifert, and S. Heim, *E_T^{miss} performance in the ATLAS detector using 2015-2016 LHC p - p collisions*, Tech. Rep. ATL-COM-PHYS-2017-1732, CERN, Geneva, Dec, 2017. <https://cds.cern.ch/record/2294891>. Cited on page 141.
- [191] G. Avoni et al., *The new LUCID-2 detector for luminosity measurement and monitoring in ATLAS*, *JINST* **13** (2018) P07017. Cited on page 141.
- [192] ATLAS Collaboration, *SUSY Theoretical Uncertainties*, <https://twiki.cern.ch/twiki/bin/view/AtlasProtected/SUSYTheoreticalUncertainties>. Cited on page 141.
- [193] J. Butterworth et al., *PDF4LHC recommendations for LHC Run II*, *J. Phys. G* **43** (2016) 023001, [arXiv:1510.03865 \[hep-ph\]](#). Cited on page 142.
- [194] ATLAS Collaboration, *Combination of searches for Higgs boson pairs in pp collisions at $\sqrt{s} = 13$ TeV with the ATLAS detector*, [arXiv:1906.02025 \[hep-ex\]](#). Cited on page 153.
- [195] ATLAS Collaboration, *Search for non-resonant Higgs boson pair production in the $b\bar{b}\nu\bar{\nu}$ final state with the ATLAS detector in pp collisions at $\sqrt{s} = 13$ TeV*, [arXiv:1908.06765 \[hep-ex\]](#). Cited on page 153.
- [196] ATLAS Collaboration, *Measurements of b -jet tagging efficiency with the ATLAS detector using $t\bar{t}$ events at $\sqrt{s} = 13$ TeV*, *Journal of High Energy Physics* **2018** (2018) 89, [https://doi.org/10.1007/JHEP08\(2018\)089](https://doi.org/10.1007/JHEP08(2018)089). Cited on page 161.
- [197] ATLAS Collaboration, *Calibration of the ATLAS b -tagging algorithm in $t\bar{t}$ semi-leptonic events*, ATLAS-CONF-2018-045, 2018, <https://atlas.web.cern.ch/Atlas/GROUPS/PHYSICS/CONFNOTES/ATLAS-CONF-2018-045/>. Cited on page 162.
- [198] E. Jones, T. Oliphant, P. Peterson, et al., *SciPy: Open source scientific tools for Python*, 2001–. <http://www.scipy.org/>. Cited on page 171.